UNIVERSITÉ DU QUÉBEC

DÉTECTION DES ÉTATS GEL-DÉGEL DU SOL À L'AIDE DES DONNÉES DE RADAR À SYNTHÈSE D'OUVERTURE (RSO) SENTINEL-1 SUR LES TERRES AGRICOLES CANADIENNES ET ANALYSE DE LEURS EFFETS SUR L'HYDROLOGIE.

THÈSE PRÉSENTÉE
COMME EXIGENCE PARTIELLE DU

DOCTORAT EN SCIENCES DE L'ENVIRONNEMENT
OFFERT PAR L'UNIVERSITÉ DU QUÉBEC À MONTRÉAL
EN ASSOCIATION AVEC
L'UNIVERSITÉ DU QUÉBEC À TROIS-RIVIÈRES

PAR
SHAHABEDDIN TAGHIPOURJAVI

Mai 2026

UNIVERSITÉ DU QUÉBEC
DOCTORAT EN SCIENCES DE L'ENVIRONNEMENT (PH. D.)

Programme offert par l'Université du Québec à Montréal (UQAM) en association avec l'Université du Québec à Chicoutimi (UQAC) l'Université du Québec à Rimouski (UQAR) l'Université du Québec en Abitibi-Témiscamingue (UQAT) et l'Université du Québec à Trois-Rivières (UQTR)

Direction de recherche:

Christophe Kinnard, Ph. D.	Université du Québec à Trois-Rivières
Prénom et nom	directeur de recherche
Alexandre Roy, Ph. D.	Université du Québec à Trois-Rivières
Prénom et nom	codirecteur de recherche

Jury d'évaluation

Christophe Kinnard, Ph. D.	Université du Québec à Trois-Rivières
Directeur de recherche	
Alexandre Roy, Ph. D.	Université du Québec à Trois-Rivières
Codirecteur de recherche	
Léo Chassiot, Ph. D.	Université du Québec à Trois-Rivières
Président du jury	
Michel Baraër, Ph. D.	École de technologie supérieure – ÉTS, Montréal
Évaluateur externe	
Saeid Homayouni, Ph. D.	Centre Eau Terre Environnement, INRS, Québec
Évaluateur externe	

Thèse soutenue le 12 mars 2026

ACKNOWLEDGEMENTS

This thesis represents not only a research project, but also a long process supported by many people along the way.

To begin, I would like to sincerely thank my supervisor, Professor Christophe Kinnard, and my co-supervisor, Professor Alexandre Roy, for their guidance, support, and trust throughout this work. Your feedback and availability helped me move forward at every stage of this research, and I am truly grateful to both of you for everything I have learned during this time.

I would also like to thank the members of my evaluation committee for their time and valuable contributions: Professor Léo Chassiot, as jury president, Professor Michel Baraër (École de technologie supérieure-ÉTS), and Professor Saeid Homayouni (INRS Centre Eau Terre Environnement). Your careful review and constructive comments have contributed to improving the quality and clarity of this thesis. I would also like to acknowledge Ms. Joanie Trudel, who served as the institutional representative during my defense, for ensuring that the process was conducted in accordance with university regulations and for her role in facilitating the examination.

A special acknowledgement goes to my wife. Your constant support, encouragement, patience, and understanding throughout this entire period have been essential. You stood by me during both the most challenging and the most rewarding moments, and this achievement would not have been possible without you. Love you.

My appreciation extends to the academic environment at Université du Québec à Trois-Rivières, particularly to the members of the GlacioLab and the RIVE research community, for their collaboration, valuable discussions, and continuous support throughout this work. I would especially like to thank Charles and Chantal for their help and support.

I would like to sincerely thank my friends and colleagues who supported me during both fieldwork and laboratory activities. Your help and companionship made this journey much easier and more enjoyable. In particular, I would like to thank Arthur, Lisa, Hadi Mohamadzadeh, Hadi Mahmoudi, Rodrigo, Farshad, Arash, Vasana, Lisanne, Azza, Ismaguil, Mickaël, and Alex Gelinas for their support at different stages of this work.

I gratefully acknowledge the financial support received during my doctoral studies, including the FRQNT PBEEE scholarship, as well as institutional support from the UQTR through internal funding programs.

Finally, I would like to thank our families for their continuous support, encouragement, and understanding. Your support has been very important throughout this process.

TABLE OF CONTENTS

LIST OF TABLES

CHAPTER I:

CHAPTER II:

CHAPTER III:

LIST OF FIGURES

CHAPTER III:

RÉSUMÉ

Les transitions saisonnières gel-dégel des sols affectent près de 50 millions de km² de la surface terrestre mondiale et jouent un rôle central dans la régulation des échanges sol–atmosphère, du fonctionnement hydrologique des sols et de la génération du ruissellement dans les environnements agricoles des régions froides. Dans les paysages agro-forestiers, la répétition des cycles de gel-dégel modifie les régimes thermiques du sol, la capacité d'infiltration, la rugosité de surface et la connectivité hydrologique, influençant ainsi à la fois les processus à l'échelle de la parcelle et la réponse hydrologique des bassins versants. Toutefois, la dynamique spatiale et temporelle du gel des sols demeure difficile à caractériser aux échelles pertinentes, en raison de la couverture spatiale limitée des mesures in situ et de la résolution spatiale grossière des produits issus de la télédétection micro-ondes passive. En conséquence, le rôle du sol gelé dans le contrôle de la génération du ruissellement, en particulier lors des épisodes de pluie hivernale et de fonte nivale, reste encore insuffisamment contraint.

Cette thèse évalue la capacité des observations radar à synthèse d'ouverture (SAR) en bande C du satellite Sentinel-1 à restituer les conditions de gel–dégel du sol de surface dans des environnements agricoles et agro-forestiers, et examine dans quelle mesure l'information spatialisée sur l'état de gel des sols permet d'expliquer la réponse hydrologique en saison froide. L'objectif général est de développer, d'évaluer et d'appliquer un cadre robuste de détection du gel–dégel, allant au-delà d'une classification binaire rigide et favorisant une interprétation fondée sur les processus des dynamiques de ruissellement. Pour ce faire, la thèse combine une restitution probabiliste du gel des sols à partir des données Sentinel-1 SAR, des approches d'apprentissage automatique et des analyses hydrologiques événementielles, à des échelles locales, régionales et de bassin versant au Canada.

La première composante porte sur la détection fine du gel–dégel dans des environnements agro-forestiers du sud du Québec, au Canada. Des séries temporelles Sentinel-1 SAR ont été analysées sur deux sites instrumentés (St-Marthe et St-Maurice), où la température du sol a été mesurée à 2 et 10 cm de profondeur sur 18 parcelles au

cours des saisons froides 2020–2021 et 2021–2022. La probabilité de gel du sol a été estimée à l'aide d'une formulation probabiliste tenant compte des incertitudes de mesure et de la variabilité spatiale à petite échelle. Trois indicateurs radar du gel-dégel ont été évalués : une différence simple de rétrodiffusion par rapport à une référence dégelée (Delta), l'indice de gel-dégel (Freeze-Thaw Index, FTI) et un nouvel algorithme exponentiel de gel-dégel (Exponential Freeze-Thaw Algorithm, EFTA), dérivé des polarisations VV et VH. Les résultats montrent que l'EFTA basé sur la polarisation VH présente les meilleures performances prédictives, en particulier pour les conditions de surface, avec un pseudo-R^2 de 0,54 à 2 cm de profondeur, tout en réduisant significativement les fausses détections de gel durant les périodes de transition automnale et printanière. La modélisation à effets mixtes révèle en outre que les interactions entre l'EFTA et les types de cultures modulent la sensibilité radar au gel, assurant une robustesse spatiale et temporelle élevée, avec des précisions de classification supérieures à 85 %.

La deuxième composante étend la détection du gel-dégel à l'échelle nationale en évaluant la prévisibilité à grande échelle de l'état de gel du sol de surface dans les paysages agricoles canadiens. Les observations de température du sol à 5 cm de profondeur provenant de 174 stations agro-météorologiques réparties en Alberta, au Manitoba, en Saskatchewan et au Québec (2016–2023) ont été utilisées pour dériver à la fois des états binaires de gel–dégel et des probabilités continues de gel. La rétrodiffusion VH de Sentinel-1 SAR a été traitée dans Google Earth Engine selon une chaîne de traitement standardisée, et les indicateurs de gel-dégel ont été calculés à partir de la rétrodiffusion brute et de l'EFTA. Des modèles de classification et de régression par forêts aléatoires ont été entraînés afin de comparer les approches binaires et probabilistes de détection du gel. Les analyses diagnostiques indiquent que la variabilité de l'EFTA-VH est principalement contrôlée par la probabilité de gel du sol, expliquant l'essentiel de la variance prédictible du signal radar, tandis que les indicateurs liés à la neige contribuent de manière marginale. L'application de l'EFTA améliore la discrimination du gel–dégel, avec une précision passant d'environ 66 % pour la rétrodiffusion VH brute à plus de 81 %, l'EFTA-VH représentant plus de 90 % de l'importance des variables du modèle. Les validations croisées spatiales et temporelles confirment une forte transférabilité des modèles entre régions et années. Le cadre optimisé a été implémenté dans un outil web interactif

permettant la cartographie à la demande du gel-dégel pour des régions définies par l'utilisateur.

La composante finale de la thèse examine les implications hydrologiques des états de sol gelé spatialement distribués dans un bassin versant à vocation agricole intensive du sud du Québec. En s'appuyant sur le bassin de la rivière l'Acadie (2015–2025), l'étendue du sol gelé, dérivée du rétrodiffusion VH de Sentinel-1 (EFTA), a été intégrée aux données de précipitations et de fonte nivale d'ERA5-Land ainsi qu'aux débits observés afin d'analyser la réponse du ruissellement durant la saison froide. Les analyses à l'échelle journalière ont révélé des coefficients de ruissellement systématiquement plus élevés sous des conditions majoritairement gelées, atteignant environ 2,4 pour des fenêtres temporelles courtes et diminuant jusqu'à environ 1,0 en cinq jours, ce qui indique une capacité d'infiltration réduite et une connectivité hydrologique accrue. L'analyse de corrélation croisée a montré un décalage dominant d'un jour dans la réponse du débit, avec un couplage maximal en hiver ($r \approx 0{,}64$). L'analyse événementielle a mis en évidence des relations faibles entre l'étendue du sol gelé et les coefficients de ruissellement à l'échelle des événements ($R^2 \approx 0{,}04$; $p \approx 0{,}12$), indiquant que le sol gelé à lui seul n'explique pas la variabilité du ruissellement. Les modèles linéaires généralisés (GLM) à distribution gamma ont montré que la génération du ruissellement est principalement contrôlée par les apports d'eau liquide ($AIC = 176{,}75$; $p < 0{,}001$), tandis que les effets du sol gelé sont systématiquement positifs mais non significatifs sur le plan statistique ($p \approx 0{,}06$–$0{,}12$). En revanche, l'humidité antécédente n'a montré aucune influence significative ($p > 0{,}25$). Ces résultats indiquent que les conditions de sol gelé influencent le développement et l'efficacité du ruissellement, sans constituer un facteur de contrôle statistiquement dominant de son intensité.

Pris ensemble, ces résultats montrent que les données Sentinel-1 en bande C, combinées à l'algorithme exponentiel de gel-dégel et à des approches d'apprentissage automatique, offrent un cadre robuste et transférable pour la détection des dynamiques de gel-dégel du sol de surface dans des environnements agricoles et agroforestiers. À l'échelle hydrologique, les apports d'eau liquide apparaissent comme le principal facteur

de contrôle de la génération du ruissellement, tandis que les conditions de sol gelé spatialement distribuées reflètent des états environnementaux plus larges qui coévoluent avec la réponse hydrologique. Les analyses à l'échelle événementielle indiquent que le sol gelé n'agit pas comme un prédicteur indépendant de l'intensité du ruissellement, mais qu'il capte plutôt des conditions sous-jacentes liées au calendrier et à la structure de la réponse hydrologique. Ces résultats soulignent l'importance d'intégrer l'information spatialement distribuée sur le gel-dégel avec des données hydrométéorologiques afin d'améliorer la compréhension et la représentation, fondées sur les processus, des dynamiques hydrologiques de la saison froide dans les bassins versants agricoles.

Mots-clés

Rétrodiffusion SAR en bande C Sentinel-1; Algorithme exponentiel de gel-dégel (EFTA); Probabilité de gel du sol de surface; Modélisation par forêts aléatoires; Paysages agro-forestiers de St-Marthe et St-Maurice; Détection gel–dégel à la demande via plateforme web; Analyse hydrologique événementielle; Gel saisonnier des sols et réponse du ruissellement ; Bassins versants agricoles canadiens.

ABSTRACT

Seasonal soil freeze-thaw (FT) transitions affect nearly 50 million km² of the global land surface and play a central role in regulating land-atmosphere exchanges, soil hydrological functioning, and runoff generation in cold-region agricultural environments. In agro-forested landscapes, repeated FT cycles modify soil thermal regimes, infiltration capacity, surface roughness, and hydrological connectivity, thereby influencing both field-scale processes and catchment-scale discharge response. However, the spatial and temporal dynamics of soil freezing remain difficult to characterize at relevant scales due to the sparse coverage of in situ measurements and the coarse spatial resolution of passive microwave remote sensing products. As a result, the role of frozen soil in controlling runoff generation, particularly during cold-season rainfall and snowmelt events, remains insufficiently constrained.

This thesis evaluates the capability of Sentinel-1 C-band synthetic aperture radar (SAR) observations to retrieve near-surface soil FT conditions in agricultural and agro-forested environments and examines how spatially distributed frozen soil states can be used to explain cold-season hydrological response. The overarching objective is to develop, evaluate, and apply a robust FT detection framework that moves beyond rigid binary classification and supports process-based interpretation of runoff dynamics. To achieve this, the thesis integrates probabilistic FT retrieval from Sentinel-1 SAR with machine-learning methods and event-based hydrological analysis across local, regional, and catchment scales in Canada.

The first component of this work focuses on fine-scale FT detection in agro-forested environments of southern Québec, Canada. Sentinel-1 SAR time series were evaluated at two instrumented sites (St-Marthe and St-Maurice), where soil temperature was measured at 2 and 10 cm depths across 18 plots during the 2020–21 and 2021–22 cold seasons. Soil freezing probability was derived using a probabilistic formulation accounting for measurement uncertainty and small-scale spatial variability. Three radar-based FT indicators were assessed: a simple backscatter difference relative to a thawed reference (Delta), the Freeze-Thaw Index (FTI), and a newly developed Exponential Freeze-Thaw

Algorithm (EFTA), derived from VV and VH polarizations. Results demonstrate that the VH-based EFTA provides the strongest predictive performance, particularly for near-surface conditions, achieving a Pseudo-R^2 of 0.54 at 2 cm depth and substantially reducing false frozen detections during fall and spring transition periods. Mixed effects modeling further revealed that interactions between EFTA and crop type modulate radar sensitivity to freezing, yielding robust spatial and temporal transferability with classification accuracies exceeding 85%.

The second component extends FT detection to the national scale by evaluating the large-scale predictability of near-surface soil FT states across Canadian agricultural landscapes. Soil temperature observations at 5 cm depth from 174 agricultural weather stations distributed across Alberta, Manitoba, Saskatchewan, and Québec (2016–2023) were used to derive both binary FT states and continuous freezing probabilities. Sentinel-1 SAR VH backscatter was processed in Google Earth Engine using a standardized workflow, and FT indicators were derived from raw backscatter and EFTA. Random Forest classification and regression models were trained to compare binary and probabilistic FT detection frameworks. Diagnostic analyses showed that variability in VH-based EFTA is primarily controlled by soil freezing probability, explaining most predictable variance in the radar signal, while snow-related indicators contributed marginally. Application of EFTA improved FT discrimination from approximately 66% accuracy using raw VH backscatter to over 81% accuracy, with VH_{EFTA} accounting for more than 90% of model importance. Spatial and temporal cross-validation confirmed strong model transferability across regions and years. The optimized framework was implemented within an interactive web-based tool enabling on-demand FT mapping for user-defined regions.

The final component of the thesis examines the hydrological implications of spatially distributed frozen soil states in an intensively agricultural catchment in southern Québec. Using the Acadie River basin (2015–2025), frozen soil extent retrieved from Sentinel-1 VH backscatter (EFTA) was integrated with ERA5-Land rainfall and snowmelt data and observed discharge to analyze cold-season runoff response. Daily-scale analyses

revealed consistently higher runoff coefficients under predominantly frozen conditions, reaching ~2.4 at short time windows and decreasing to ~1.0 within 5 days, indicating reduced infiltration capacity and enhanced hydrological connectivity. Cross-correlation analysis showed a dominant one-day discharge response lag, with the strongest coupling during winter ($r \approx 0.64$). Event-based analysis showed weak relationships between frozen soil extent and event-scale runoff coefficients ($R^2 \approx 0.04$; $p \approx 0.12$), indicating that frozen soil alone does not explain runoff variability. Gamma generalized linear models (GLMs) indicated that runoff generation is primarily governed by liquid water input (AIC = 176.75; $p < 0.001$), while frozen soil effects were consistently positive but not statistically significant ($p \approx 0.06$–0.12). In contrast, antecedent wetness showed no significant influence ($p > 0.25$). These results indicate that frozen soil conditions influence runoff development and efficiency but do not emerge as a statistically dominant control on runoff magnitude.

Together, these results demonstrate that Sentinel-1 C-band SAR, combined with the Exponential Freeze–Thaw Algorithm and machine-learning approaches, provides a robust and transferable framework for detecting near-surface soil FT dynamics across agricultural and agro-forested environments. At the hydrological scale, liquid water input emerges as the primary control on runoff generation, while spatially distributed frozen soil conditions reflect broader environmental states that co-evolve with runoff response. Event-scale analyses indicate that frozen soil does not act as an independent predictor of runoff magnitude, but rather captures underlying conditions linked to the timing and structure of hydrological response. These findings highlight the importance of integrating spatially distributed FT information with hydrometeorological data to advance the process-based understanding and representation of cold-season hydrological dynamics in agricultural catchments.

Keywords

Sentinel-1 SAR C-band backscatter; Exponential Freeze-Thaw Algorithm (EFTA); Near surface soil freezing probability; Random Forest modeling; St-Marthe and St-Maurice agro-forested lands; On-demand web-based freeze-thaw detection; Event-based

runoff analysis; Seasonal soil freezing and hydrological runoff response; Canadian agricultural catchments.

INTRODUCTION

Freeze–thaw (FT) processes constitute a fundamental land-surface process in cold and temperate terrestrial environments. In the Northern Hemisphere, large-scale assessments show that FT-affected soils occupy well over half of the land surface, highlighting the broad geographic reach of these seasonal transitions (Li et al, 2021b). Recent observations further indicate that the timing and duration of FT patterns are shifting in response to contemporary climate warming (IPCC, 2019; Yang et al, 2024). These broad spatial and temporal changes highlight the importance of FT dynamics in regulating surface hydrological processes, soil–vegetation interactions, and land-atmosphere exchanges. A clear definition of FT cycles is therefore essential for understanding their environmental impacts. Beyond their role as a thermal indicator, FT transitions act as a dynamic regulator of soil physical state, governing the availability and mobility of water at the land surface and thereby exerting a first-order control on cold-season hydrological responses across agricultural and mixed land-use landscapes.

In most studies, FT cycles are identified by tracking daily fluctuations in shallow soil temperature (e.g., 0–10 cm), where characteristic alternations between colder and warmer conditions signal periods of freezing and subsequent thawing (Li et al, 2021a; Li et al, 2024). From a near-surface perspective, a “diurnal” FT cycle occurs when the daily maximum soil temperature rises above 0 °C while the minimum falls below 0 °C, so that soil freezes at night and thaws during the day (Guo et al, 2011; Li et al, 2024). Beyond diurnal variability, seasonal FT refers to the natural annual process during which soils undergo repeated freezing and thawing cycles (Li et al, 2021c; Williams et al, 2015). During the cold season, soil temperatures drop below 0 °C, causing water in the soil to freeze; as temperatures rise in spring, the soil thaws, and this cycle can repeat several times within a season depending on local climate conditions (Moradi et al, 2023a; Shi et al, 2025).

In seasonally frozen ground, the zone above a certain depth experiences temperatures below 0 °C for weeks to months, but the soil beneath a characteristic depth remains unfrozen throughout the year (Frauenfeld & Zhang, 2011; Zheng et al, 2020).

This characteristic depth is known as the maximum seasonal freezing depth (SFD), and it varies by region, climate, soil type, and surface conditions (Chen et al, 2022). The downward-moving freezing front is controlled by the balance between heat loss at the surface, thermal conductivity of the soil, and the latent heat associated with the phase change of pore water. In many temperate and sub-boreal regions, seasonal freezing can penetrate tens of centimeters to several meters, depending on snow insulation, soil moisture, and climate. For instance, agricultural regions show pronounced spatial variability in frost penetration: in the Canadian Prairies, field observations indicate that soils typically freeze to depths of roughly 80 cm in lowland croplands and close to 100 cm in upland fields(Sanchez-Rodriguez et al, 2025), whereas in arid and semi-arid farming areas of the Loess Plateau in China, seasonal freezing is much shallower, commonly limited to about 20–50 cm (Chou & Wang, 2021). Although seasonal freezing depth provides an important indicator of subsurface conditions, hydrological responses during rainfall and snowmelt events are often influenced by the near-surface freezing state, where even shallow frozen layers can restrict infiltration and promote rapid runoff generation; however, at the catchment scale, this influence is often modulated by broader hydrological conditions and spatial variability (Appels et al, 2018; Shanley & Chalmers, 1999).

Additionally, the duration and severity of soil freezing commonly exhibit an inverse relationship with snow cover thickness (Fitzhugh et al, 2001). Thicker snow acts as an effective insulator, reducing heat loss from the soil to the atmosphere and thereby limiting both the depth and persistence of soil freezing. Experimental studies have shown that when snow cover is removed or reduced, the frequency of FT cycles at the soil surface can increase by over 50%, and the intensity of freezing can be significantly greater, with colder minimum soil temperatures and deeper frost penetration (Sarady & Sahlin, 2016). However, it is not only the presence of snow but also the sequence of its accumulation and disappearance that determines soil temperature evolution. When snowfall arrives unusually late in autumn or early winter and melt occurs late in spring, the combined effect can lead to substantial cooling of the ground, with mean annual surface temperatures reduced by up to 3 °C (Zhang, 2005). Hence, natural snow accumulation can prolong the duration of the seasonal FT cycle by up to a month, but with less severe freezing conditions due to the insulating effect of snow.

Therefore, the frequency and intensity of the soil FT process may be enhanced by the increased occurrence of discontinuous snow cover and rain-on-snow events (Putkonen & Roe, 2003). Discontinuous or patchy snow cover, as well as midwinter thaw events caused by rain or snowmelt, can reduce the insulating capacity of the snowpack, exposing soils to more rapid and extreme temperature fluctuations. This leads to more frequent and intense FT cycles, which can disrupt soil structure, increase nutrient leaching, and alter greenhouse gas emissions. Field and modeling studies have demonstrated that reduced or intermittent snow cover, as well as rain-on-snow events, can double the number of FT cycles and substantially increase the depth and severity of soil freezing, with important implications for soil biogeochemistry and ecosystem processes (Ruan & Robertson, 2017; Watanabe et al, 2019). From a hydrological perspective, these amplified FT dynamics increase the likelihood of rapid runoff generation during winter and early spring by repeatedly disrupting soil permeability and altering the timing at which liquid water becomes available at the surface.

Frozen soils, particularly through the action of FTCs, play an important role in regulating terrestrial ecosystem functioning by physically modifying soil structure and influencing the timing and pathways of biogeochemical processes (Gao et al, 2018a; Song et al, 2017). Repeated freezing and thawing disrupt soil aggregates and organic matter associations, altering pore structure and facilitating the redistribution of water and dissolved constituents during critical transition periods such as spring thaw (Kreyling et al, 2020). The physical breakdown of plant tissues and microbial cells during FTCs can temporarily increase the availability and mobility of nutrients, especially during the first thawing events of the season (Joseph & Henry, 2008; Matzner & Borken, 2008). The magnitude of these responses varies across climatic and land-use contexts and is strongly modulated by soil moisture, organic matter content, and the frequency and intensity of FT events (Ji et al, 2022; Song et al, 2017). In cold, snow-affected regions, changes in snow cover and winter temperature regimes can increase exposure of soils to FTCs, enhancing the physical disturbance of the soil matrix and modifying seasonal patterns of nutrient mobilization (Kreyling et al, 2020). Conversely, soils in regions with frequent winter temperature fluctuations may exhibit dampened biogeochemical responses, reflecting both microbial adaptation and reduced availability of labile substrates (Jansson &

Hofmockel, 2020). Although FT states have been associated with pronounced pulses of nutrient release and greenhouse gas emissions in agricultural systems, these responses are largely indirect and mediated by the physical state of the soil, its thermal regime, and hydrological connectivity during thaw periods (Ji et al, 2022; Leuther & Schlüter, 2021). Consequently, the spatial and temporal evolution of soil FT conditions constitutes a fundamental control on downstream biogeochemical and ecological responses, highlighting the importance of accurately characterizing FT dynamics even when biogeochemical processes are not explicitly quantified. In this thesis, biogeochemical implications are not analyzed directly; however, they provide critical context for understanding why accurate characterization of spatial and temporal FT visibility is essential for interpreting hydrological connectivity and downstream environmental impacts.

The depth and severity of soil freezing are strongly influenced by land cover and management: bare, tilled soils without vegetation are most vulnerable, as the absence of insulating plant residue or snow allows rapid heat loss from the soil to the atmosphere, resulting in deeper and more abrupt FT fronts, often reaching 30–100 cm depending on climate and snow cover, with the most pronounced changes typically in the upper 10–30 cm (Fu et al, 2017; Zhang et al, 2021). In contrast, soils under perennial vegetation, cover crops, or shelterbelts experience shallower and more gradual freezing, as plant cover insulates the surface, buffers temperature fluctuations, and slows the advance of the freezing front, leading to higher soil temperatures and reduced FT damage at all depths (Bo et al, 2021; Ding et al, 2023). Soil texture is a key determinant of FT response: clay-rich and silty clay loam soils, with high water retention, are more susceptible to frost heave, aggregate breakdown, and macropore collapse during FTCs, especially when tilled or left bare, resulting in significant reductions in shear strength, porosity, and aggregate stability, and making them more prone to compaction and erosion (Deng et al, 2025; Kloffel et al, 2024). Loam and sandy soils, with lower water-holding capacity, freeze and thaw more quickly and are less prone to heaving, but can experience rapid changes in hydraulic conductivity and water redistribution, especially near the surface, which can affect water availability for crops and increase the risk of surface runoff (Ren & Vanapalli, 2020; Xu et al, 2022).

Snow cover plays a central role in regulating soil freezing by altering surface thermal insulation and moderating temperature variability at the ground surface. In snow-free conditions, such as bare land or post-harvest agricultural fields, the energy balance is dominated by net radiation (shortwave and longwave), sensible and latent heat fluxes, and ground heat flux (Leonardini et al, 2020; Pozníková et al, 2018). When the soil is frozen and exposed, energy loss to the atmosphere is high, especially at night, leading to rapid soil cooling and deeper frost penetration (Sakai & Larcher, 2012). The addition of crop residues (e.g., corn or canola sticks) can slightly reduce heat loss by increasing surface roughness and trapping thin snow, but their insulating effect is minor compared to a full snowpack (Liu & Lobb, 2021; Sanchez-Rodriguez et al, 2025; Sharratt, 2002). With the onset of snowpack during transitional shoulder seasons, the energy balance shifts dramatically. Even a thin layer of snow increases surface albedo, reflecting more solar radiation and reducing net energy input (Sedlar et al, 2011). However, snow's most profound effect is its thermal insulation: as snow accumulates, it reduces conductive heat loss from the soil to the cold atmosphere, slowing further soil freezing and moderating temperature fluctuations (Fu et al, 2018; Peng et al, 2024). The insulating effect is strongly dependent on snow depth and density thicker, low-density dry snow provides greater insulation, while thin or compacted wet snow is less effective (Pomeroy & Brun, 2001; Zhang, 2005). In early winter, rapid snow accumulation can trap residual ground heat, resulting in warmer soils beneath the snowpack, while delayed snow onset allows deeper soil freezing (Lafrenière et al, 2013). During winter, when frozen soil lies beneath a persistent snowpack, the snow acts as a thermal buffer. The ground surface temperature is decoupled from air temperature, with the snowpack's properties (depth, density, wetness) controlling the rate of heat loss (Kondo & Yamazaki, 1990; Zhang, 2005). Wet snow, with higher density and thermal conductivity, transmits more heat than dry, fluffy snow, leading to colder soils under wet snow conditions (Chen et al, 2021; Royer et al, 2021). Conversely, deep, dry snow maximizes insulation, keeping soils warmer and reducing frost depth (Peng et al, 2024). On agricultural fields, snowmelt infiltration into frozen soils is governed by soil structure and macropores; bare or compacted soils may generate more runoff, while fields with crop residue or macropores allow greater infiltration and groundwater recharge (Roy et al, 2017b; Sanchez-Rodriguez et al, 2025).

From a hydrological perspective, soil freezing directly controls infiltration–runoff partitioning, linking FT dynamics closely to hydrological extremes in agricultural and mixed land-use watersheds. When near-surface soils freeze, ice formation within pore spaces reduces effective hydraulic conductivity and limits vertical infiltration, even when deeper soil layers remain unfrozen (Jiang et al, 2021; Watanabe & Osada, 2017b). As a result, rainfall and snowmelt inputs are more readily converted into surface runoff, enhancing hydrological connectivity and accelerating streamflow response. Importantly, the degree to which these processes operate depends not only on whether soil is frozen, but on the spatial extent and continuity of frozen areas across the landscape, which governs the balance between infiltration-excess and saturation-excess runoff mechanisms. When the ground remains frozen at the onset of snowmelt, the majority of meltwater cannot infiltrate and instead flows rapidly overland, leading to higher and earlier streamflow peaks and increasing the probability of floods (Ala-Aho et al, 2021; Sanchez-Rodriguez et al, 2025). For example, modeling studies show that in cold midlatitude regions, the most consistent hydrological response to frozen soil is the earlier occurrence of snowmelt floods and an overall increase in winter streamflow, while summer flows may decrease due to reduced soil moisture recharge (Aygün et al, 2020a). The timing and depth of soil freezing are critical: early and deep freezing can trap more water in the soil, reducing baseflow and increasing the proportion of runoff generated during thaw (Luo et al, 2020b). Conversely, later or shallower freezing allows more water to drain before the soil becomes impermeable, moderating flood risk. Rain-on-snow events, which can occur in late fall or early spring, add further complexity by introducing liquid water to a snow-covered, often frozen landscape, leading to rapid runoff generation if the soil is impermeable, or to enhanced infiltration if preferential flow paths remain open (Zhao et al, 2021). The interplay between temperature, precipitation phase, and soil FT status thus creates a highly dynamic and spatially variable hydrological regime in seasonally frozen regions, with important implications for flood forecasting in agroecosystem areas. These mechanisms explain why accurate characterization of soil FT state is essential for hydrological prediction in cold agricultural watersheds.

During the transition from autumn to winter in seasonally frozen landscapes, soil begins to freeze as air temperatures drop, and the water content present at the time of

freeze-up is largely retained in the soil profile throughout the winter, a phenomenon known as soil moisture memory, which can significantly influence the hydrological response during the subsequent spring melt period (Coles et al, 2016). As snow accumulates on the frozen ground, the soil remains largely dormant, with minimal hydrological activity until temperatures rise again in late winter or early spring (Sanchez-Rodriguez et al, 2025). When spring arrives, snowmelt typically begins while the soil is still partially or fully frozen, resulting in a complex partitioning of meltwater between infiltration and surface runoff, with the degree of infiltration highly dependent on the presence of macropores, antecedent soil moisture, and the rate of melt (Mohammed et al, 2021a). In many agricultural and prairie landscapes, such as those in the Canadian Prairies, field observations and modeling show that preferential flow through air-filled macropores can allow some infiltration even when the soil is frozen, but as repeated melt events occur, refreezing of infiltrated water along these pathways can progressively reduce infiltrability and increase surface runoff generation (Mohammed et al, 2019). The timing and magnitude of spring runoff are therefore not only a function of snowmelt volume but are also strongly controlled by the antecedent soil moisture at freeze-up, the depth and persistence of soil frost, and the rate and duration of the melt event itself (Coles et al, 2016; Kinnard et al, 2024). These interacting controls imply that hydrological responses during the cold season cannot be adequately interpreted without explicit information on the spatial distribution and temporal persistence of frozen soil conditions.

FT transitions occur gradually and exhibit strong spatial variability; consequently, the representation of FT “state” (binary versus probabilistic) directly influences both interpretation and mapping. Both binary and probabilistic approaches are widely used to represent the soil FT “state,”(Walker et al, 2022) even though, FT is a continuous multiphase process in which liquid water, ice, and supercooled water coexist rather than a simple frozen–unfrozen dichotomy (An et al, 2024; Bi et al, 2023; Wan et al, 2022). As soil temperature decreases, ice tends to form first in larger pores, while smaller pores and adsorbed layers retain supercooled liquid water (Wang et al, 2023; Xusheng et al, 2023). This phase separation creates gradients in matric potential and temperature, which drive water migration toward the freezing front and promote ice lens growth and frost heave (Lai et al, 2014). This multiphase system results in temperature-dependent changes in

hydraulic conductivity, mechanical strength, and soil structure, as the presence and distribution of unfrozen water control both the movement of water and the mechanical response of the soil matrix (Ren & Vanapalli, 2020; Zou et al, 2023). Although binary FT classification methods are widely used and highly effective for operational soil state monitoring (Rodriguez-Alvarez et al, 2024; Shao & Zhang, 2020a), they may not fully capture the complexity of FT transitions, especially in heterogeneous landscapes or during shoulder seasons. On the other hand, approaches that treat soil freezing as a continuous or probabilistic process offer a more physically realistic and nuanced representation of FT states. Continuous models recognize that not all water in soil freezes at the same temperature; some unfrozen water remains even at subzero temperatures, and phase change occurs over a temperature range (Bi et al, 2023; Shan et al, 2025). Together, these complementary representations support more realistic characterization of soil FT transitions and improve the interpretation of gradual changes, such as the migration of freezing fronts and the evolution of near-surface temperature and moisture profiles (Soltanpour & Foriero, 2025; Sweidan et al, 2022). This conceptual distinction between binary and probabilistic representations forms a central theme of this thesis, motivating the development, evaluation, and application of both binary and probabilistic FT retrievals derived from active microwave observations.

In-situ and traditional methods for monitoring soil FT cycles such as soil temperature sensors, dielectric permittivity probes, frost tubes, and geophysical techniques—form the foundation for understanding FT processes at the point and field scales (Gao et al, 2018b; Shao & Zhang, 2020a). These approaches provide high temporal resolution and direct measurements of soil temperature and moisture dynamics, enabling detailed investigation of FT processes and their effects on soil physical properties and hydrological behavior (Li et al, 2021a; Pardo Lara et al, 2020). However, their spatial coverage remains inherently limited due to the cost, labor intensity, and logistical challenges associated with installing and maintaining dense monitoring networks, particularly in remote or environmentally harsh regions (Comite et al, 2020; Wu et al, 2017). As a result, observation sites are often sparse and unevenly distributed, restricting their ability to capture the spatial heterogeneity of FT processes or to support regional- to continental-scale assessments (Wang et al, 2017). In addition, near-surface in-situ FT

measurements are strongly influenced by local soil texture, vegetation cover, and microclimatic conditions, complicating inter-site comparisons and limiting generalization across landscapes (Lundberg et al, 2016a; Wang et al, 2017). Although laboratory experiments and numerical models including analytical formulations such as Stefan's equation and physically based energy-balance approaches offer valuable mechanistic insights, they require extensive parameterization and validation and remain constrained by uncertainties in soil thermal properties, latent heat representation, and dielectric behavior (Alpar et al, 2024; Norouzi et al, 2024). Consequently, despite their importance for process-level understanding, traditional observation and modeling approaches alone remain insufficient for operational monitoring of FT dynamics over large, heterogeneous regions.

Passive microwave remote sensing addresses this limitation by exploiting the sensitivity of land-surface brightness temperature (TB) to changes in soil dielectric properties associated with freezing and thawing (Hallikainen et al, 1985). The physical basis of FT detection lies in the strong contrast between the dielectric permittivity of liquid water and ice: as soil water freezes, the effective dielectric constant decreases, producing measurable changes in microwave emission (Mavrovic et al, 2021; Wu et al, 2022). Brightness temperature therefore responds not only to soil temperature but also to variations in unfrozen water content, making passive microwave observations particularly sensitive to FT transitions near 0 °C (Zhang et al, 2010; Zheng et al, 2017). Early studies demonstrated the use of spectral gradients at 18–37 GHz from Nimbus-7 SMMR and later SSM/I observations to discriminate frozen and thawed soil conditions under snow-free surfaces (Chang & Cao, 1996; Zuerndorfer et al, 1990). Subsequent work showed that negative spectral gradients and changes in vertically polarized TB at higher frequencies, such as 37 GHz, provide robust indicators of soil freezing due to reductions in unfrozen water content and surface emissivity (Zhang & Armstrong, 2001).

Building on these principles, passive FT retrieval algorithms evolved from simple threshold-based classifications to more advanced change-detection and ratio-based approaches using multi-frequency and dual-polarization observations (Kim et al, 2010b;

Zhao et al, 2011). Sensors such as AMSR-E and AMSR2 have been widely applied to derive FT indicators from vertically polarized TB at 19 and 37 GHz, benefiting from frequent revisit times and sensitivity to near-surface thermal conditions (Du et al, 2017; Kim et al, 2017). More recent developments emphasize L-band (1.4 GHz) observations from SMOS and SMAP, which are more sensitive to soil permittivity changes associated with the liquid–ice transition and less affected by vegetation and surface roughness than higher-frequency sensors (Gao et al, 2018b; Rautiainen et al, 2014). At L-band, freezing modifies both the dielectric properties of soil and the effective emitting depth sensed by the radiometer, producing distinct TB responses that support the development of dedicated FT products (Donahue et al, 2023a; Rowlandson et al, 2018).

Passive microwave FT products have therefore become central to large-scale monitoring of seasonal freezing and thawing due to their broad spatial coverage and frequent temporal sampling (Gao et al, 2021b; Kim et al, 2017). Missions such as SMAP provide routine Level-3 FT classifications on grids of approximately 36 km resolution across northern land areas, with generally good agreement relative to in-situ soil temperature observations at shallow depths (Derksen et al, 2017a; Kim et al, 2019). However, the coarse spatial resolution of passive microwave observations, typically 10–40 km, limits their applicability for field-scale analysis, particularly in heterogeneous agricultural landscapes where individual pixels integrate mixed land-cover types, surface water, vegetation, and snow conditions (Rowlandson et al, 2018; Roy et al, 2017a). In addition, passive FT retrievals are sensitive to variable snow depth, wet snow conditions, vegetation density, and transient surface water, which can mask soil emission signals and introduce uncertainty during freeze-up and spring thaw periods (Kim et al, 2017; Kim et al, 2019). These limitations motivate the use of higher-resolution active microwave observations for resolving spatially detailed FT changes. Resolving FT heterogeneity at the scale of agricultural fields and catchments requires observations that combine physical sensitivity to soil freezing with spatial resolutions compatible with hydrological process analysis.

Active microwave remote sensing, particularly synthetic aperture radar (SAR), provides the necessary spatial resolution and physical sensitivity to characterize FT patterns at the field scale. SAR observations combine meter- to tens-of-meters spatial resolution with strong sensitivity of radar backscatter to the phase state of water in soil, vegetation, and snow (Wang et al, 2022; Zhou et al, 2021). At microwave frequencies, the transition from liquid to frozen water causes a pronounced reduction in the real part of the dielectric constant, which is the primary driver of FT-related backscatter change (Rignot & Way, 1994; Wu et al, 2022). Soil and surface water freezing generally reduce surface scattering by lowering the Fresnel reflection coefficient, while simultaneously modifying volume scattering within porous media such as the soil active layer, crop canopies, and snowpacks (Cohen et al, 2024a; Park, 2015). The magnitude and sign of FT-induced backscatter change depend on polarization and surface conditions. Co-polarized channels (e.g., VV) are often more directly linked to surface scattering and are therefore strongly influenced by soil roughness. In contrast, cross-polarized (VH) returns are more sensitive to multiple scattering and structural complexity arising from vegetation, soil aggregates, crop residues, and small-scale roughness (Baghdadi et al, 2017; Singh et al, 2023). These interactions promote partial depolarization and enhance VH backscatter relative to smooth bare surfaces. As a result, even in sparsely vegetated or post-harvest agricultural fields, VH can exhibit increased sensitivity to changes in near-surface conditions, making it particularly suitable for detecting FT transitions.

Radar backscatter over agricultural landscapes is governed by the combined influence of polarization, surface roughness, structural heterogeneity, and incidence angle (Figure 1). Variations in these factors modulate the observed signal and must be considered when interpreting FT changes, particularly in heterogeneous agricultural areas where surface conditions evolve throughout the season.

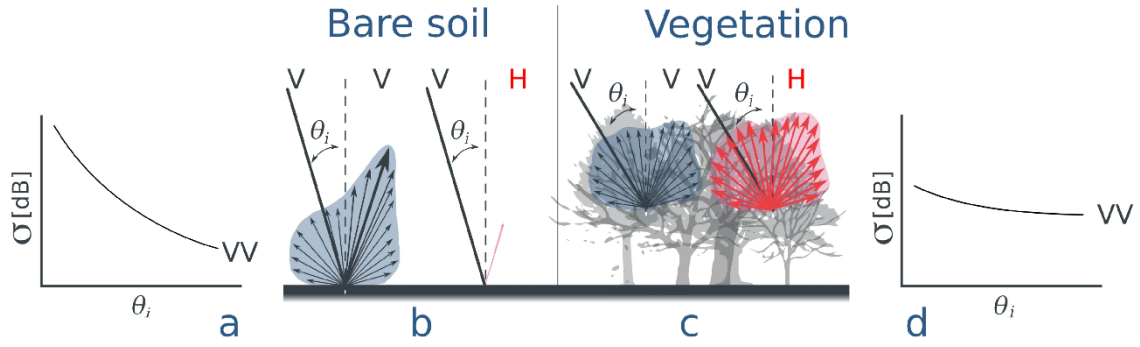

Figure 1. Conceptual representation of SAR backscatter mechanisms over agricultural surfaces and their dependence on incidence angle (θ_i), polarization, and surface conditions. Panels (**a–b**) illustrate bare soil responses, where backscatter (σ^0) decreases with increasing incidence angle under smooth conditions due to dominant specular reflection, resulting in a steep angular response. As surface roughness increases, diffuse scattering becomes more important, leading to higher backscatter and reduced angular dependence. Panels (**c–d**) show vegetated or structurally complex surfaces, where volume scattering dominates due to randomly distributed elements within the canopy or residue layer, producing a flatter angular response with limited sensitivity to incidence angle. Multiple scattering within these media induces depolarization, enhancing cross-polarized (VH) backscatter relative to co-polarized (VV) returns. Together, these mechanisms demonstrate how polarization, surface roughness, structural heterogeneity, and incidence angle control radar backscatter and influence its interpretation in FT studies. (Adapted from Vreugdenhil et al (2020)).

Most radar-based FT detection approaches exploit temporal variations in backscatter rather than absolute signal levels, which are strongly influenced by surface roughness, vegetation structure, and acquisition geometry behavior (Kimball et al, 2001; Wang et al, 2022). Change-detection techniques therefore emphasize relative deviations in σ^0 time series by defining frozen and thawed reference states and applying seasonal normalization to reduce site-specific biases (Baghdadi et al, 2002a; Bergstedt et al, 2020; Taghavi-Bayat et al, 2024). Difference- and ratio-based indices, such as $\Delta\sigma$ metrics, highlight departures from reference conditions associated with freeze-up and thaw onset (Rautiainen et al, 2016; Wang et al, 2022). FT transitions commonly produce multi-decibel changes in σ^0,

typically on the order of 3–6 dB at C- and Ku-band and up to approximately 7–8 dB at L-band over seasonally frozen non-forested terrain (Kimball et al, 2004; Park, 2015; Podest et al, 2014).

Within this framework, radar-based FT retrieval has evolved from simple binary classification toward more nuanced probabilistic representations of soil freezing state. Classical threshold-based methods remain attractive for operational mapping due to their simplicity and computational efficiency and form the basis of many Sentinel-1 and ASCAT FT products (Taghavi-Bayat et al, 2024; Wang et al, 2022). However, fixed thresholds often perform poorly during transitional periods characterized by mixed frozen–thawed conditions, shallow freezing, or dynamic snow and vegetation states (Bartsch et al, 2025; Kim et al, 2017). To address these limitations, probabilistic approaches increasingly treat FT as a continuous multiphase process by estimating freezing probability or fractional frozen area rather than discrete states (Shao & Zhang, 2020a; Walker et al, 2022). Such approaches allow FT dynamics to be represented more realistically across heterogeneous landscapes and provide a stronger physical basis for linking microwave observations to soil thermal and hydrological behavior.

The primary objective of this thesis is to improve the detection, representation, and application of near-surface soil FT changes in agricultural environments using Sentinel-1 C-band SAR observations. To move beyond rigid frozen–thawed classifications, this work explores how empirical, change-detection-based radar metrics derived from Sentinel-1 SAR backscatter can be related to soil freezing probability in order to better capture the gradual, heterogeneous, and multiphase nature of soil freezing. Accordingly, the thesis first examines the relationship between radar-based FT detection and near-surface soil freezing probability in agro-forested agricultural settings of southern Québec, where site-specific conditions such as soil texture, crop type, crop residue, and surface roughness modulate radar backscatter responses (chapter 1). At a broader spatial scale, the thesis extends this approach to spatially distributed and on-demand FT monitoring across Canadian agricultural landscapes by evaluating the large-scale performance and generalizability of radar-based FT detection through both binary classification and

probability-based prediction models, integrating change-detection–based radar metrics with machine-learning approaches and implementing the best-performing models within a web-based on-demand FT mapping tool (chapter 2). Finally, the thesis applies the retrieved FT information to investigate the influence of near-surface frozen soil extent on winter and spring runoff generation in an agro-forested catchment of southern Québec, linking spatially distributed FT conditions to event-scale hydrological responses under varying rainfall, snowmelt, and antecedent wetness conditions (chapter 3).

CHAPTER I

Chapter I

Sentinel-1-Based Soil Freeze-Thaw Detection in Agro-Forested Areas: A Case Study in Southern Québec, Canada

Shahabeddin Taghipourjavi, Christophe Kinnard and Alexandre Roy

Remote Sensing. 2024, 16(7), 1294; https://doi.org/10.3390/rs16071294

Abstract

Nearly 50 million km^2 of global land experiences seasonal transitions from predominantly frozen to thawed conditions, significantly impacting various ecosystems and hydrologic processes. In this study, we assessed the capability to retrieve surface freeze-thaw (FT) conditions using Sentinel-1 synthetic aperture radar (SAR) data time series at two agro-forested study sites, St-Marthe and St-Maurice, in southern Québec, Canada. In total, 18 plots were instrumented to monitor soil temperature and derive soil freezing probabilities at 2 and 10 cm depths during 2020–21 and 2021–22. Three change detection algorithms were tested: backscatter differences ($\Delta\sigma$) derived from thawed reference (Delta), the freeze-thaw index (FTI), and a newly developed exponential freeze-thaw algorithm (EFTA). Various probabilistic mixed models were compared to identifying the model and predictor variables that best predicted soil freezing probability. VH polarization backscatter signals processed with the EFTA and used as predictors in a logistic model led to improved predictions of soil freezing probability at 2 cm (Pseudo-R^2 = 0.54) compared to other approaches. The EFTA could effectively address the limitations of the Delta algorithm caused by backscatter fluctuations in the shoulder seasons, resulting in more precise estimates of FT events. Furthermore, the inclusion of crop types as plot-level effects within the probabilistic model also slightly improved the soil freezing probability prediction at each monitored plot, with marginal and conditional R^2 values of 0.59 and 0.61, respectively. The model accurately classified observed binary 'frozen' or

‘thawed’ states with 85.2% accuracy. Strong cross-level interactions were also observed between crop types and the EFTA derived from VH backscatter, indicating that crop type modulated the backscatter response to soil freezing. This study represents the first application of the EFTA and a probabilistic approach to detect frozen soil conditions in agro-forested areas in southern Quebec, Canada.

Keywords

Freeze-Thaw Probability; Mixed Models; Exponential Freeze-Thaw Algorithm (EFTA); Sentinel 1 SAR; Agro-forested areas.

1.1. Introduction

Seasonal soil freezing is a widespread natural process that occurs in a significant portion of land areas, spanning over more than half of the northern hemisphere (Henry, 2007; Zhang et al, 2003). Nearly 50 million km^2 of land surfaces experience the seasonal transition from predominantly frozen to thawed states every year (Gao et al, 2021a; McDonald et al, 2004). The impact of frozen soils in cold regions can be observed in various aspects of climate, hydrology, and terrestrial ecosystems. These effects manifest in surface energy balance, seasonal runoff patterns, and the biogeochemical cycling of elements on Earth, operating at diverse scales (Walvoord & Kurylyk, 2016; Wang et al, 2019). In farmlands, the repeated FT cycles in soils can significantly impact the availability of effective soil nutrients and modify vital soil biochemical components, which in turn affect plant growth and development in agricultural ecosystems (Cober et al, 2018; Krogstad, 2021). The soil structure is highly sensitive to freezing and thawing events, wherein repeated freeze-thaw (FT) cycles lead to decreased strength and size of aggregates, breaking up of soil into microscopic particles, and increased soil erodibility during snow melting (Edwards, 2013; Leuther & Schlüter, 2021).

Earlier research has focused on the local scale or at individual sites to monitor near-surface FT state in soils (Guo & Wang, 2014; Wang et al, 2015). Nevertheless, traditional approaches such as in situ point measurements, geophysical methods, and numerical

simulations are inadequate in capturing the temporal variations of freezing and thawing states near the surface across extensive geographical areas (Peng et al, 2016a; Wang et al, 2017). Environmental conditions such as hydrological and climate variables, soil properties, and vegetation cover can induce spatial and temporal variability in the FT state of seasonally frozen ground at various scales (Luo et al, 2020a; Xu et al, 2021). The spatial-temporal variability of FT processes significantly impact various aspects of agriculture, including crop growth and germination, soil water distribution, heat balance, soil moisture availability, and redistribution of organic matter (Qin et al, 2021a). Understanding the spatio-temporal patterns of FT provides valuable insights into hydrological processes, enabling effective water resource management and mitigation of flood risks (Li et al, 2021e). Additionally, FT changes play a pivotal role in nutrient cycling, carbon sequestration, and microbial activity, which are essential for the functioning of ecosystems (Cheng et al, 2018; Zhao et al, 2020).

Remote sensing is a valuable method to capture the spatial variability of frozen ground conditions related to environmental conditions. Detecting near-surface FT states can be carried out with both active and passive microwave data. Several studies have demonstrated that microwave remote sensing can estimate soil freezing/thawing states (Roy et al, 2017b; Shao & Zhang, 2020a). In addition, microwave observations can penetrate cloud cover, rain, and dust to detect FT conditions. Passive microwave sensors, including the Soil Moisture Ocean Salinity (SMOS) (Rautiainen et al, 2011), the Soil Moisture Active Passive (SMAP) (Derksen et al, 2017c), the Scanning Multi-channel Microwave Radiometer (SMMR) (Jin et al, 2015), and the Advanced Microwave Scanning Radiometer Enhanced (AMSR-E) (Zhao et al, 2011), have proven their capability to monitor seasonal FT conditions of surface soil. While passive microwave remote sensing products provide valuable insights into FT changes at a large spatial scale, their ability to monitor and assess such dynamics in agricultural fields is hindered by the presence of significant spatial variability. This limitation stems from the coarse spatial resolution of these products (>10 km), which makes them less suitable for accurately capturing fine-scale variations in soil freeze–thaw within agricultural contexts. Hence, the coarse spatial resolution of passive microwave remote sensing products poses challenges for precise monitoring of soil freeze–thaw in agricultural fields (Roy et al, 2017a).

Meanwhile, several space-borne synthetic aperture radar (SAR) sensors, such as Advanced SAR (ASAR) L-band (Park et al, 2011) and Phrase Array L-band Synthetic Aperture Radar (PALSAR) L-band (Du et al, 2014) have been used to provide near-surface FT state detection. Theoretical principles driving the use of active microwave sensors to discern soil FT states rely on the intricate interplay between backscatter and soil surface properties, particularly dielectric constants, and surface roughness, during FT processes. The radar signal primarily responds to variations in the soil's dielectric constant, which is influenced by the presence of water and ice; higher levels of free liquid water correspond to elevated dielectric constants (McDonald et al, 2012). This transition from water to ice alters the dielectric permittivity, typically ranging from 2 to 3 for dry soil (Rodionova, 2019a). In croplands, the behavior of C-band radar signals is strongly influenced by surface roughness and soil moisture, shaping microwave scattering at the soil's upper layers and impacting backscattering coefficients observed by radar sensors (Baghdadi et al, 2018; Fayad et al, 2020). However, when soil moisture levels exceed 35%, the impact of surface roughness on backscattering signals diminishes (Escobar, 2017). Agricultural practices like tillage directly affect surface roughness, influencing radar return. Smooth surfaces act as specular reflectors, deflecting most radar energy and resulting in weak signals, while rough surfaces scatter microwave energy, producing strong and diffuse signals (Hudier & Gosselin, 2010). Co- and cross-polarized waves interact with the surface differently, yielding distinct backscatter amplitudes to the sensor. Holah et al (2005), in an ASAR (Advanced Synthetic Aperture Radar) data analysis of soil surface parameter (surface roughness and soil moisture) over bare fields, found HH and HV polarizations to exhibit greater sensitivity to soil roughness compared to VV polarization. These findings underscore the importance of surface roughness and radar polarization in interpreting radar data in agricultural fields. For instance, Khaldoune et al (2011) established a threshold algorithm for frozen soil, employing linear regression to differentiate between frozen and unfrozen fields based on HH backscattering coefficients (σ°). The study's findings emphasized the effectiveness of the RADARSAT-1 sensor to map frozen soil in agricultural fields at the Bras d'Henri site in southern Quebec. Rodionova (2019b) investigated the relationship between radar and in situ observations of frozen soil state by analyzing the dual-polarization (VV + VH) signals of Sentinel-1 (S1) C-band radar in Interferometric Wide Swath (IW) Mode. The study revealed a significant

relationship between the VV backscatter and soil temperature at a depth of 5 cm. The establishment of threshold values for the VV backscatter coefficient facilitated the generation of maps capable of distinguishing between frozen and thawed soils.

Over the past few years, S1 C-band SAR products have proven particularly useful for soil FT detection at local and regional scales due to their high spatial resolution (10 m). Baghdadi et al (2018) retrieved land surface FT states using the C-band SAR data from S1 by thresholding the SAR data by 3 dB, assuming that soil roughness is stable, and crop types have an insignificant effect. Fayad et al (2020) nonetheless found that the difference between the acquired σ° and the mean of the previous three calculated maximum σ° values mitigated the influence of roughness effects over agricultural areas and pastures. Previous approaches for FT retrieval relied on strict temperature references and a binary method with predetermined thresholds for frozen conditions. However, this approach has limitations, including sensitivity to temperature variations leading to misclassification, lack of flexibility due to fixed thresholds that oversimplify freezing dynamics, and failure to consider the non-binary nature of soil freezing. Furthermore, the effectiveness of fixed thresholds in radar signal interpretation is limited by the potential influence of other soil surface conditions, particularly in agricultural contexts, such as soil type, crop variety, and residues, leading to shortcomings in their applicability across different regions.

While previous studies on frozen states have primarily employed a rigid classification system, i.e., frozen versus thawed states, this work introduces the concept of soil freezing probability, allowing us to use a probabilistic interpretation of soil FT states and study their complex spatio-temporal dynamics in agro-forested landscapes. This complexity arises from various factors that influence radar signals by altering surface roughness, such as spatial variability in soil texture and changes in crop types, along with the intricate interactions among these variables (Escobar, 2017; Holah et al, 2005). The aim of this study encompasses three objectives: First, we analyze the freeze–thaw variability using freezing probability derived from in situ soil temperature at 2 and 10 cm at two study sites over the study periods of 2020–21 and 2021–22. Afterwards, we

compare three change detection algorithms with different S1 SAR polarizations to determine their ability to predict the near-surface (2 and 10 cm) soil freezing probability using generalized linear models (GLM). Finally, different probabilistic mixed model structures are tested, taking into account the effect of site conditions (crop residues, soil, and crop types) on the predictions.

1.2. Materials and Methods

1.2.1. Study Sites

Two agro-forested sites, St-Maurice (46.48°N, 72.50°W) and St-Marthe (45.41°N, 74.30°W) in southern Quebec (Figure 1.1), were equipped with soil temperature data loggers in order to monitor soil temperature and identify FT states in fall of 2020 and 2021. Both sites exhibit a landscape blend of agriculture and forest, though each has distinct characteristics. The St-Maurice site encompasses agricultural areas as well as a mixed forest consisting of poplars (*Populus x canadensis*), red maples (*Acer rubrum*), white pines (*Pinus strobus*), and balsam firs (*Abies balsamea*) (Dharmadasa et al, 2022). Meanwhile, the St-Marthe site is located between the St. Lawrence and Ottawa rivers west of Montreal Island. The site is characterized by a diverse deciduous forest surrounded by agricultural fields. Within the forested area, sugar maple (*Acer saccharum*) and red maple (*Acer rubrum*) trees dominate the landscape, alongside a conifer plantation (Dharmadasa et al, 2022).

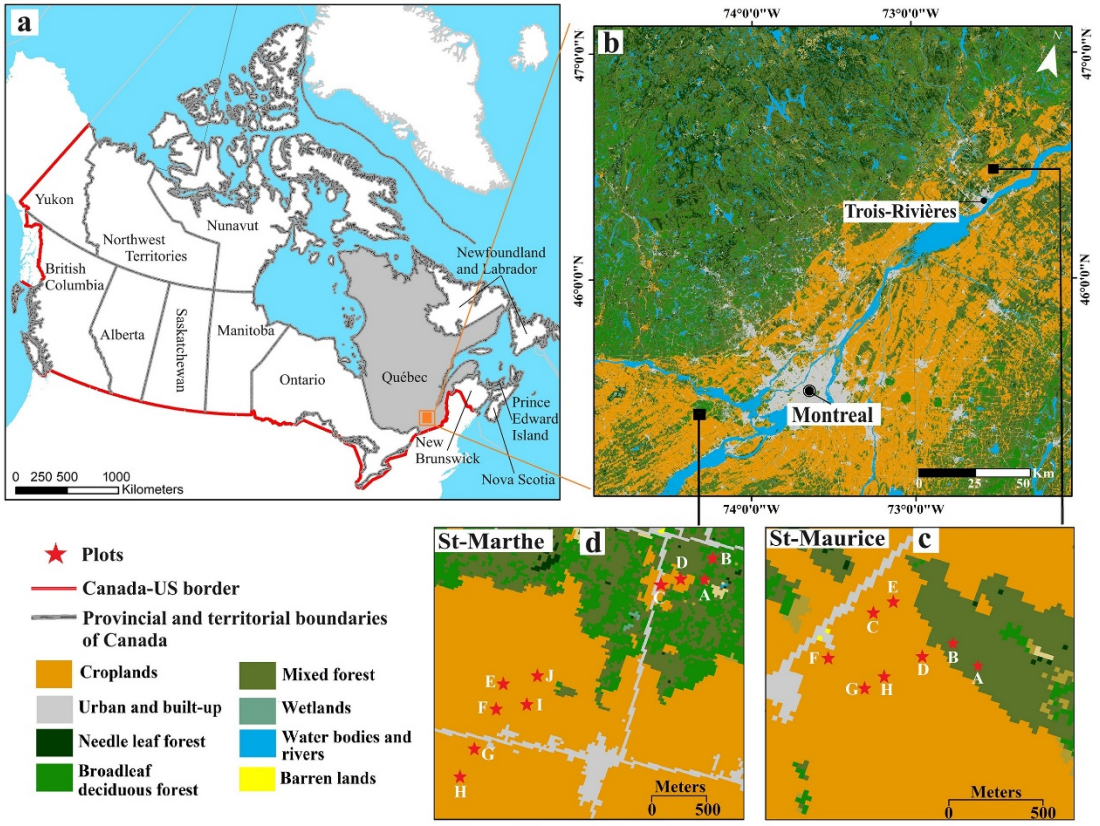

Figure 1.1. Overview of the study sites with land cover map in 2020 (https://open.canada.ca/data/en/dataset/ee1580ab-a23d-4f86-a09b-79763677eb47, accessed on 1 April 2024). (**a**) Geographical depiction of the study area located in Canada. (**b**) The geographical location of study sites in the agro-forested areas in southern Québec. (**c**) Study plot locations in St-Maurice (six in farmlands and two in forest). (d) Study plot locations in St-Marthe (eight in agricultural lands and two in forest). The map was created using ArcGIS version 10.3 software (Esri, Redlands, CA).

Considering the sensitivity of radar backscattering to surface roughness, we have assessed key influencing factors, such as crop residues, crop types, and soil types, in our predictive model for FT states. The soil type information for the St-Marthe and St-Maurice sites was obtained from the Info-Sols database (https://dev.info-sols.ca/, accessed on 1 April 2024), developed by GéoMont for the Ministry of Agriculture, Fisheries, and Food of Quebec (MAPAQ). Crop type information for the study years 2020–21 and 2021–22 was gathered from the Annual Crop Inventory data provided by Agriculture and Agri-Food Canada (AAFC). A comprehensive and current dataset on crop distribution and acreage across various regions is accessible on AAFC's online platform

(https://www.agr.gc.ca/atlas/apps/metrics/index-en.html?appid=aci-iac, accessed on 1 April 2024).

Table 1.1 provides a detailed description of the crops, soils, and crop residues for each instrumented plot. These sites have a variety of crop and soil agricultural aspects. The farmland plots in St-Maurice vary from finer types (silty clay) to coarser types (fine sand).

Table 1.1. Soil, crop type, and crop residue at each instrumented plot (plot size: 5 m × 5 m).

	Plot	Soil Type	Land Cover/Crop Type		Residues	
			2020–21	2021–22	2020–21	2021–22
St-Maurice	A	Fine sand	Forest	Forest	Forest litter	Forest litter
	B	Fine sand	Forest	Forest	Forest litter	Forest litter
	C	Silty clay	Potato	Corn	Bare field	Corn stalks
	D	Silty clay	Potato	Corn	Bare field	Corn stalks
	E	Loamy sand	Potato	Corn	Bare field	Corn stalks
	F	Silty clay	Corn	Soybean	Corn stalks	Soybean debris
	G	Silty clay	Corn	Soybean	Corn stalks	Soybean debris
	H	Silty clay	Corn	Soybean	Corn stalks	Soybean debris
St-Marthe	A	Loam	Forest	Forest	Forest litter	Forest litter
	B	Fine loamy sand	Forest	Forest	Forest litter	Forest litter
	C	Fine loamy sand	Grassland	Grassland	Grass	Grass
	D	Fine loamy sand	Grassland	Grassland	Grass	Grass
	E	Clay	Potato	Corn	Grass	Grass
	F	Clay	Potato	Corn	Grass	Grass
	G	Clay	Soybean	Ploughed	Soybean debris	Bare field
	H	Clay	Soybean	Ploughed	Soybean debris	Bare field
	I	Clay	Corn	Ploughed	Corn stalks	Scattered debris
	J	Clay	Corn	Ploughed	Corn stalks	Scattered debris

Meanwhile, in the agricultural plots of St-Marthe, clay (the finest type) and fine loamy sand (coarser) were found. Throughout the entire study period, the cultivation of a diverse range of crops is observed in the St-Maurice area, with soybean, corn, and potatoes being commonly grown. On the other hand, in St-Marthe, the primary crops grown include corn, soybeans, and peas. In both study sites, corn is the most extensively cultivated crop, while soybeans are the second most widely cultivated crop (Table 1.1).

1.2.2. In-Situ Data

In situ soil temperature measurements were collected for two consecutive years, from mid-October to the end of April, covering the periods of 2020–21 and 2021–22. Eight and ten temperature plots were instrumented in St-Maurice and St-Marthe, respectively, to monitor in situ FT states. At each plot, five soil pits equipped with two soil temperature sensors at near-surface (2 cm) and 10 cm depths were installed along a cross shape with 5 m between each soil pit. This specific sampling configuration was chosen to ensure that the in-situ measurements align with the S1 pixel size of 10 m (See Supplementary Material Figure S1.1). The vegetation covers and crop residue conditions of the different agricultural plots at the end of the crop season and post-harvest are depicted in Figure 1.2.

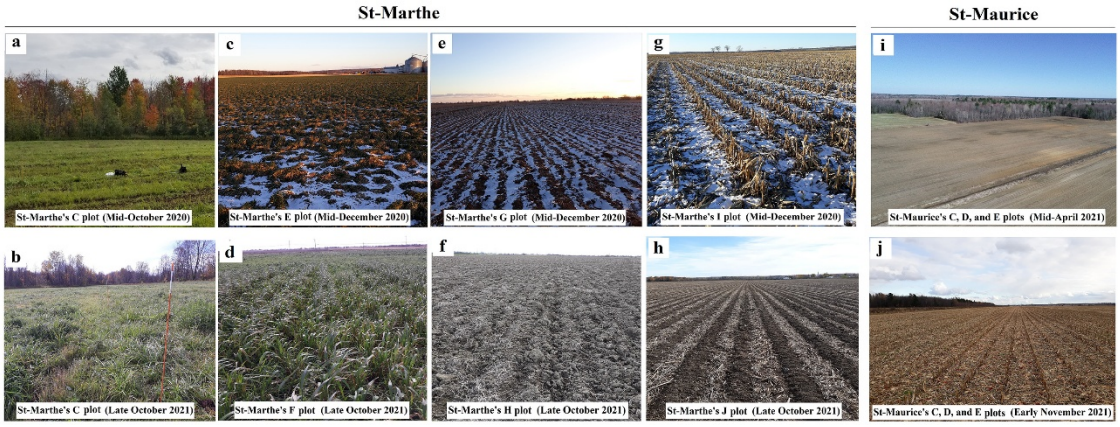

Figure 1.2. Field observations of crop residues at both sites during the study periods 2020–21 and 2021–22. (**a**, **b**) Grass presence in St-Marthe's C plot over the study period. (**c**) Snow-covered grass in St-Marthe's E plot. (**d**) Snow-free grass in St-Marthe's F plot. (**e**) Plowed soils in St-Marthe's G plot. (**f**) Plowed soils in St-Marthe's H plot. (**g**) Corn

stalks residues and scattered debris in St-Marthe's I plot. (**h**) Corn stalks residues and scattered debris in St-Marthe's J plot. (**i**, **j**) Fields with bare lands and corn stalks scattered throughout St-Maurice's C, D, and E plots.

1.2.3. Deriving Soil Freezing Probability

We used the standard normal distribution (z), which is a continuous probability distribution (Wackerly, 2008), to determine the probability of soil freezing at each instrumented plot. This distribution enabled us to calculate the probability that the soil is frozen ($T \leq 0$) given the uncertainty of the sensors and the small-scale spatial heterogeneity within each plot (Equation (1.1)).

$$P\ (T \leq 0) = 1 - P\ \left(z < \left(\frac{T-\mu}{\sigma}\right)\right) \tag{1.1}$$

where '$P\ (T \leq 0)$' represents the cumulative probability that the measured soil temperature (T) is less than or equal to zero, which corresponds to the frozen state, μ represents the mean of the distribution which is set to zero (freezing point), and σ indicates the standard deviation. The quantity $\left(\frac{T-\mu}{\sigma}\right)$ is called a z score whose cumulative probability distribution is 'P'. To determine σ, the accuracy of both sensor types is reported as a two-sigma value of ±0.5 °C, resulting in a sigma value of 0.25 °C.

In our analysis, we assumed a normal distribution for the errors in the temperature data. Temperature measurements in the soil were measured using DS1922L iButton sensors and UA-001 HOBO pendant temperature sensors, with temperature resolutions of 0.0625 °C and 0.14 °C, respectively. The measured soil temperature (T) in Equation (1.1) corresponds to the observed 3-hourly soil temperature.

For every instrumented plot, the probability of freezing was computed for each three-hourly recorded temperature, at each logger. Subsequently, the frozen probability for each plot was determined by averaging the freezing probabilities obtained at each of

the five temperature loggers inside the plot. The plot's freezing probability was separately calculated at the 2 cm and 10 cm soil depths.

1.2.4. Satellite Data Acquisition

The S1 satellite carries a dual-polarization (VV and VH) C-band SAR instrument that operates at 5.405 GHz (corresponding wavelength 5.55 cm) with an active phased array antenna. In this study, S1 Interferometric Wide Swath Mode (IW) imagery was used, using both ascending and descending orbits during the time frame of early October to early June, covering the periods of 2020–21 and 2021–22. S1A/B Imagery Ingestion in Google Earth Engine (GEE) (Gorelick et al, 2017) uses S1 Ground Range Detected (GRD) products, which have been preprocessed operating the S1 Toolbox of the European Space Agency (ESA) to derive the backscatter coefficients of each pixel. In the IW GRD collections, the incidence angle ranges between 31° and 46° from near to far range for S1 over land (Torres et al, 2012). To remove the remaining noise and artifacts from the SAR images, we applied speckle filtering and angle corrections procedures, as described next.

1.2.4.1. Speckle Filtering

The speckle noise in SAR images causes them to appear grainy and prevents target recognition and texture analysis, and therefore speckle filtering is an essential part of SAR image preprocessing. Many studies have suggested that the refined Lee filter has a high potential for reducing speckles (Domg & Milne, 2001; Filipponi, 2019); SAR data can be filtered using rectangular scanning windows, with pixel spacing in azimuth greater than that in range. While a larger window generally leads to more effective speckle reduction (Lee et al, 2008), it can also result in increased smoothing and loss of fine details. A 7-by-7 filter window is commonly used for speckle reduction in agricultural lands (Amani et al, 2019), as it provides a balance between reducing speckle noise and preserving important features. In this work, we utilized the refined Lee filter with the 7-by-7 window size within the GEE platform.

1.2.4.2. Local Incidence Angle (LIA) Corrections

Radar backscatter is affected not only by the dielectric properties and roughness of the surface but also by the geometry of the incident beam. The SAR incidence angle is defined by the angle between the incident beam and the vertical to the local geodetic ground surface (Fuhrmann & Garthwaite, 2019). Rough surfaces exhibit less of this effect than smooth surfaces. Since radar backscatter depends greatly on incident angle, the need for correction should be determined in accordance with the application. Previous research demonstrated the importance of correcting the LIA to minimize radar backscatter dependence on the incidence angle. For this study, the incidence angle of each plot was normalized independently using Schaufler's equation (Schaufler et al, 2018).

$$\sigma°(40°) = \sigma°(\theta_L) - \beta(\theta_L - 40°) \quad (1.2)$$

Due to S1's IW backscatter being acquired between 29 and 46 incidence angles, a reference angle of 40 was chosen for reference. Backscatter is expressed in terms of $\sigma°$ (sigma nought) for VV and VH polarizations. According to Equation (1.2), the $\sigma°$ derived from a given local incidence angle is corrected to the reference angle of 40° based on the slope parameter (β), which is derived from a regression analysis between $\sigma°$ and LIA (see example in Supplementary Material Figure S1.2). The angle correction was implemented on the dual-polarized S1 VV/VH images within the GEE platform.

1.2.5. FT Algorithms

Two existing change detection algorithms were first used to retrieve the FT state at the studied plots. First, we used the FT Index (FTI) algorithm introduced by Rautiainen et al (2014) which involved comparing the radar signatures obtained during seasonal reference frozen states and thawed states. The FTI is calculated from backscattering values scaled by reference backscattering values for frozen and thawed states (Derksen et al, 2017b; Touati et al, 2021) (Equation (1.3)).

$$\text{FTI} = \frac{\sigma(t) - \sigma_F}{\sigma_T - \sigma_F} \quad (1.3)$$

where $\sigma(t)$ refers to the backscattering coefficient acquired at time *t*, and σ_F and σ_T are the reference backscattering coefficient for frozen and thawed conditions, respectively. σ_F was derived as the average of the three lowest backscatters the during the January–February period, while σ_T was derived from the average of the three highest backscatters during the early October to end of November and mid-April to early June periods. This period was chosen as it occurs after the onset of harvesting activities in the fall and before significant crops growing in the spring, thus minimizing the potential influence of crop harvesting and growth on roughness changes and backscattering signals. The FTI algorithm was applied for each plot over each study period for VV and VH polarizations.

Next, a simple difference (Delta) between the measured backscatter, $\sigma(t)$, and the prescribed thawed reference, σ_T, as defined before, was used as a predictor of soil freezing (Equation (1.4)) (Baghdadi et al, 2018).

$$\Delta(\text{t}) = \sigma_T - \sigma(t) \quad (1.4)$$

The Delta approach demonstrated efficacy in identifying frozen states during winter when backscatter remained consistently low throughout the winter season, in contrast to thawed periods in fall and spring. However, a notable challenge emerged when confronted with substantial drops in backscatter during thawed periods (this point will be discussed in detail in the Discussion Section). In such instances, the Delta algorithm erroneously categorized these thaw events as frozen states, contradicting in situ measurements that indicated non-frozen conditions.

To overcome limitations identified in the Delta algorithm, particularly its reduced performance during transitional fall and spring seasons, a new 'exponential freeze-thaw algorithm' (EFTA) is introduced in this study. The proposed approach seeks to address the

inherent limitations of the Delta algorithm and mitigate the challenge of overestimating frozen events during thawed periods. This is achieved by incorporating an exponential decay function that decreases the influence of backscatter fluctuations during the expected thawed periods in the shoulder seasons, while enhancing those during the expected frozen period. The concept behind the formulation of the EFTA derives from findings obtained from radar signal analysis research, especially studies on L-, C-, and X-band data (Baghdadi et al, 2002a; Zribi et al, 2016), which highlight the effect of soil surface roughness on radar signals. The algorithm selectively incorporates quantitative aspects from these studies, but it does not directly model the relationship between radar signals and surface roughness. The EFTA is represented by the following equation:

$$EFTA = \left[e^{-K\left(1+\left(\frac{\sigma_T}{\sigma(t)}\right)\right)}\right]\left(\Delta(\mathrm{t})\right) \tag{1.5}$$

where the expression $\left[e^{-K\left(1+\left(\frac{\sigma_T}{\sigma(t)}\right)\right)}\right]$ denotes an exponential decay function, ensuring that the outcome remains constrained within the range of 1 to 0. The binary parameter *K* represents the expected thaw (*K* = 1) and frozen period (*K* = 0), which are, respectively, defined by the most negative and positive differences between radar signals at time t and at the preceding time ($t-1$). The operationalization of this approach involves setting *K* to zero within the range defined by the most negative backscatter difference observed before February and the most positive backscatter difference observed after February. Conversely, *K* is assigned a value of 1 for radar signals occurring before the most negative backscatter differences in fall and after the most positive backscatter differences in spring, signifying the anticipated thaw periods. An example of the approach used to identify the soil freezing and thawing transitions in backscatter signals in the EFTA method is given in Supplementary Material Figure S1.3.

The EFTA was applied on both VH backscatter (VH_{EFTA}) and VV (VV_{EFTA}) backscattering signals. This facilitates identifying the greater sensitivity of either VV or

VH polarizations to surface roughness in the context of FT prediction, thereby evaluating their effectiveness in delivering essential information for forecasting freeze and thaw states. A greater positive value of EFTA corresponds to increased backscatter differences between the thawed references and the given date of interest under freezing conditions, which indicates a higher probability of freezing for the corresponding date.

1.2.6. Probabilistic Statistical Analysis

A generalized linear model (GLM), a statistical probabilistic method, was used to predict the freezing probability. To fit logistic regression models, the logit link function was used in the GLM to predict the freezing probability from potential predictors. The model was first applied to all instrumented plots across the two study sites and for the two studied years. By fitting the GLM model on the combined dataset, we could first evaluate the overall significance of the potential predictors and compare their effectiveness in predicting freezing probability for the agricultural plots.

In GLMs, Pseudo-R^2 fit statistics are calculated using maximum likelihood estimates. Higher values of Pseudo-R^2 indicate that the model explains more of the variance of the observed data. The Akaike Information Criterion (AIC) was used as a model comparison metric, allowing us to evaluate the relative quality of the different candidate statistical models of soil freezing probability. The AIC takes into account both the goodness of fitness and the complexity of the model. The model with the lowest AIC value is considered the best fit among the candidate models.

We then added plot-level potential predictors, including soil types, crop types, and crop residues, to examine the effect of different plot conditions on soil freezing predictions in agricultural plots. The six candidate models tested can be classified into three categories based on their increasing complexity, starting with a global (i.e., on the combined datasets) GLM model (model 1), a mixed GLM model with a random effect on plots (model 2), and mixed models including plot-level predictors, cross-level interactions (interactions between time-dependent VH_{EFTA} and spatially variable plot conditions), and a plot random effect (models 3 to 6).

Soil freezing probability ~ 1 + VH_{EFTA};

Soil freezing probability ~ 1 + VH_{EFTA} + (1|Plot);

Soil freezing probability ~ 1 + VH_{EFTA} × Soil types + (1|Plot);

Soil freezing probability ~ 1 + VH_{EFTA} × Crop types + (1|Plot);

Soil freezing probability ~ 1 + VH_{EFTA} × Soil types + VH_{EFTA} × Crop types + (1|Plot);

Soil freezing probability ~ 1 + VH_{EFTA} × Soil types + VH_{EFTA} × Crop types + VH_{EFTA} × Crop residues + (1|Plot).

Within the framework of mixed models, we calculated marginal and conditional R^2 to discern the contributions of fixed and random effects. Marginal R^2 in this context quantifies the variance explained by fixed effects, while conditional R^2 considers both fixed and random effects, clarifying the proportions of variation attributed to each (Domg & Milne, 2001).

1.2.7. Model Calibration and Validation

Spatial and temporal cross-validation was used to evaluate the ability of the calibrated models to transpose between years and between plots. For temporal validation, the chosen model was calibrated on the first (2020–21) year and validated on the second year (2021–22). Then, the procedure was repeated after inverting the calibration and validation years.

For spatial cross-validation, we utilized a leave-one-out cross-validation (LOOCV) approach, incorporating data from both the 2020–21 and 2021–22 study years. This method involved evaluating the model's performance by systematically excluding the data of one plot at a time from the calibration process, followed by testing the model on these excluded data. With 14 plots and data spanning 2 consecutive years, this approach resulted in 28 unique folds (14 plots each evaluated across 2 years). Data from each plot, whether from the first or second year of the study, were successively removed from the calibration dataset and used as a test sample. This comprehensive strategy ensured a rigorous assessment of the model's performance across all agricultural plots.

The Brier score, mean absolute error (MAE), and R^2 were employed to assess model accuracy, prediction errors, and goodness of fit during cross-validation. The Brier score is specifically used in the context of probabilities. A Brier score of 0 indicates perfect accuracy, reflecting precise alignment between the model's forecasts and observed data, while a score of 1 signifies perfect inaccuracy (Steyerberg et al, 2010). In this research, we conducted statistical analysis and formulated our results using RStudio version 2022.07.2 Build 576, developed by RStudio, PBC, ©2009-2022.

1.3. Results

1.3.1. Observed FT Spatiotemporal Variability

The near-surface (2 cm) soil freezing probability displays variability between the two studied sites, monitored plots, and years (Figure 1.3). In both study sites, the observed probability of soil freezing in forest plots (A and B) demonstrated significantly fewer instances of freezing, despite experiencing a high frequency of FT transitions, compared to agricultural plots. The agricultural plots in St-Maurice (Figure 3c, d) experienced a prolonged duration of frozen conditions in comparison to St-Marthe (Figure 1.3a, b). While there is spatial variation in freezing probability within both agricultural and forest plots, temporal variations in freezing probability are also apparent during the two study periods at both sites. Spatial heterogeneity in frozen probability was observed within both agricultural and forest plots across the study site.

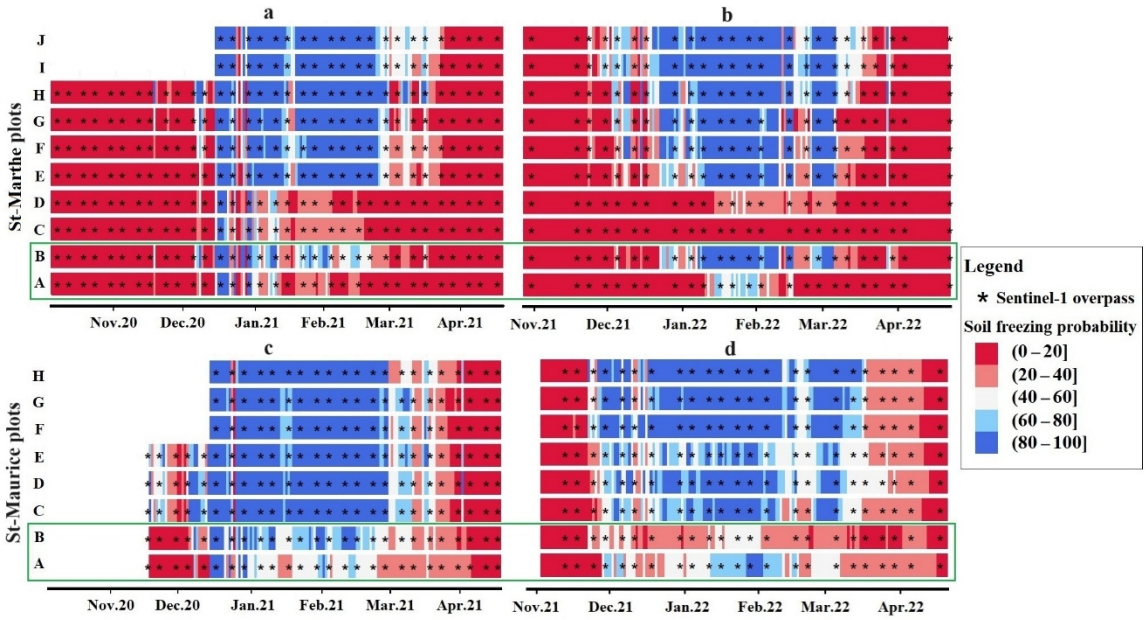

Figure 1.3. Spatial and temporal variations in freezing probability at 2 cm depth along with corresponding S1 overpasses for all study plots. (**a**, **b**) St-Marthe for 2020–21 and 2021–22. (**c**, **d**) St-Maurice for 2020–21 and 2021–22. A and B plots in each site located in forest (green rectangles). For St-Marthe's J and I and St-Maurice's F, G, and H plots, the initiation of soil temperature monitoring started later, resulting in an absence of freezing probability values.

In St-Marthe, the forest plots (A and B) displayed notable spatial heterogeneity, marked by more frequent freeze–thaw transitions (Figure 1.3a, b). Meanwhile, the agricultural plots located near the forest edges (C and D) in the same vicinity were less frozen and exhibited less variability, with fewer FT transitions. In these plots, only a few isolated freezing events with a freezing probability exceeding 80% were observed during the two study periods. This occurrence can be primarily attributed to the insulating properties of snow cover, especially prevalent in areas near the forest edge. The dense accumulation of snow in these plots forms a significant thermal layer, providing effective insulation against soil freezing. However, during the second study period, as depicted in Figure 1.3d, these agricultural plots exhibited an increased frequency of freezing and thawing transitions (C, D, and E plots). This phenomenon can be attributed to the spatial and temporal variability of snow depth, particularly the redistribution of snow, which

affects its insulating properties at these plots. For a detailed depiction of spatial and temporal variations in freezing probability at 10 cm for all agro-forested plots at both sites, refer to Supplementary Material Figure S1.4.

1.3.2. Comparisons of Predictors for Modelling Freezing Probability

We conducted a comparative analysis using the logistic linear model to assess the performance of the EFTA, Delta, and FTI algorithms derived from VV and VH backscattering in explaining soil freezing probabilities at 2 cm and 10 cm soil depth. The results of this analysis are summarized in Table 1.2. In the context of modeling soil freezing probabilities, the AIC scores reflect the complexity and fit of the models at different soil depths. At a depth of 10 cm, where freezing probabilities trend towards thawing (indicated by probabilities tending to 0), the model exhibits a lower AIC score, adequately fitting the model due to more frequent thawing events. Thus, the variation in AIC scores between depths underscores the importance of tailoring model complexity to the specific characteristics and dynamics of soil freezing at different depths. According to the findings presented in Table 1.2, the logistic model utilizing the EFTA derived from VH polarization demonstrated better performance in predicting ground temperature observations at 2 cm, as indicated by its higher Pseudo-R^2 value of 0.54. Furthermore, the predictions generated by the EFTA display a stronger ability to accurately predict frozen soil states across different soil depths and polarizations, outperforming both the Delta and FTI algorithms. As a result, further models were developed using the EFTA derived from VH backscattering.

Table 1.2. Statistical logistic model summary for the EFTA, Delta, and FTI at 2 and 10 cm.

Algorithms	Soil Depth (cm)	Polarization	Pseudo-R^2	AIC
EFTA	2	VH	0.54	199
		VV	0.36	623
	10	VH	0.49	115
		VV	0.36	194
Delta	2	VH	0.32	706
		VV	0.22	879
	10	VH	0.27	333
		VV	0.21	468
FTI	2	VH	0.31	714
		VV	0.20	918
	10	VH	0.22	445
		VV	0.16	546

For the comparative analysis of EFTA and Delta algorithms, Figure 1.4 depicts multiple plots illustrating the outcomes of both algorithms for the two study plots. As depicted in the upper plots of Figure 1.4, the Delta freeze–thaw algorithm effectively identified frozen states during winter when backscatter consistently remained low, distinguishing them from thawed periods. However, a significant challenge arose when encountering substantial drops in backscatter during the thawed periods in fall (early October to mid-October) and spring (mid-May to mid-June). In most plots, we observed one or two consecutive sudden drops in backscatter, particularly during mid-May to mid-June. Based on the time series of daily precipitation and air temperature presented in Supplementary Material, Figure S1.5, this phenomenon appears to be linked to a lack of rainfall over several weeks. This was evident during early fall (early October to mid-October) and, more notably, at the end of spring (mid-May to mid-June). The combination of no precipitation and rising air temperatures during these periods led to increasingly dry soil conditions, which preceded the sudden backscatter drops observed at the two study sites. In these instances, the Delta algorithm inaccurately identified these thawed events as frozen states, while the probability of soil freezing indicates non-frozen conditions. This misidentification of thawed conditions, observed across all plots, was attributed to the decrease in backscatter. Consequently, the proposed EFTA, illustrated in the lower

plots of Figure 1.4, overcomes this limitation and brings a notable improvement in FT state detection across all plots and years. This enhancement is apparent in the coefficient of determination (R^2) between the predicted and observed probability of freezing at 2 cm.

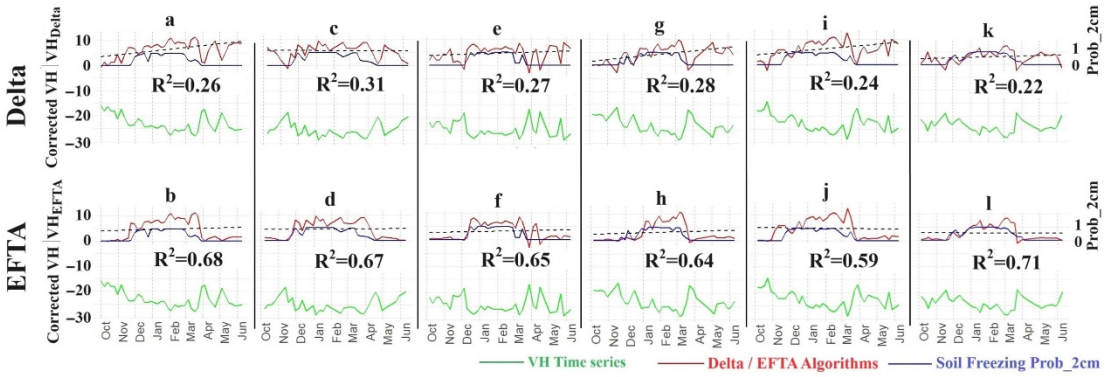

Figure 1.4. Comparison of observed 2 cm soil freezing probabilities (dark blue, right Y-axis) with that predicted by the Delta method (top row, in red) and EFTA (bottom row, in red). The S1 corrected VH polarization backscatter signal is also displayed in green. On the left Y-axis, values less than 0 correspond to corrected VH backscatters (green curve), while values greater than 0 correspond to the predicted freezing probability (red curves). (**a**, **b**) St-Maurice's H plot in 2020–21. (**c**, **d**) St-Maurice's H plot in 2021–22. (**e**, **f**) St-Marthe's H plot in 2020–21. (**g**, **h**) St-Marthe's H plot in 2021–22. (**i**, **j**) St-Marthe's I plot in 2020–21. (**k**, **l**) St-Marthe's I plot in 2021–22. The R^2 values, derived from the correlation between the soil freezing probability at 2 cm depth and VH_{Delta} (top plots) / and VH_{EFTA} (bottom plots). A dashed line represents the overall trend between VH_{Delta} and the date (top plots) or VH_{EFTA} and the date (bottom plots).

1.3.3. Spatially Variable Probabilistic Modelling of FT Detection

Figure 1.5 illustrates examples of locally (at each plot) fitted logistic models, depicting the 2 cm depth observed freezing probability against VH_{EFTA}. This representation aims to showcase the spatial and temporal variability of frozen soil between the plots. The fitted logistic regression model exhibited distinct Pseudo-R^2 values for each agricultural or forest plot in each study period (Figure 1.5). Specifically, the H agricultural plot in St-Marthe (Figure 1.5a) displayed a higher goodness of fit in the first study year compared to the second year. This plot, characterized by clay soil type and soybean

residues, had Pseudo-R^2 values of 0.59 and 0.47 in the first (green curve) and second (sky blue curve) study years, respectively. In the agricultural plot I, the fitted logistic model showed a more robust correlation in the second year, marked by a ploughed crop type and scattered debris (Pseudo-R^2: 0.57), compared to the first year of the study (Pseudo-R^2: 0.48), as illustrated in Figure 1.5b. The presence of soybean debris and scattered crop residues in the plots may affect surface roughness. This roughness variability, in turn, influences the interaction of VH polarization with the surface.

Figure 1.5. Local fitted logistic models for observed freezing probability (2 cm) against VH_{EFTA} in St-Marthe (top) and St-Maurice (bottom). (**a**) St-Marthe's H agricultural plot. (**b**) St-Marthe's I agricultural plot. (**c**) St-Marthe's B forest plot. (**d**) St-Maurice's F

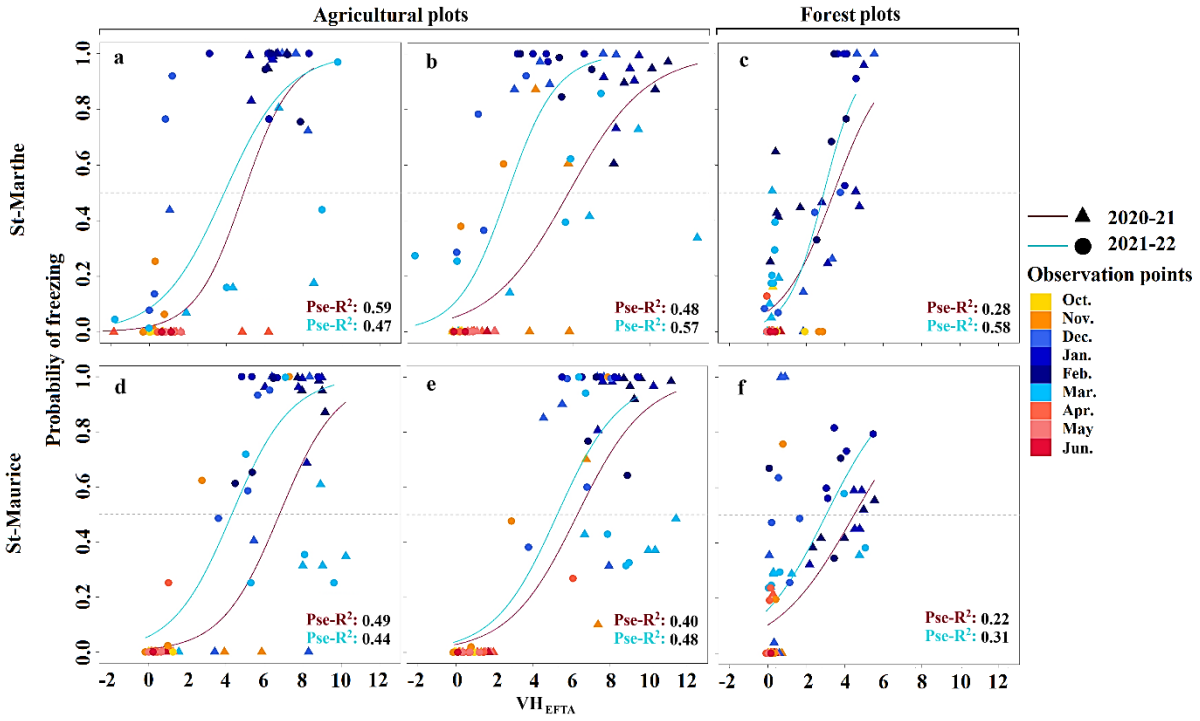

agricultural plot. (**e**) St-Maurice's H agricultural plot. (**f**) St-Maurice's A forest plot. The top and bottom Pseudo-R^2 (Pse-R^2) values of each plot are shown for 2020–21 and 2021–22.

Despite the consistent conditions observed across the two study years, the goodness of fit of the logistic model exhibited variations between these years in plots F and H at St-Maurice, as evidenced by the data presented in Table 1.2. The observed differences in

model performance may be explained by other possible conditions, such as changes in other backscattering properties, changes in surface conditions, and variations in soil moisture content. These factors highlight the complexity of the interactions influencing radar signals and soil freezing dynamics within specific plots over time. The performance of the fitted GLM in predicting soil freezing probabilities varied across the different forest plots. Generally, the model exhibited lower efficacy in forest plots compared to agricultural plots across the two study sites. Notably, in the second year of the study, the highest correlation was observed in St-Marthe's B forest plot, with Pseudo-R^2 values reaching 0.58.

The mixed modelling approach, as outlined in Section 2.6, accommodates spatial variability. An analysis and comparison of the various candidate probabilistic models are presented in Table 1.3. As indicated in Table 1.3, the more complex mixed models, accounting for both fixed and random effects, explain relatively high variances in site-level predictors. However, it is noteworthy that the full complex model (Model 6) exhibits a lower level of performance compared to its fewer complex counterparts (Models 4 and 5).

Table 1.3. Comparing probabilistic models of 2 cm depth soil freezing probability based on different site-level predictors. Refer to Section 2.6 for model definitions.

Models	***R^2***		***Pseudo-R^2***	***AIC***
	Marginal	**Conditional**		
1			0.54	241
2	0.56	0.57		239
3	0.55	0.58		231
4	0.59	0.61		232
5	0.59	0.60		252
6	0.59	0.60		271

The model results reveal that Model 4, a mixed model incorporating the interaction between VH_{EFTA} and crop types (Crop-Mixed' model) with a random effect on plots, displays a low AIC (231) and the highest marginal/conditional R^2 values (0.59/0.61).

Hence, the Crop-Mixed model accounts for 61% of the variance of observed soil freezing probability (conditional R^2), of which 59% is attributed to fixed effects (marginal R^2) and only 2% to random (plot) effects.

This model provides the most precise and parsimonious model to predict freezing probability, taking into account fixed (crop-type) and random (plot) spatial variability in agricultural plots. Table 1.4 provides a comprehensive overview of predictor effects derived from the Crop-Mixed model, showing their impact on soil freezing probabilities at the plot level. Notably, the *p* values associated with each predictor highlight the significant influence of EFTA derived from VH backscatter on model predictions.

While the main effects of crop types on soil freezing were not individually significant, the substantial interactions between crop types and VH backscatter signals underscore that the type of crop present modulates the VH backscatter response to soil freezing. Specifically, ploughed fields, as well as potato and soybean fields, exhibited the most pronounced modulating effects, with an interaction term estimate of 0.06. This was followed by maize with an estimate of 0.04, and grassland fields which served as the reference category with an estimate of 0. These findings indicate the presence of a 'cross-over interaction', where the influence of VH_{EFTA} on soil freezing probabilities is not uniform across all crop types.

Table 1.4. Predictor effects for the Crop-Mixed model. σ2 denotes the residual variance, τ00 is the random effect variance at the plot level, and ICC is the intra-class correlation and represents the proportion of total variance attributable to between-group variability, and N Plot denotes the number of agricultural plots used in the analysis. The bold values in the 'p' column indicate statistically significant effects.

Predictors	Estimates	CI	*p*
(Intercept)	0.04	−0.06–0.14	0.441
VH_{EFTA}	0.04	0.02–0.06	**<0.001**
Crop type			
Grassland	***Reference***		
Maize	−0.03	−0.14–0.08	0.593
Ploughed	0.09	−0.03–0.21	0.142
Potato	−0.05	−0.17–0.07	0.398
Soybean	0.00	−0.12–0.12	0.989
Crop type and VH_{FFTA} interactions			
VH_{EFTA}: Maize	0.04	0.02–0.07	**0.001**
VH_{EFTA}: Ploughed	0.06	0.03–0.09	**<0.001**
VH_{EFTA}: Potato	0.06	0.03–0.08	**<0.001**
VH_{EFTA}: Soybean	0.06	0.03–0.09	**<0.001**
Random Effects			
σ^2	0.07		
$\tau_{00\ Plot}$	0.00		
ICC	0.05		
$N_{\ Plot}$	14		
Observations	1036		
Marginal R^2/Conditional R^2	0.586/0.608		

In Figure 1.6, cross-over interactions between different crop types and the relationship with VH_{EFTA} regarding the predicted soil freezing probability are depicted. The data indicates that with rising VH_{EFTA} values, there is a correspondingly increased probability of soil freezing across all crop types, although this trend occurs at varying rates for each type. For crop types such as ploughed fields, potatoes, and soybeans, the slopes indicate that the effect of VH_{EFTA} on soil freezing probability is relatively stable across these crop types. However, the magnitude of the effect varies.

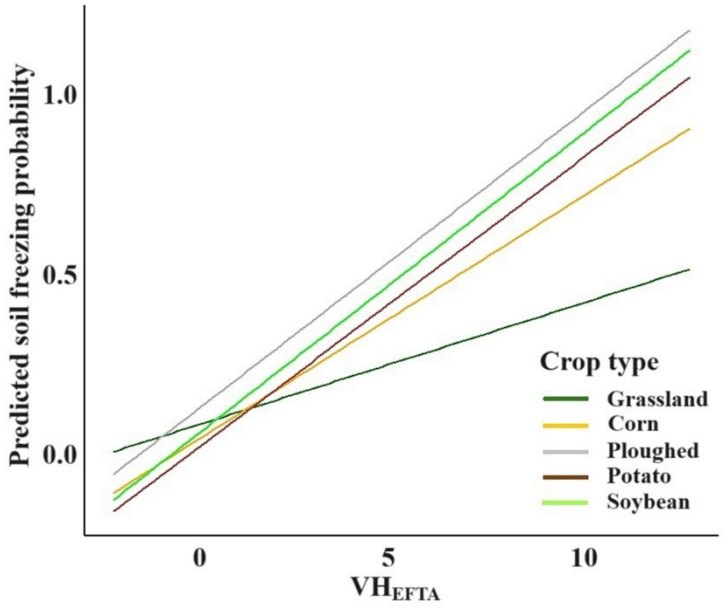

Figure 1.6. Cross-over interactions of different crop types on the relationship between VH_{EFTA} and the predicted soil freezing probability.

1.3.4. Model Validation

The results of the temporal cross-validation for the Crop-Mixed soil freezing model are presented in Table 1.5. The results indicated that the model performed more effectively when calibrated with the first year's data and validated against the data from the subsequent year of the study. This effectiveness was evidenced by a robust squared correlation coefficient (R^2) value of 0.60, a low Mean Absolute Error (MAE) of 0.18, and a Brier score of 0.19, which collectively indicate moderately high performance by the model.

Table 1.5. Temporal cross-validation of the Crop-Mixed soil freezing model. The R^2, MAE, and the Brier score are given for the validation period.

State	***R^2***	***MAE***	***Brier Score***
Calibration 2020–21, validation 2021–22	0.60	0.18	0.19
Calibration 2021–22, validation 2020–21	0.56	0.18	0.17

The leave-one (plot)-out spatial cross validation (LOOCV) yielded a mean R^2 score of 0.79, along with small MAE and Brier scores of 0.14 and 0.17, respectively (Figure 1.7), suggesting a good spatial transferability of the model. The lowest R^2 observed was for St-Marthe's C plot in 2020–21, indicating that the model's predictions are comparatively less precise for this plot than for others.

When considering the average cross-validation R^2 values from the first and second years of the study, a higher R^2 of 0.60 is observed for 2021–22 compared to an R^2 of 0.55 for 2020–21. This implies that the model, when trained using all available data while excluding the specific plot in the second year under consideration, more effectively identifies the FT predictions.

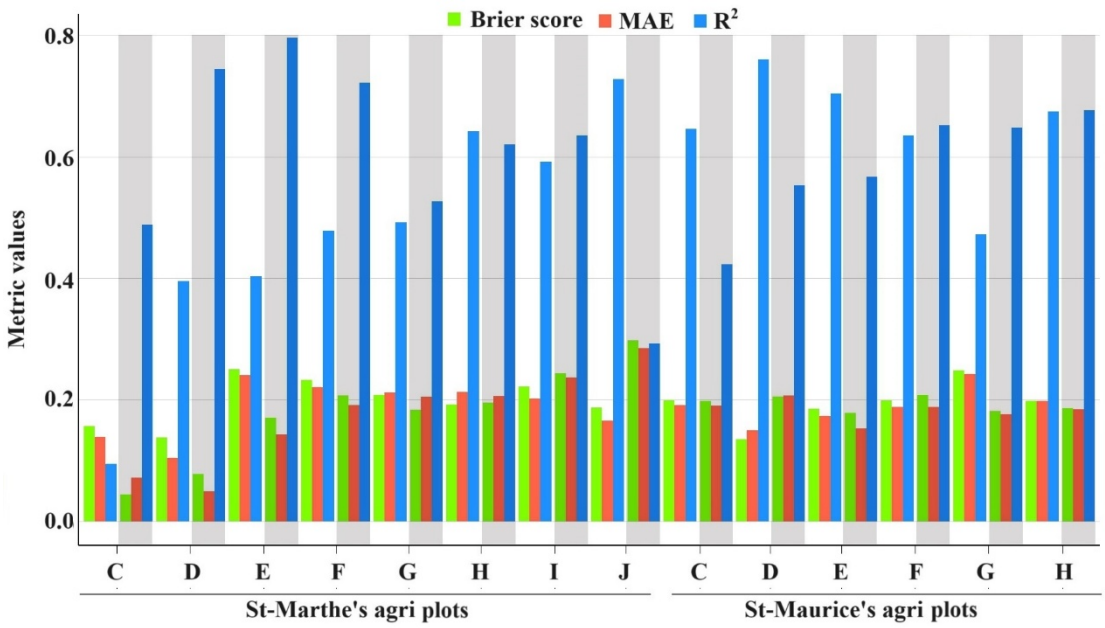

Figure 1.7. Spatial cross-validation results of the Crop-Mixed soil freezing probability model with 28 single folds, showing 14 plots evaluated across two study years: 2020–21 (gray) and 2021–22 (white). The figure displays the Brier score, MAE, and R^2 for each fold when individually excluded from calibration and used for validation. The statistical metrics averages for the plots across the study years 2020–21 and 2021–22 exhibited the following respective values: For 2020–21: $R^2 = 0.55$, Brier Score = 0.19, and MAE = 0.18; and for 2021–22: $R^2 = 0.60$, Brier Score = 0.18, and MAE = 0.17.

The comparison between predicted and observed 2 cm depth soil freezing probability shows significant scatter, without any clear relationship with crop types (Figure 1.8a). The good performance of the model is thus partly due to the clustering of values at low and high probabilities, i.e., the model is able to discriminate between thawed and frozen conditions but yields more uncertain predictions at intermediate probabilities. To evaluate the ability of the model to classify the observed freezing probabilities into 'frozen' or 'thawed' conditions, the predicted and observed freezing probabilities were converted into binary states of frozen and thawed using a threshold of 0.5. The model accurately predicted the frozen status with an overall accuracy of 85.2%, confirming that it successfully classified most freezing and thawing events in agricultural plots across two sites over two study periods (Figure 1.8b).

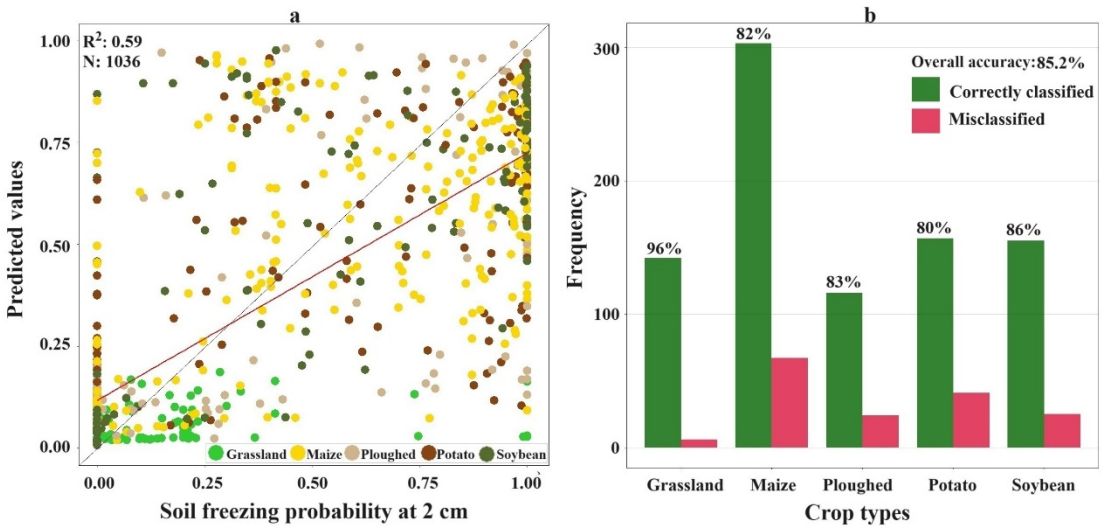

Figure 1.8. Comparison of the soil freezing probability predicted by the Crop-Mixed model vs. observed values. (**a**) Scatter plot of predicted vs. observed data; (**b**) frequency histogram showing the accuracy (true positive/negative) and misclassification (false positive/negative) for the different crop types. In the left plot, the red line depicts the best fit for the plotted points, while the gray line illustrates the hypothetical scenario where predicted values perfectly align with observed ones. A smaller gap between these lines signifies the higher model's performance.

The classification accuracy varied among crop types, with grassland plots showing the highest classification accuracy (96%), followed by soybeans (86%), ploughed fields (83%), maize (82%), and potatoes (80%). In plots C and D of St-Marthe, which are grassland areas, a predominantly thawed state was observed, as depicted in Figure 1.3a, b. This thawed state represented the majority class in these specific plots. Consequently, the model demonstrated high classification accuracy, particularly in identifying this prevalent thawed condition. The ability of the model to accurately classify the more common thawed states contributed significantly to its overall effectiveness in these grassland areas.

1.4. Discussion

1.4.1. FT Spatial and Temporal Variability

By the analysis of spatial and temporal variations in soil freezing probability, derived from soil temperature measurements at 2 cm depth, we have noted considerable variations in freezing probability among the plots of study sites (Figure 1.3). This variability is evident regardless of whether the plots are situated in agricultural or forested areas. The primary likely factors contributing to this variability are the spatial and temporal variations in local plot attributes, including variations in soil properties, vegetation cover, and snow depth conditions across the study sites.

As compared to agricultural plots, forested areas in St-Marthe and St-Maurice exhibit fewer freezing occurrences, which can be attributed to the substantial amount of forest litter acting as an insulating barrier between the soil and the air (Smith, 1975). This insulation effectively reduces heat loss from the soil, thereby impeding rapid freezing. Additionally, the attenuated winds in forested areas can further reduce sensible heat loss through turbulent fluxes. Moreover, the presence of trees contributes to ground heating through longwave radiation (Pomeroy et al, 2009).

Ground-based measurements of snow depth in St-Maurice over two study periods reveal that forest plots (plots A and B) typically display the highest snow depths. This is largely due to the forest canopies' ability to intercept snowfall, which leads to greater

accumulation in the forest. Additionally, the canopy cover provides protection against direct sunlight and wind, mitigating snow sublimation. As shown in Figure 1.3c, the most events of soil freezing in 2020–21 occurred in forest plot B in St-Maurice, with the lowest recorded snow depths (see Supplementary Material Figure S1.6).

In contrast, agricultural plots demonstrated notable temporal variability in snow depth, with the first study year showing relatively higher snow accumulation. This may explain the rather shorter duration of soil freezing experienced by the agricultural plots in the first study period compared to the second year. Despite all agricultural plots in St-Maurice being sufficiently far from forest edges, there was also spatial variability in snow depth between plots.

Figure 1.3 illustrates that the agricultural plots in St-Maurice experienced extended periods of soil freezing during the two study periods, compared to the relatively shorter freezing durations observed in St-Marthe's agricultural plots. Despite variations in spatial and temporal snow cover, factors such as soil properties and climate conditions significantly influenced the duration of soil freezing in St-Maurice compared to St-Marthe. Notably, the soil composition differs between these locations, with predominantly clay soil in St-Marthe and silty clay in St-Maurice. Clay, being a finer-textured soil, contrasts with the more coarse-textured silty clay. According to Jagtar Bhatti et al (2006), fine-textured soils have a larger mineral surface area and a more extensive network of fine pores. These characteristics impede ice formation, primarily restricting it to larger pore spaces. Consequently, fine-textured soils are more likely to experience super-cooling, remaining unfrozen or partially unfrozen even under sub-zero temperatures. This phenomenon is less pronounced in coarser-textured soils, such as the silty clay found in St-Maurice, which explains the longer and more intense soil freezing observed there compared to St-Marthe. On the other hand, the average daily air temperature during the two study periods for St-Marthe and St-Maurice was 3.07 °C and 2.10 °C, respectively (see Supplementary Material Figure S1.5). The data indicate that, during the two study periods, St-Maurice was approximately one °C colder than St-Marthe. The higher latitude

of St-Maurice compared to St-Marthe could be a contributing factor to this temperature difference, which in turn may influence the extent of soil freezing.

Regarding the variation in soil freezing occurrences among plots, complex interactions among plot-level variables can play a considerable influence. For instance, the F plot in St-Marthe during 2021–22 displayed prolonged soil freezing events compared to the F plot in 2020–21, despite having identical site conditions (Figure 1.4). A key factor under consideration is the variability in snow cover across the two study years. FT events are highly dependent on both snow depth and soil temperature. Decker et al (2003) observed that in snow-free plots, there was a significant negative correlation between the average ambient temperature and the number of days the soil remained frozen at various soil depths. This finding is particularly relevant to our study, given the absence of in situ snow depth data for the plots. A plausible explanation for the more prolonged soil freezing observed in the second year might be linked to the differences in average daily air temperatures during the two periods. The 2020–21 study year had an average temperature of 3.73 °C, while the subsequent 2021–22 year recorded a lower average temperature of 2.41 °C (see Supplementary Material Figure S1.5a). This relatively lower average temperature in the second year likely led to more severe soil-freezing episodes.

1.4.2. Retrieving Ground Frozen State from VH Backscatter

When it comes to the S1 polarization ability to predict frozen soil, better model performances were obtained when using VH backscatter signals within the EFTA logistic models to predict 2 cm depth soil freezing probability. This can be explained by the increased sensitivity of cross-polarized VH backscatter to surface characteristics (soil roughness, soil types, ground vegetation density, soil state) (Bauer-Marschallinger et al, 2021). Further, as compared to VV polarization, VH backscattering correlates more strongly with soil water content (Soudani et al, 2021). Irrespective of the algorithm employed, the model predictions exhibited a more suitable goodness of fit for soil freezing at a depth of 2 cm. Due to the limited penetration depth of the C-band backscattered SAR signal, its sensitivity to dielectric variations decreases with increasing depth of the frozen soil, thereby making the prediction of frozen soil less reliable for deeper layers compared

to the near-surface (Asmuß et al, 2019). Furthermore, the dielectric discontinuity between soil and air results in distinct radar backscattering coefficients, making the signal particularly sensitive to soil freezing near the surface (Rowlandson et al, 2018; Roy et al, 2017b). The improved performance of the probabilistic approach employing the suggested EFTA derived from VH radar data (Pseudo-R^2 = 0.54) indicates its enhanced capability to detect variations in backscatter during frozen and thawed episodes (Table 1.2).

1.4.3. GLM Prediction and Influencing Variables on Radar Signals

In St-Marthe, during both study years, the locally fitted GLM results indicated that the H plot showed improved model performance in the first year compared to the second one, despite sharing similar soil types (Figure 1.5a). A plausible explanation for this phenomenon is the presence of crop debris on the surface during fall, which contributes to a significant impact on radar backscattering through two primary mechanisms. Firstly, it introduces additional roughness to the soil surface, thereby influencing the scattering of radar waves. Secondly, the debris assists in retaining soil moisture, thereby altering the soil dielectric constant and modifying the interaction between the radar signal and the ground.

Generally, the different GLM model performances observed between agricultural plots in the two study periods (Figure 1.5a, b, d, e) can largely be attributed to several interconnected aspects. Firstly, the local variability in snow depth, influenced by microtopographic variations, differing vegetation covers, and wind patterns across sites in St-Marthe and St-Maurice (Dharmadasa et al, 2023), significantly impacts the ground's thermal regime. These changes in ground surface temperature within the plots result in alterations to the soil's freezing and thawing state. Secondly, even minor changes in soil moisture content can notably alter the soil's complex permittivity (Huang et al, 2019), a phenomenon that is particularly evident during fall and spring. During the thawing period, spatial and temporal variations in wet soil across different plots independently affect the VH radar. An increase in soil moisture correlates with a rise in the backscattering coefficient. This complex interplay between local snow depth variability and soil moisture

dynamics is crucial for understanding the varied backscatter response and, consequently, the differing model performances in agricultural plots across distinct study periods.

The logistic model fitted to the forest plots indicated higher performance in cases where the plots exhibited a relatively balanced distribution of frozen and thaw events (Figure 1.5c: 2021–22). This balance contributed to more accurate predictions. Specifically, the forest plot A in St-Maurice experienced only a limited number of frozen episodes over the two study years. In such instances, the lower predictive performance for frozen states is maintained, as the imbalanced dataset biases the model's predictions toward the dominant class, which is the thaw state. This highlights the significance of having a sufficiently extensive and balanced training dataset for model calibration and validation. Mixed models are well-suited for this purpose as they enable fitting the model on the whole dataset, accounting for spatial variabilities through plot-level predictors, cross-level interactions, and random effects.

1.4.4. Crop-Mixed Model and Predictor Effects

The results revealed that among the tested mixed models, the Crop-Mixed model, incorporating the interplay between VH_{EFTA} and crop type predictors, exhibited the most favorable performance among the candidate models. Additionally, the Crop-Mixed model brought to light discernible effects of predictors, including cross-level interactions between VH_{EFTA} and crop types which improved the prediction of soil freezing probability (Table 1.3). Accordingly, the obtained conditional R^2 of 0.61 emphasizes the collective effect of both fixed and random effects in explaining the variability within the dependent variable.

The analysis revealed that while the inclusion of crop-type interactions improved the model's predictions, this improvement remains relatively small compared to the Model 2 results, which only considered random effects. A significant observation is the absence of random variability in the Crop-Mixed model, as indicated by a τ_{00} Plot value of 0.00 (Table 1.4). This finding suggests that the incorporation of crop types effectively explained

the random variability, which was more pronounced in the model featuring only random effects.

Comparatively, the analysis of Model 2, detailed in Table 1.3, provided insightful results. There was minimal spatial variability between plots based on the closeness of the conditional R^2 (0.56) and marginal R^2 values (0.57) in this model. This suggests that, while random effects are indeed present, they do not significantly contribute to the variability in soil freezing probability across different plots. This highlights the importance of cross-level interaction in the Crop-Mixed model, where crop types modulate the backscatter response to soil freezing. Accordingly, the results of cross-over interactions among different crop types demonstrated varied relationships between VH_{EFTA} and the predicted probability of soil freezing. Specifically, ploughed fields, as well as potato and soybean fields, showed an increased susceptibility to soil freezing across all VH_{EFTA} values. Conversely, grasslands typically exhibited a lower predicted probability of soil freezing in response to changes in VH_{EFTA}, compared to other crop types. These variations underscore the significant influence of specific crop types on the prediction of soil freezing.

The temporal variability of the VH_{EFTA} at the plot-level offers insight into the varying results of temporal cross-validation. Despite consistent soil types and similar crop types across the agricultural plots, the differences in snow depth and air temperature across the two study periods are notable. The presence of the relatively higher snow depth in agricultural plots (see Supplementary Material Figure S1.6) and higher average air temperatures during the first year (see Supplementary Material Figure S1.5) potentially account for the improved performance of the Crop-Mixed model's temporal cross-validation compared to the second year (Table 1.5). Specifically, these conditions are possibly key drivers that significantly influence the probability of soil freezing. Furthermore, the results of spatial cross-validation for the Crop-Mixed model (Figure 1.7) emphasize the importance of accounting for the spatial heterogeneity of snow cover in plots, as well as the complexities of surface roughness in different agricultural plots, when developing predictive models for soil freezing in farmlands. The observation of very

limited soil freezing events for St-Marthe's C and D plots in the 2020–21 period and apparently no freezing events in the 2021–22 period near the forest edge, as indicated in Figure 1.3a, b, can be scientifically explained by the presence of high snow depth in these areas.

In this study, a novel freeze–thaw algorithm, the EFTA, was developed specifically for agro-forested areas where seasonal FT transitions are dominant. The developed EFTA demonstrated significantly improved results compared to both Delta (Table 1.2 and Figure 1.4) and FTI methods (Table 1.2). However, future research should consider certain limitations, particularly the effects of high backscatter noise before the onset of the frozen period and during the onset of snow melting in spring. To address these challenges, it is advisable to experiment with identifying the potential frozen period by selecting the most negative and positive backscatter differences before and after the frozen period, while excluding months with a high probability of thawing (e.g., June and later). As a result, the algorithm performance will improve in situations with significant backscatter noise. Additionally, for study sites with limited frozen conditions, fine-tuning the K parameter becomes essential to align the algorithm's output with the specific conditions of the study site, thereby enhancing its adaptability and robustness.

1.5. Conclusions

This study represents a new application of a probabilistic approach for identifying locally frozen soil conditions in agro-forested environments in southern Québec, Canada, using Sentinel-1 SAR observations. The utilization of the GLM proved to be a robust statistical framework for analyzing soil freezing probability and conducting spatially variable probabilistic modeling of freeze–thaw detection. Through the incorporation of mixed models, this study significantly advanced our understanding of FT changes and enabled more precise and spatially explicit predictions within the study area. Notably, the Crop-Mixed model demonstrated a superior ability to capture the variability of site-level predictors for freezing probability, emphasizing the advantages of employing the VH_{EFTA} and the mixed model approach. These methods offer enhanced accuracy and explanatory power in predicting the probability of freezing in mixed agro-forested areas. In light of

the results, the newly developed EFTA has shown capability in detecting frozen and thawed states in both agricultural and forested areas. The results underscore the importance of a deeper comprehension of spatial and temporal dynamics in radar signal interactions with surfaces, providing valuable insights for optimizing model calibration and validation strategies of soil freezing retrieval models in contexts where surface conditions exhibit seasonal variations.

1.6. Statements

Author Contributions: Conceptualization, C.K. and A.R.; methodology, C.K., A.R., and S.T.; formal analysis, S.T., C.K., and A.R.; data curation, S.T.; writing-original draft preparation, S.T.; writing-review and editing, C.K. and A.R.; supervision, C.K. and A.R.; project administration, C.K. and A.R.; funding acquisition, C.K. and A.R. All authors have read and agreed to the published version of the manuscript.

Funding: This study was financially supported by Fonds de Recherche du Québec Nature et Technologies (FRQNT) under the Merit scholarship program for foreign students (PBEEE) program for doctoral research scholarships (File number: 275403; DOI: https://doi.org/10.69777/275403), Canadian Space Agency FAST (19FAQCTB19), and the FRQNT Team Research Project grant 2022-PR-299776 (C. Kinnard).

Data Availability Statement: The datasets utilized in this study are publicly available in the Borealis repository at the following link: https://doi.org/10.5683/SP3/LGLCKW.

Acknowledgments: The authors extend their appreciation to the members of GlacioLab for their help during our fieldwork.

Conflicts of Interest: The authors declare no conflicts of interest.

1.7. References

Amani, M., Brisco, B., Afshar, M., Mirmazloumi, S. M., Mahdavi, S., Mirzadeh, S. M. J., Huang, W. & Granger, J. (2019) A generalized supervised classification scheme to produce provincial wetland inventory maps: An application of Google Earth Engine for big geo data processing. *Big Earth Data*, 3(4), 378-394. doi:10.1080/20964471.2019.1690404

Asmuß, T., Bechtold, M. & Tiemeyer, B. (2019) On the potential of Sentinel-1 for high resolution monitoring of water table dynamics in grasslands on organic soils. *Remote Sensing*, 11(14), 1659. doi:10.3390/rs11141659

Baghdadi, N., Bazzi, H., El Hajj, M. & Zribi, M. (2018) Detection of frozen soil using Sentinel-1 SAR data. *Remote Sens.*, 10(8), 1182. doi:10.3390/rs10081182

Baghdadi, N., King, C., Bourguignon, A. & Remond, A. (2002) Potential of ERS and RADARSAT data for surface roughness monitoring over bare agricultural fields: application to catchments in Northern France. *Int. J. Remote Sens.*, 23(17), 3427-3442. doi:10.1080/01431160110110974

Bauer-Marschallinger, B., Cao, S., Navacchi, C., Freeman, V., Reuß, F., Geudtner, D., Rommen, B., Vega, F. C., Snoeij, P. & Attema, E. (2021) The normalised Sentinel-1 Global Backscatter Model, mapping Earth's land surface with C-band microwaves. *Scientific Data*, 8(1), 277. doi:10.1038/s41597-021-01059-7

Cheng, Y., Li, P., Xu, G., Li, Z., Wang, T., Cheng, S., Zhang, H. & Ma, T. (2018) The effect of soil water content and erodibility on losses of available nitrogen and phosphorus in simulated freeze-thaw conditions. *Catena*, 166, 21-33. doi:10.1016/j.catena.2018.03.015

Cober, J. R., Macrae, M. L. & Van Eerd, L. L. (2018) Nutrient release from living and terminated cover crops under variable freeze–thaw cycles. *Agronomy Journal*, 110(3), 1036-1045. doi:10.2134/agronj2017.08.0449

Decker, K., Wang, D., Waite, C. & Scherbatskoy, T. (2003) Snow removal and ambient air temperature effects on forest soil temperatures in northern Vermont. *Soil Science Society of America Journal*, 67(4), 1234-1242. doi:10.2136/sssaj2003.1234

Derksen, C., Xu, X., Dunbar, R. S., Colliander, A., Kim, Y., Kimball, J. S., Black, T. A., Euskirchen, E., Langlois, A. & Loranty, M. M. (2017a) Retrieving landscape freeze/thaw state from Soil Moisture Active Passive (SMAP) radar and radiometer measurements. *Remote Sensing of Environment*, 194, 48-62. doi:10.1016/j.rse.2017.03.007

Derksen, C., Xu, X., Dunbar, R. S., Colliander, A., Kim, Y., Kimball, J. S., Black, T. A., Euskirchen, E., Langlois, A. & Loranty, M. M. J. R. S. o. E. (2017b) Retrieving landscape freeze/thaw state from Soil Moisture Active Passive (SMAP) radar and radiometer measurements. *Remote Sensing of Environment*, 194, 48-62. doi:10.1016/j.rse.2017.03.007

Dharmadasa, V., Kinnard, C. & Baraër, M. (2023) Topographic and vegetation controls of the spatial distribution of snow depth in agro-forested environments by UAV lidar. *The Cryosphere*, 17(3), 1225-1246. doi:10.5194/tc-17-1225-2023

Dharmadasa, V., Kinnard, C. & Baraër, M. J. R. S. (2022) An accuracy assessment of snow depth measurements in agro-forested environments by UAV lidar. *Remote Sensing*, 14(7), 1649. doi:10.3390/rs14071649

Domg, Y. & Milne, A. K. (2001) Toward edge sharpening: a SAR speckle filtering algorithm. *IEEE Transactions on Geoscience Remote Sensing*, 39(4), 851-863. doi:10.1109/36.917910

Du, J., Kimball, J. S., Azarderakhsh, M., Dunbar, R. S., Moghaddam, M. & McDonald, K. C. (2014) Classification of Alaska spring thaw characteristics using satellite L-band radar remote sensing. *IEEE Transactions on Geoscience Remote Sensing*, 53(1), 542-556. doi:10.1109/TGRS.2014.2325409

Edwards, L. M. (2013) The effects of soil freeze–thaw on soil aggregate breakdown and concomitant sediment flow in Prince Edward Island: A review. *Can. J. Soil Sci.*, 93(4), 459-472. doi:10.4141/cjss2012-059

Escobar, A. M. d. A. (2017) *Analysis of Surface Roughness in Agricultural Soils Using In-Situ Measurements and Remote Sensing Techniques*. Ph.D. Thesis PhD. Public University of Navarre.

Fayad, I., Baghdadi, N., Bazzi, H. & Zribi, M. (2020) Near real-time freeze detection over agricultural plots using Sentinel-1 data. *Remote Sens.*, 12(12), 1976. doi:10.3390/rs12121976

Filipponi, F. (2019) Sentinel-1 GRD preprocessing workflow, *International Electronic Conference on Remote Sensing*. MDPI.

Fuhrmann, T. & Garthwaite, M. C. (2019) Resolving three-dimensional surface motion with InSAR: Constraints from multi-geometry data fusion. *Remote Sensing*, 11(3), 241. doi:10.3390/rs11030241

Gao, C., Bai, W., Wang, Z., Wu, X., Liu, L., Deng, N. & Xia, J. (2021) Simulations and Analysis of GNSS Multipath Observables for Frozen and Thawed Soil under Complex Surface Conditions. *Water*, 13(14), 1986. doi:10.3390/w13141986

Gorelick, N., Hancher, M., Dixon, M., Ilyushchenko, S., Thau, D. & Moore, R. (2017) Google Earth Engine: Planetary-scale geospatial analysis for everyone. *Remote Sens. Environ.*, 202, 18-27. doi:10.1016/j.rse.2017.06.031

Guo, D. & Wang, H. (2014) Simulated change in the near-surface soil freeze/thaw cycle on the Tibetan Plateau from 1981 to 2010. *Chinese Science Bulletin*, 59(20), 2439-2448. doi:10.1007/s11434-014-0347-x

Henry, H. A. (2007) Soil freeze–thaw cycle experiments: trends, methodological weaknesses and suggested improvements. *Soil Biology Biochemistry*, 39(5), 977-986. doi:10.1016/j.soilbio.2006.11.017

Holah, N., Baghdadi, N., Zribi, M., Bruand, A. & King, C. (2005) Potential of ASAR/ENVISAT for the characterization of soil surface parameters over bare agricultural fields. *Remote sensing of environment*, 96(1), 78-86. doi:10.1016/j.rse.2005.01.008

Huang, S., Ding, J., Zou, J., Liu, B., Zhang, J. & Chen, W. (2019) Soil moisture retrival based on sentinel-1 imagery under sparse vegetation coverage. *Sensors*, 19(3), 589. doi:10.3390/s19030589

Hudier, E. & Gosselin, J.-S. (2010) Impact of daily melt and freeze patterns on sea ice large scale roughness features extraction, *Geoscience and Remote Sensing New Achievements*IntechOpen.

Jagtar Bhatti, V. B., Mark Castonguay, R. E. & Arp, P. A. (2006) Modeling snowpack and soil temperature and moisture conditions in a jack pine, black spruce and aspen forest stand in central Saskatchewan (BOREAS SSA). *Canadian Journal of Soil Science*, 86(Special Issue), 203-217. doi:10.4141/S05-088

Jin, R., Zhang, T., Li, X., Yang, X. & Ran, Y. (2015) Mapping surface soil freeze-thaw cycles in China based on SMMR and SSM/I brightness temperatures from 1978 to 2008. *Arctic, Antarctic, Alpine Research*, 47(2), 213-229. doi:10.1657/AAAR00C-13-304

Khaldoune, J., Van Bochove, E., Bernier, M. & Nolin, M. C. (2011) Mapping agricultural frozen soil on the watershed scale using remote sensing data. *Applied Environmental Soil Science*, 2011(1), 193237. doi:10.1155/2011/193237

Krogstad, K. (2021) *Impact of Winter Soil Processes on Nutrient Leaching in Cold Region Agroecosystems*. Master of Science Master of Science in Earth Sciences (Water). University of Waterloo, 2021.

Lee, J.-S., Wen, J.-H., Ainsworth, T. L., Chen, K.-S. & Chen, A. (2008) Improved sigma filter for speckle filtering of SAR imagery. *IEEE Transactions on Geoscience and Remote Sensing*, 47(1), 202-213. doi:10.1109/TGRS.2008.2002881

Leuther, F. & Schlüter, S. J. S. (2021) Impact of freeze–thaw cycles on soil structure and soil hydraulic properties, 7(1), 179-191.

Li, Y., Fu, Q., Li, T., Liu, D., Hou, R., Li, Q., Yi, J., Li, M. & Meng, F. (2021) Snow melting water infiltration mechanism of farmland freezing-thawing soil and determination of meltwater infiltration parameter in seasonal frozen soil areas. *Agricultural Water Management*, 258, 107165. doi:10.1016/j.agwat.2021.107165

Luo, S., Wang, J., Pomeroy, J. W. & Lyu, S. (2020) Freeze–thaw changes of seasonally frozen ground on the Tibetan Plateau from 1960 to 2014. *Journal of Climate*, 33(21), 9427-9446. doi:10.1175/JCLI-D-19-0923.1

McDonald, K., Podest, E., Dunbar, S., Njoku, E. & Kimball, J. (2012) *Algorithm Theoretical Basis Document (ATBD) SMAP Level 3 Radar Freeze/Thaw Data Product (L3_FT_A)* California (USA): Technology, J. P. L. C. I. o.

McDonald, K. C., Kimball, J. S., Zhao, M., Njoku, E., Zimmermann, R. & Running, S. W. (2004) Spaceborne microwave remote sensing of seasonal freeze-thaw processes in the terrestrial high latitudes: Relationships with land-atmosphere CO2 exchange, *Microwave Remote Sensing of the Atmosphere and Environment IV*. International Society for Optics and Photonics.

Park, S.-E., Bartsch, A., Sabel, D., Wagner, W., Naeimi, V. & Yamaguchi, Y. (2011) Monitoring freeze/thaw cycles using ENVISAT ASAR Global Mode. *Remote Sensing of Environment*, 115(12), 3457-3467. doi:10.1016/j.rse.2011.08.009

Peng, X., Frauenfeld, O. W., Cao, B., Wang, K., Wang, H., Su, H., Huang, Z., Yue, D. & Zhang, T. (2016) Response of changes in seasonal soil freeze/thaw state to climate change from 1950 to 2010 across china. *Journal of Geophysical Research: Earth Surface*, 121(11), 1984-2000. doi:10.1002/2016JF003876

Pomeroy, J. W., Marks, D., Link, T., Ellis, C., Hardy, J., Rowlands, A. & Granger, R. (2009) The impact of coniferous forest temperature on incoming longwave radiation to melting snow. *Hydrological Processes: An International Journal*, 23(17), 2513-2525. doi:10.1002/hyp.7325

Qin, Y., Bai, Y., Chen, G., Liang, Y., Li, X., Wen, B., Lu, X. & Li, X. (2021) The effects of soil freeze–thaw processes on water and salt migrations in the western Songnen Plain, China. *Scientific Reports*, 11(1), 1-12. doi:10.1038/s41598-021-83294-x

Rautiainen, K., Lemmetyinen, J., Pulliainen, J., Vehvilainen, J., Drusch, M., Kontu, A., Kainulainen, J., Seppanen, J. J. I. T. o. G. & Sensing, R. (2011) L-band radiometer observations of soil processes in boreal and subarctic environments, 50(5), 1483-1497.

Rautiainen, K., Lemmetyinen, J., Schwank, M., Kontu, A., Ménard, C. B., Mätzler, C., Drusch, M., Wiesmann, A., Ikonen, J. & Pulliainen, J. (2014) Detection of soil freezing from L-band passive microwave observations. *Remote Sensing of Environment*, 147, 206-218. doi:10.1016/j.rse.2014.03.007

Rodionova, N. (2019a) Identification of Frozen/Thawed Soils in the Areas of Anadyr (Chukotka) and Belaya Gora (Sakha) from the Sentinel 1 Radar Data. *Atmospheric and Oceanic Physics*, 55(9), 1314-1321. doi:10.1134/S0001433819090433

Rodionova, N. V. (2019b) Correlation of the Sentinel 1 Radar Data with Ground-Based Measurements of the Soil Temperature and Moisture. *Izvestiya, Atmospheric and Oceanic Physics*, 55, 939-948. doi:10.1134/S0001433819090421

Rowlandson, T. L., Berg, A. A., Roy, A., Kim, E., Lara, R. P., Powers, J., Lewis, K., Houser, P., McDonald, K. & Toose, P. (2018) Capturing agricultural soil freeze/thaw state through remote sensing and ground observations: A soil freeze/thaw validation campaign. *Remote sensing of environment*, 211, 59-70. doi:10.1016/j.rse.2018.04.003

Roy, A., Toose, P., Derksen, C., Rowlandson, T., Berg, A., Lemmetyinen, J., Royer, A., Tetlock, E., Helgason, W. & Sonnentag, O. (2017a) Spatial variability of L-band brightness temperature during freeze/thaw events over a prairie environment. *Remote Sensing*, 9(9), 894. doi:10.3390/rs9090894

Roy, A., Toose, P., Williamson, M., Rowlandson, T., Derksen, C., Royer, A., Berg, A. A., Lemmetyinen, J. & Arnold, L. (2017b) Response of L-Band brightness temperatures to freeze/thaw and snow dynamics in a prairie environment from ground-based radiometer measurements. *Remote Sensing of Environment*, 191, 67-80. doi:10.1016/j.rse.2017.01.017

Schaufler, S., Bauer-Marschallinger, B., Hochstöger, S. & Wagner, W. (2018) Modelling and correcting azimuthal anisotropy in Sentinel-1 backscatter data. *Remote Sens. Lett.*, 9(8), 799-808. doi:10.1080/2150704X.2018.1480071

Shao, W. & Zhang, T. (2020) Assessment of Four Near-Surface Soil Freeze/Thaw Detection Algorithms Based on Calibrated Passive Microwave Remote Sensing Data Over China. *Earth and Space Science*, 7(7), e2019EA000807. doi:10.1029/2019EA000807

Smith, M. W. J. C. J. o. E. S. (1975) Microclimatic influences on ground temperatures and permafrost distribution, Mackenzie Delta, Northwest Territories. *Canadian Journal of Earth Sciences*, 12(8), 1421-1438. doi:10.1139/e75-129

Soudani, K., Delpierre, N., Berveiller, D., Hmimina, G., Vincent, G., Morfin, A. & Dufrêne, É. (2021) Potential of Synthetic Aperture Radar Sentinel-1 time series for the monitoring of phenological cycles in a deciduous forest. *bioRxiv*, 2021.02. 04.429811. doi:10.1016/j.jag.2021.102505

Steyerberg, E. W., Vickers, A. J., Cook, N. R., Gerds, T., Gonen, M., Obuchowski, N., Pencina, M. J. & Kattan, M. W. (2010) Assessing the performance of prediction models: a framework for traditional and novel measures. *Epidemiology*, 21(1), 128-138. doi:10.1097/EDE.0b013e3181c30fb2

Torres, R., Snoeij, P., Geudtner, D., Bibby, D., Davidson, M., Attema, E., Potin, P., Rommen, B., Floury, N. & Brown, M. (2012) GMES Sentinel-1 mission. *Remote sensing of environment*, 120, 9-24. doi:10.1016/j.rse.2011.05.028

Touati, C., Ratsimbazafy, T., Poulin, J., Bernier, M., Homayouni, S. & Ludwig, R. (2021) Landscape freeze/thaw mapping from active and passive microwave Earth observations over the Tursujuq National Park, Quebec, Canada. *Écoscience*, 28(3-4), 421-433. doi:10.1080/11956860.2021.1969790

Wackerly, D. D. (2008) Mathematical Statistics with Applications. 7th Edition ed. USA: Thomson Learning, Inc.

Walvoord, M. A. & Kurylyk, B. L. (2016) Hydrologic impacts of thawing permafrost—A review. *Vadose Zone Journal* 15(6), vzj2016. 01.0010. doi:10.2136/vzj2016.01.0010

Wang, K., Zhang, T. & Zhong, X. (2015) Changes in the timing and duration of the near-surface soil freeze/thaw status from 1956 to 2006 across China. *The Cryosphere*, 9(3), 1321-1331. doi:10.5194/tc-9-1321-2015

Wang, R., Zhu, Q., Ma, H. & Ai, N. (2017) Spatial-temporal variations in near-surface soil freeze-thaw cycles in the source region of the Yellow River during the period 2002–2011 based on the Advanced Microwave Scanning Radiometer for the Earth Observing System (AMSR-E) data. *Journal of Arid Land*, 9(6), 850-864. doi:10.1007/s40333-017-0032-4

Wang, T., Li, P., Li, Z., Hou, J., Xiao, L., Ren, Z., Xu, G., Yu, K. & Su, Y. (2019) The effects of freeze–thaw process on soil water migration in dam and slope farmland on the Loess Plateau, China. *Science of The Total Environment* 666, 721-730. doi:10.1016/j.scitotenv.2019.02.284

Xu, G., Huang, M., Li, P., Li, Z. & Wang, Y. (2021) Effects of land use on spatial and temporal distribution of soil moisture within profiles. *Environmental Earth Sciences*, 80(4), 1-12. doi:10.1007/s12665-021-09464-2

Zhang, T., Armstrong, R. & Smith, J. (2003) Investigation of the near-surface soil freeze-thaw cycle in the contiguous United States: Algorithm development and validation. *Journal of Geophysical Research: Atmospheres*, 108(D22). doi:10.1029/2003JD003530

Zhao, T., Zhang, L., Jiang, L., Zhao, S., Chai, L. & Jin, R. (2011) A new soil freeze/thaw discriminant algorithm using AMSR-E passive microwave imagery. *Hydrological Processes*, 25(11), 1704-1716. doi:10.1002/hyp.7930

Zhao, Y., Li, Y. & Yang, F. (2020) Critical review on soil phosphorus migration and transformation under freezing-thawing cycles and typical regulatory measurements. *Science of the Total Environment*, 141614. doi:10.1016/j.scitotenv.2020.141614

Zribi, M., Sahnoun, M., Baghdadi, N., Le Toan, T. & Hamida, A. B. (2016) Analysis of the relationship between backscattered P-band radar signals and soil roughness. *Remote Sensing of Environment* 186, 13-21. doi:10.1016/j.rse.2016.08.006

Chapter I Supplementary Information

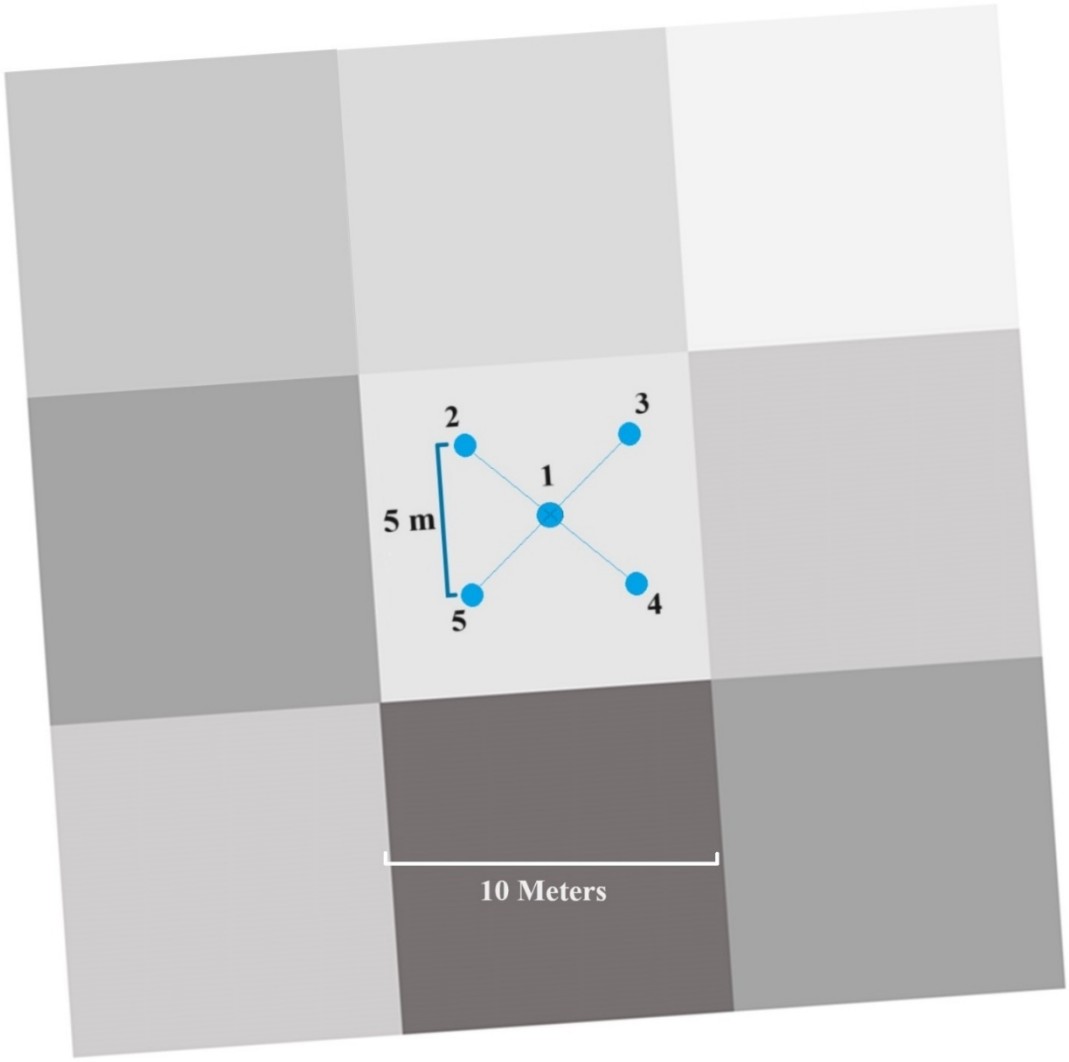

Figure S1.1. Schematic representation of the measurement configuration for soil temperature measurements (2 cm and 10 cm depths), aligned with the Sentinel 1 pixel size of 10 meters. The geometry of the configuration includes five soil pits (blue points) arranged in a cross shape with 5 meters between each pit.

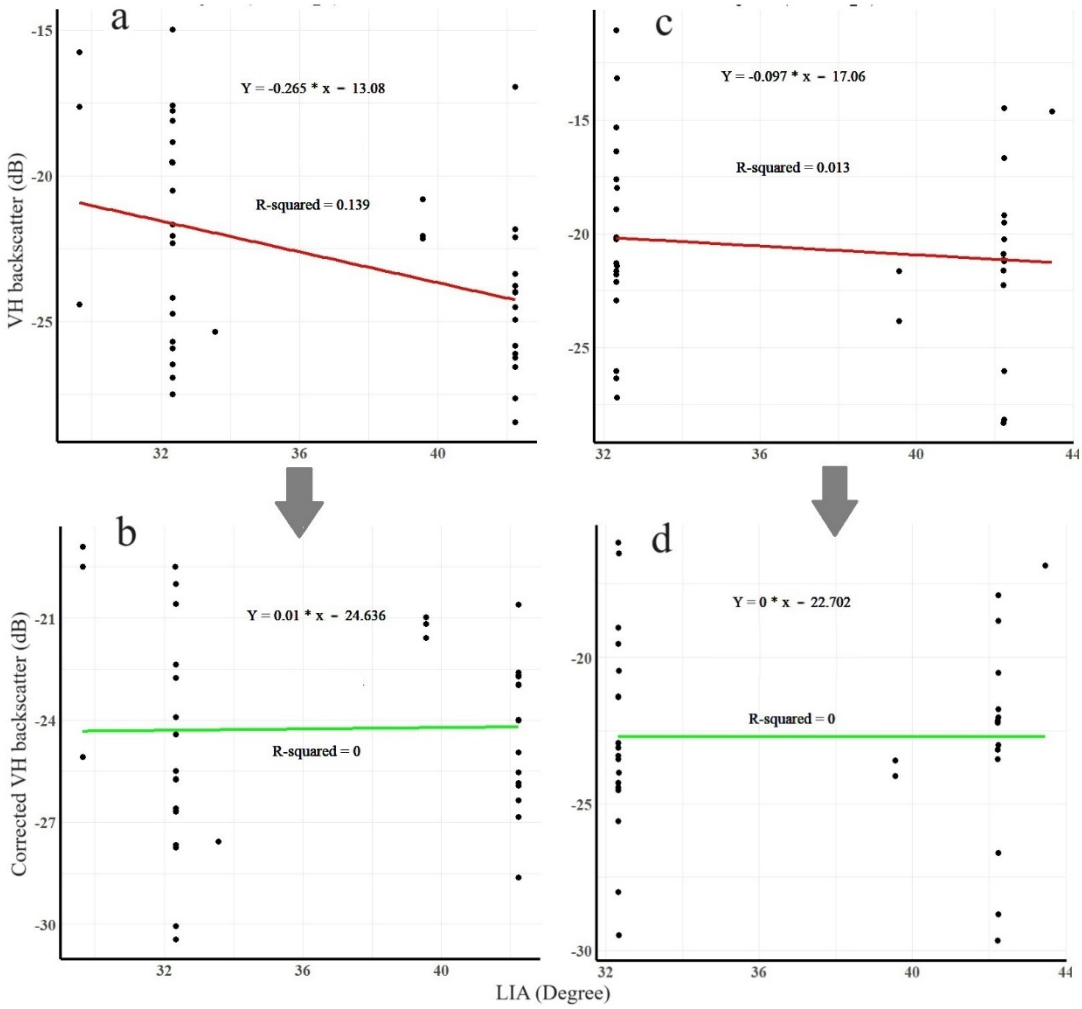

Figure S1.2. Correction of local incidence angles in St-Maurice's C plot with the corresponding linear equation. (**a**) VH backscatter before correction in 2020–21. (**b**) The corrected VH backscatter in 2020–21. (**c**) VH backscatter before correction in 2021–22. (**d**) The corrected VH backscatter in 2021–22.

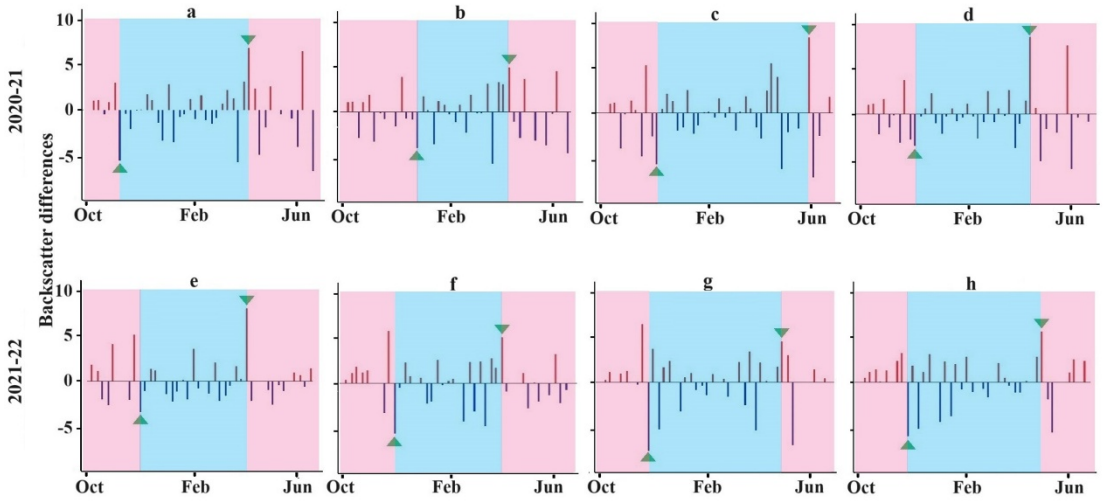

Figure S1.3. Examples of the approach used to identify the soil freezing and thawing transitions in backscatter signals in the of the EFTA method. The most negative backscatter differences (upward green triangles) before February represents the most probable onset of the freezing period (delineated in light blue), while the most positive difference (downward green triangles) after February represent the most probable onset of soil thawing (delineated in light red). (**a**–**d**) correspond to St-Marthe's I and J plots and St-Maurice's G and H plots, respectively, for the year 2020–21. (**e**–**h**) correspond to St-Marthe's I and J plots and St-Maurice's G and H plots, respectively, for the year 2021–22.

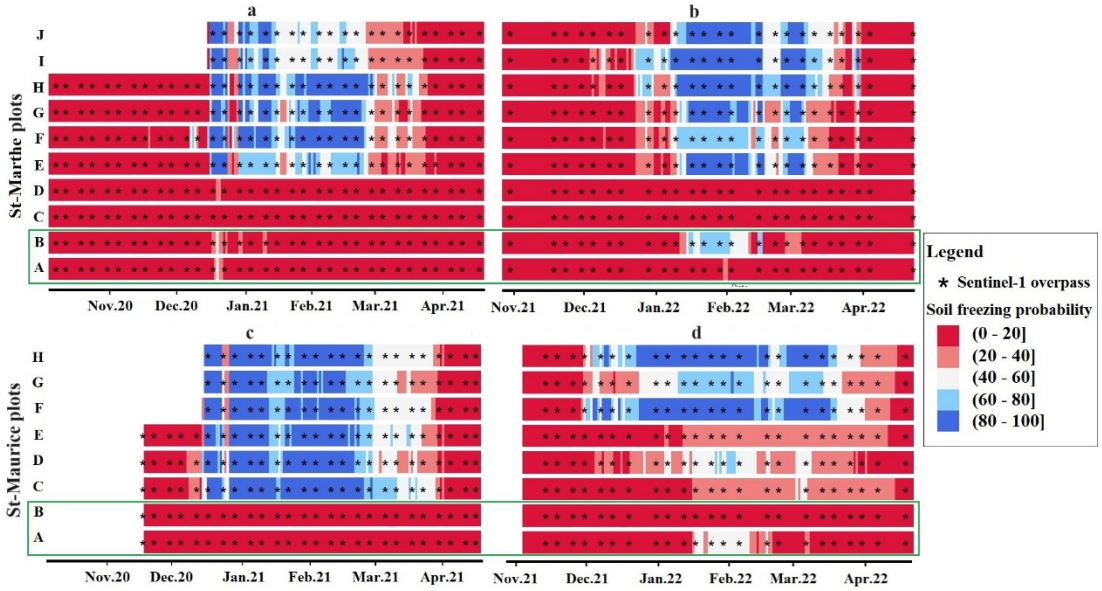

Figure S1.4. Spatial and temporal variations in freezing probability (10 cm) along with corresponding the S1 overpass for all agro-forest plots in St-Marthe. (**a**, **b**) FT variations based on freezing probability in St-Marthe's plots over two study periods (2020–21 and 2021–22). (**c**, **d**) FT variations based on freezing probability in St-Maurice's plots over two study periods (2020–21 and 2021–22). In each site, forest plots are represented by A and B plots (green rectangle). For St-Marthe's J and I and St-Maurice's F, G, and H plots, the initiation of soil temperature monitoring started later, resulting in an absence of freezing probability values.

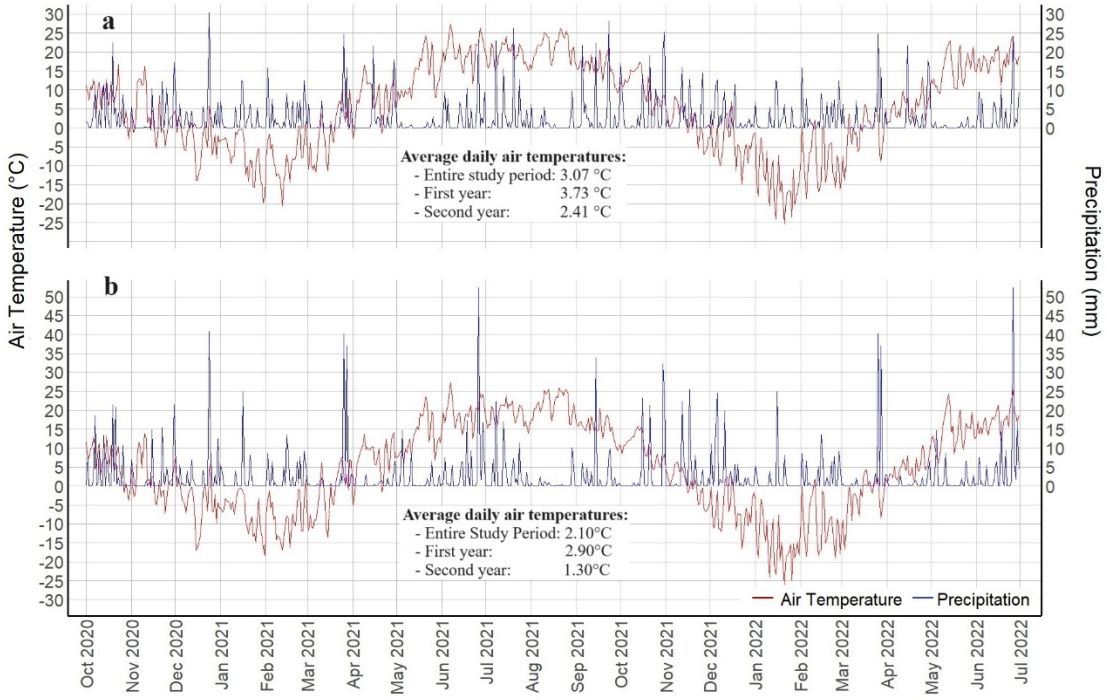

Figure S1.5. Time series plot of daily precipitation and air temperature, October 2020 to June 2022, for two study sites. (**a**) St-Marthe. (**b**) St-Maurice. Note: the average daily air temperatures for the entire study period, as well as for the first and second years (October to June), were calculated for both St-Marthe and St-Maurice.

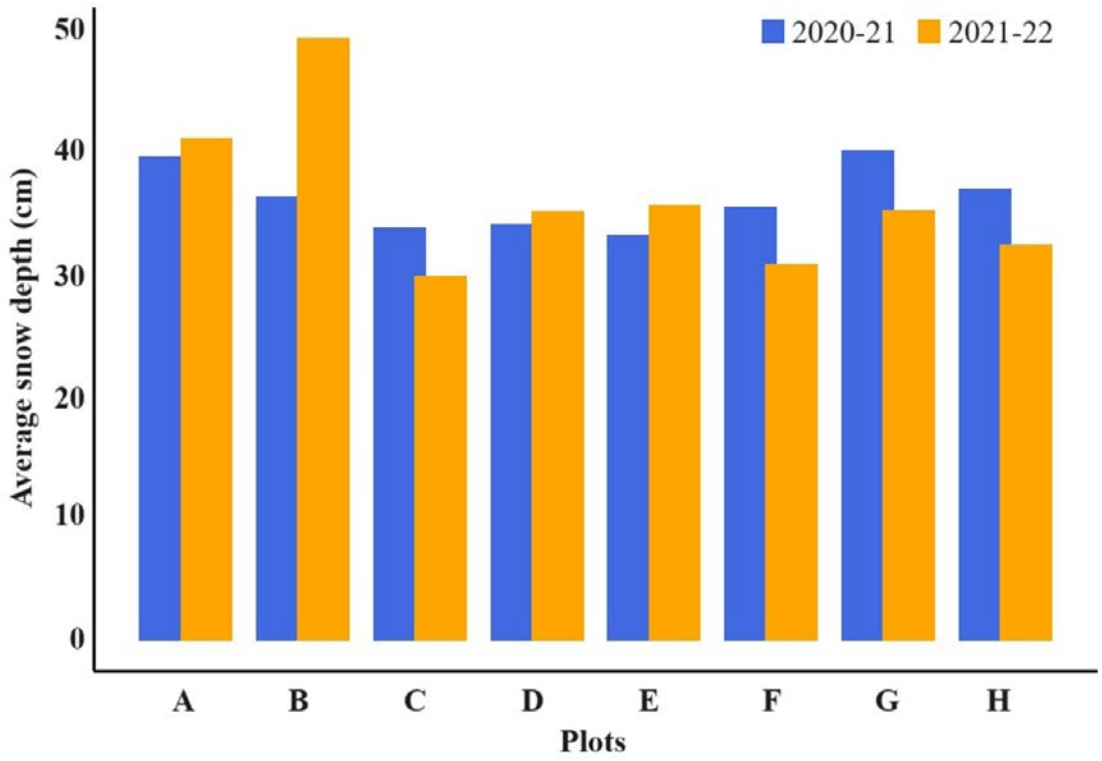

Figure S1.6. Average snow depth (meters) in agro-forested plots of St-Maurice over two study years in 2020–21 and 2021–22. Plot classification: 'A' and 'B' as forest plots; 'C' to 'H' as agricultural plots. Measurement period: End of November to March each year. Method: Using snow ruler, snow depth recorded at five points within 5m x 5m square per plot, including a central point. Calculation: Average of five measurements per plot, aggregated to represent overall snow depth for each plot.

CHAPTER II

Chapter II

On Demand Machine Learning-Driven Surface Freeze-Thaw Retrieval Across Canadian Agricultural Regions Using Sentinel-1 SAR Data

Shahabeddin Taghipourjavi, Christophe Kinnard, Alexandre Roy

Frontiers in Remote Sensing-Microwave Remote Sensing. 2026, 6; *https://doi.org/10.3389/frsen.2025.1728399*

Abstract

This study explores the prediction of freeze-thaw (FT) states across agricultural fields in four Canadian provinces-Alberta, Manitoba, Saskatchewan, and Québec-using Random Forest classification and regression models. Soil temperature data at a 5 cm depth were gathered from 174 agricultural weather stations from 2016 to 2023. Sentinel-1 SAR VH radar backscatter indicators were processed using Google Earth Engine (GEE). Two modeling approaches were evaluated: a classification model trained on in situ data, where soil states were rigidly classified as either frozen or thawed, and a regression model trained against in situ soil freezing probabilities. Additionally, other site-specific ancillary variables such as latitude, altitude, crop type, and soil type were tested as potential predictors. The regression model using the Exponential Freeze-Thaw Algorithm (EFTA) derived from VH radar backscatter (VH_{EFTA}) demonstrated strong discrimination between frozen and thawed states, and emerged as the most influential factor, accounting for over 90% of the model's predictive ability. Models using VH_{EFTA} alone achieved up to 81.4% accuracy for classifying FT state, with only a slight improvement to 82.1% when combined with other predictors. Spatial and temporal validation showed stable accuracy (0.79–0.83) and F1-scores (0.75–0.88) across regions and years. Evaluation of model sensitivity to seasonal and temperature variability revealed that although uncertainties

were not fully eliminated during transitional periods for both binary and probability-based FT models, binary-based models consistently showed lower error rates and stronger performance. The final FT model was implemented within an interactive web-based tool that generates on-demand FT maps for user-supplied regions of interest across Canadian agricultural and open-land areas.

Keywords

Sentinel-1 SAR VH backscatter, Exponential Freeze-Thaw Algorithm (EFTA), Random Forest Models, Soil Freezing Binary and Probability, Interactive Online FT Detection Tool, Canadian agricultural fields.

2.1. Introduction

More than half of the world's land experiences seasonal freezing and thawing (Kim et al, 2010a), which significantly impacts hydrological processes (Cade-Menun et al, 2013; Gray et al, 1985), agricultural activities (Osei et al, 2024), and biogeochemical cycles by altering surface energy balances (Black et al, 2000; Schuur et al, 2015), vegetation growth (Beer et al, 2007), and soil moisture (Wei et al, 2019). Soil freeze-thaw (FT) cycles occur at high latitudes (Moradi et al, 2023b; Schuur et al, 2022) and high elevations (Ekici et al, 2015; Peng et al, 2016b), and play a crucial role in regulating the water cycle and carbon exchange, particularly in seasonally frozen ground and permafrost regions. From an agricultural perspective, FT cycles play a crucial role in crop growth, soil moisture availability, and the vertical redistribution of organic matter within farmland soil (Hou et al, 2020; Sun et al, 2021). From a hydrological perspective, regional and local hydrological processes have been affected by the reduction and eventual disappearance of the freezing period in seasonally frozen regions, as well as by the accelerated melting of ice and snow (Ireson et al, 2013a; Niu & Yang, 2006). These changes further emphasize the importance of understanding FT cycles in the context of climate change. Accurate characterization of soil FT transitions and freezing duration in cold regions can help to understand how precipitations are partitioned between surface runoff and infiltration in soils, thereby helping to better predict catchment-scale hydrology.

Station-based measurements with data loggers offer high-resolution temporal data, making them valuable for monitoring near-surface FT states. However, their sparse distribution limits their spatial coverage, rendering them inadequate for assessing long-term FT cycle impacts across larger landscapes (Gao et al, 2018b; Shao & Zhang, 2020b; Wu et al, 2020). In contrast, remote sensing provides an effective alternative for spatiotemporal monitoring of soil surface FT status, enabling coverage across broader areas with consistent observations. Space-borne active and passive remote sensing observations operating at microwave frequencies have been used for the continuous monitoring of the soil FT state over large, extensive areas, regardless of cloud cover and seasonal daylight changes (Karthikeyan et al, 2017).

Active microwave techniques, particularly those utilizing synthetic aperture radar (SAR), provide the higher spatial resolution needed to accurately capture FT variability in heterogeneous landscapes (Cohen et al, 2024a). As part of Copernicus, Sentinel-1's C-band SAR instruments are particularly well suited to monitor soil FT states at local to regional scales due to their high spatial resolution (5 × 20 m in IW mode) and frequent revisit times (approximately every 6 days), making them ideal for complex environments such as agro-forested mosaic landscapes.

Several studies have leveraged SAR data to detect seasonal near-surface FT conditions. For example, Baghdadi et al (2018) demonstrated that both VV and VH polarizations from Sentinel-1 are sensitive to frozen soils, with VH showing greater responsiveness to near-surface freezing (< 5 cm). Building on this foundation, recent research in southern Québec introduced the Exponential Freeze-Thaw Algorithm (EFTA) to enhance FT detection in agro-forested landscapes, particularly when applied to VH backscatter signals (Taghipourjavi et al, 2024b).

Although C-band SAR is highly responsive to near-surface FT conditions through associated changes in soil dielectric constant, snow cover can also modify radar backscatter in ways that complicate the interpretation of FT signals (Cohen et al, 2024a; Cohen et al, 2024b; McNairn & Brisco, 2004). Wet snow, characterized by a markedly higher dielectric constant due to its liquid-water content, can substantially attenuate or mute the radar return, often producing backscatter values that resemble those of frozen soil surfaces (Benninga et al, 2019; Lund et al, 2022). For example, in agricultural fields in North Dakota, the onset of wet snow during spring melt led to a clear decrease in VH backscatter, making it challenging to distinguish wet snow from frozen ground solely based on backscatter signals (Manickam & Barros, 2020). In open agricultural fields of southern Quebec, C-band SAR backscatter was found to decrease by up to 1 dB on snow-covered days when the soil was frozen, with the reduction becoming more pronounced as snow depth and snow water equivalent increased, although the total effect for shallow, dry snowpacks (up to about 20 cm snow water equivalent) remained below the system's measurement uncertainty of approximately 1 dB (Bernier & Fortin, 1998). These effects,

driven by differences in dielectric behavior and snowpack structure, illustrate that both wet-snow conditions and variations in dry-snow depth can potentially impact alter C-band backscatter independently of soil FT processes.

To further improve the precision of FT state detection, integrating machine learning approaches offers a promising avenue for leveraging large datasets and uncovering complex spatial and temporal patterns at regional scales (Mugunthan et al, 2023). Despite limitations in the quantity and quality of ground truth data used for training, machine learning (ML) approaches can provide robust predictions of FT status with minimal bias, enabling more accurate and reliable FT monitoring. Among these methods, the Random Forest (RF) algorithm, a widely used shallow learning technique, has proven to be highly effective in various studies. For instance, Zhong et al (2022) showed that the RF algorithm significantly improved the accuracy of FT onset detection in Alaska. Similarly, Donahue et al (2023b) developed a continuous daily classification record of surface (0–5 cm depth) soil FT dynamics across all Northern Hemisphere land areas using RF models informed by multifrequency brightness temperature (TB) observations from passive microwave sensors, such as AMSR2 and SMAP.

Given the reliance of ML models on observations for training, it is also important to examine the broader context of how soil FT states can be derived from soil temperature data. Although various studies have employed rigid classification methods to model surface soil freezing, categorizing soil distinctly as either frozen or thawed, these methods often fail to capture the inherent uncertainties and spatial variability in FT states, which are crucial for accurate predictions (Donahue et al, 2023b; McColl et al, 2016). In contrast, incorporating soil freezing probability into a probabilistic FT modeling approach would provide a more nuanced understanding of the transitions between frozen and thawed states, as well as the associated uncertainties and variability in soil freezing conditions (Walker et al, 2022). While previous study using Sentinel-1 C-band data at two agro-forested sites in southern Québec have demonstrated the potential of SAR observations for local FT monitoring (Taghipourjavi et al, 2024b), these efforts remain spatially and temporally limited and do not capture the broader heterogeneity of Canadian agricultural

landscapes. In practice, FT variability across croplands, pastures, and open lands is strongly shaped by differences in soil types, crop cover, and snow depth and density, as well as regional climate gradients. However, none of these variables have been systematically evaluated within a unified SAR-based framework. Consequently, there is a need for remote sensing-based soil FT retrieval methods that generalize beyond site-specific conditions and work reliably across diverse environments. This study addresses that need by scaling FT detection to the Canadian agricultural domain through the integration of Sentinel-1 SAR data with large-sample machine-learning analyses, enabling a consistent and operational framework for monitoring FT detections across Canada's major agricultural regions.

Accordingly, this research aims to evaluate the large-scale capabilities of SAR-based indicators, particularly the EFTA derived from VH backscatter (VH_{EFTA}) for detecting and predicting FT states in agricultural fields across Canada. We begin by investigating the potential drivers of radar backscatter, including soil FT state, soil and crop type, as well as the possibly confounding effects of snow depth and snow wetness, in order to identify the dominant drivers of radar backscatter. Then, two modeling approaches are implemented to predict soil FT: a RF classification model trained on binary in situ FT labels (frozen vs. thawed), and a RF regression model trained on continuous soil freezing probabilities, both derived from an extensive network of 174 agricultural weather stations across four Canadian provinces (2016–2023). The study also assesses the contribution of different radar polarization configurations (VH, VV, and VH/VV) to FT detection performance and applies EFTA to each to enhance signal interpretability during transitional periods. In addition, various combinations of site-specific predictors including soil type, crop type, altitude, and latitude are integrated to evaluate their added value in improving FT classification and probabilistic prediction at the near-surface FT state. The research further explores model sensitivity to seasonal and temperature variability to better understand classification and prediction accuracy during transitional periods, when radar signal fluctuations are more pronounced. We then implement the best FT model within an interactive web-based tool that allows users to generate on-demand FT maps for any regions of interest across Canadian agricultural and open-land areas.

2.2. Materials and Methods

2.2.1. Study area and data

The study area spans across four Canadian provinces: Alberta, Manitoba, Saskatchewan, and Québec, each characterized by diverse climatic, soil, and agricultural conditions. The diversity of these regions provides a comprehensive landscape for examining FT states. This study utilized publicly available soil temperature data from 174 agricultural weather stations, ensuring broad spatial coverage. These provinces cover various climatic zones (See supplementary Figure S2.1), crop types, and soil conditions, allowing for a broad analysis of soil freezing and thawing events. The spatial distribution of stations is illustrated in Figure 2.1, showing that they are primarily located in agricultural regions across each province in Canada. Stations are grouped by region, with distinct colors and shapes indicating differences in observational periods. Map views (Figures 2.1A-E) provide detailed representations of station locations and IDs for Manitoba, Alberta, Saskatchewan, St-Marthe (Québec), and St-Maurice (Québec), respectively. As illustrated by the spatial distribution of observational stations in Figure 2.1, the coverage is uneven across provinces, reflecting the density of agricultural monitoring networks rather than a uniform sampling design. Stations are concentrated in intensively cultivated regions of the Prairies and southern Québec, with fewer sites in sparsely farmed areas. Consequently, the dataset predominantly represents croplands, pastures/grasslands, and open agricultural lands, consistent with the agricultural focus of this study.

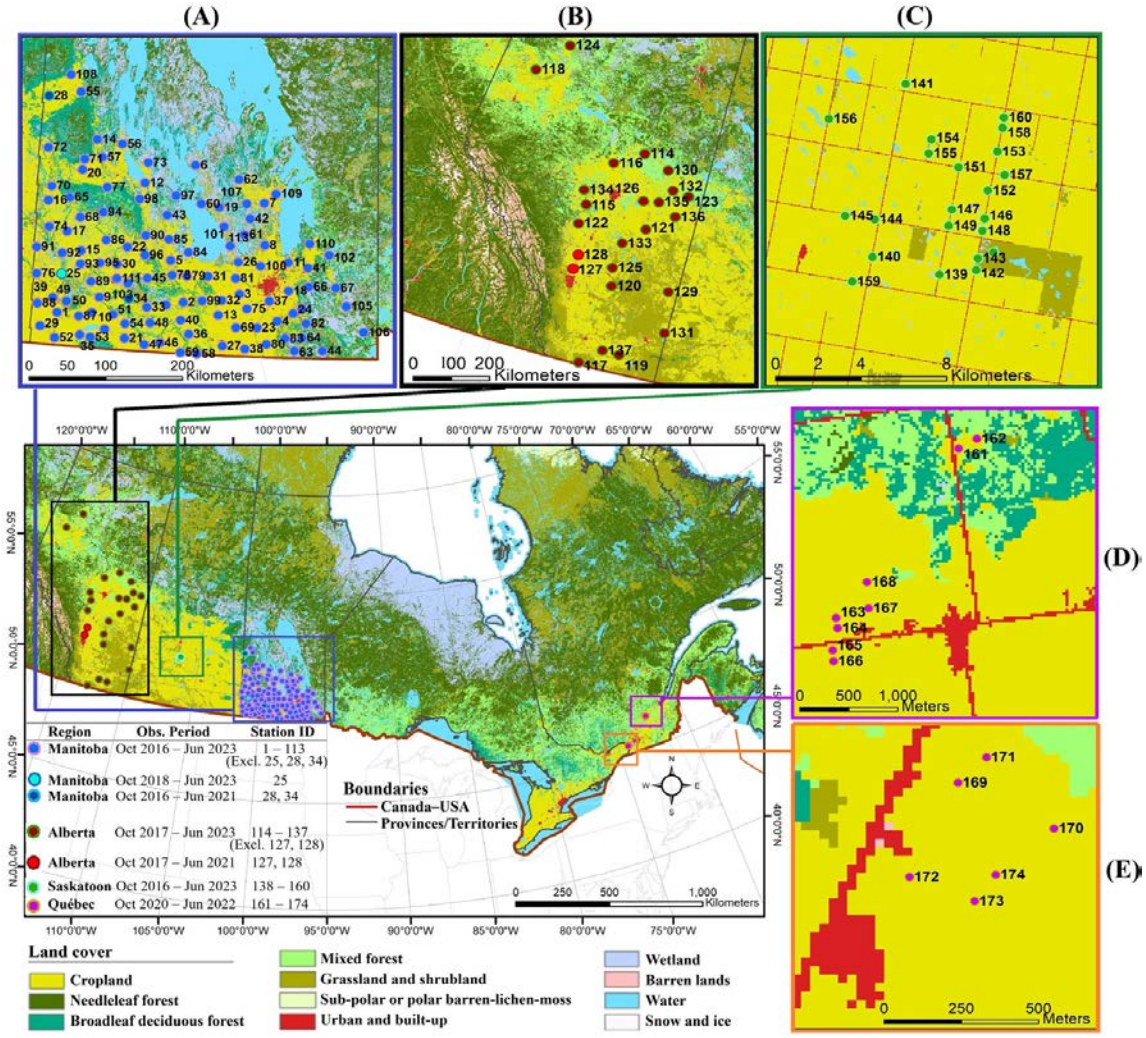

Figure 2.1. Geographic distribution of agricultural weather stations with soil temperature measurements across five Canadian provinces, overlaid on Canada's 2020 land cover map (source: https://open.canada.ca/data/en/dataset/ee1580ab-a23d-4f86-a09b-79763677eb47, accessed on 15 October 2025). Station groups are color-coded by province or region to indicate differences in observational periods (see legend, lower left). Subplots show the spatial distribution and assign station IDs for each region. (A) Manitoba; (B) Alberta; (C) Saskatchewan; (D) St-Marthe (Québec); and (E) St-Maurice (Québec).

2.2.2. Soil temperature data

Table 2.1 presents a summary of weather stations with available soil temperature data at a depth of 5 cm across the four studied Canadian provinces. In Manitoba, the station network is well distributed across its southern agricultural fields. Soil temperature data is collected by the Manitoba Agriculture Weather Program (MAWP), which maintains a comprehensive database of historical meteorological information (https://www.gov.mb.ca/agriculture/weather/manitoba-ag-weather.html, accessed 05 December 2025). A total of 113 weather stations actively recorded hourly soil temperature from October 2016 to June 2023 (Figure 2.1A). 24 weather stations were available in Alberta (Figure 2.1B), managed by the Alberta Climate Information Service under the Ministry of Agriculture and Irrigation. These stations recorded 5cm-depht hourly soil temperature from October 2017 to April 2023. The stations are relatively well distributed across the province, albeit more sparsely, and with more stations in southern farmlands.

Saskatchewan has a network of 23 weather stations (Figure 2.1C), primarily concentrated in the southern part of the province, specifically within the mixed grassland landscapes of the Kenaston Network, an experimental farm located approximately 80–100 km south of Saskatoon. This network spans the Brightwater Creek basin, a representative prairie agricultural region within Canada's Prairies/Boreal Plains Ecozones (Tetlock et al, 2019). Established in 2011 by Agriculture and Agri-Food Canada (AAFC), the network complements an existing network managed by Environment Canada (EC) and the University of Guelph (Tetlock et al, 2019). The EC-Guelph network supports various research efforts, including hydrological studies, land surface modeling, and satellite data validation. The AAFC sites, located on pasture lands, complement EC-Guelph sites situated on annual cropland. The data for these stations was recorded at 30-minute intervals from October 2016 to May 2020.

In Québec, while more than 60 stations provide multi-year soil temperature data at 10 cm depth, these were excluded because Sentinel-1 SAR C-band primarily reflects

conditions in the upper few centimeters of soil. Instead, soil temperature data at 5 cm depth was obtained from in-situ measurements collected during recent fieldwork (Taghipourjavi et al, 2024a). These measurements span two consecutive years (2020–21 and 2021–22) and were gathered from agricultural plots instrumented in St-Marthe (Figure 2.1D) and St-Maurice (Figure 2.1E) sites.

Table 2.1. Overview of weather stations for soil temperature measurements across four Canadian provinces.

Provinces	Number of stations	Data Availability
Manitoba	113	Oct 2016 – June 2023
Alberta	24	Oct 2017 – April 2023
Saskatchewan	23	Oct 2016 – May 2020
Québec	14	Oct 2020 – June 2022

2.2.3. Snowpack variables

As snowpack conditions were not available at most of the stations, snow depth (SD) and snowpack temperature (Ts) were acquired from the ERA5-Land reanalysis (Muñoz-Sabater et al, 2021) from October 2016 to April 2023 (See supplementary Figure S2.2). A snow-wetness indicator was derived by identifying periods when SD > 0 and Ts > 0 °C, corresponding to conditions under which liquid water is expected within the snowpack. With its ~10 km spatial resolution, ERA5-Land does not capture field-scale variability at individual stations, but its physically based snow energy-balance scheme and consistent temporal coverage offer a useful representation of regional snow conditions across the four provinces included in this study. The mean monthly snow depths across all sites (See supplementary Figure S2.2) range from approximately 1–8 cm in October, 6–17 cm in November, and 13–29 cm in December. Peak snow depths are observed in January and February, reaching 20–32 cm in the prairies and up to 43 cm in Québec. The snowpack gradually decreases through March and typically melts by April, with mean depths falling below 10 cm across all provinces. These values indicate that agricultural landscapes in the study area generally experience shallow to moderate snowpacks, conditions under which C-band backscatter is expected to remain predominantly sensitive to near-surface soil FT changes (Fayad et al, 2020; Moradi et al, 2024). Since radar backscatter is sensitive to

both surface roughness and water content, which vary spatially and temporally across different soil and crop types, these variables were considered as potential additional predictors of soil freeze-thaw. Crop type data were gathered from Agriculture and Agri-Food Canada (AAFC) annual crop inventory data from 2016 to 2022 (https://open.canada.ca/data/en/dataset/ba2645d5-4458-414d-b196-6303ac06c1c9, accessed 05 December 2025), while soil type data were primarily sourced from the Detailed Soil Survey (DSS) compilations from the National Soil Database (NSDB) (2016–2023) (https://sis.agr.gc.ca/cansis/nsdb/dss/v3/index.html, accessed 05 December 2025). However, the DSS data are based on general soil information for large polygons, where each polygon may contain multiple soil components. These components are not explicitly mapped, and only the proportion of the area covered by each soil type is provided. As a result, the DSS dataset lacks the precision needed for site-specific mapping of soil characteristics at weather stations, particularly at exact UTM points. To overcome this limitation, soil texture data from the World Soil Information Service (WoSIS) (https://soilgrids.org/, accessed 05 December 2025) were incorporated. Soil texture data from WoSIS, based on the exact locations of the installed stations, were used to assign relevant soil properties to each weather station.

The resulting distribution of soil types across all sites (Figure S2.3A) shows that clay loam is the dominant soil type in both Alberta (46.0%) and Manitoba (51.6%), followed closely by loam in both provinces (45.1% in Alberta and 17.8% in Manitoba). In Québec, clay is the predominant soil type (42.9%), followed by silty clay (35.7%). Regarding crop types, pasture and grassland are the primary crops in Alberta (31.3%) and Manitoba (22.0%), respectively, while corn is the most prevalent crop in Québec (35.7%), and spring wheat is dominant in Saskatchewan (32.2%) (Figure S2.3B).

In addition to soil and crop types, which directly influence radar backscatter through their effects on soil moisture and surface roughness, altitude and latitude were included as potential site predictor variables. Altitude affects local climatic conditions such as temperature, precipitation, and soil moisture, which in turn influence near-surface soil freezing heterogeneity (Johnston et al, 2021), while latitude governs broader climatic

gradients that shape the extent, depth, and persistence of seasonal soil freezing (Chang et al, 2022).

2.2.4. Sentinel-1 SAR Imagery

We utilized Sentinel-1 satellite data, which are part of the Copernicus Sentinel constellation and are equipped with C-band SAR sensors operating at a frequency of 5.405 GHz. These sensors operate in Interferometric Wide swath (IW) mode, offering a single-looked backscatter resolution ranging from 5 m to 20 m at incidence angles between 29° and 46° over flat terrain, and covering a swath width of 250 km. In Google Earth Engine (GEE), this data is resampled to a 10–meter grid to simplify analysis and integration with other datasets, providing both cross-polarization (VH) and co-polarization (VV) backscatter, which offers valuable insights into surface characteristics (Gorelick et al, 2017).

Preprocessing in GEE involved several steps to ensure accurate and consistent backscatter measurements across the study area. These included the application of orbit files for precise geolocation, removal of thermal and border noise, and radiometric calibration. To account for terrain-induced distortions, terrain correction was performed using high-resolution DEMs. Speckle noise, which degrades SAR image quality, was mitigated using the Refined Lee filter (Yu et al, 2018). In addition, local incidence angle (LIA) normalization was applied following Schaufler's method, which adjusts σ° values to a reference angle of 40° based on a linear regression with LIA (Schaufler et al, 2018; Taghipourjavi et al, 2024b). To maximize data coverage for FT modeling, both ascending and descending Sentinel-1 passes were used, although ascending acquisitions were more frequent across the study area.

2.2.5. Exponential freeze-thaw algorithm (EFTA)

The exponential freeze-thaw algorithm (EFTA, Equation 2.1) was applied using the VH and VV backscatter indicators, given their demonstrated sensitivity, particularly VH polarization, to changes in surface permittivity relevant to FT prediction (Baghdadi et al, 2018; Taghipourjavi et al, 2024b).

$$\boldsymbol{EFTA} = \left[\boldsymbol{e}^{-\boldsymbol{K}\left(\mathbf{1}+\left(\frac{\sigma_T}{\sigma(t)}\right)\right)}\right]\left(\Delta_{\boldsymbol{\theta}}(\boldsymbol{t})\right) \quad (2.1)$$

Where the expression $\left[e^{-K\left(1+\left(\frac{\sigma_T}{\sigma(t)}\right)\right)}\right]$ denotes an exponential decay function, ensuring that the outcome remains within the range of 0 to 1. The binary parameter K represents the expected thaw ($K = 1$) and frozen ($K = 0$) periods, respectively defined based on the most negative and positive differences between radar signals at time t and at the preceding time $(t - 1)$. Specifically, K is set to 0 between the largest drop in backscatter before February and the largest rise in backscatter after February, reflecting anticipated frozen periods, and is set to 1 otherwise. The term $\Delta_\theta(\mathrm{t})$ is defined as $\Delta_\theta(\mathrm{t}) = \sigma_T - \sigma(t)$, where $\sigma(t)$ refers to the backscattering coefficient acquired at time t, and σ_T is a reference backscattering coefficient for thawed conditions. The algorithm implements an exponential decay function that mitigates the effect of backscatter fluctuations during the anticipated thaw periods in the shoulder seasons, while amplifying them during the expected frozen periods.

The physical basis of the EFTA approach derives from the strong dielectric contrast between thawed and frozen soil. Liquid water has a high dielectric constant (~80), whereas ice exhibits much lower permittivity (~3–4), producing a pronounced reduction in surface and volume scattering as soils freeze (Mavrovic et al, 2021; Wu et al, 2022). At C-band, VH polarization is particularly responsive to these changes because its cross-polarized signal captures scattering from small-scale roughness elements, soil–vegetation interfaces, and dielectric heterogeneity, all of which diminish as the water content decreases and the soil freezes (Baghdadi et al, 2018; Jagdhuber et al, 2014). Conversely, VV polarization is dominated by coherent surface scattering and is therefore less sensitive to these structural and dielectric transitions (Baghdadi et al, 2018). As a result, VH backscatter exhibits a clearer and more consistent decay between thawed and frozen states, providing a more stable basis for the exponential decay formulation used in EFTA.

2.2.6. Probabilistic approach for Soil freezing

The 5 cm-depth soil temperature data from weather stations (Table 2.1) were converted to FT status using two different approaches. The first is a rigid classification, where negative soil temperatures (T ≤ 0°C) are classified as frozen and thawed otherwise (T > 0°C). This binary classification ignores the uncertainties introduced by temperature sensor accuracy and the spatial heterogeneity in soil temperatures within the satellite footprint, which can confound the detection of freezing conditions. For example, temperature data loggers typically have accuracies of ±0.5°C, and small-scale spatial variability (e.g., within a typical 10 × 10 m S1 pixel) can contribute additional uncertainty of up to ±0.5°C, as observed in St-Marthe and St-Maurice in the Québec Province (Taghipourjavi et al, 2024b). These uncertainties are particularly significant during zero-curtain periods, when soil temperatures hover around 0°C, typically under deep snowpacks or during seasonal transitions (Outcalt et al, 1990). To address this, a probabilistic approach was applied to predict the probability of soil freezing, P (T ≤ 0°C), at each measuring station. The standard normal distribution (z), a continuous probability distribution (Wackerly, 2008), was used to parameterize the uncertainty in soil temperature measurements (Equation 2.2):

$$P\ (T \leq 0) = 1 - P\left(z < \left(\frac{T-\mu}{\sigma}\right)\right) \tag{2.2}$$

where $P\ (T \leq 0)$ represents the cumulative probability that the measured soil temperature (T) is less than or equal to zero (the frozen state). The mean μ is set to zero, corresponding to the freezing point, and σ was set to 0.25 °C, assuming a typical T sensor uncertainty of ±0.5 °C corresponding to a two-sigma (±2σ) range. The calculated z score represents the standardized value of the measured soil temperature relative to the freezing point, and P is its cumulative probability distribution. The classified binary FT states and the calculated soil freezing probabilities were extracted for the times matching the Sentinel-1 overpass, to be used for further analysis and model development.

2.2.7. Random Forest modelling

Random Forest (RF) is a robust ensemble learning method known for its resistance to overfitting and its ability to handle predictors with varying value ranges without requiring data normalization (Breiman, 2001). In addition, the interactions between radar backscatter, soil thermal state, crop types, soil texture, and geographical variables are inherently nonlinear, and RF models are able to capture such complexities without assuming linearity or requiring explicit functional forms. Its bootstrap aggregation approach improves model stability and reduces sensitivity to noise, which is essential given the diverse observational conditions across stations (Fox et al, 2017). RF is also advantageous because it naturally accommodates both categorical and continuous predictors, allowing seamless integration of variables such as soil and crop type (categorical), binary soil-freezing state (categorical), SAR-derived indicators (continuous), and probabilistic soil-freezing values (continuous) within a single modeling framework. Before developing the FT prediction models, we first explored the key drivers of radar backscatter using an exploratory Random Forest regression with VH_{EFTA} as the response variable and soil freezing probability, snow depth, wet-snow conditions, soil type, and crop type as predictors. These predictors represent all know potential physical drivers of radar backscatter, and this exploratory model aimed at identifying which of these contribute most to backscatter variations. Our hypothesis is that soil FT status should be the key driver and guide further model development to predict soil FT state. Three model configurations were evaluated to quantify the relative explanatory contribution of these predictors: (i) a full model including all predictors, (ii) a reduced model including only soil freezing probability and snow depth, and (iii) a baseline model using soil freezing probability alone. This analysis focused on the snow-related predictors to determine whether variations in snow depth or wet-snow conditions introduce measurable effects on VH_{EFTA} relative to the dominant influence of soil FT conditions. The outcome of this step provides a physically grounded basis for interpreting the FT classification and regression models described below.

An RF classification model was then trained on observed binary FT data, where the target variable was already classified as either frozen (1) or thawed (0) based on soil temperature measurements. The modelling framework examined a variety of indicator

combinations, including raw Sentinel-1 backscatter signals (VV, VH), their ratio (VH/VV), and corresponding EFTA-derived metrics (VV_{EFTA}, VH_{EFTA}, and VH_{EFTA} /VV_{EFTA}). These indicators were used alone or in combination with static predictors such as latitude, altitude, crop type, and soil type to evaluate their possible contribution to FT classification performance. Since this model was trained directly on discrete FT states, it performed a standard binary classification task optimized to recognize patterns in categorical FT data. The classification performance was evaluated using Overall Accuracy (OA), F1-score, and the area under the Receiver Operating Characteristic curve (ROC-AUC). OA measures the proportion of correctly classified samples relative to the total number of samples. ROC-AUC (Equation 2.3) quantifies the area under the ROC curve, which illustrates the trade-off between the true positive rate (Equation 2.4) and the false positive rate (Equation 2.5) across classification thresholds.

$$AUC = \int_0^1 TPR(FPR)d(FPR) \tag{2.3}$$

$$True\ Positive\ Rate\ (TPR): \frac{TP}{TP+FN} \tag{2.4}$$

$$False\ Positive\ Rate\ (FPR): \frac{FP}{FP+TN} \tag{2.5}$$

where TP (true positives) refers to correctly predicted positive cases, TN (true negatives) to correctly predicted negative cases, FP (false positives) to negative cases incorrectly predicted as positive, and FN (false negatives) to positive cases incorrectly predicted as negative. ROC-AUC was selected for its robustness to class imbalance, as demonstrated by Richardson et al (2024), who showed that when the distribution of predicted classification scores remains unchanged, ROC-AUC remains stable despite variations in class proportions.

A second model based on RF regression was trained on continuous soil freezing probability data to predict FT probabilities, providing a more nuanced representation of FT conditions, particularly during transitional periods when soil temperatures fluctuate around 0°C. The regression model was trained using the same predictors as the classification models. Unlike classification models that output discrete frozen/thawed

states, the regression model predicted continuous probability values, representing the probability of a site being frozen. The regression model was evaluated using R^2 (coefficient of determination) to measure how well predicted freezing probabilities aligned with observed freezing probabilities and RMSE (Root Mean Squared Error) to quantify the magnitude of prediction errors.

To ensure comparability between the regression and classification models, the continuous outputs of the probability-based regression model were binarized using a fixed threshold of 0.5, predicted probabilities ≥ 0.5 were classified as frozen (1), and those < 0.5 as thawed (0). The chosen threshold represents a balanced decision boundary between the two frozen and thawed states, corresponding to equal classification probabilities. This binarization allowed us to evaluate the regression model's ability to classify FT states by directly comparing its thresholded predictions to observed binary FT labels using standard classification metrics. Through this approach, we assessed whether the regression model, originally trained on continuous FT probabilities, could serve as an effective alternative to models explicitly trained on binary FT data.

To optimize model performance and limit overfitting, key RF hyperparameters were tuned using a GridSearchCV approach from Scikit-learn with 5-fold cross-validation. The cv = 5 configuration provided a balanced trade-off between training data size and validation robustness while maintaining a manageable computational cost. Stratified splitting was applied within the cross-validation procedure to preserve the proportion of frozen and thawed samples in each fold. During model training, the Out-of-Bag (OOB) approach was used to provide an internal and unbiased estimate of model accuracy, as approximately one-third of the samples are excluded from the bootstrap sample used to train each tree. In addition, an independent stratified split of the dataset was performed, with 70% of the samples used for training and 30% reserved for testing, to evaluate overall model performance.

2.2.8. Feature importance

Feature importance analysis was conducted to assess each variable's contribution to the model's performance by calculating the average reduction in impurity across all trees in the ensemble (Aldrich, 2020; Saarela & Jauhiainen, 2021). Partial Dependence Plots (PDPs) were used to further understand how individual features influence the model predictions. PDPs illustrate how varying a single feature affects the model's average prediction, revealing the marginal relationship between each feature and the target variable (Goldstein et al, 2015). As such, PDPs provide insights into the key variables influencing the prediction of FT conditions.

2.2.9. Spatial and temporal model validation

A spatial K-fold cross-validation approach was employed to evaluate the model's ability to generalize across different sites and accurately classify FT states. Given the uneven distribution of stations, a leave-one-station-out cross-validation approach was employed to evaluate the model's spatial transferability. In each fold, all the data from a single station was excluded from calibration and used as the test set, while the model was trained on the remaining stations.

Temporal cross-validation was conducted to evaluate the model's temporal transferability. The data was split chronologically by year, and the model was trained on all years except one, which was used for validation. This leave-one-year-out approach ensures that the model is tested on unseen data from different sub-time periods within the period of data availability (October to June from 2016 to 2023). All hyperparameters were kept constant throughout the process, with no retuning between folds. Data processing, statistical analysis, and modeling were conducted using Python programming in Google Colab.

2.3. Results

2.3.1. Diagnostic assessment of controls on VH_{EFTA} variability

The full exploratory Random Forest regression model explained 47% (OOB $R^2 \approx 0.47$; RMSE ≈2.43dB) of the variability in VH_{EFTA} (Table 2.2). The feature-importance analysis shows that soil freezing probability is by far the dominant predictor, contributing approximately half of the total importance, with snow depth as second most important predictor (Figure 2.2A). The remaining predictors, i.e., wet-snow indicator, soil type and crop type account for only a negligible share (Figure 2.2A). When these predictors are removed from the full model, the prediction performance remains almost unchanged (Table 2.2: reduced model: OOB $R^2 \approx 0.41$; RMSE ≈2.56) and soil freezing probability explains approximately 75% of the total importance, with snow depth contributing the remainder (Figure 2.2B). When snow depth is removed and soil freezing is used as sole predictor, the performance is unchanged (Table 2.2: baseline model: OOB $R^2 \approx 0.41$; RMSE ≈2.56). This indicates that adding snow depth does not improve the predictive capability beyond what is already captured by soil freezing probability, and that nearly all explainable variation in VH_{EFTA} originates from soil FT changes.

Table 2.2. Performance of exploratory Random Forest regression models used to identify the physical drivers of VH_{EFTA} variability. Model comparison is based on OOB R^2 and RMSE.

Model Configuration	Predictors Included	OOB R^2	RMSE
Full model	Soil FT probability, Snow depth, Snow wetness, Soil type, Crop type	0.47	2.43
Reduced Model	Soil FT probability, Snow depth	0.41	2.56
Baseline Model	Soil FT prob	0.41	2.56

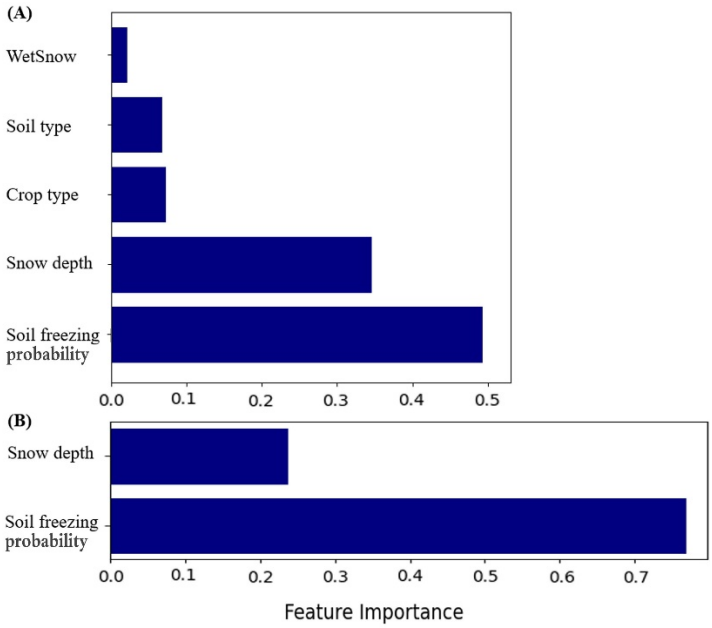

Figure 2.2. Random Forest feature importance for VH_{EFTA} variability. (**A**) Full model including soil freezing probability, snow depth, wet-snow indicator, soil type, and crop type. (**B**) Reduced model including only soil freezing probability and snow depth.

This preliminary diagnostic analysis thus reveals that VH-based FT indicators are controlled primarily by dielectric effects arising from soil FT processes, with snow depth and wetness contributing only minimally to the overall signal variability. Consequently, the FT prediction models presented in the subsequent sections were developed under this assumption, and snow variables were excluded as potential predictors. Another first insight from this preliminary analysis is the relatively low R^2 coefficient obtained, which may arise because soil FT probabilities that are larger than zero (thawed) and smaller than one (frozen) may have a limited correlation with VH_{EFTA} variations. This point is developed further in the next section.

2.3.2. Spatial and temporal distribution of soil freezing probability

The near surface (5cm -depth) soil freezing probability derived at each agricultural weather station shows distinct spatial and temporal FT patterns (Figure 2.3). Soil freezing probabilities in Manitoba, Saskatchewan, and Alberta frequently exceeded 80%, lasting between 4 to 6 continuous months each year from mid-October to late April. The transition to frozen conditions typically began in early November, with thawing starting in early

April. Notably, Manitoba exhibited longer spring transition periods compared to the other provinces, often extending up to a month, with soil freezing probabilities ranging from 40 to 60 percent during that time in several years. The two study sites in Québec show reduced freezing durations compared to the other sites. These sites also exhibited a higher frequency of FT transitions during the frozen period, indicating both temporal variability at these locations and spatial heterogeneity when compared to the more consistent FT patterns observed across sites in Manitoba, Saskatchewan, and Alberta.

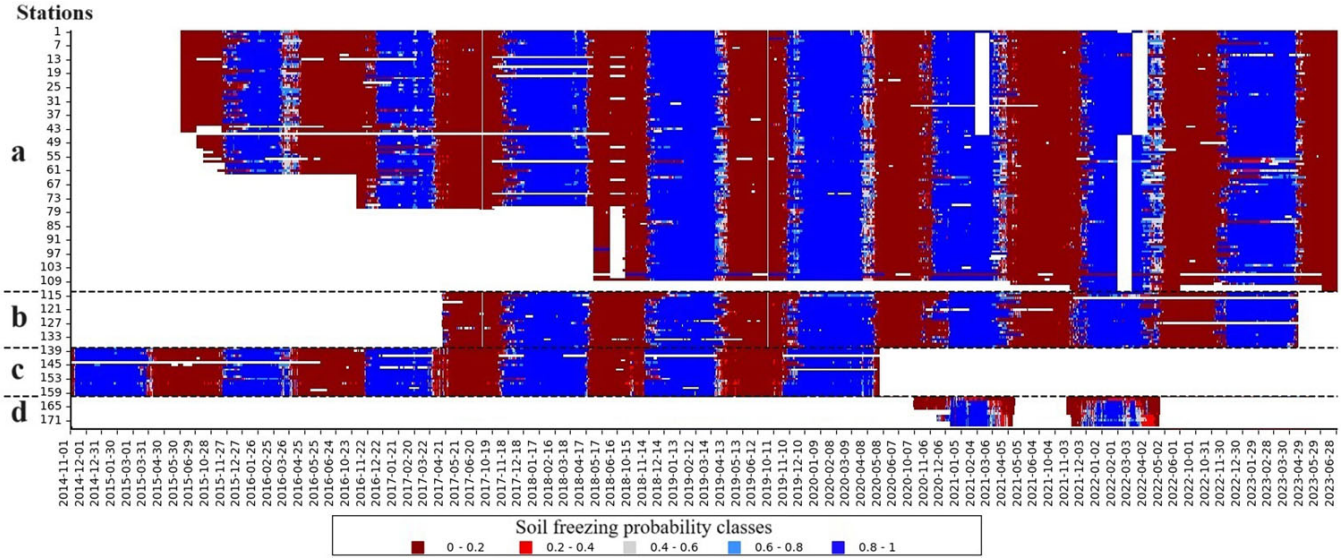

Figure 2.3. Temporal and spatial visualization of freezing probability across four Canadian provinces using soil temperature at 5 cm depth measured at agricultural weather stations (November 2014 to June 2023). The Y axis indicates the distribution of stations in (A) Manitoba; (B) Alberta; (C) Saskatchewan; (D) St-Marthe and St-Maurice sites (Québec), respectively.

2.3.3. RF model performance in binary FT classification

To assess the potential of different radar polarizations in capturing FT transitions, Classification models were initially evaluated using VH, VV, and VH/VV backscatter as individual predictors. The baseline RF model based on VH backscatter alone achieved the highest performance, with an overall accuracy of 66.64% and an F1-score of 66.80% (Table 2.3). The VV-based model performed moderately worse (60.18% accuracy, 62.19% F1-score), indicating a weaker sensitivity to FT state detection, possibly due to its lower responsiveness to vegetation structure. Interestingly, the VH/VV ratio, despite

integrating both volume and surface scattering behaviors, resulted in the lowest performance (56.66% accuracy, 60.29% F1-score). When combined with ancillary variables such as soil type, crop type, latitude, and altitude, each of these models exhibited a modest yet consistent improvement, with increases in overall accuracy and F1-score of up to 3 percentage points across all three input configurations: VV, VH, and the VH/VV ratio.

Table 2.3. Summary of RF classification performance using observed binary FT data with optimized hyperparameters across combinations of predictors and indicators. Bold values correspond to results using the VH backscatter indicator, italic values represent VV backscatter results, and regular font refers to the VH/VV ratio. Indicator groups include original VH and VV backscatters as well as the VH/VV ratio (left), and EFTA-derived metrics (right).

Indicators / Predictors	**VH backscatter** *VV backscatter* VH/VV					**VH_{EFTA}** *VV_{EFTA}* VH_{EFTA}/VV_{EFTA}			
Soil type		■	■	■			■	■	■
Crop type		■	■	■			■	■	■
Latitude			■	■				■	■
Altitude				■	■				■
Overall Accuracy	**66.64**	**66.57**	**67.57**	**68.04**	**67.80**	**81.36**	**81.42**	**81.87**	**82.11**
F1–score	**66.80**	**66.99**	**68.70**	**68.65**	**68.23**	**80.32**	**80.38**	**80.88**	**81.02**
Overall Accuracy	*60.18*	*60.69*	*62.25*	*63.33*	*61.51*	*78.21*	*78.26*	*78.69*	*78.81*
F1–score	*62.19*	*61.95*	*63.21*	*63.89*	*62.53*	*76.31*	*76.16*	*76.80*	*76.95*
Overall Accuracy	56.66	58.27	59.02	59.39	58.23	59.78	60.63	62.06	62.19
F1–score	60.29	60.45	61.53	63.06	60.42	61.21	62.65	63.50	64.26

To improve classification beyond raw backscatter, we applied the EFTA-derived indicators from each polarization configuration. The VH_{EFTA} -based model showed a substantial performance boost, achieving 81.36% accuracy and an F1-score of 80.32% (Table 2.3). Models based on VV_{EFTA} and VH_{EFTA}/VV_{EFTA} also outperformed their corresponding raw backscatter inputs; however, their performance remained notably lower than that of VH_{EFTA}, with a maximum accuracy of 78.71%. The integration of ancillary predictors with the EFTA-based models led to only marginal gains-typically less

than 1 percentage point-suggesting that soil type, crop type, latitude, and altitude contribute limited additional discriminatory power once the EFTA indicator is applied.

The features importance analysis for the model combining VH_{EFTA} with all the ancillary predictors shows that the VH_{EFTA} index contributes more than 90% of the total feature importance in predicting soil freezing states, indicating its dominant role in the model (Figure 2.4). Meanwhile, the contributions from the other predictors collectively account for less than 10% of the model's importance, in accordance with the OOB performance metrics (Table 2.3). Among these, altitude and latitude show slightly higher relative importance, suggesting some influence of geographical factors on soil freezing predictive capability, albeit modest.

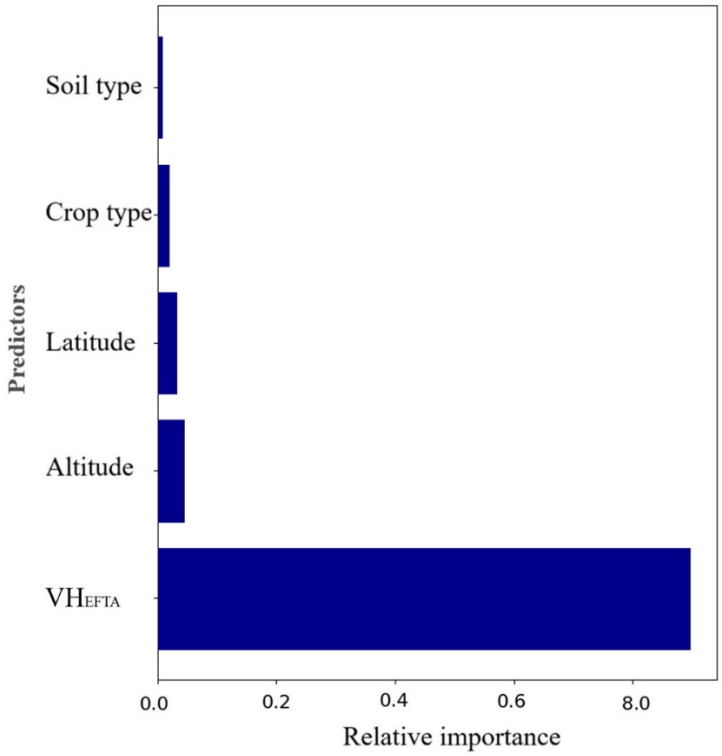

Figure 2.4. Feature Importance Plot illustrates the relative importance of each predictor in predicting soil freezing state using a Random Forest classifier model.

The PDPs in Figure 2.5 show the marginal effect of each predictor on the predicted freezing probabilities from the FT classification model. VH_{EFTA} exhibits a strong and non-linear influence on soil freezing probability, showing its dominant influence on FT prediction (Figure 2.5A). The average partial dependence line shows that higher values of VH_{EFTA} correlate with a greater probability of frozen states, with a threshold around 2 on the VH_{EFTA} scale separating frozen from thawed conditions ($P = 0.5$). In contrast, the other predictors exhibit more stable, less important associations with FT state (Figures 2.5 B-E).

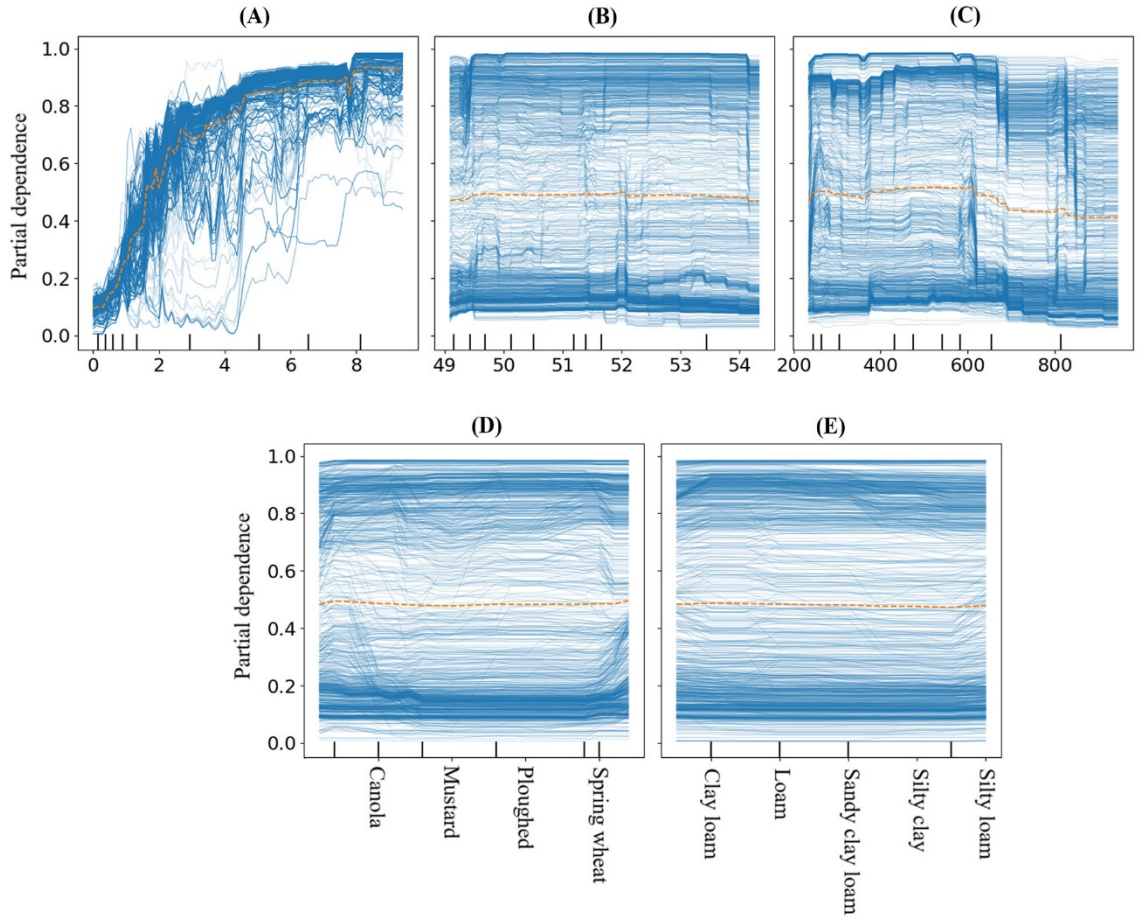

Figure 2.5. Partial dependence analysis of predictors in the FT classification model using VH_{EFTA} and other predictors. (**A**) VH_{EFTA}; (**B**) latitude; (**C**) altitude; (**D**) crop type; and (**E**) soil type. The orange dashed line indicates the average partial dependence for each predictor, while the blue lines represent the individual simulations for each predictor's value. The spread of the blue lines reflects the variability or uncertainty in the model's prediction for that predictor. Larger spreads suggest higher variability in the model's

response to changes in the predictor, indicating that the predictor has a more complex or less predictable effect on soil freezing probability.

2.3.4. Radar-based FT detection and VH_{EFTA}

Although soil and crop types did not significantly enhance model performance, the analysis investigates how VH backscatter and the VH_{EFTA} index respond to surface heterogeneity-particularly variations in soil and crop types-to assess their ability to distinguish between frozen and thawed conditions. However, there is considerable overlap between the two states, particularly in most soil and crop types (Figures 2.6A, C), which reduces the effectiveness of VH backscatter alone in discriminating FT states. In contrast, the VH_{EFTA} shows a clearer distinction between frozen and thawed conditions compared to VH backscatter signals (Figures 2.6B, D).

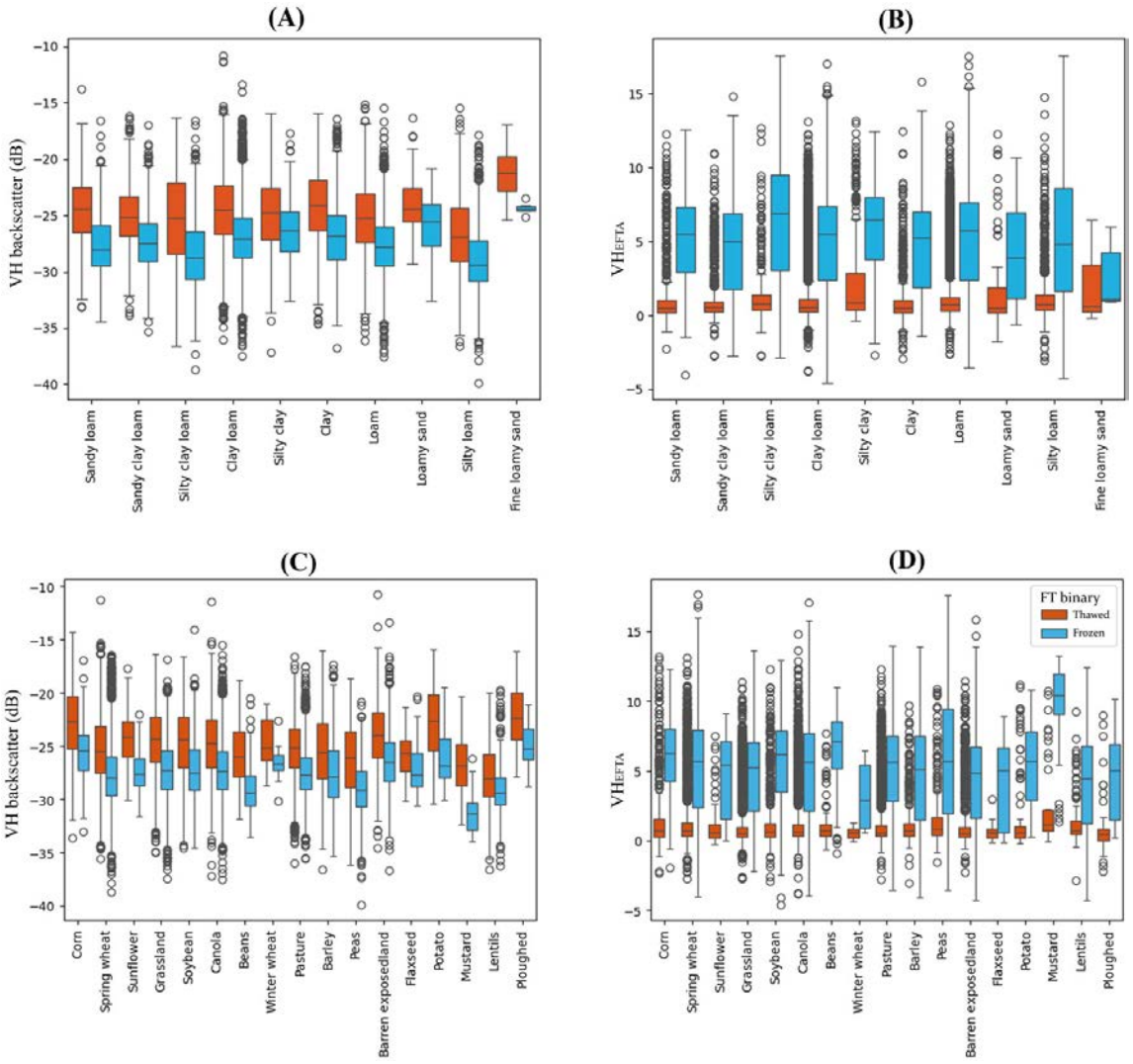

Figure 2.6. Comparison of radar signal variations and VH_{EFTA} algorithm changes across different crop and soil types in frozen and thawed conditions. (**A**) VH radar backscatter signal variations across different soil types; (**B**) VH_{EFTA} indicator variations across different soil types; (**C**) radar backscatter signal variations across different crop types; (**D**) VH_{EFTA} indicator variations across different crop types. Note: Outliers cases are illustrated in supplementary material (Fig. S2.2 and S2.3).

Outliers in the boxplots were statistically identified using the standard interquartile range (IQR) rule, where values falling below 1.5 times the IQR below the first quartile (Q1) or exceeding 1.5 times the IQR above the third quartile (Q3) were flagged as outliers. A detailed analysis of the occurrence and distribution of outliers in FT detection using VH and VH_{EFTA} predictors is provided in the Supplementary Material (See supplementary Figures S2.4, S2.5).

2.3.5. Spatial and temporal validation

Spatial cross-validation resulted in an averaged accuracy of 0.82 and F1-score of 0.80, indicating overall consistent model performance and spatial transferability in detecting FT states (Figure 2.7A). Most stations exhibited a balanced distribution between frozen and thawed states over the October-June period (Figure 2.7B), however some stations departed from this pattern. However, some stations, such as 106 (Manitoba), 136 (Alberta), 141 (Saskatchewan), and 162 (Quebec), show a clear dominance of thawed conditions. These stations have cross-validated accuracy values ranging 0.79-0.87 and F1-scores from 0.77 to 0.87, showing that class imbalance at a given site does not affect model prediction performance.

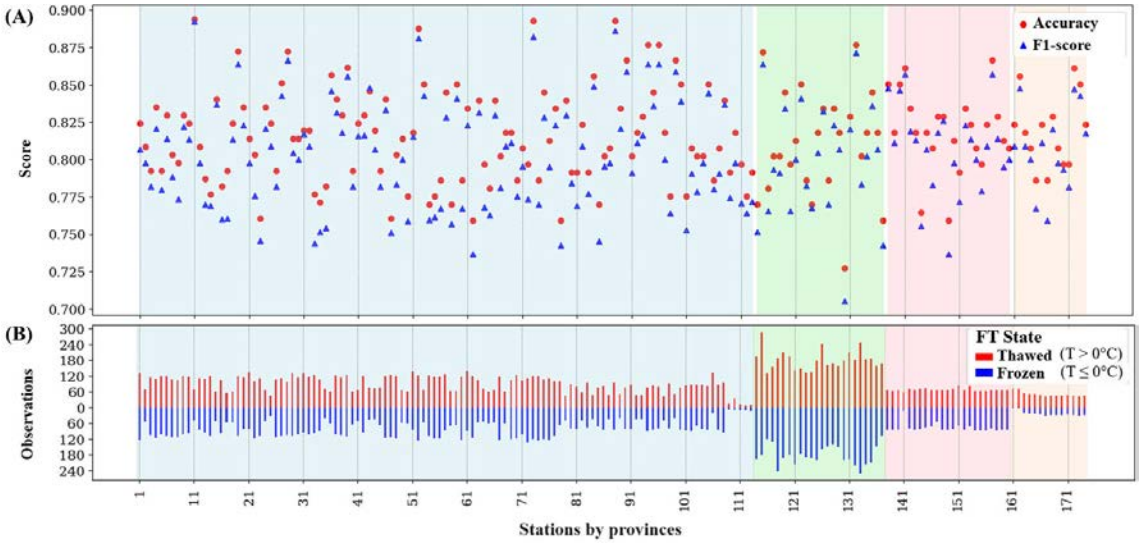

Figure 2.7. Spatial cross-validation results and freeze-thaw data distribution by station. Stations from Manitoba are shaded in light blue, Alberta in light green, Saskatchewan in light pink, and Québec in light orange. (**A**) Station spatial cross-validation scores (accuracy and F1-score); (**B**) frequency of freeze and thaw occurrences at each station. The blue and red bars in the background represent the number of frozen (≥ 0.5) and thawed (< 0.5) occurrences, respectively, for each year, revealing the temporal variability of freeze-thaw events.

The mean temporal cross-validation model accuracy and F1-score are 0.81 and 0.80, respectively, indicating overall consistent performance across all years (Figure 2.8). This stable performance across years highlights the model's ability to transfer to years not used in model training, despite annual class imbalance having only a slight impact on cross-validated accuracy.

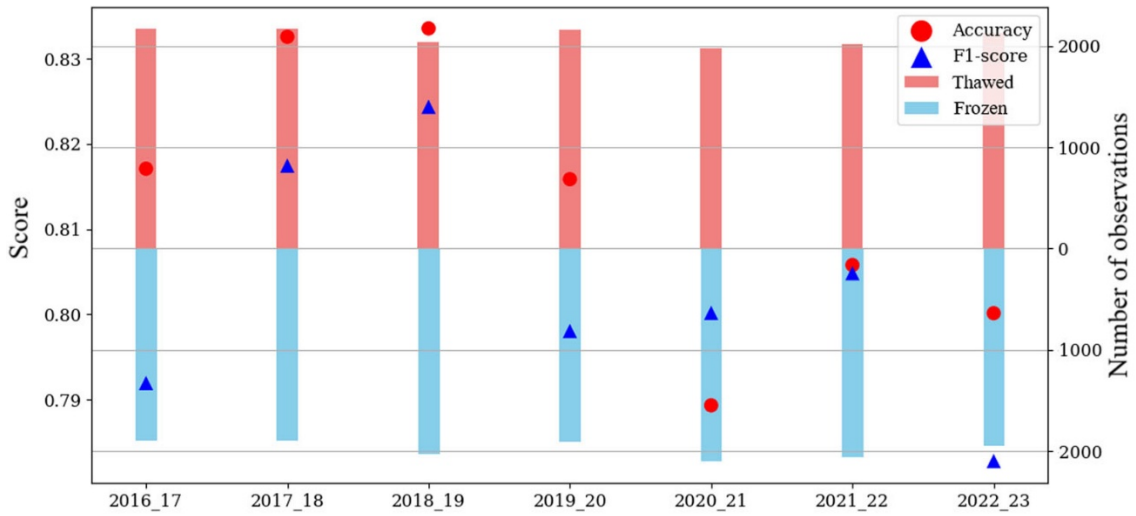

Figure 2.8. Temporal model cross-validation scores and annual FT frequency distribution (October-June period). Model performance is presented using accuracy and F1-score metrics (red and blue dots), while the secondary Y-axis shows the number of thawed (blue) and frozen (red) occurrences for each validation fold (left-out year).

2.3.6. FT binary and probability-based models to soil freezing probability

The optimized RF regression model using all potential predictors predicted the observed soil freezing probability with an R^2 of 0.50 and an RMSE of 0.32 (Figure 2.9A). Using VH_{EFTA} as sole predictor in the RF regression model yielded comparable performance, with an R^2 of 0.46 and an RMSE of 0.31 (Figure 2.9B). The scatter plots of predicted/observed probabilities against VH_{EFTA} show considerable scatter in observed probabilities compared to model predictions. Observed freezing probabilities are strongly clustered near 0 and 1, corresponding to strong thawed and freezing conditions, while intermediate probability values indicate transitional FT states. Hence the RF regression model has limited ability to accurately predict transitional FT phases but appears better to capture the thawed/frozen extremes.

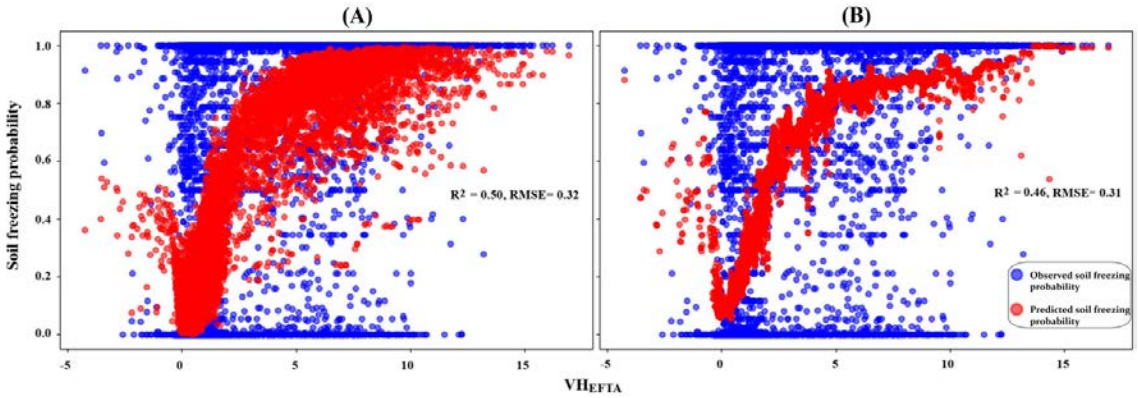

Figure 2.9. Prediction of soil freezing probability. (**A**) Optimized RF regression model with VH_{EFTA}, Latitude, Station's Elevation, Crop Type, and Soil Type as predictor variables; (**B**) Optimized RF regression model with only VH_{EFTA}.

To compare the regression and classification models, the continuous probabilities from the RF regression model were converted into binary FT states. Table 2.4 presents the metrics for the binarized RF regression model, including both the full-predictor model and the VH_{EFTA}-only model. The model using all predictors achieved an accuracy of 81.66% and an F1-score of 80.26%, demonstrating strong classification capability in distinguishing frozen and thawed conditions. The models using only VH_{EFTA} performed similarly, with an accuracy of 80.79% and an F1-score of 79.36%. When comparing these results to those of the binary classification model (Table 2.3), the binarized RF regression model performs similarly, but with slightly lower accuracy.

Table 2.4. Comparison of FT Binary and FT Probability-Based Models for Soil Freezing Probability Prediction.

Models	**Statistical metrics**	**All Predictors**	**VH_{EFTA}**
Probability-based prediction	R^2	50.18	46.01
	RMSE	32.15	31.48
Binary-based prediction	Accuracy	81.66 %	80.79 %
	F1 score	80.26 %	79.36 %

2.3.7. Evaluation of model sensitivity to seasonal and temperature variability

To evaluate seasonal variability in model performance for both regression (soil freezing probability-based) and binary-based FT detection, we computed daily classification error and regression RMSE for each day of the year (DOY) from October 1 (DOY 1) to June 30 (DOY 273). Figure 2.10 provides a detailed characterization of model errors during transitional FT periods, showing how classification errors and regression RMSE sharply increase during fall and spring, as well as around the 0 °C threshold. This targeted analysis enables explicit evaluation of transitional-period performance and supports interpretation of the underlying physical drivers of misclassification. As shown in Figure 2.10A, the probabilistic-based model exhibits pronounced error peaks during Fall (DOY 40–68) and early Spring (DOY 160–205), where errors are assumed to be significant when exceeding a threshold of 0.4. For the binary-based model, the error peaks are more temporally confined, occurring during Fall (DOY 45–68) and early Spring (DOY 175–205). Outside the transitional periods, particularly in October, January, February, and June, model performance remains relatively stable, with both error metrics consistently falling below 0.25. Binary-based FT detection errors remain slightly lower than probabilistic-based RMSEs across most periods, particularly during non-transitional phases. The distribution of observations throughout the season remains consistent (Figure 2.10A, gray bars), indicating reliable Sentinel-1 coverage and sufficient data availability across the monitoring period. For further analysis of temperature-related variability, Figure 2.10B shows classification error (red line) for the binary FT model and regression RMSE (blue line) for the probability model, plotted across soil temperature intervals (°C). Model errors from both approaches peak around the 0 °C threshold, where the soil transitions between frozen and thawed states, a range that also corresponds to the most substantial presence of observational data. Outside this transition zone, error levels gradually decrease as soil temperatures move farther from the freezing point. Notably, across the full temperature range, errors from the binary-based model remain consistently lower than from the probabilistic-based model, indicating stronger performance. At the extreme soil temperatures, around −22 °C and +32 °C, unexpectedly high model errors are observed, corresponding to low observational data availability.

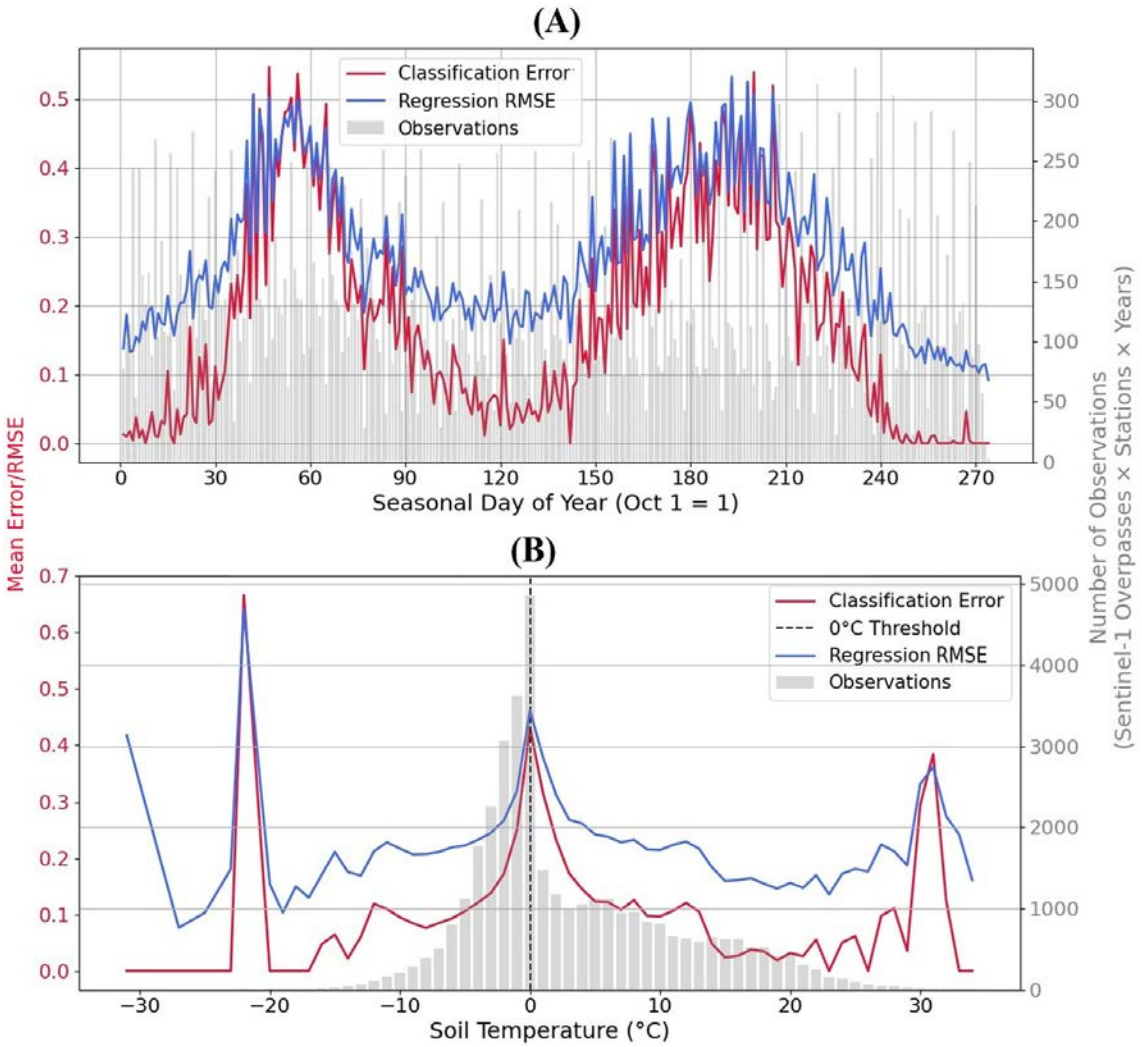

Figure 2.10. Seasonal and temperature-dependent variability in model error for classification (binary-based) and regression (probabilistic-based) FT detection models. (**A**) Daily classification error (red) and regression RMSE (blue) from October 1 (Day 1) to June 30 (Day 273), with observation counts (gray bars) representing the number of Sentinel-1 overpasses aggregated across all stations and years. (**B**) Error trends as a function of soil temperature. The vertical dashed line denotes the 0 °C threshold used to distinguish frozen and thawed states.

2.3.8. Web-Based On-Demand Freeze-Thaw Mapping Tool

To generalize the FT retrieval beyond station-based analyses, we developed a web-based FT mapping tool that enables large-scale and user-driven application of the method (Figure 2.11). Through the Streamlit frontend, users can define the region of interest and select a temporal window restricted to the cold-season period (October 1–June 30), when

soil FT transitions occur, choose the spatial resolution (10 m, 30 m, or 100 m), and optionally apply land-cover filters. These inputs trigger a cloud-based processing workflow where the Google Earth Engine (GEE) backend automatically handles data preparation, including Sentinel-1 collection filtering, application of a Refined Lee speckle filter, terrain normalization, image mosaicking, and optional land-cover clipping. When the agricultural-land option is selected, the workflow restricts computation to cropland and related classes including tropical/sub-tropical grassland, temperate/sub-polar grassland, cropland, and barren land using the 2020 Land Cover of North America at 30 m dataset (Commission for Environmental Cooperation (CEC), 2021) available in GEE. All processing is performed through the GEE API, providing seamless access to the full Sentinel-1 archive and ensuring consistent, scalable FT retrieval.

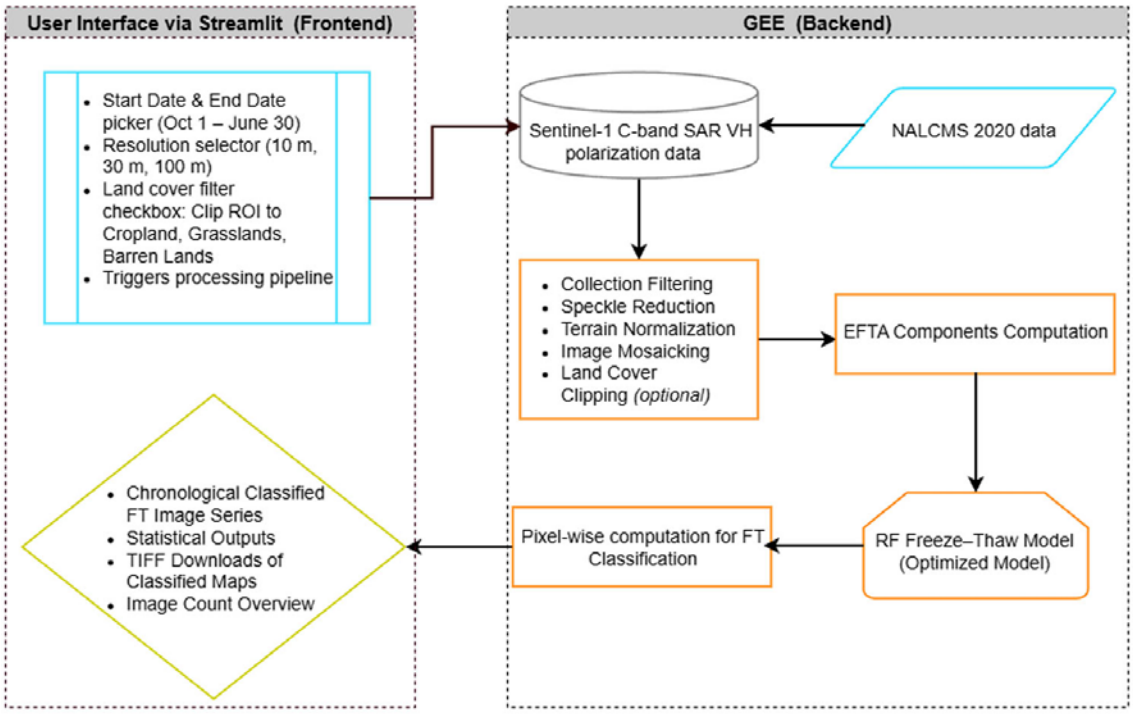

Figure 2.11. Schematic workflow of the web-based FT Detection Tool. Color conventions: light blue for user-interface components; grey for primary Sentinel-1 SAR data input; cyan for the NALCMS 2020 land-cover layer used for optional clipping; orange for processing modules within the GEE backend; and yellow green for consolidated FT output products. The processing pipeline was established within a Python environment in Google Colab.

The workflow then computes the EFTA components and applies the optimized Random Forest FT classifier pixel-wise to all available acquisitions within the user-selected period. The platform returns a chronological series of classified FT maps within the region of interest, summary statistics, and downloadable GeoTIFF layers, enabling rapid visualization and export of results. This cloud-enabled architecture generalizes the VH-based FT detection to any user-defined area, providing an operational framework suitable for regional monitoring, agricultural assessment, and research applications. The tool and supporting Python scripts are openly available through the project's GitHub repository (https://github.com/Shahab-J/Freeze-Thaw-Detection, accessed 05 December 2025), and the fully deployed web application is accessible at https://freeze-thaw-detection-kmpqcuusaqtf5ypu5h3vyg.streamlit.app/ (accessed 05 December 2025).

2.4. Discussion

2.4.1. Implications of the Diagnostic Assessment of VH_{EFTA} Controls

The diagnostic assessment indicates that variations in VH_{EFTA} are primarily governed by near-surface soil freezing conditions, while snow-related variables exert a more limited influence. Although wet snow has been reported to affect C-band radar backscatter through enhanced attenuation and volume scattering (Brangers et al, 2024; Gill et al, 2015), it did not emerge as a dominant control in the present analysis. Although not explicitly tested, the exponential decay structure of EFTA, combined with the seasonal constraint imposed by K, may partially attenuate short-term VH perturbations associated with wet snow during thaw and shoulder periods, thereby reducing the sensitivity of VH_{EFTA} to transient snow wetness effects.

Snow depth appeared as a contributing factor in the feature-importance analysis; however, its inclusion did not enhance predictive performance relative to models based solely on soil freezing probability. This behavior is consistent with the well-established transparency of dry snow at C-band frequencies, which generally limits its direct influence on radar backscatter (Bernier & Fortin, 1998; Pivot, 2012). The apparent importance of snow depth is therefore more likely to reflect its phenological co-occurrence with frozen soil conditions rather than an independent physical control on the radar signal. This

interpretation is further supported by a strong positive Spearman rank correlation (See supplementary Figure S2.6) between soil freezing probability and snow depth ($\rho = 0.79$), indicating pronounced seasonal co-occurrence rather than an independent explanatory role of snow depth on VH_{EFTA} variability.

2.4.2. RF Classification Performance for Observed Binary FT

The performance differences observed across VH, VV, and VH/VV-based models can be explained by their respective sensitivity to surface and vegetation characteristics. The model using VH backscatter achieved the highest accuracy, attributed to VH's strong sensitivity to vegetation structure and surface roughness due to its stronger volume-scattering sensitivity. This makes it more responsive to surface changes associated with FT transitions in agricultural lands. In contrast, VV polarization, which primarily reflects surface scattering and responds better to smooth, bare soil conditions, showed weaker performance. This limits its ability to detect FT-related variations where vegetation and roughness are present. The VH/VV ratio, despite integrating information from both polarizations, exhibited the lowest performance. Its strong vegetation sensitivity and weaker soil-moisture response (Vreugdenhil et al, 2018) educe the dielectric contrast critical for FT detection.

From a physical standpoint, the enhanced performance of VH_{EFTA} over raw VH backscatter can be attributed to the pronounced contrast in dielectric properties between frozen and thawed soils. Liquid water has a high dielectric constant of approximately 80, as reported by Skolunov (1997), while ice exhibits a much lower value near 3.2, according to Matzler & Wegmuller (1987). This strong dielectric contrast significantly affects radar signal interaction, particularly at C-band frequencies during FT transitions. During frozen conditions, the reduction in dielectric constant diminishes surface and volume scattering, resulting in lower radar returns. VH polarization, being more sensitive to volume scattering and surface structure, responds markedly to these changes. The application of EFTA further enhances FT discrimination by reducing signal ambiguity during transitional periods. VH_{EFTA} improves FT state detection by attenuating thaw-related noise through exponential smoothing, particularly during transitional periods when VH signals

are affected by surface variability. The logistic exponential decay function applied to the VH signal captures variations during the fully frozen winter period while minimizing ambiguous fluctuations during spring and fall transitions, which are often affected by surface heterogeneity such as roughness, thin water films, and patchy snow cover. By suppressing these transient effects and emphasizing the frozen-phase signal, VH_{EFTA} improves contrast between FT states and enhances detection reliability.

The strong performance of VH_{EFTA} underscores its effectiveness in capturing FT transitions and its importance as the primary indicator for FT classification. While VV_{EFTA} and the VH_{EFTA}/VV_{EFTA} ratio also show improvements compared to the original backscatter indicators, their relative insensitivity to vegetation-induced signal variability limits their effectiveness compared to VH_{EFTA}. These findings are consistent with the results of Fayad et al (2020), which showed that VH-based detection of frozen agricultural plots is more reliable than VV, due to a greater radar signal decay under freezing conditions, making VH less ambiguous for freeze detection. They also align with Taghipourjavi et al (2024b), who demonstrated the effective use of Sentinel-1 VH polarization for identifying soil FT transitions in agro-forested areas of southern Québec, Canada. Further comparison of model performance using ROC-AUC scores also supports these findings, with an ROC-AUC score of 88% when using all predictors and 86% when using only VH_{EFTA} (See supplementary Figure S2.7).

The feature importance analysis further supported the significance of VH_{EFTA}, which accounted for over 90% of the total contribution in the RF model (Figure 2.4). Although previous studies highlighted the influence of crop and soil types on radar backscatter during FT events and suggested that adjusting thresholds based on land cover could improve accuracy (Baghdadi et al, 2018), our results indicated a limited contribution from these variables.

The additional predictors, including altitude, latitude, crop type, and soil type, collectively explained less than 10% of the overall model performance. Partial dependence plots further support these findings, revealing a strong, non-linear positive relationship

between VH_{EFTA} and soil freezing probability. Although the altitude predictor exhibited a relatively low variable importance (<5%) in our Random Forest model, the decline in frozen state probability beyond 600 m is a result that can be attributed to the presence of only a few observational stations at higher altitudes (See supplementary Figure S2.8). While model accuracy varied slightly among crop and soil types, no substantial variation could be attributed to either variable (See supplementary Figures S2.9, S2.10). Accordingly, the RF model exhibits consistent adaptability across multiple crop and soil types, indicating robust generalization in diverse agricultural areas. This is primarily due to the computation of a site-specific thawed reference backscatter value σ_T for the derivation of VH_{EFTA} (Equation 2.1), which accounts for spatial and interannual variability in soil or crop roughness effects on reference backscatter values before soil freezing occurs.

2.4.3. FT discrimination by VH and VH_{EFTA} indicators

Although soil and crop types showed limited contribution to model improvement in FT discrimination, exploring this aspect helps clarify how the VH and VH_{EFTA} predictors perform in distinguishing frozen and thawed conditions under high soil and crop heterogeneity in Canadian agricultural fields. According to Figure 2.6, VH_{EFTA} consistently provides better separation between FT classes than the raw VH predictor across different soil (Figures 2.6A, B) and crop types (Figures 2.6C, D). VH backscatter signals display substantial overlap between frozen and thawed states, especially under variable soil textures and vegetation structures. In contrast, VH_{EFTA} reduces this overlap by attenuating signal noise associated with soil moisture variability and surface roughness. This improvement could be driven by EFTA's capacity to better capture signal variations during fully frozen winter periods while reducing the impact of unstable fluctuations during transitional phases, compared to the raw VH predictor.

Several outliers in both VH backscatter and VH_{EFTA} predictors can be observed in Figure 2.6. These appear most frequently during FT transition periods, as illustrated in Supplementary Figures S2.4 and S2.4. During these transitions, the surface often experiences mixed-phase states, temporary surface water accumulation, or patchy snow

cover, which can cause local variations in dielectric properties and backscatter response (Bergstedt & Bartsch, 2017). Although both predictors encounter challenges under such conditions, the VH_{EFTA} predictor still demonstrates a clearer separation between frozen and thawed states. It does, however, exhibit more thawed-classified outliers compared to raw VH, suggesting that increased sensitivity may come with the cost of detecting additional transient variations. Nevertheless, VH_{EFTA}'s enhanced detection capability contributes to the model's overall higher classification performance. These additional thaw-classified outliers, representing only 7.6% of total data, do not significantly degrade the model's ability to distinguish between frozen and thawed states.

2.4.4. Spatial and temporal validation

The FT spatial and temporal variability observed throughout this study can arise from variability in surface roughness, driven by soil conditions and crop types and phenology, as well as fluctuating climate and soil moisture, particularly during spring thaw. Uneven surface conditions resulting from diverse land practices and tillage methods can influence radar backscatter signals and could bias model training and transferability to unseen conditions. However, the spatial cross-validation analysis showed effective spatial model transferability (Figure 2.7A), even on stations with less observations or imbalanced distribution between thawed and frozen occurrences (Figure 2.7B). This result aligns with the earlier finding that VH_{EFTA} effectively captures local surface conditions, minimizing reliance on site-specific ancillary predictors to represent the spatial heterogeneity of FT changes. Although the spatial distribution of agricultural stations is uneven across provinces, the model generalized well across the range of agricultural environments represented in the dataset, indicating that the FT classification framework is transferable within croplands, pastures/grasslands, and open agricultural lands despite regional differences in station coverage.

Despite the observed FT temporal variations, the model also transferred well to unseen years, i.e. on years removed from model training (Figure 2.8). This stable model performance indicates that it effectively adapts to the changing conditions over time, such

as variations in surface roughness caused by seasonal soil moisture, diverse crop vegetation, and land management practices like tillage.

2.4.5. Evaluating Binary and Probability-Based FT Prediction Models

Our results demonstrate that the RF regression model, once binarized, performs comparably to the direct classification model, suggesting its outputs can still be reliably used to predict frozen and thawed conditions. The regression model, though, does not predict FT probabilities as reliably as it classifies binary states. As illustrated in Figure 2.9B, while the probabilistic model for FT states is overall effective, many discrepancies are evident, particularly when high VH_{EFTA} values coincide with low freezing probabilities (observations in the lower-right quadrant of Figure 2.9B). This discrepancy likely arises because even minor changes in soil moisture can significantly alter the soil's complex permittivity, a phenomenon that becomes especially pronounced during spring thawing. These effects are especially evident during transitional periods, where the EFTA algorithm inherently introduces discrepancies in FT state detections. Specifically, the identification of the most negative backscatter difference prior to February (interpreted as the fall freeze onset) and the most positive difference after February (interpreted as the spring thaw onset) defines the expected frozen and thawed periods within the EFTA framework. During shoulder periods, a small number of thawed or frozen events per study year occurring just before or after these key thresholds result in EFTA that do not fully reflect the actual FT state. For instance, in fall, a few freeze events occurring before the identified most negative backscatter difference are assigned lower EFTA values, despite corresponding to frozen conditions, explaining the presence of freeze-related outliers in the upper-left quadrant of Figure 2.9B. Similarly, in spring, some thawed events occurring shortly before the detected maximum positive difference receive higher EFTA values, although they represent thawed soil with low freezing probability. These limitations help explain the occurrence of thaw-related outliers in the lower-right quadrant of Figure 2.9B. Understanding these surface dynamics is essential for interpreting backscatter extremes that guide EFTA's identification of FT phases. Since surface changes during transitional periods alter radar backscatter by modifying the physical and dielectric properties of the near surface, factors such as spring snowmelt and fall harvest become especially relevant to the interpretation of EFTA values.

For additional insight, the seasonal distribution of model errors highlights the variability in soil surface conditions during FT transitions. In fall, elevated error levels in both models can be attributed to the onset of surface freezing and shifts in dielectric properties caused by declining soil temperatures and early snow accumulation. These changes affect radar backscatter, leading to increased errors in binary-based FT detection and higher RMSEs in FT probability predictions. Similarly, the spring transition exhibits the most prolonged and elevated error values, highlighting the difficulty in capturing the onset of thaw. During this period, near-surface soil moisture increases rapidly due to snowmelt, introducing significant dielectric variability and variable radar backscatter. This variability contributes to greater uncertainty in FT state prediction, particularly for probability-based models. Although both models follow similar seasonal trends, binary-based model errors remain consistently lower outside the transitional periods. This indicates that binary classification provides more stable performance under consistent surface conditions, whereas FT probabilistic predictions respond more variably depending on the complexity of transitional states.

During winter, when soils remain fully frozen for an extended period, as well as in early fall and late spring when soils are fully thawed, backscatter remains relatively stable, leading to reduced binary-based model errors and lower RMSEs in FT probability predictions. However, FT detection uncertainty remains highest during transitional periods, when changing surface roughness, increasing soil moisture, and post-harvest surface alterations such as crop residue and tillage practices especially under snowmelt conditions, introduce radar backscatter variability and complicate FT state interpretation. As shown in Figure 2.10B, both classification errors and regression RMSEs peak near the 0 °C threshold, indicating reduced model reliability during late fall and early spring. During these periods, partial soil freezing, rising soil moisture from snowmelt, and evolving surface conditions intensify signal changes. Soil moisture, in particular, directly influences the dielectric constant and thus radar backscatter, making it a critical driver of FT detection error. Seasonal wetting and drying strongly impact the EFTA algorithm, which identifies the most extreme backscatter differences to detect frozen and thawed periods. Accurate interpretation of FT transitions, especially during shoulder seasons, would benefit from concurrent soil moisture observations. However, such data were not

available across the 174 agricultural weather stations used in this study, limiting direct validation of moisture-related influences on EFTA responses. Future research should integrate co-located soil moisture observations and conduct statistical analyses to examine their relationship with radar backscatters during transitional periods, to assess their role in refining FT classification and prediction based on both binary and probabilistic approaches.

Outside the critical 0 °C transition range, model performance improves considerably. In colder conditions (below −5 °C), soils remain consistently frozen with minimal surface variability, resulting in lower model errors. Similarly, temperatures above +5 °C correspond to fully thawed states with more stable dielectric properties, further enhancing model performance. Throughout all temperature ranges, classification models exhibit lower error values than regression models, indicating greater robustness to short-term radar backscatter variations. However, at the extreme ends of the temperature spectrum (below −20 °C and above +30 °C), two noticeable spikes in error appear, which can be primarily attributed to the limited number of observations available under these conditions.

To support broader applicability, this study leveraged in-situ weather stations distributed across diverse climatic regimes, as illustrated in the Köppen climate classification map (See supplementary Figure S2.1). These stations primarily span hot-summer humid continental and cold semi-arid zones, with limited representation from subarctic regions. Together, these zones encompass the dominant agro-climatic settings across Canadian agricultural lands, reinforcing the relevance of the proposed approach at a national scale. Given the climatic representativeness of these regions, the proposed FT detection method shows strong potential for transferability to other FT-affected agricultural regions with similar climatic and land cover characteristics. However, its application in areas marked by distinct cryospheric and topographic conditions such as mountainous environments with steep orographic gradients, variable snowpack dynamics, and heterogeneous surface structures-would require further algorithmic optimizations and regional calibration to ensure reliable FT state detection.

2.4.6. Translating Findings into an Operational FT Retrieval Framework

The strong and consistent performance of EFTA derived from VH backscatter, explaining more than 90% of the predictive importance and outperforming all other radar- and ancillary-based indicators provided a clear basis for adopting it as the core input for operational FT mapping. Its demonstrated robustness across diverse soil textures, crop types, and climatic conditions supports a streamlined modelling framework that avoids dependence on weakly influential ancillary variables. Accordingly, the web-based FT detection platform was designed around VH_{EFTA} as the main radar-derived indicator, enabling efficient pixel-wise FT classification across Canadian croplands, pastures, grasslands, and barren lands. This architecture ensures full scalability within the GEE environment and supports user-driven mapping across any region of interest without site-specific recalibration.

Although the web-based FT mapping tool developed in this study provides an operational platform for on-demand retrieval of FT states from historical Sentinel-1 data, it is not designed to predict future FT conditions. All outputs reflect observed SAR acquisitions within the selected period, rather than forecasted FT states. Future research could therefore focus on developing predictive FT modelling frameworks, where machine-learning or physics-informed approaches integrate meteorological forecasts, soil-temperature projections, or climate-scenario data to anticipate upcoming FT transitions. The current modelling and validation rely mainly on stations located in croplands, pastures/grasslands, and barren lands. A useful extension would be to test, adapt and calibrate the FT detection framework for forested regions, where canopy structure and stronger volume scattering may require adjustments to the retrieval approach.

2.5. Conclusion

This study employed RF classification and regression models to predict soil FT states over Canadian agricultural fields, using both binary FT and probabilistic FT indicators derived from soil temperature data. The analysis confirmed the dominance of VH_{EFTA} as the primary predictor, reinforcing its ability to capture radar backscatter

variations linked to FT transitions. VH_{EFTA} demonstrated the highest reliability in detecting FT transitions due to its sensitivity to surface roughness and vegetation structure. In contrast, VV- and VH/VV-based indicators showed reduced effectiveness, reflecting their limited interaction with heterogeneous surface conditions. Additional predictors such as soil type, crop type, latitude, and altitude provided only marginal improvements, indicating that VH_{EFTA} effectively captures the dominant site-specific influences on radar backscatter.

By incorporating snow depth and a wet-snow indicator into the diagnostic analysis, we confirmed that snow processes exert only a minor influence on VH_{EFTA} compared to soil freezing probability. Although snow-related variables contributed measurably to backscatter variability, their limited predictive value indicates that VH_{EFTA} remains primarily governed by near-surface thermal conditions across the agricultural landscapes studied

While the probability-based regression model, once binarized, achieved classification accuracy similar to that of the RF classification model, transitional FT states remained more complex to capture. These difficulties were most evident during shoulder periods, where fluctuations in radar signals-driven by combinations of soil moisture variation, snow presence, and evolving surface roughness-introduced greater uncertainty in prediction. Model performance was reduced near the 0 °C threshold, likely due to rapid changes in surface roughness and near-surface wetness; however, the extent of their influence on FT detection accuracy remains to be quantified. FT detection uncertainty was largely confined to transitional periods marked by pronounced soil surface changes, and classification models demonstrated greater robustness compared to regression approaches under such conditions. Improving FT algorithms to better handle signal instability around the freezing point remains essential for advancing prediction accuracy.

Despite these limitations, the overall consistency in performance across diverse agricultural settings suggests that the approach is broadly transferable to other cold-region farmlands. Given the climatic representativeness of the study areas, the proposed method

demonstrates strong potential for application in other agricultural regions affected by FT events. However, additional calibration and regional adjustment may be necessary for regions with complex snowpack variability, strong altitude gradients, or heterogeneous soil surface conditions.

2.6. Statements

Author Contributions: Conceptualization, C.K., A.R., S.T.; methodology, C.K., A.R., and S.T.; formal analysis, S.T., C.K., and A.R.; data curation, S.T.; writing-original draft preparation, S.T.; writing-review and editing, C.K. and A.R.; supervision, C.K. and A.R.; project administration, C.K. and A.R.; funding acquisition, C.K. and A.R. All authors have read and agreed to the published version of the manuscript.

Funding: This study was financially supported by Fonds de Recherche du Québec Nature et Technologies (FRQNT) under the Merit scholarship program for foreign students (PBEEE) program for doctoral research scholarships (File number: 275403; DOI: https://doi.org/10.69777/275403), Canadian Space Agency FAST (19FAQCTB19), and the FRQNT Team Research Project grant 2022-PR-299776 (C. Kinnard).

Data Availability Statement: The datasets used in this study are publicly available in the Borealis repository at https://doi.org/10.5683/SP3/ZJ03SX.

Acknowledgments: We would like to express our sincere gratitude to Madam Alison Sass at Manitoba Agriculture and Resource Development for kindly providing us with Manitoba's soil temperature data from all available stations over the full available period. As per the Data Use Agreement, the data is acknowledged as coming from the Manitoba Agriculture Weather Program as part of Manitoba Agriculture. Her support and assistance were invaluable in enabling this research, and we deeply appreciate her contribution to the data collection process.

Generative AI Statement: The authors declare that generative artificial intelligence (OpenAI's GPT-4) was used to assist in the grammatical correction of text and in generating alternative phrasing for certain sentences within this manuscript.

Conflicts of Interest: The authors declare that the research was conducted in the absence of any commercial or financial relationships that could be construed as a potential conflict of interest.

2.7. References

Aldrich, C. (2020) Process variable importance analysis by use of random forests in a shapley regression framework. *Minerals*, 10(5), 420. doi:10.3390/min10050420

Baghdadi, N., Bazzi, H., El Hajj, M. & Zribi, M. (2018) Detection of frozen soil using Sentinel-1 SAR data. *Remote Sens.*, 10(8), 1182. doi:10.3390/rs10081182

Beer, C., Lucht, W., Gerten, D., Thonicke, K. & Schmullius, C. (2007) Effects of soil freezing and thawing on vegetation carbon density in Siberia: A modeling analysis with the Lund-Potsdam-Jena Dynamic Global Vegetation Model (LPJ-DGVM). *Global Biogeochem. Cycles*, 21(1). doi:10.1029/2006GB002760

Benninga, H.-J. F., van der Velde, R. & Su, Z. (2019) Impacts of radiometric uncertainty and weather-related surface conditions on soil moisture retrievals with Sentinel-1. *Remote Sens.*, 11(17), 2025. doi:10.3390/rs11172025

Bergstedt, H. & Bartsch, A. (2017) Surface state across scales; temporal and spatial patterns in land surface freeze/thaw dynamics. *Geosci.*, 7(3), 65. doi:10.3390/geosciences7030065

Bernier, M. & Fortin, J.-P. (1998) The potential of times series of C-band SAR data to monitor dry and shallow snow cover. *IEEE Trans. Geosci. Remote Sens.*, 36(1), 226-243. doi:10.1109/36.655332

Black, T., Chen, W., Barr, A., Arain, M., Chen, Z., Nesic, Z., Hogg, E., Neumann, H. & Yang, P. (2000) Increased carbon sequestration by a boreal deciduous forest in years with a warm spring. *Geophys. Res. Lett.*, 27(9), 1271-1274. doi:10.1029/1999GL011234

Brangers, I., Marshall, H.-P., De Lannoy, G., Dunmire, D., Mätzler, C. & Lievens, H. (2024) Tower-based C-band radar measurements of an alpine snowpack. *TC*, 18(7), 3177-3193. doi:10.5194/tc-18-3177-2024

Breiman, L. (2001) Random forests. *Mach. Learn.*, 45, 5-32. doi:10.1023/A:1010933404324

Cade-Menun, B. J., Bell, G., Baker-Ismail, S., Fouli, Y., Hodder, K., McMartin, D. W., Perez-Valdivia, C. & Wu, K. (2013) Nutrient loss from Saskatchewan cropland and pasture in spring snowmelt runoff. *Can. J. Soil Sci.*, 93(4), 445-458. doi:10.4141/cjss2012-042

Chang, Z., Qi, P., Zhang, G., Sun, Y., Tang, X., Jiang, M., Sun, J. & Li, Z. (2022) Latitudinal characteristics of frozen soil degradation and their response to climate change in a high-latitude water tower. *Catena*, 214, 106272. doi:10.1016/j.catena.2022.106272

Cohen, J., Lemmetyinen, J., Ruiz, J. J., Rautiainen, K., Ikonen, J., Kontu, A. & Pulliainen, J. (2024a) Detection of soil and canopy freeze/thaw state in the boreal region with L and C Band Synthetic Aperture Radar. *Remote Sens. Environ.*, 305, 114102. doi:10.1016/j.rse.2024.114102

Cohen, J., Lemmetyinen, J., Ruiz, J. J., Rautiainen, K., Ikonen, J., Kontu, A. & Pulliainen, J. J. R. S. o. E. (2024b) Detection of soil and canopy freeze/thaw state in the boreal region with L and C Band Synthetic Aperture Radar, 305, 114102. doi:10.1016/j.rse.2024.114102

Commission for Environmental Cooperation (CEC) ((2021)) *North American Land Cover, 2020 (Landsat, 30m)*, (2021). Available online: https://www.cec.org/north-american-environmental-atlas/land-cover-30m-2020/ [Accessed.

Donahue, K., Kimball, J. S., Du, J., Bunt, F., Colliander, A., Moghaddam, M., Johnson, J., Kim, Y. & Rawlins, M. A. (2023) Deep learning estimation of northern hemisphere soil freeze-thaw dynamics using satellite multi-frequency microwave brightness temperature observations. *Front. Big Data*, 6, 1243559. doi:10.3389/fdata.2023.1243559

Ekici, A., Chadburn, S., Chaudhary, N., Hajdu, L., Marmy, A., Peng, S., Boike, J., Burke, E., Friend, A. & Hauck, C. (2015) Site-level model intercomparison of high latitude and high altitude soil thermal dynamics in tundra and barren landscapes. *TC*, 9(4), 1343-1361. doi:10.5194/tc-9-1343-2015

Fayad, I., Baghdadi, N., Bazzi, H. & Zribi, M. (2020) Near real-time freeze detection over agricultural plots using Sentinel-1 data. *Remote Sens.*, 12(12), 1976. doi:10.3390/rs12121976

Fox, E. W., Hill, R. A., Leibowitz, S. G., Olsen, A. R., Thornbrugh, D. J. & Weber, M. H. (2017) Assessing the accuracy and stability of variable selection methods for random forest modeling in ecology. *Environ. Monit. Assess.*, 189(7), 316. doi:10.1007/s10661-017-6025-0

Gao, H., Zhang, W. & Chen, H. (2018) An improved algorithm for discriminating soil freezing and thawing using AMSR-E and AMSR2 soil moisture products. *Remote Sensing*, 10(11), 1697. doi:10.3390/rs10111697

Gill, J. P., Yackel, J. J., Geldsetzer, T. & Fuller, M. C. (2015) Sensitivity of C-band synthetic aperture radar polarimetric parameters to snow thickness over landfast smooth first-year sea ice. *Remote Sens. Environ.*, 166, 34-49. doi:10.1016/j.rse.2015.06.005

Goldstein, A., Kapelner, A., Bleich, J. & Pitkin, E. (2015) Peeking inside the black box: Visualizing statistical learning with plots of individual conditional expectation. *J. Comput. Graphical Stat.*, 24(1), 44-65. doi:10.1080/10618600.2014.907095

Gorelick, N., Hancher, M., Dixon, M., Ilyushchenko, S., Thau, D. & Moore, R. (2017) Google Earth Engine: Planetary-scale geospatial analysis for everyone. *Remote Sens. Environ.*, 202, 18-27. doi:10.1016/j.rse.2017.06.031

Gray, D., Landine, P. & Granger, R. (1985) Simulating infiltration into frozen prairie soils in streamflow models. *Can. J. Earth Sci.*, 22(3), 464-472. doi:10.1139/e85-045

Hou, R., Wang, L., O'Connor, D., Tsang, D. C., Rinklebe, J. & Hou, D. (2020) Effect of immobilizing reagents on soil Cd and Pb lability under freeze-thaw cycles: Implications for sustainable agricultural management in seasonally frozen land. *Environ. Int.*, 144, 106040. doi:10.1016/j.envint.2020.106040

Ireson, A., Van Der Kamp, G., Ferguson, G., Nachshon, U. & Wheater, H. (2013) Hydrogeological processes in seasonally frozen northern latitudes: understanding, gaps and challenges. *Hydrogeol. J.*, 21(1), 53. doi:10.1007/s10040-012-0916-5

Jagdhuber, T., Stockamp, J., Hajnsek, I. & Ludwig, R. (2014) Identification of soil freezing and thawing states using SAR polarimetry at C-band. *Remote Sens.*, 6(3), 2008-2023. doi:10.3390/rs6032008

Johnston, J. M., Houser, P. R., Maggioni, V., Kim, R. S. & Vuyovich, C. (2021) Informing improvements in freeze/thaw state classification using subpixel temperature. *IEEE Trans. Geosci. Remote Sens.*, 60, 1-19. doi:10.1109/TGRS.2021.3099292

Karthikeyan, L., Pan, M., Wanders, N., Kumar, D. N. & Wood, E. F. (2017) Four decades of microwave satellite soil moisture observations: Part 1. A review of retrieval algorithms. *Adv. Water Resour.*, 109, 106-120. doi:10.1016/j.advwatres.2017.09.006

Kim, Y., Kimball, J. S., McDonald, K. C. & Glassy, J. (2010) Developing a global data record of daily landscape freeze/thaw status using satellite passive microwave remote sensing. *IEEE Trans. Geosci. Remote Sens.*, 49(3), 949-960. doi:10.1109/TGRS.2010.2070515

Lund, J., Forster, R. R., Deeb, E. J., Liston, G. E., Skiles, S. M. & Marshall, H.-P. (2022) Interpreting Sentinel-1 SAR backscatter signals of snowpack surface melt/freeze, warming, and ripening, through field measurements and physically-based SnowModel. *Remote Sens.*, 14(16), 4002. doi:10.3390/rs14164002

Manickam, S. & Barros, A. (2020) Parsing synthetic aperture radar measurements of snow in complex terrain: Scaling behaviour and sensitivity to snow wetness and landcover. *Remote Sens.*, 12(3), 483. doi:10.3390/rs12030483

Matzler, C. & Wegmuller, U. (1987) Dielectric properties of freshwater ice at microwave frequencies. *J. Phys. D: Appl. Phys.*, 20(12), 1623. doi:10.1088/0022-3727/20/12/013

Mavrovic, A., Pardo Lara, R., Berg, A., Demontoux, F., Royer, A. & Roy, A. (2021) Soil dielectric characterization during freeze–thaw transitions using L-band coaxial and soil moisture probes. *Hydrol. Earth Syst. Sci.*, 25(3), 1117-1131. doi:10.5194/hess-25-1117-2021

McColl, K. A., Roy, A., Derksen, C., Konings, A. G., Alemohammed, S. H. & Entekhabi, D. (2016) Triple collocation for binary and categorical variables: Application to validating landscape freeze/thaw retrievals. *Remote Sens. Environ.*, 176, 31-42. doi:10.1016/j.rse.2016.01.010

McNairn, H. & Brisco, B. (2004) The application of C-band polarimetric SAR for agriculture: A review. *Can. J. Remote Sens.*, 30(3), 525-542. doi:10.5589/m03-069

Moradi, M., Cho, E., Jacobs, J. M. & Vuyovich, C. M. (2023) Seasonal soil freeze/thaw variability across North America via ensemble land surface modeling. *Cold Reg. Sci. Technol.*, 209, 103806. doi:10.1016/j.coldregions.2023.103806

Moradi, M., Kraatz, S., Johnston, J. & Jacobs, J. M. J. R. S. (2024) Comparing Three Freeze-Thaw Schemes Using C-Band Radar Data in Southeastern New Hampshire, USA, 16(15), 2784. doi:10.3390/rs16152784

Mugunthan, J. S., Duguay, C. R. & Zakharova, E. (2023) Machine learning based classification of lake ice and open water from Sentinel-3 SAR altimetry waveforms. *Remote Sens. Environ.*, 299, 113891. doi:10.1016/j.rse.2023.113891

Muñoz-Sabater, J., Dutra, E., Agustí-Panareda, A., Albergel, C., Arduini, G., Balsamo, G., Boussetta, S., Choulga, M., Harrigan, S. & Hersbach, H. (2021) ERA5-Land: A state-of-the-art global reanalysis dataset for land applications. *Earth Syst. Sci. Data*, 13(9), 4349-4383. doi:10.5194/essd-13-4349-2021

Niu, G.-Y. & Yang, Z.-L. (2006) Effects of frozen soil on snowmelt runoff and soil water storage at a continental scale. *J. Hydrometeorol.*, 7(5), 937-952. doi:10.1175/JHM538.1

Osei, A. K., Rezanezhad, F. & Oelbermann, M. (2024) Impact of freeze-thaw cycles on greenhouse gas emissions in marginally productive agricultural land under different perennial bioenergy crops. *J. Environ. Manage.*, 357, 120739. doi:10.1016/j.jenvman.2024.120739

Outcalt, S. I., Nelson, F. E. & Hinkel, K. M. (1990) The zero-curtain effect: Heat and mass transfer across an isothermal region in freezing soil. *Water Resour. Res.*, 26(7), 1509-1516. doi:10.1029/WR026i007p01509

Peng, X., Zhang, T., Cao, B., Wang, Q., Wang, K., Shao, W. & Guo, H. (2016) Changes in freezing-thawing index and soil freeze depth over the Heihe River Basin, western China. *AAAR*, 48(1), 161-176. doi:10.1657/AAAR00C-13-127

Pivot, F. C. (2012) C-band SAR imagery for snow-cover monitoring at Treeline, Churchill, Manitoba, Canada. *Remote Sens.*, 4(7), 2133-2155. doi:10.3390/rs4072133

Richardson, E., Trevizani, R., Greenbaum, J. A., Carter, H., Nielsen, M. & Peters, B. (2024) The receiver operating characteristic curve accurately assesses imbalanced datasets. *Patterns*, 5(6). doi:10.1016/j.patter.2024.100994

Saarela, M. & Jauhiainen, S. (2021) Comparison of feature importance measures as explanations for classification models. *SN Appl. Sci.*, 3(2), 272. doi:10.1007/s42452-021-04148-9

Schaufler, S., Bauer-Marschallinger, B., Hochstöger, S. & Wagner, W. (2018) Modelling and correcting azimuthal anisotropy in Sentinel-1 backscatter data. *Remote Sens. Lett.*, 9(8), 799-808. doi:10.1080/2150704X.2018.1480071

Schuur, E. A., Abbott, B. W., Commane, R., Ernakovich, J., Euskirchen, E., Hugelius, G., Grosse, G., Jones, M., Koven, C. & Leshyk, V. (2022) Permafrost and climate change: carbon cycle feedbacks from the warming Arctic. *Annu. Rev. Environ. Resour.*, 47, 343-371. doi:10.1146/annurev-environ-012220-011847

Schuur, E. A., McGuire, A. D., Schädel, C., Grosse, G., Harden, J. W., Hayes, D. J., Hugelius, G., Koven, C. D., Kuhry, P. & Lawrence, D. M. (2015) Climate change and the permafrost carbon feedback. *Nat.*, 520(7546), 171-179. doi:10.1038/nature14338

Shao, W. & Zhang, T. (2020) Assessment of Four Near-Surface Soil Freeze/Thaw Detection Algorithms Based on Calibrated Passive Microwave Remote Sensing Data Over China. *ESS*, 7(7), e2019EA000807. doi:10.1029/2019EA000807

Skolunov, A. (1997) Frequency-temperature curve of the complex dielectric constant and refractive index of water. *Fibre Chem.*, 29(6), 367-373. doi:10.1007/BF02418871

Sun, L., Chang, X., Yu, X., Jia, G., Chen, L., Wang, Y. & Liu, Z. (2021) Effect of freeze-thaw processes on soil water transport of farmland in a semi-arid area. *Agric. Water Manag.*, 252, 106876. doi:10.1016/j.agwat.2021.106876

Taghipourjavi, S., Kinnard, C. & Roy, A. (2024a) *In-situ Soil Temperature Data (2 and 10 cm) in Agro-forested Areas of St-Marthe and St-Maurice for 2020-21 and 2021-22*. (2024, Borealis. Available online: https://doi.org/10.5683/SP3/LGLCKW.

Taghipourjavi, S., Kinnard, C. & Roy, A. (2024b) Sentinel-1-Based Soil Freeze–Thaw Detection in Agro-Forested Areas: A Case Study in Southern Québec, Canada. *Remote Sens.*, 16(7), 1294. doi:10.3390/rs16071294

Tetlock, E., Toth, B., Berg, A., Rowlandson, T. & Ambadan, J. T. (2019) An 11-year (2007–2017) soil moisture and precipitation dataset from the Kenaston Network in the Brightwater Creek basin, Saskatchewan, Canada. *Earth Syst. Sci. Data*, 11(2), 787-796. doi:10.5194/essd-11-787-2019

Vreugdenhil, M., Wagner, W., Bauer-Marschallinger, B., Pfeil, I., Teubner, I., Rüdiger, C. & Strauss, P. (2018) Sensitivity of Sentinel-1 backscatter to vegetation dynamics: An Austrian case study. *Remote Sens.*, 10(9), 1396. doi:10.3390/rs10091396

Wackerly, D. D. (2008) Mathematical Statistics with Applications. 7th Edition ed. USA: Thomson Learning, Inc.

Walker, V. A., Colliander, A. & Kimball, J. S. (2022) Satellite retrievals of probabilistic freeze-thaw conditions from SMAP and AMSR brightness temperatures. *IEEE Trans. Geosci. Remote Sens.*, 60, 1-11. doi:10.1109/TGRS.2022.3174807

Wei, X., Huang, C., Wei, N., Zhao, H., He, Y. & Wu, X. (2019) The impact of freeze–thaw cycles and soil moisture content at freezing on runoff and soil loss. *LDD*, 30(5), 515-523. doi:10.1002/ldr.3243

Wu, S., Zhao, T., Pan, J., Xue, H., Zhao, L. & Shi, J. (2022) Improvement in modeling soil dielectric properties during freeze-thaw transitions. *IEEE Geosci. Remote Sens. Lett.*, 19, 1-5. doi:10.1109/LGRS.2022.3154291

Wu, X., Dong, Z., Jin, S., He, Y., Song, Y., Ma, W. & Yang, L. (2020) First measurement of soil freeze/thaw cycles in the Tibetan Plateau using CYGNSS GNSS-R data. *Remote Sens.*, 12(15), 2361. doi:10.3390/rs12152361

Yu, Z., Wang, W., Li, C., Liu, W. & Yang, J. (2018) Speckle noise suppression in SAR images using a three-step algorithm. *Sens.*, 18(11), 3643. doi:10.3390/s18113643

Zhong, W., Yuan, Q., Liu, T. & Yue, L. (2022) Freeze/thaw onset detection combining SMAP and ASCAT data over Alaska: A machine learning approach. *J. Hydrol.*, 605, 127354. doi:10.1016/j.jhydrol.2021.127354

Chapter II Supplementary Information

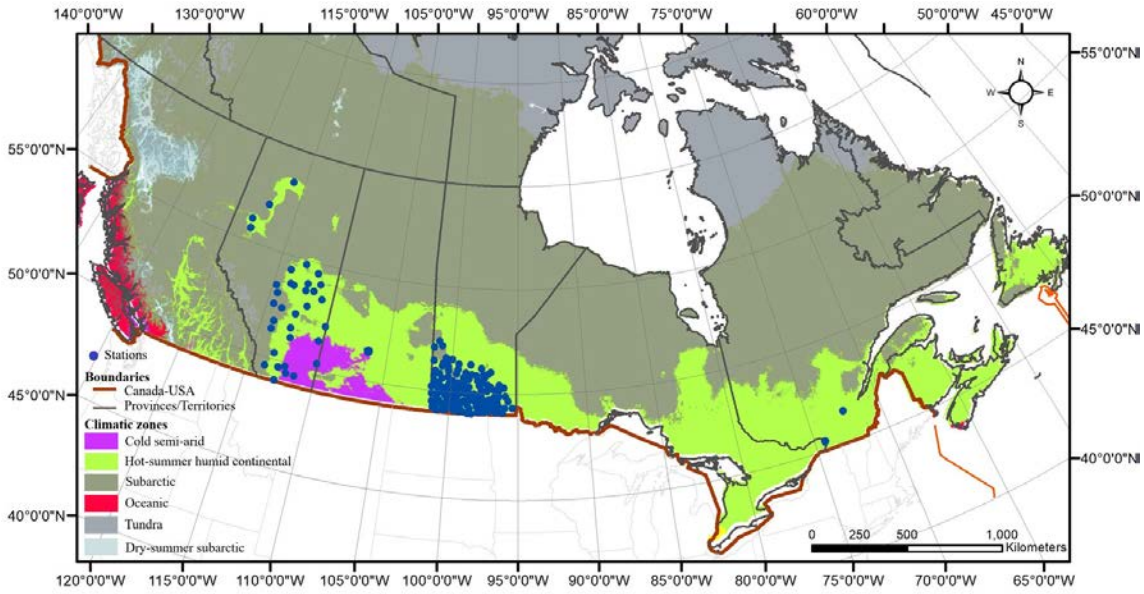

Figure S2.1. Köppen climate classification types of Canada (Source: Original map based on WorldClim data (www.worldclim.org, accessed on 05 December 2025) and adapted from a version previously published on Wikipedia (https://en.wikipedia.org/wiki/Temperature_in_Canada, accessed on 05 December 2025)

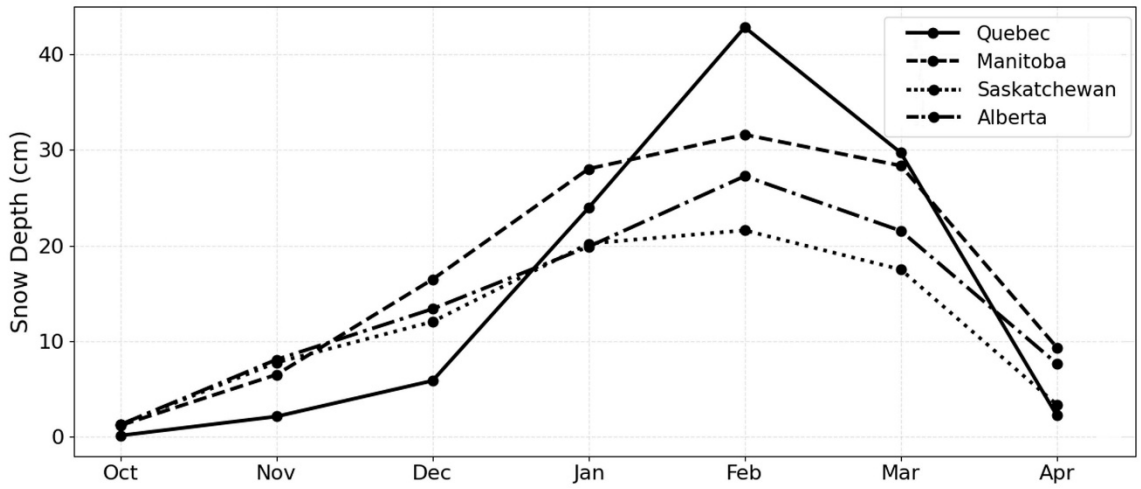

Figure S2.2. Mean monthly snow depth derived from ERA5-Land across the four study provinces (Québec, Manitoba, Saskatchewan, and Alberta) for the October-April period (2016–2023).

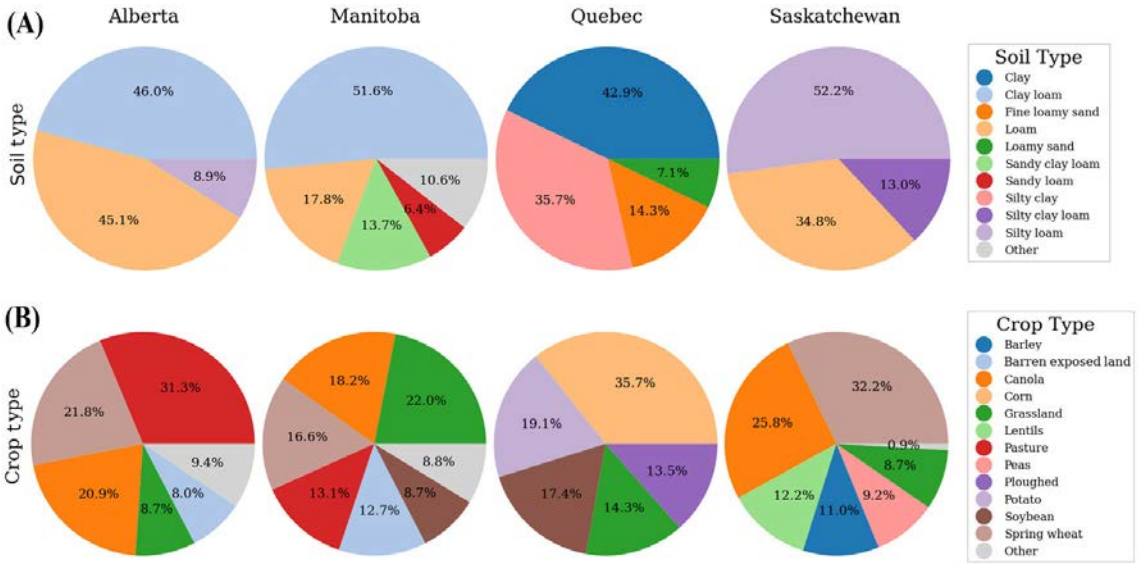

Figure S2.3. Distribution of soil and crop types across all sites in the four studied Canadian provinces. (**A**) Distribution of soil types across all sites by province; (**B**) Distribution of crop types across all sites by province.

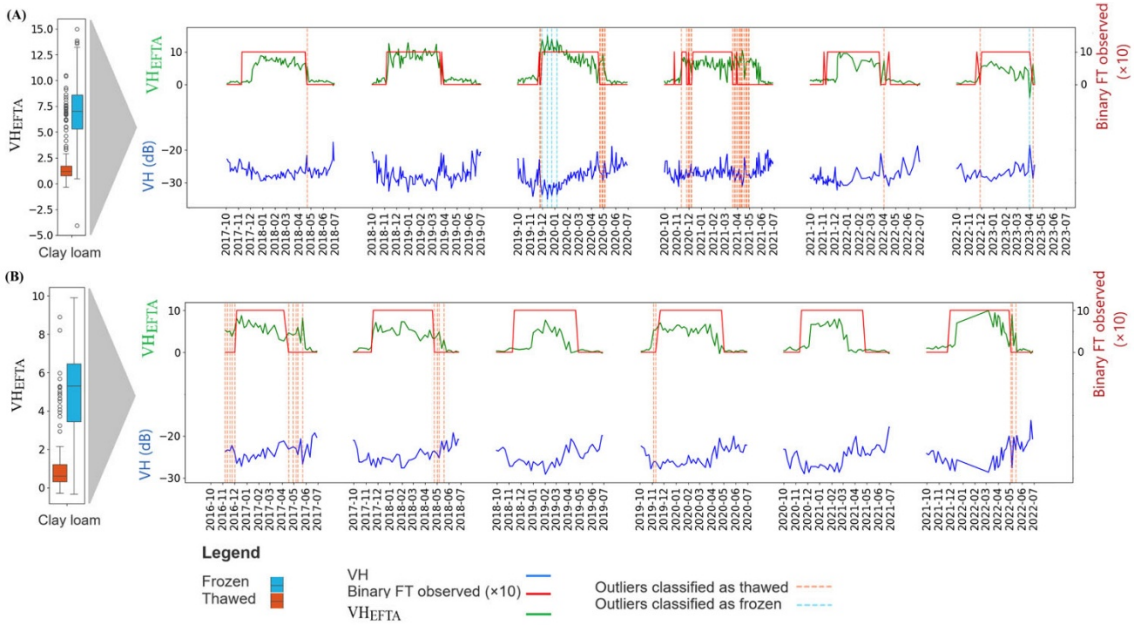

Figure S2.4. Detailed analysis of FT detection at two stations with numerous outlier values in the VH_{EFTA} indicator. Two stations with 'clay-loamy' soil type were chosen, which exhibited the highest occurrence of outliers. (**A**) Station 133 from the Alberta station network; (**B**) Station 72 from Manitoba. The figure showcases box plots and time series plots of VH corrected backscatter and VH_{EFTA} indicator on the primary Y-axis, with observed binary FT (from soil temperature sensor) displayed on the secondary Y-axis. The data spans from October to the end of June each year.

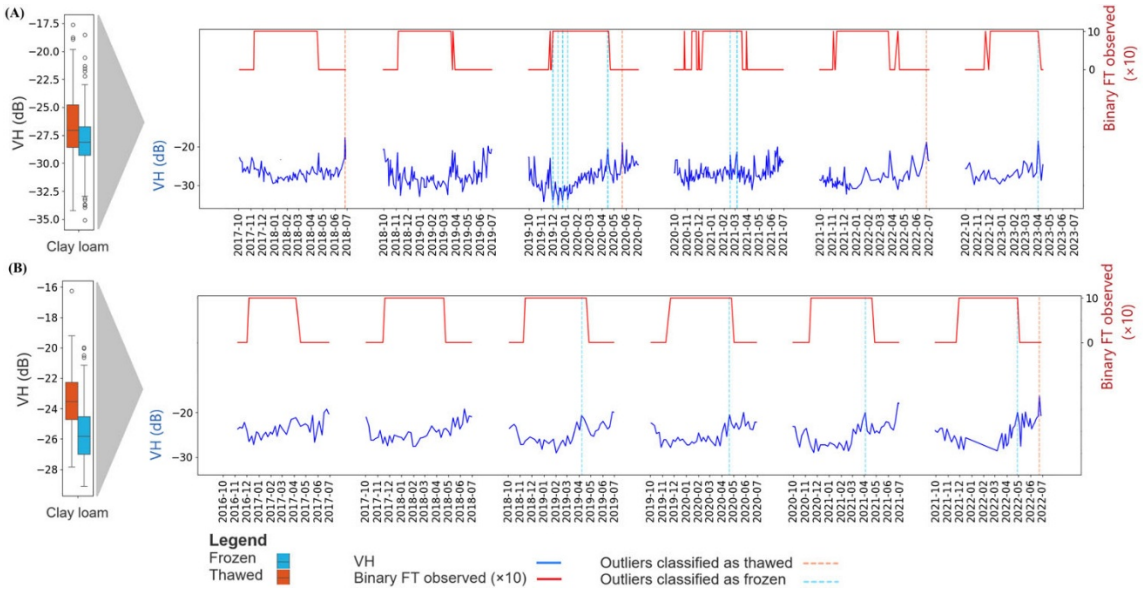

Figure S2.5. Detailed analysis of FT detection at two stations with outlier values in the VH backscatter indicator. Two stations with 'Clay-loamy' soil type were chosen, which exhibited the highest occurrence of outliers. (**A**) Station 133 from the Alberta station network; (**B**) Station 72 from Manitoba. The figure showcases box plots and time series plots of VH corrected backscatter on the primary Y-axis, with observed binary FT displayed on the secondary Y-axis. The data spans from October to the end of June each year.

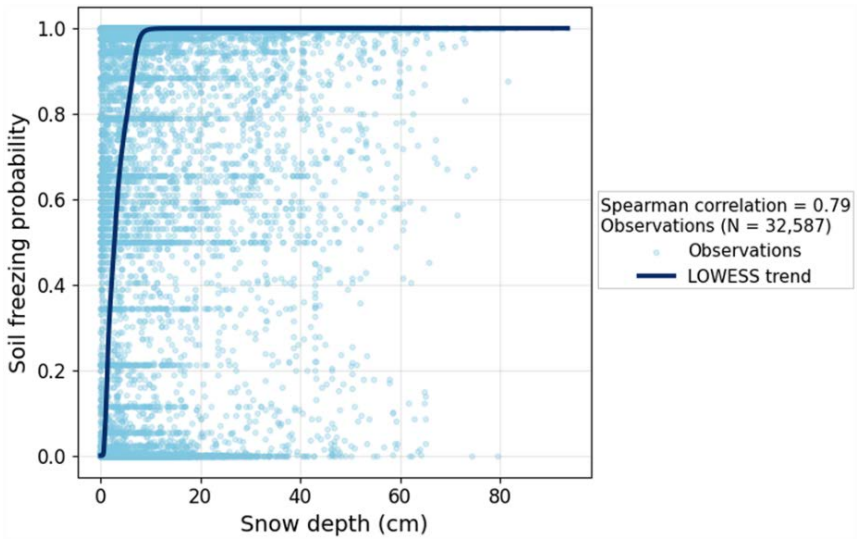

Figure S2.6. Spearman correlation between snow depth and soil freezing probability.

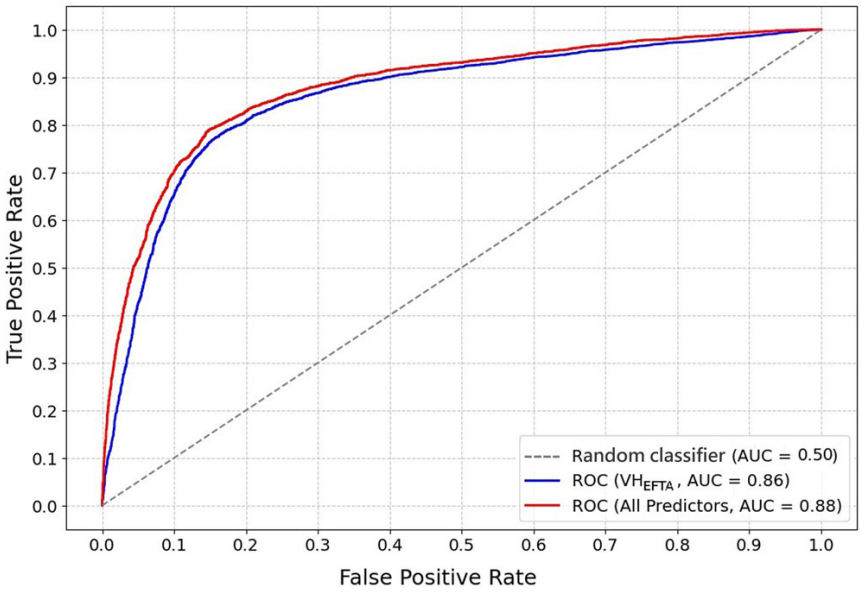

Figure S2.7. Receiver Operating Characteristic (ROC) curve for RF model performance in classifying FT states. RF classification trained on observed binary FT data.

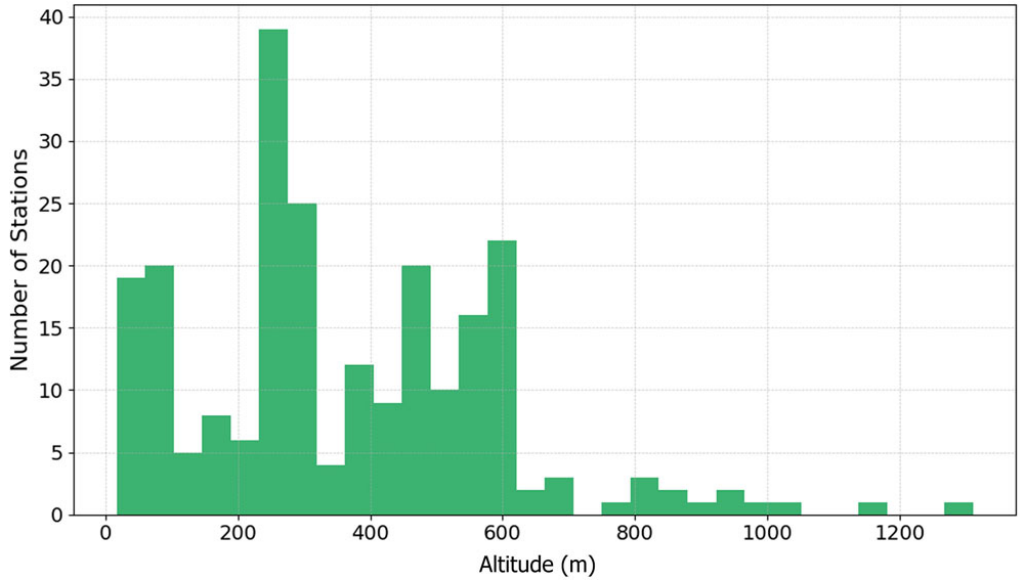

Figure S2.8. Altitude distribution of observational stations

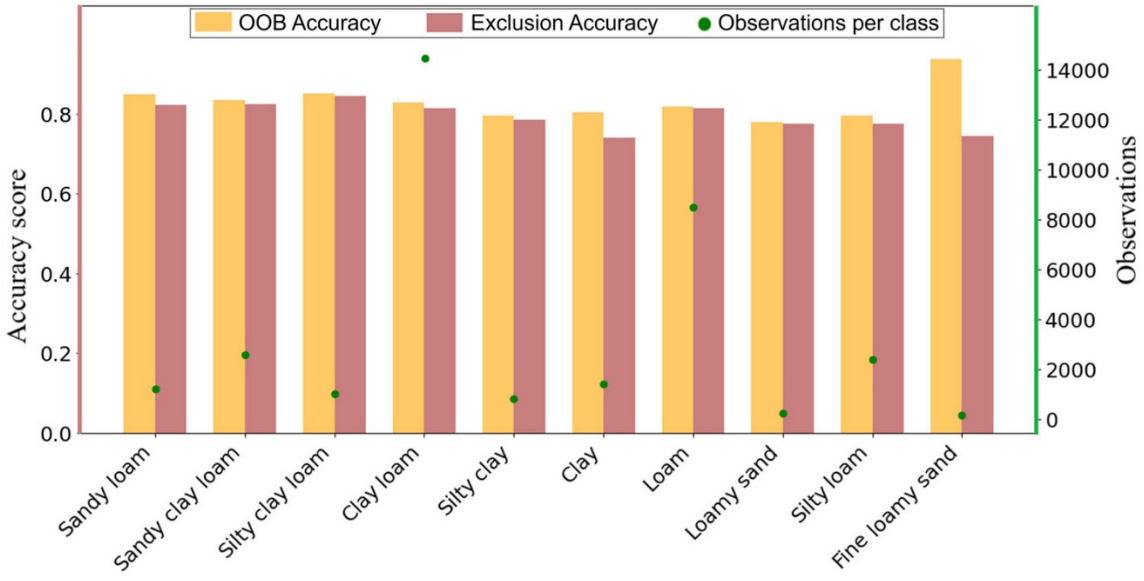

Figure S2.9. A visual depiction of model performance by grouped soil type, illustrating the accuracy of FT classifications using VH_{EFTA}.

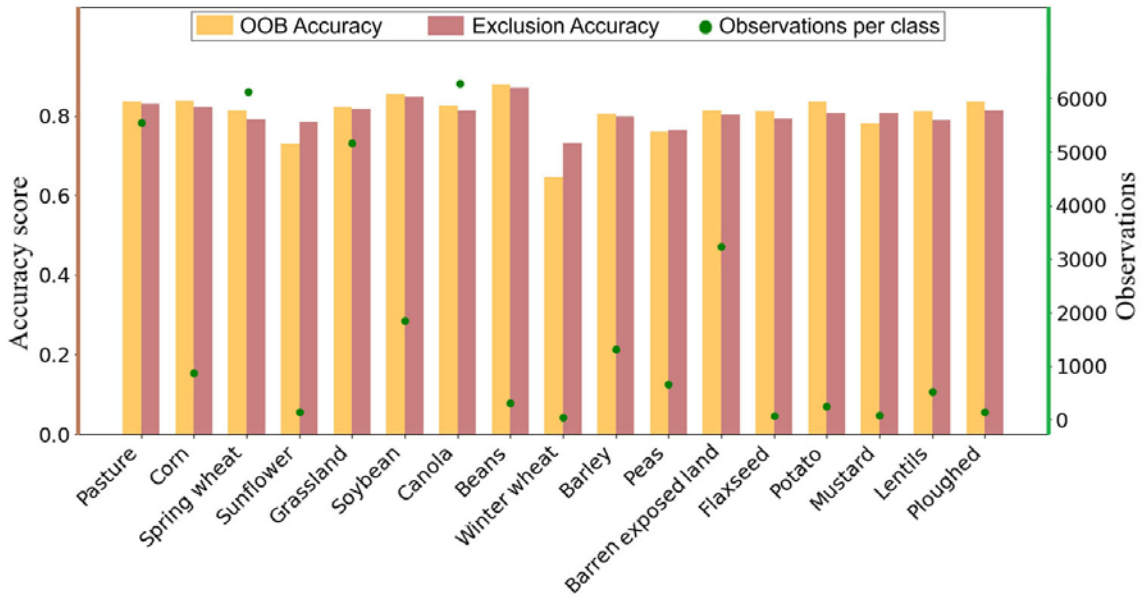

Figure S2.10. A visual depiction of model performance by grouped crop type, illustrating the accuracy of FT classifications using VH_{EFTA}.

CHAPTER III

Chapter III

The Effects of Frozen Soil Extent on Event-Based Runoff Generation in an Agricultural Catchment, Eastern Canada

Shahabeddin Taghipourjavi, Christophe Kinnard, Alexandre Roy

Abstract

This study examines the hydrological influence of near-surface soil freeze–thaw (FT) states on runoff response in the agricultural Acadie River catchment in southern Québec, Canada, during the cold season (October–April) from 2015 to 2025. Catchment-scale frozen soil extent was derived from Sentinel-1 C-band VH backscatter using the Exponential Freeze–Thaw Algorithm (EFTA) and integrated with ERA5-Land rainfall and snowmelt estimates and observed discharge. Runoff coefficients were consistently higher under frozen conditions, reaching ~2.4 at short timescales compared to ~1.55 under thawed conditions, and stabilizing at ~0.70–0.75 versus ~0.50–0.55 at longer windows. Cross-correlation analysis revealed a dominant 1-day lag between liquid water input and discharge, with stronger coupling in winter ($r \approx 0.64$) than in fall and spring ($r \approx 0.60$–0.61), indicating enhanced short-term runoff response under frozen conditions. Hydrological events were defined using a 3.5 mm day^{-1} liquid water input threshold and were predominantly short (1–3 days). Event-scale analysis showed weak relationships between runoff response and frozen soil extent ($R^2 \approx 0.04$; $p \approx 0.12$), indicating that frozen soil alone does not explain event-scale variability. Gamma generalized linear models (GLMs) showed that liquid water input is the dominant control on runoff response (AIC = 176.75; $p < 0.001$). Frozen soil effects were consistently positive across model structures but did not reach statistical significance ($p \approx 0.06$–0.12), indicating that their influence is

not strongly supported statistically at the event scale. Interaction-based models suggested steeper input–runoff relationships under higher frozen conditions, consistent with reduced infiltration capacity, although confidence intervals were wide. In contrast, antecedent wetness showed no significant effect ($p > 0.25$). Model diagnostics confirmed adequate fit, and mixed-effects models did not improve performance. Overall, runoff generation is primarily controlled by liquid water input, while frozen soil conditions are associated with enhanced runoff response but do not emerge as a statistically robust predictor at the event scale. These findings highlight the value of integrating satellite-derived FT information with hydrometeorological data to improve the characterization of runoff dynamics in cold-region agricultural systems.

Keywords

Event-Based Runoff, Near Surface Frozen Soil, Sentinel 1 C-band data, Gamma generalized linear mixed modeling (GLMM), Sentinel 1 C-band data, Acadie agricultural catchment.

3.1. Introduction

Seasonal freeze-thaw (FT) cycles, occurring throughout the terrestrial cryosphere where water is permanently or seasonally frozen, exert an important control on biospheric and hydrological processes as well as land–atmosphere exchanges (Kim et al, 2010; Kimball et al, 2006). Near-surface FT cycles represent recurring processes in which soil water alternates between frozen and liquid phases in response to periodic temperature fluctuations across mid- to high-latitude regions, fundamentally shaping soil hydrothermal dynamics, altering soil structure and stability, and influencing infiltration, runoff generation, and erosion under changing climatic conditions (Li et al, 2021a). In cold-region hydrology, FT processes operate along a broad climatic gradient from continuous to intermittent freezing and act as a key mechanism that governs surface and subsurface hydrological processes by altering soil permeability between frozen and unfrozen states (Ireson et al, 2013). Several long-term studies have demonstrated that FT transitions influence soil water redistribution across landscapes (Qin et al, 2021; Yang et al, 2019). Farmlands typically experience more intense and frequent freezing than forests or deserts, largely due to differences in vegetation cover and initial soil moisture conditions (Yi et al, 2014). These factors influence surface insulation and the exchange of latent heat during freezing, which in turn affect the timing and magnitude of soil water availability during thaw (Guo et al, 2021). Enhanced soil water migration and storage during FT cycles in farmlands can contribute to increased moisture supply for early spring plant growth, while forests and areas with higher vegetation cover tend to buffer temperature fluctuations and reduce FT intensity, leading to more stable soil hydrothermal regimes (Chen et al, 2020; Ding et al, 2023). During frozen soil periods, the hydraulic conductivity decreases sharply with temperature as the unfrozen water content diminishes, greatly restricting infiltration and promoting rapid surface runoff even under moderate precipitation or snowmelt conditions (Burt & Williams, 1976; Wang et al, 2009).

However, snowmelt infiltration into frozen ground is scale-dependent, as the infiltrability of frozen soils varies with the spatial distribution and thickness of the snowpack, which controls soil thermal insulation and the extent of frozen versus unfrozen surface conditions. Partially frozen surfaces can therefore act as temporary impermeable

layers that restrict infiltration until thawing progresses (Gray et al, 2001; Lundberg et al, 2016b).

Antecedent hydrological conditions, including prior precipitation and the presence of frozen soil, are critical hydrological drivers controlling event-based runoff responses (Favaro & Lamoureux, 2014; Tramblay et al, 2010). Higher cumulative antecedent precipitation increases catchment wetness and reduces the remaining soil storage capacity through progressive saturation, thereby enhancing runoff generation and producing non-linear event responses depending on antecedent conditions (Song & Wang, 2019). Since large-scale soil moisture measurements are rare, proxies such as the antecedent precipitation index (API) have been used effectively to estimate initial catchment wetness and the potential for enhanced runoff and resulting high streamflow (Ali et al, 2010; Liang et al, 2022a). Under frozen conditions, infiltration is restricted to thin unfrozen layers, leading to enhanced overland flow and higher runoff coefficients during snowmelt or rainfall on frozen ground events (Collins, 2019; Starkloff et al, 2018).

Numerous field and laboratory studies have demonstrated that soil freezing restricts water infiltration in soils, either completely or partially, by reducing hydraulic conductivity and limiting liquid water pathways (Jiang et al, 2021; Watanabe & Osada, 2017). At the local scale, this process is well established and commonly leads to enhanced surface runoff during rainfall on frozen ground events and snowmelt events (Mohammed et al, 2018; Niu & Yang, 2006). Field observations nevertheless show that frozen soils do not always behave as impermeable layers, as infiltration may still occur through air-filled macropores under partially frozen conditions, particularly in agricultural soils (Sanchez-Rodriguez et al, 2025). However, the influence of soil freezing on catchment-scale discharge remains much more ambiguous. Previous studies have reported contrasting responses, with some observing a significant increase in peak flows under frozen conditions (Fang & Pomeroy, 2016; Shanley & Chalmers, 1999), while others report weak or negligible impacts depending on region, basin characteristics, and scale of observation (Lindström et al, 2002; Stähli, 2017). This variability has been documented particularly in

agricultural landscapes, where runoff responses to frozen conditions differ markedly between sites and years (Ding et al, 2023; Sanchez-Rodriguez et al, 2025).

A recent systematic review by Ala-Aho et al (2021) showed that the hydrological influence of seasonally frozen ground is generally evident at small spatial scales but becomes increasingly variable as the scale of measurement increases. This scale-dependent behavior is likely related to the strong spatial heterogeneity of freezing and infiltration processes, whereby unfrozen or more permeable soil patches may act as preferential foci for infiltration within partially frozen basins, thereby modulating the discharge response (Lundberg et al, 2016a)

While most hydrological models explicitly account for soil moisture storage and antecedent wetness (Bronstert et al, 2023; Lane et al, 2024; Schoener & Stone, 2019), very few explicitly represent soil freezing and its impact on infiltration and runoff partitioning. As a result, frozen-soil processes remain underrepresented in many cold-region hydrological simulations, contributing to persistent uncertainty in cold-season runoff prediction (Kompanizare et al, 2024; Pomeroy et al, 2022). This limitation is partly attributable to the scarcity of spatially distributed observations of soil FT conditions at the catchment scale. Although in-situ measurements provide precise temporal information on FT transitions, their sparse spatial coverage and sensitivity to local variability limit their applicability for basin-scale analyses (Gao et al, 2018; Rowlandson et al, 2018). Numerical simulations and geophysical approaches can complement field measurements, but they are often computationally demanding and logistically constrained when applied over large regions or heterogeneous landscapes (Cao et al, 2017; Shao & Zhang, 2020). Quantifying the spatiotemporal distribution of frozen versus unfrozen soils is therefore essential for testing hypotheses linking soil freezing extent to runoff generation and discharge changes during the cold season.

At the global scale, remotely sensed soil FT products already exist, most of which rely on passive microwave observations from sensors such as SMAP and AMSR-E/2 and provide daily FT status at grid resolutions of roughly 9–36 km (Gao et al, 2018; Walker et

al, 2022). While these products offer valuable information on seasonal FT changes over cold-region land areas worldwide (Kim et al, 2017; Kim et al, 2019), their coarse spatial resolution and mixed-pixel effects limit their ability to capture fine-scale heterogeneity that controls infiltration and runoff processes at the catchment scale, particularly in heterogeneous and agricultural landscapes (Gao et al, 2021; Roy et al, 2017).

Multispectral observations have long been used to characterize land surface conditions, but their applicability to FT detection is limited by cloud cover, atmospheric effects, and the absence of solar illumination during winter at high latitudes, leading to data gaps during critical FT transition periods (Miller et al, 2013; Tsai et al, 2019). In contrast, microwave remote sensing, particularly in the active domain, overcomes these limitations by directly responding to changes in the soil's dielectric constant, which differs markedly between frozen and thawed states (Podest et al, 2014). This sensitivity enables day-and-night, all-weather monitoring, making active microwave systems particularly well suited for continuous FT detection in cold regions.

Several studies have demonstrated the potential of SAR-based approaches for mapping seasonal near-surface FT conditions, emphasizing the sensitivity of radar backscatter to soil dielectric properties, surface roughness, and moisture changes (Chen et al, 2024; Wang et al, 2022). Early work highlighted that SAR backscatter is primarily controlled by soil permittivity and surface roughness, with physical models such as the Integral Equation Model (IEM) linking radar responses to soil and acquisition parameters (Baghdadi et al, 2012). In agricultural environments, variations in surface roughness due to tillage and vegetation structure can significantly influence backscatter through enhanced scattering mechanisms, including double-bounce effects, thereby complicating the interpretation of FT signals (Baghdadi et al, 2002; Fayad et al, 2020). Using Sentinel-1 C-band SAR data, Baghdadi et al (2018) showed that soil freezing leads to a decrease in backscattering coefficients (≈3–4 dB in VV and 1–2 dB in VH) due to reduced dielectric permittivity, although the detectability of FT transitions is constrained by sensor radiometric accuracy and can be further masked under wet snow conditions. To address spatial variability, Fayad et al (2020) proposed adaptive baseline approaches across land-

cover types to reduce the impact of roughness heterogeneity. At the watershed scale, threshold-based classification methods using RADARSAT-1 have also demonstrated robust performance for distinguishing frozen and unfrozen soils, with accuracies exceeding 85%, while highlighting the strong influence of soil type, land use, and snow cover on backscatter variability (Khaldoune et al, 2011). These studies collectively show that SAR-based FT detection relies on change-detection or threshold-based strategies but remains sensitive to surface conditions, motivating the development of more flexible approaches that better account for spatial heterogeneity and transitional FT states. In southern Québec, Canada, the Exponential Freeze-Thaw Algorithm (EFTA), a change-based approach that applies an exponential weighting to Sentinel-1 VH backscatter changes to reduce the influence of fluctuations during expected thawed periods and emphasize changes during expected frozen periods, particularly across fall and spring transitions, was applied to delineate frozen and thawed surface states across agricultural and forested landscapes (Taghipourjavi et al, 2024). Following its initial development, the algorithm was trained and evaluated across 174 agricultural monitoring stations distributed throughout Canada by integrating Sentinel-1 backscatter with in-situ soil temperature observations and site-level variables within classification and regression frameworks (Taghipourjavi et al, 2026a). This work resulted in an on-demand, machine-learning–driven framework for retrieving surface FT states from Sentinel-1 data across Canadian agricultural regions, opening new opportunities to investigate the influence of surface FT on catchment-scale hydrology.

The goal of this study is to use satellite-based synthetic aperture radar (SAR) observations to better quantify how near-surface soil FT conditions influence cold-season runoff generation in agricultural catchments. To address this objective, the analysis is applied to the Acadie River agricultural catchment of southern Québec, Canada, which exhibits strong seasonal freezing, a combined snowmelt and rainfall runoff regime, and pronounced hydrological variability during winter and spring (Aygün et al, 2020). Catchment-scale FT states were retrieved through an on-demand, web-based processing framework applied to Sentinel-1 C-band VH backscatter, producing a 10-year record (2015–2025) of frozen and thawed soil conditions across the study area (Taghipourjavi et al, 2026b). These FT states were analyzed alongside with rainfall and snowmelt estimates

and observed river discharge to examine discharge response timing and magnitude during cold-season conditions.

Runoff response was examined using a multi-scale framework combining daily, event-based, and statistical modeling approaches to characterize discharge timing and controls under contrasting FT regimes. Daily-scale analyses using runoff coefficients and cross-correlation were used to evaluate short-term runoff response under contrasting frozen and thawed conditions. An event-based framework was then applied to isolate discrete rainfall–snowmelt episodes and assess how frozen soil extent interacts with hydrometeorological forcing and catchment antecedent wetness. To this purpose, generalized linear mixed-effects models were used to quantitatively evaluate the role of near-surface frozen soil conditions in event-based runoff generation, while accounting for liquid water inputs, antecedent storage, and intra-seasonal variability, allowing the relative contribution of FT conditions to be assessed alongside dominant hydrological drivers.

3.2. Materials and Methods

3.2.1. Study area

The Acadie River catchment is located in the intensively agricultural Montérégie region of southern Québec, Canada (45°17′ N, 73°10′ W) (Figure 3.1). The basin drains northward into the Richelieu River near the south shore of the St. Lawrence River, draining a catchment area of 367 km², including a minor portion (about 1%) extending into the United States, and the river flows over an approximately 82 km course through the southern St. Lawrence Lowlands.

The catchment's flat to gently rolling topography (40–125 m above sea level) results from its Quaternary glacial legacy, which left behind marine and fluvial deposits in the lowlands and stony till toward the Adirondack foothills (Lévesque et al, 2019). Furthermore, fine-textured and poorly drained clayey and organic soils, overlying discontinuous glacial till, dominate the basin and promote surface ponding and seasonal soil freezing

Furthermore, fine-textured and poorly drained clayey and organic soils, overlying discontinuous glacial till, dominate the basin. This type of surficial geology has been shown to promote surface ponding and seasonal soil freezing (Kloffel et al, 2024; Xu et al, 2025). To compensate for low natural permeability, an extensive subsurface tile-drainage network channels excess water through artificial ditches and canals, directly connecting farmlands to the river (Aygün et al, 2020). Land use is dominated by agriculture, which covers approximately 72% of the basin, and forests represent about 17.4% of the catchment, consisting primarily of deciduous (58%), mixed (28%), and coniferous (15%) stands, while the remaining 10% includes urban areas, wetlands, lakes, and shrubland, based on the 30-meter spatial resolution North American Environmental Atlas-Land Cover of 2020 (https://www.cec.org/north-american-environmental-atlas/land-cover-30m-2020/, accessed on 01 January 2026). Soybeans and corn are the main crops, occupying about 43% and 33% of cultivated areas, based on the Annual Crop Inventory 2024 provided by Agriculture and Agri-Food Canada (AAFC; https://open.canada.ca/data/en/dataset/ba2645d5-4458-414d-b196-6303ac06c1c9, accessed on 01 January 2026). The catchment has a cold, humid continental climate (Dfb), which is defined by warm summers and cold winters (Beck et al, 2018).

Based on records from the Acadie weather station (Station No. 030421; October 2000-October 2025), obtained from the Historical Climate Data of Canada (Environment and Climate Change Canada; https://climat.meteo.gc.ca/index_e.html, accessed on 01 January 2026), the mean annual temperature was 7.1 °C, with an average of −2.4 °C during the cold season (November-April). Furthermore, the mean annual precipitation totals approximately 1005 mm, with snow contributing 20–25% of this total. This mixed rain-snow regime subsequently results in two typical high-flow periods: the early spring snowmelt and late fall rainfall. Consequently, mid-winter floods may occur, driven by rain-on-snow events and limited water infiltration into frozen soils (e.g., Katz et al, 2023). Fine-textured soils, such as silty clay and loam, exhibit high water retention and capillary connectivity, which enhance water redistribution during FT cycles and make these soils particularly susceptible to FT-induced changes in pore structure, leading to locally increased hydraulic conductivity, especially within the upper soil layers (e.g., Kloffel et al, 2024; Leuther & Schlüter, 2021).

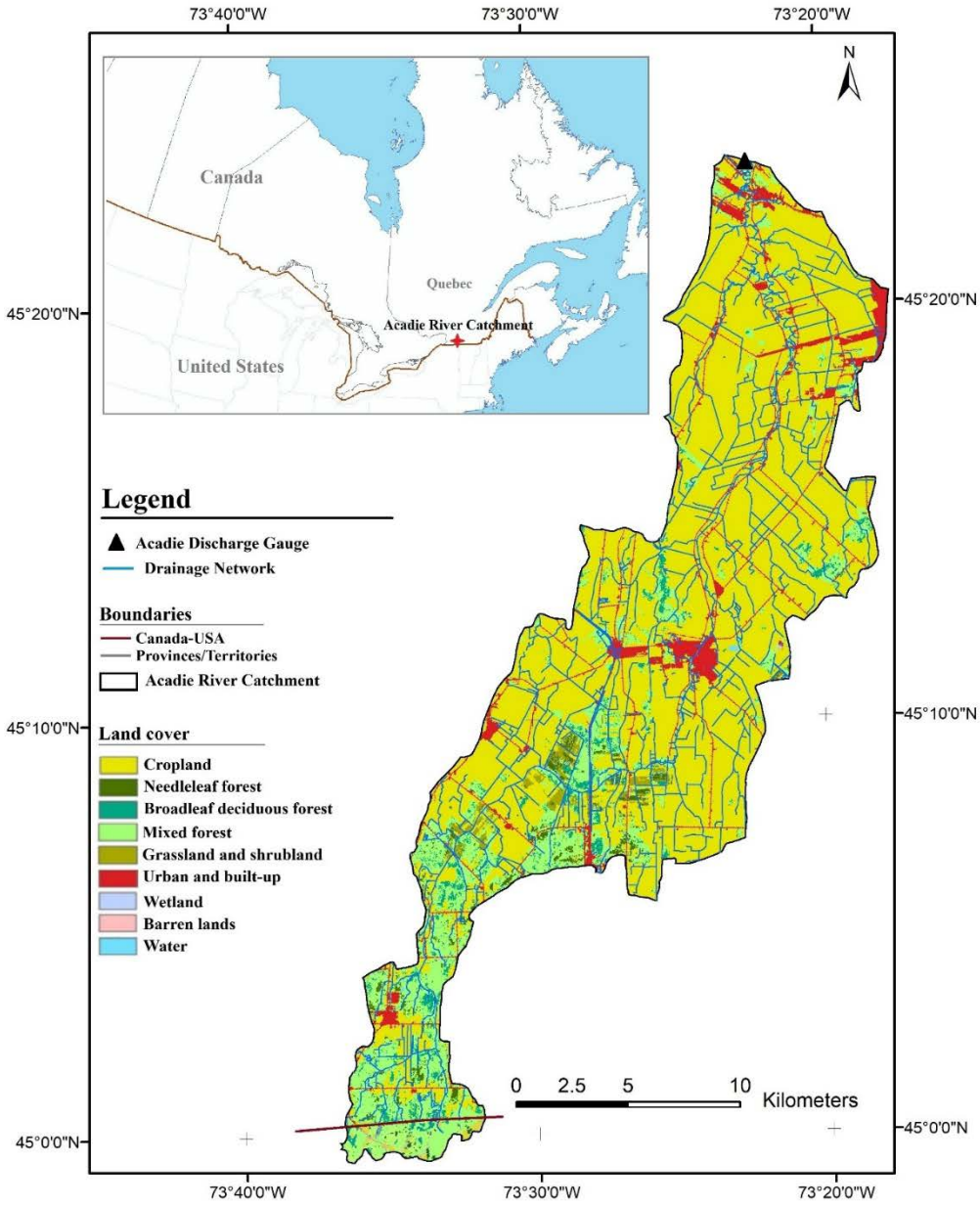

Figure 3.1. Location and land cover of the Acadie River catchment in southern Québec, Canada. Land cover is derived from the North American Land Cover 2020 dataset (Commission for Environmental Cooperation (CEC), 30 m resolution; https://www.cec.org/north-american-environmental-atlas/land-cover-30m-2020/, accessed on 01 January 2026).

Furthermore, flat topography can promote surface water accumulation and lateral redistribution, increasing hydrological connectivity during thaw events, although runoff transmission is generally more rapid in steeper catchments (Appels et al, 2016; Coles &

McDonnell, 2018). These conditions promote rapid variations in infiltration-runoff partitioning, making the Acadie catchment an appropriate environment for investigating the effects of FT states on runoff responses. Such dynamics, combined with the formation of ice jams, pose significant flood risks to downstream communities, including Chambly and Carignan regions (Lévesque et al, 2019).

3.2.1.1. Sentinel-1–Derived FT Retrieval

A framework was applied to retrieve and classify FT states for each available Sentinel-1 VH acquisition during the cold-season period (October-April) from 2015 to 2025 over the Acadie River catchment. Although Sentinel-1 does not provide daily observations, all available overpasses within the cold-season window were processed, resulting in a 10-year series of FT classifications with revisit intervals typically ranging from 5 to 12 days (mean ≈ 6 days), depending on acquisition geometry and data availability. For each acquisition date, classified FT maps were spatially aggregated to compute the frozen soil ratio (F), defined as the fraction of pixels classified as frozen relative to the total number of pixels corresponding to croplands, grasslands, and barren land within the catchment, thereby excluding forested, urban, and open-water areas not relevant to soil FT processes (Taghipourjavi et al, 2026a). Land-cover masking was based on the Land Cover of North America dataset at 30-m resolution (2020) available in Google Earth Engine (Commission for Environmental Cooperation (CEC), 2021). All computations were performed through the GEE API, ensuring access to the complete Sentinel-1 archive and efficient cloud-based processing. The methodology for FT map classification and production is described in detail in Taghipourjavi et al (2026b).

3.2.1.2. Hydrological Variables for the Acadie catchment

Daily discharge measurements (Q, in $m^3\ s^{-1}$) for the October–April period between 2015 and 2025 were obtained from the Québec Centre of Water Expertise (CEHQ; www.cehq.qc.ca, accessed on accessed on 01 January 2026) at the Acadie gauging station (Station No. 030421). Hydrometeorological forcing variables were derived from the ERA5-Land reanalysis product (Muñoz-Sabater et al, 2021), provided by the European Centre for Medium-Range Weather Forecasts (ECMWF) through Google Earth Engine

(GEE), at a spatial resolution of approximately 11.1 km. ERA5-Land was used due to its temporal and spatial consistency, compared to station data that suffer from temporal gaps and limited spatial coverage. Daily sums of snowmelt (mm), total precipitation (mm) and snowfall (mm) were extracted and spatially averaged over the delineated watershed. Rainfall was calculated by subtracting snowfall from total precipitation. The daily liquid water input to the catchment surface, denoted as I_{liq} (mm), was calculated as the sum of rainfall and snowmelt. I_{liq} was quantified using rainfall and snowmelt, rather than total precipitation, as it accounts for the temporal decoupling between solid precipitation accumulation and its subsequent release as meltwater (Li et al, 2019; Molotch et al, 2009).

3.2.2. Methods

3.2.2.1. Runoff Coefficient Estimation

In the Acadie River catchment, cold-season runoff changes are predominantly controlled by episodic rainfall and snowmelt inputs, which together drive significant variability in streamflow during winter and early spring (Aygün et al, 2020). These water inputs interact with soils that undergo alternating FT cycles which is hypothesized to control the partition between infiltration and surface runoff. To examine the control of FT on the hydrological response, the analysis focused on the period from early October through late April, when evapotranspiration losses are minimal, and FT is most active. This temporal window captures key seasonal transitions, including the fall pre-freeze, mid-winter frozen conditions, and the spring thaw when snowmelt becomes the dominant water input. The runoff coefficient was used as an initial diagnostic metric to characterize runoff response in relation to FT conditions in the catchment. The runoff coefficient was defined as (Chow, 1971):

$$\overline{RC} = \frac{\sum_{t-\Delta t}^{t} Q(t)}{\sum_{t-\Delta t}^{t} I(t)} \tag{3.1}$$

where $Q(t)$ is the mean daily specific river discharge (mm day^{-1}), I is the daily liquid water input (mm day^{-1}), calculated as the sum of rainfall and snowmelt, and t is time (days). To explore how timescale influences the relationship between FT conditions

and runoff response, the RC was calculated over periods ranging from Δt = 1 to 30 days. For a given day, discharge and liquid water input were averaged over the preceding Δt days, including the current day, such that RC reflects hydrological conditions integrated backward in time over the selected window length and reduces the uncertainties du to water transit times.

Only days with total liquid water inputs exceeding 0.1 mm were retained to exclude negligible inputs that can introduce numerical instability when computing runoff metrics based on near-zero denominators (DeGuzman et al, 2023; Ross et al, 2021). This threshold also reduces the influence of spurious low-intensity precipitation, commonly referred to as the "drizzle effect" (Lazoglou et al, 2024). The drizzle effect is a known artifact in atmospheric reanalysis and numerical weather prediction models such as ERA5, in which light precipitation is unrealistically distributed over large areas and extended periods (Shrestha et al, 2023). Such minor precipitation events are often not hydrologically effective and can introduce noise into hydrological analyses. By filtering out these small inputs, we suppress non-meaningful variability and focus on events that contribute significantly to runoff generation, thereby improving the robustness and interpretability of runoff metrics.

The frozen state of the catchment was characterized independently using the catchment *F* derived from Sentinel-1 observations. Accordingly, the comparison between RC values and *F* is made only for days with available FT maps.

3.2.2.2. Discharge Response Time Analysis

To characterize the dominant response time between liquid water inputs and streamflow under contrasting FT regimes, a cross-correlation analysis was performed between daily specific discharge (*Q*) and the daily total liquid water input (*I*). The analysis was conducted separately for three cold-season intervals representative of distinct FT conditions: fall (1 October-15 December), winter (16 December-30 March), and spring (April). Pearson cross-correlation coefficients were computed for time lags Δ_t ranging from 0 (same-day response of river discharge to liquid water input) to 5 days. 95%

confidence intervals were calculated using Fisher's z transformation to estimate the uncertainty on estimated correlations (Hedges & Olkin, 2014). Because both liquid water input and discharge time series exhibit serial autocorrelation (KOVAčIč, 2010), the effective sample size (Neff) was estimated using the lag-1 autocorrelation of the paired series. Confidence intervals were computed on the Fisher z scale and then back transformed to the Pearson correlation scale. The statistical significance of correlations was evaluated using N_{eff} - adjusted tests to account for the reduced degrees of freedom caused by temporal persistence in the hydrological data. This diagnostic analysis aimed to identify the characteristic timing of the discharge response to water inputs at the daily scale. The resulting lag structure is subsequently used to interpret short-term event-onset runoff diagnostics but is not incorporated into event-integrated runoff calculations (see next section).

3.2.2.3. Event-Based Hydrological Analysis

An event-based framework was adopted to analyze the short-term discharge response to liquid water inputs under varying FT conditions. This approach isolates discrete runoff-generating episodes rather than relying on continuous time series, allowing the influence of frozen soil and antecedent moisture conditions to be evaluated at the scale of individual hydrometeorological events (Odey & Cho, 2025). Hydrological events were defined as contiguous periods of one or more consecutive days during which *I* exceeded a predefined daily threshold. The event onset day (t) corresponds to the first day on which daily liquid input exceeds the threshold, while event duration varies depending on the persistence of input exceedance and hydrometeorological conditions. Events therefore include both single-day input pulses and multi-day input episodes.

To support the selection of the liquid water input threshold used for event definition, short-term streamflow response was evaluated using the one-day change in discharge, defined as:

$$\Delta Q = Q_t - Q_{t-1} \tag{3.2}$$

where Q_t and Q_{t-1} represent daily discharge at day t and the preceding day, respectively. Positive ΔQ values indicate rising discharge conditions, whereas negative values represent recession. For the threshold-selection analysis, only positive ΔQ values were retained to isolate runoff-generating responses associated with liquid water input. This diagnostic analysis was used to identify the range of liquid water input (I_{liq}) associated with increasing runoff response, thereby helping define a runoff-relevant threshold for event separation. The analysis was used only for threshold selection and does not represent event-integrated runoff response.

3.2.2.4. Multivariate Analysis of Frozen Soil and Antecedent Baseflow Effects on Runoff

To quantify runoff response at the event scale, an event-integrated runoff coefficient ($\overline{RC}_{event}$) was computed as:

$$\overline{RC}_{event} = \frac{\bar{Q}_{event}}{\bar{I}_{event}} \tag{3.3}$$

where $\bar{Q}_{event}$ is the mean daily specific discharge averaged over all days belonging to the event and $\bar{I}_{event}$ is the mean I averaged over the same event window. Prior daily-scale cross-correlation analysis identified a dominant discharge response lag of approximately one day across seasons (Section 3.2.2.2). At the event scale, runoff response was evaluated using event-averaged liquid water input and discharge aggregated over the same event period. This formulation was intended to characterize integrated event-scale runoff response rather than short-term discharge timing.

3.2.2.5. Statistical Modeling Framework for Frozen-Soil Runoff Analysis

An Antecedent Precipitation Index (API) was computed to quantify cumulative precipitation memory effects using a standard exponential decay formulation:

$$API_t = k(API_{t-1} + P_t) \tag{3.4}$$

where P_t denotes daily liquid water input, taken here to be I, i.e. the sum of rainfall and snowmelt. This definition differs from conventional API formulations based solely on rainfall and was adopted to better represent cold-region hydrological processes. The decay constant (k) was set to 0.85, a commonly adopted value within the empirically derived range of 0.80–0.98 for daily runoff modeling.(Li et al, 2021b; Liang et al, 2022b). The API was mean centered prior to model fitting to improves numerical stability and interpretability of interaction terms in statistical models. It should be noted that API does not explicitly account for soil freezing processes, and its interpretation under frozen conditions may therefore be limited. The inclusion of interaction terms with frozen soil extent was used to partially address this limitation.

3.2.2.6. Event-Based Runoff Modeling Framework

Event-scale runoff response was modeled using a generalized linear model (GLM) with a Gamma distribution and a log-link function, selected to accommodate the strictly positive and right-skewed nature of discharge (Q) data and to capture potential non-linear and multiplicative effects in runoff generation. This formulation allows runoff response to vary proportionally with changes in hydrometeorological drivers rather than assuming linear additive responses. Event-scale runoff response was modeled using generalized linear models (GLMs) with a Gamma distribution and a log-link function. This formulation is appropriate for strictly positive and right-skewed hydrological variables and allows multiplicative relationships between predictors and runoff response to be represented.

The modeling framework was based on the conceptual hypothesis that event runoff is primarily driven by liquid water input, while antecedent wetness and frozen soil conditions modulate the efficiency by which this input is converted into streamflow, due to their control on the soil infiltration capacity:

$$Q_{sf} = I \times g(API\ , F) \tag{3.5}$$

where Q_{sf} represents event-scale stormflow, i.e. the portion of streamflow associated with a precipitation or snowmelt event, I denotes the total liquid water input during the event (rainfall + snowmelt), API is the antecedent precipitation index representing prior catchment wetness conditions, F is the frozen soil ratio, and g is a 'modulator' function. In this formulation, antecedent wetness and frozen soil extent do not act as independent additive drivers of runoff but instead regulate the fraction of input water that is converted into quick (storm) flow.

The event-scale stormflow (Q_{sf}) was estimated as:

$$Q_{sf} = Q_{event} - Q_{base} \tag{3.6}$$

where Q_{event} is the mean discharge during the event period and Q_{base} is the pre-event baseflow estimated as the mean discharge during the event onset day and the two preceding days. In this formulation Q_{sf} represents the incremental runoff generated during the event, removing the confounding contributions from antecedent baseflow.

3.2.2.7. Model Formulation

Two complementary approaches were used to represent the conceptual relationship between runoff, input water, antecedent conditions, and frozen soil extent.

Approach A: Modelling stormflow

In this formulation, the event-scale stormflow (Q_{sf}) was used as the target variable and liquid water input (I) as direct predictor, allowing the effect of I on Q_{sf} to vary as a function of antecedent wetness (API) and frozen soil conditions (F) through interaction terms:

A1: $Log(Q_{sf}) = \beta_0 + \beta_1 \log(I)$ (3.7)

$$\mathbf{A_2}: Log(Q_{sf}) = \beta_0 + \beta_1 \log(I) + \beta_2 \log(I) \cdot API \quad (3.8)$$

$$\mathbf{A_3}: Log(Q_{sf}) = \beta_0 + \beta_1 \log(I) + \beta_2 \log(I) \cdot F \quad (3.9)$$

$$\mathbf{A_4}: Log(Q_{sf}) = \beta_0 + \beta_1 \log(I) + \beta_2 \log(I) \cdot API + \beta_3 \log(I) \cdot F \quad (3.10)$$

$$\mathbf{A_5}: Log(Q_{sf}) = \beta_0 + \beta_1 \log(I) + \beta_2 \log(I) \cdot API + \beta_3 \log(I) \cdot F + \beta_4 \log(I) \cdot API \cdot F \quad (3.11)$$

In these models, *API* and *F* modify the sensitivity of runoff response to input water, rather than acting as direct predictors.

Approach B: Modelling the Runoff Coefficient

The second approach aims at modelling the event-scale runoff coefficient ($\overline{RC}$), which represents the fraction of input water that contributed to event stormflow. Because modeling ratios is challenging, with treat this problem by using stormflow (Q_{sf}) as target variable but including water input (*I*) as an offset in the model:

$$\mathbf{B_1}: Log(Q_{sf}) = \log(I) + \beta_0 \quad (3.12)$$

$$\mathbf{B_2}: Log(Q_{sf}) = \log(I) + \beta_0 + \beta_1 API \quad (3.13)$$

$$\mathbf{B_3}: Log(Q_{sf}) = \log(I) + \beta_0 + \beta_1 F \quad (3.14)$$

$$\mathbf{B_4}: Log(Q_{sf}) = \log(I) + \beta_0 + \beta_1 API + \beta_2 F \quad (3.15)$$

$$\mathbf{B_5}: Log(Q_{sf}) = \log(I) + \beta_0 + \beta_1 API + \beta_2 F + \beta_3 API \cdot F \quad (3.16)$$

Since log(*I*) has no coefficient, it is used as an offset, which amounts to modelling log(*Q*/*I*), or log ($\overline{RC}$), while avoiding the complexity of modelling a ratio. This formulation can be interpreted as modeling the efficiency with which input water is converted into runoff under varying antecedent moisture and frozen soil conditions.

3.2.2.8. Model Selection

The nested models of increasing complexity enumerated in the previous section were evaluated and compared using the Akaike Information Criterion (AIC). Models with $\Delta AIC<2$ were considered to have comparable support. To account for potential temporal variability, an additional set of models was fitted using a generalized linear mixed modeling (GLMM) framework including a random intercept for month (1 | month). This formulation allows baseline runoff response to vary across months while preserving the fixed-effect structure of the predictors. The mixed-effects formulation was used to evaluate whether the relationships identified in the fixed-effect models remained consistent after accounting for month-to-month variability in cold-season hydrological conditions.

3.2.2.9. Sensitivity Analysis of Event Definition Threshold

To assess the robustness of the modeling results, the event extraction and model comparison were repeated across liquid water input thresholds ranging from 2.0 to 5.0 mm day^{-1}. For each threshold, the number of detected events, the number of events with Sentinel-1 frozen-soil observations, the final number of valid modeling events, and the best-supported model based on AIC were recorded.

3.3. Results

3.3.1. Runoff Coefficient Variability Under Frozen and Thawed Soil Conditions

Figure 3.2 illustrates the variation of the mean runoff coefficient (RC) as a function of moving-average window length (1–30 days), computed using daily data restricted to the cold-season period. Results are shown separately for days classified as frozen, thawed, and for all FT states combined. Frozen days correspond to days when more than 50% of the analyzed catchment surface area is classified as frozen (catchment $F \geq 0.50$), while thawed days correspond $F < 0.50$. The combined category includes all cold-season days, encompassing both frozen and thawed conditions.

For short window lengths (1–3 days), mean RC values are highest when the catchment is mostly experiencing frozen conditions, intermediate when all FT states are

considered together, and lowest when the catchment is predominantly thawed (Figure 3.2). As window size increases, mean RC decreases for all three subsets, with the most pronounced decline occurring within the first 5–7 days. Beyond approximately 10–15 days, RC values stabilize, while differences between frozen, thawed, and combined conditions remain evident across the full range of window sizes. At all window lengths, the curve representing all FT states lies between the frozen and thawed curves, reflecting aggregation across cold-season days characterized by varying catchment-scale FT conditions. Over the same window lengths, mean RC values for all FT states combined range from approximately 1.9 to 1.3, while thawed conditions exhibit the lowest RC values, decreasing from about 1.55 at 1 day to approximately 1.2 at 3 days. RC values exceeding 1 indicate that discharge temporarily exceeded contemporaneous liquid water input, implying that runoff response was not sustained exclusively by same-day rainfall and snowmelt inputs. These elevated values likely reflect contributions from antecedent catchment storage, delayed drainage processes, snowpack water release, and temporal mismatches between liquid water input and discharge response, particularly under frozen soil conditions where infiltration is reduced and runoff routing is enhanced over short timescales. By a 5-day window, RC values converge to approximately 1.0–1.05 for frozen conditions, 0.85–0.9 for all FT states, and 0.7–0.75 for thawed conditions. Beyond approximately 10–15 days, RC values stabilize, with frozen conditions remaining highest at around 0.70–0.75, all FT states stabilizing near 0.60–0.62, and thawed conditions near 0.50–0.55.

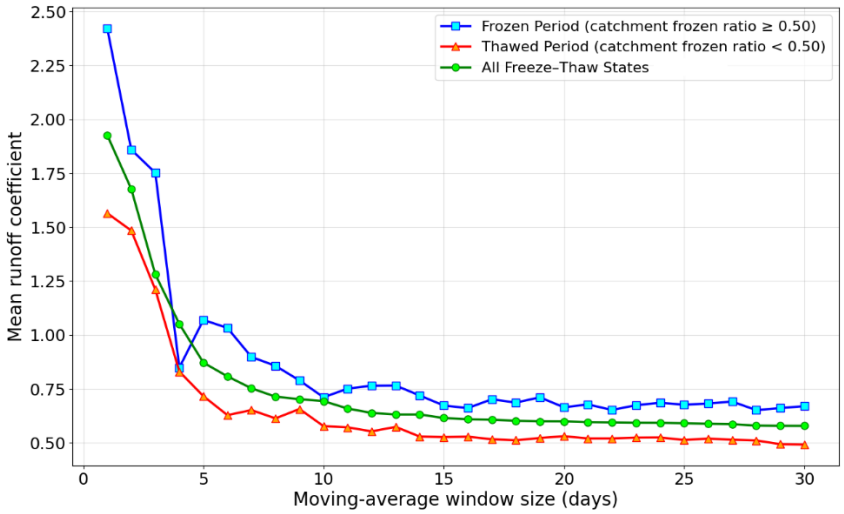

Figure 3.2. Mean RC as a function of moving-average window length (1–30 days) for frozen days (catchment F ≥ 0.50), thawed days (catchment F < 0.50), and all FT states combined, computed using daily data restricted to the cold-season period.

3.3.2. Seasonal Variability in Runoff Timing and Input-Discharge Relationships

The seasonal cross-correlation analysis reveals a consistent lag structure across all seasons, with correlation coefficients increasing from lag 0 to a maximum at lag 1 day, followed by a rapid decline at longer lags (Figure 3.3). The strongest coupling occurs during winter ($r \approx 0.64$), compared to fall ($r \approx 0.61$) and spring ($r \approx 0.60$), indicating enhanced short-term runoff response under predominantly frozen conditions.

Confidence intervals confirm that correlations at lag 1 are statistically significant across all seasons, with narrow 95% confidence intervals remaining above zero. Significant correlations persist up to lag 3 in fall and spring, and up to lag 5 in winter, although correlation strength decreases markedly beyond lag 2. This rapid decay indicates relatively fast water transfers between the catchment surface and its outlet. These results indicate that the dominant discharge response occurs approximately one day after liquid water input, with stronger and more sustained coupling during winter conditions.

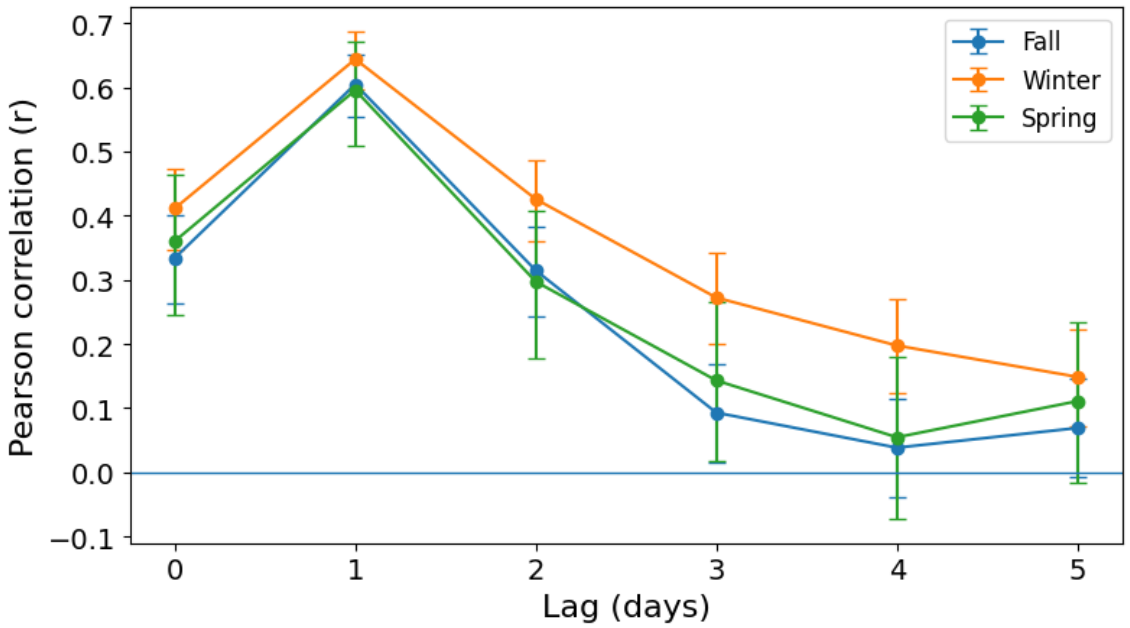

Figure 3.3. Seasonal cross-correlation between daily liquid water input (rainfall + snowmelt) and streamflow for lags from 0 to 5 days. Error bars represent 95% confidence intervals estimated using Fisher's z transformation and adjusted for autocorrelation using effective sample size (*Neff*). Statistically significant correlations ($p < 0.05$) are observed at short lags across all seasons, with the strongest response occurring at a lag of 1 day.

3.3.3. Temporal Distribution of Cold-Season Hydrological Events

Before defining hydrological events, the relationship between liquid water input magnitude and short-term streamflow response was examined across the cold season. Figure 3.4 illustrates the emergence of runoff-relevant hydrological response, quantified using the median positive one-day change in streamflow (ΔQ) associated with days exceeding progressively higher liquid water input thresholds. Median discharge response increases progressively with increasing input magnitude, reflecting enhanced runoff activation under larger liquid water inputs, although lower-intensity snowmelt events may still contribute to runoff generation. A transition toward stronger streamflow response is observed between approximately 3- and 4-mm day^{-1}, where median ΔQ increases from values below ~1.0 mm day^{-1} to values exceeding ~1.2 mm day^{-1}. This transition range was therefore used as a practical threshold range for event definition during the cold season.

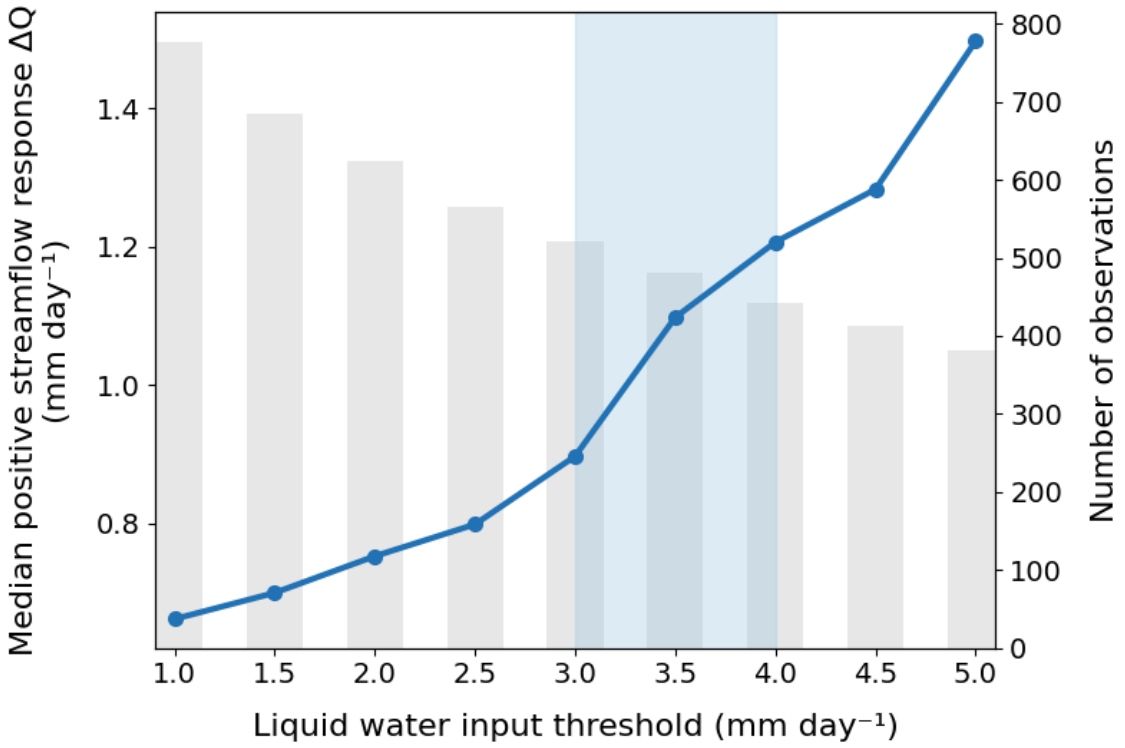

Figure 3.4. Short-term streamflow response as a function of liquid water input magnitude during the cold season. The solid line shows the median positive one-day change in ΔQ for days exceeding progressively higher liquid water input thresholds. Gray bars show the number of observations associated with each threshold class. The shaded band indicates the 3–4 mm day^{-1} input range used for event definition.

Hydrological events were defined using a fixed liquid water input threshold of 3.5 mm day^{-1}, selected within the 3–4 mm day^{-1} range where streamflow response begins to increase more rapidly (Figure 3.4). This threshold represents the onset of hydrometeorological forcing capable of activating runoff-generating flow pathways under cold-season conditions, while preserving sufficient event frequency for robust analysis. Events were defined as multi-day periods initiated when total liquid water input (I) exceeded this threshold. Event onset corresponded to the first exceedance, and events were allowed to continue over subsequent days with measurable inputs. This approach isolates

discrete runoff-generating episodes while minimizing the influence of minor inputs that do not produce a detectable hydrological response.

To provide additional context on the temporal structure of the detected hydrological events, Supplementary Figure S3.1 illustrates the joint distribution of event duration and mean liquid water input for cold-season events identified using the 3.5 mm day^{-1} threshold. Most events are short-lived (one to three days), while longer-duration events are less frequent and generally associated with moderate inputs. This pattern likely reflects both hydrological processes and the threshold definition, which preferentially captures rainfall or mixed rain–snowmelt events characterized by higher daily inputs, while potentially underrepresenting longer, lower-intensity snowmelt events. Furthermore, additional diagnostics (Figure S3.2) show that the strength of frozen soil-runoff relationships increase with input magnitude, particularly during winter months.

3.3.3.1. Sensitivity of Threshold Selection

To evaluate the robustness of the selected threshold, event extraction and model comparison were repeated across thresholds ranging from 2.0 to 5.0 mm day^{-1}. Results are summarized in Table 3.1 Across this range, the number of retained events decreased gradually with increasing threshold, but without abrupt changes in sample size. The difference in AIC between competing models remained small ($\Delta AIC < 2$), indicating that multiple formulations provide comparable support. Results show that model selection is stable across thresholds, with frozen soil effects are consistently supported across model structures. Full AIC rankings for all tested model formulations and thresholds are provided in the Supplementary Material (Table S1).

Table 3.1. Sensitivity of event-based runoff modeling results to the liquid water input threshold. For each threshold, the number of valid modeling events, the best-supported model, and the second-best model based on AIC are reported. ΔAIC represents the difference between the best and second-best models.

THRESHOLD (MM DAY^{-1})	FINAL MODEL EVENTS	BEST MODEL	AIC (BEST)	SECOND-BEST MODEL	AIC (SECOND)	ΔAIC
2.0	77	A3	197.78	A4	199.75	1.97
2.5	75	A3	191.36	B3	192.20	0.84
3.0	73	B3	184.30	A3	184.46	0.16
3.5	69	B3	177.37	A3	178.13	0.76
4.0	67	B3	184.15	A3	185.80	1.65
4.5	64	B3	183.50	B1	185.16	1.66
5.0	61	A3	174.48	B3	175.10	0.62

3.3.3.2. Seasonal Distribution of Hydrological Events

The multi-year record of water-input events defined using the 3.5 mm day^{-1} liquid water threshold shows a strong seasonal concentration, with pronounced interannual variability in both event frequency and magnitude (Figure 3.5a). Most events occurred during the fall and spring transition periods, when rainfall and snowmelt inputs are more frequent, and soils undergo active FT transitions. In contrast, mid-winter months, particularly January and February, exhibited markedly fewer or no threshold exceedances, reflecting precipitation storage as snow under persistently frozen conditions. The temporal distribution of water input varied substantially between years, with hydrological years such as 2017–2018 and 2018–2019 showing relatively elevated winter rainfall and snowmelt inputs associated with mid-winter melt or rain-on-snow episodes. Conversely, 2020–2021 (Figure 3.5b) and 2024–2025 were characterized by extended periods of minimal rainfall and snowmelt, indicative of prolonged frozen conditions and suppressed runoff generation during the coldest months.

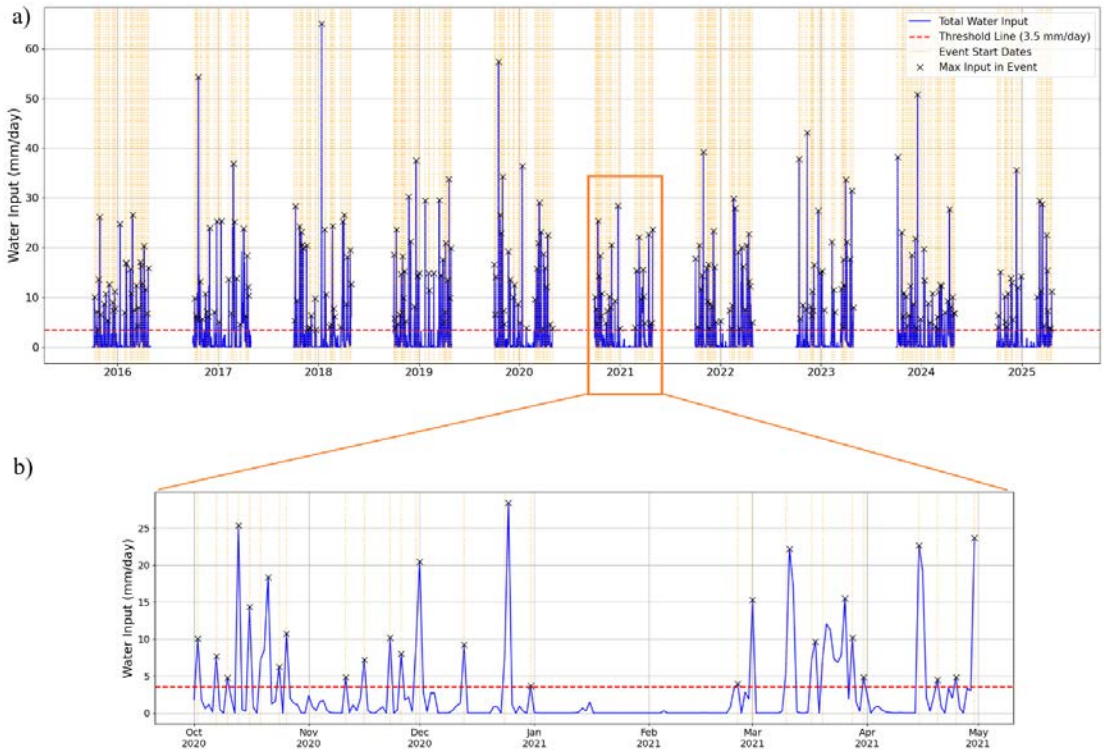

Figure 3.5. Event detection based on the 3.5 mm day^{-1} liquid water input threshold across the study period (2015–2025). (**a**) multi-year overview of *I* during the cold season, showing the temporal distribution of detected hydrological events. Vertical stippled lines indicate event start dates defined by threshold exceedance. (**b**) Enlarged view of the 2020–2021 hydrological year, illustrating how the threshold isolates discrete rainfall and snowmelt-driven input episodes.

Several events were short and isolated, represented by dashed yellow lines in Figure 3.5a, where only one hydrological pulse exceeded the threshold, while others were multi-day events with consecutive exceedances. The highest-intensity events (e.g., > 20 mm day^{-1}) occurred throughout multiple years, mostly during thawed conditions and transitional periods marking the onset of freezing in late fall and the onset of melting in early spring. A few high-intensity events were also detected during frozen periods, particularly near the shoulders of the frozen season, indicating that substantial rainfall or melt episodes can still occur even when the watershed is predominantly frozen.

3.3.3.3. Event-Based Runoff Response in Partially Frozen Agricultural Soils

Figure 3.6 shows the event-scale relationship between frozen soil extent and event-integrated runoff response for 58 cold-season hydrological events identified between 2015 and 2025. Runoff response is expressed using the event-averaged runoff coefficient $\overline{RC}_{event}$ and is shown as a function of (a) the mean F during each event and (b) the maximum F (F_{max}) observed during each event.

Across both representations, $\overline{RC}_{event}$ spans a wide range of values under both weakly frozen and predominantly frozen conditions. Ordinary least squares (OLS) regression indicates weak positive slopes for both mean F and F_{max}, with low coefficients of determination ($R^2 = 0.04$ in both cases) and non-significant p-values ($p = 0.124$ and $p = 0.120$, respectively). These results indicate that frozen soil extent alone explains only a small fraction of the variability in event-scale runoff response.

Considerable dispersion in RC_{event}^{avg} is observed at similar levels of frozen soil extent, with events characterized by comparable mean or maximum F producing markedly different runoff efficiencies. This behavior indicates that event-scale runoff generation cannot be described by frozen soil extent alone and that additional hydrometeorological controls, particularly antecedent wetness and event-scale input magnitude, play a dominant role in modulating runoff response during cold-season events. Consistent with this interpretation, daily-scale analyses (Supplementary Figure S3.3) also reveal weak but statistically significant relationships between frozen soil extent and lagged runoff response, reinforcing that FT conditions primarily act as a modulating background state rather than a sole predictor of runoff response.

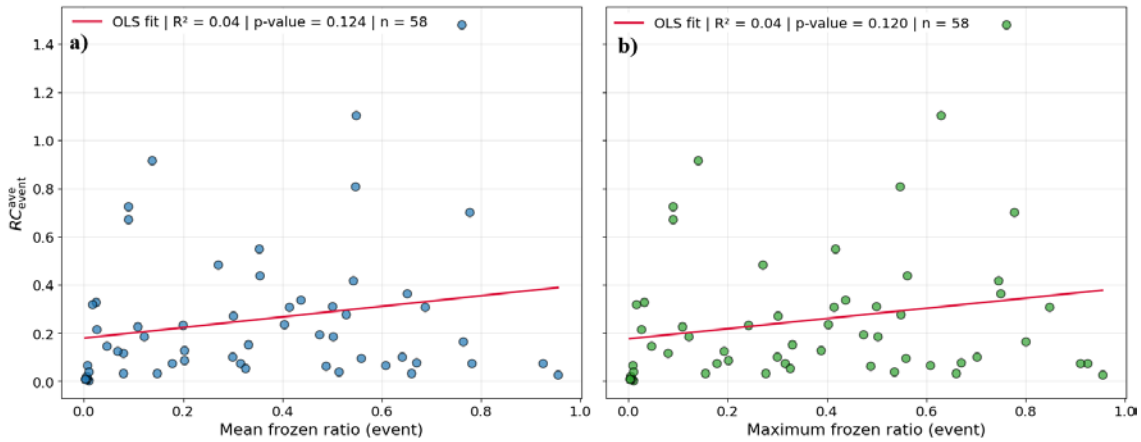

Figure 3.6. Event-scale relationship between frozen soil extent and event-averaged runoff coefficient ($\overline{RC}_{event}$)for cold-season hydrological events (n = 58) in the Acadie River catchment. (**a**) $\overline{RC}_{event}$ as a function of the mean *F* during each event. (**b**) $\overline{RC}_{event}$ as a function of the *F* observed during each event. Each point represents one threshold-defined hydrological event. The solid red lines show OLS regression fits, with corresponding R^2 and p-values indicated in the legend.

3.3.4. Event-scale runoff modeling under frozen soil conditions

Event-scale stormflow was modeled using Gamma GLMs under two complementary formulations. In A-type models, liquid water input was estimated as a free coefficient with frozen soil extent and antecedent wetness entering through interaction terms with *log(I)*. In B-type models, liquid water input was fixed as an offset, such that frozen soil extent and antecedent wetness acted as direct predictors of runoff efficiency. Candidate models were compared at the reference threshold of 3.5 mm day^{-1} using AIC, with model selection stability across thresholds supporting the consistency of the framework (Table 3.1).

Among A-type models (Table 3.2), A_3 provided the lowest AIC (177.72), with a positive interaction between liquid water input and frozen soil extent *(log(I)·F*: 0.363 ± 0.209; p = 0.089), indicating that frozen conditions amplify stormflow sensitivity to liquid water input. The input-only model A_1 (ΔAIC = 0.23) was nearly equivalent in support, confirming liquid water input as the dominant control. Models incorporating API interaction terms yielded higher AIC values with negligible and non-significant

coefficients throughout (e.g., A_2: −0.000 ± 0.005; p = 0.991), and more complex formulations such as A_4 and A_5 provided only marginal gains in explanatory power at increasing parsimony cost. Among B-type models (Table 3.3), the offset baseline B_1 provided the lowest AIC (176.75). The frozen soil model B_3 (ΔAIC = 0.06) gained explanatory power at negligible parsimony cost, while models adding antecedent wetness yielded progressively higher AIC values with non-significant API coefficients (e.g., B_2: 0.005 ± 0.014; p = 0.718; B_4: 0.017 ± 0.015; p = 0.262), confirming that antecedent wetness does not meaningfully predict runoff efficiency under the studied conditions. Across both model families, frozen soil coefficients were consistently positive (0.363 ± 0.209 in A_3; 0.844 ± 0.529 in B_3; 1.131 ± 0.579 in B_4), with p-values between 0.057 and 0.118, suggesting a physically meaningful tendency for frozen conditions to enhance runoff efficiency even if effects do not reach conventional significance thresholds at the available sample size.

Table 3.2. Gamma GLM comparison for event-scale stormflow using estimated input effects (A-models), fitted at the 3.5 mm day^{-1} liquid water input threshold. Models are ranked by Akaike Information Criterion (AIC); ΔAIC is computed relative to the best-supported A-model (A_3). Pseudo-R^2 is deviance-based. Coefficients are reported as estimates ± standard errors (SE). p denotes the two-sided Wald test p-value under the null hypothesis that the coefficient equals zero. Dashes indicate terms not included in the model.

Model	AIC	Pseudo -R^2	log(I) coef ± SE	p(I)	log(I)·F coef ± SE	p(I·F)	log(I)·API coef ± SE	p(I·API)	log(I)·API·F coef ± SE	p(I·API·F)
A3	177.72	0.197	1.348 ± 0.335	< 0.001	0.363 ± 0.209	0.089	—	—	—	—
A1	177.95	0.166	1.339 ± 0.335	< 0.001	—	—	—	—	—	—
A4	179.21	0.204	1.240 ± 0.381	0.002	0.438 ± 0.233	0.067	0.004 ± 0.006	0.454	—	—
A2	179.95	0.166	1.340 ± 0.367	< 0.001	—	—	−0.000 ± 0.005	0.991	—	—
A5	180.84	0.209	1.311 ± 0.391	0.002	0.427 ± 0.233	0.074	0.001 ± 0.007	0.832	0.016 ± 0.021	0.467

Table 3.3. Gamma GLM comparison for event-scale stormflow using a fixed input offset (B-models), fitted at the 3.5 mm day^{-1} liquid water input threshold. Models are ranked by Akaike Information Criterion (AIC); ΔAIC is computed relative to the best-supported B-model (B_1). Coefficients are reported as estimates ± standard errors (SE). p denotes the two-sided Wald test p-value under the null hypothesis that the coefficient equals zero. Dashes indicate terms not included in the model.

Model	AIC	Pseudo-R^2	F coef ± SE	p(F)	API coef ± SE	p(API)	API·F coef ± SE	p(API·F)
B1	176.75	0.000	—	—	—	—	—	—
B3	176.81	0.032	0.844 ± 0.529	0.118	—	—	—	—
B4	177.67	0.051	1.131 ± 0.579	0.057	0.017 ± 0.015	0.262	—	—
B2	178.64	0.002	—	—	0.005 ± 0.014	0.718	—	—
B5	179.55	0.053	1.113 ± 0.582	0.062	0.012 ± 0.019	0.506	0.024 ± 0.056	0.676

The A_3 model was selected for visualization because it directly represents the interaction between liquid water input and frozen soil extent. Predicted relationships (Figure 3.7) indicate a steeper input–runoff response under higher frozen soil conditions, consistent with reduced infiltration capacity, although wide confidence intervals reflect uncertainty in the magnitude of this effect.

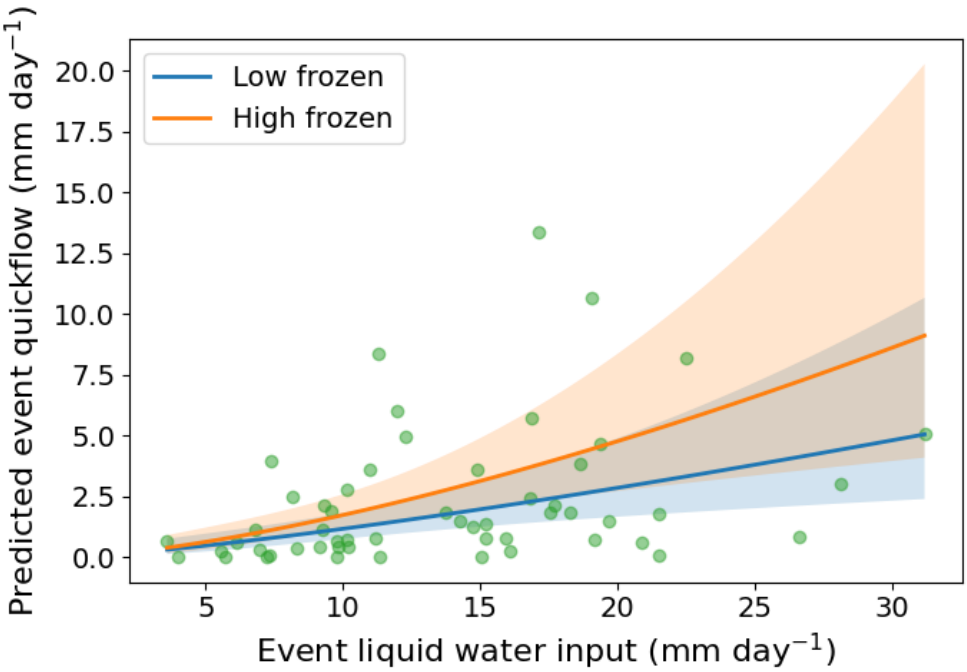

Figure 3.7. Predicted event quickflow (stormflow) as a function of event liquid water input using the A_3 interaction-based model. Curves represent low and high frozen soil conditions, defined by the 25th and 75th percentiles of maximum *F* during events. Shaded bands indicate 95% confidence intervals.

Residual diagnostics were used to evaluate the adequacy of the selected A_3 Gamma GLM before interpreting the predicted runoff response. The residuals-versus-fitted plot shows that deviance residuals are generally scattered around zero without a strong systematic pattern, although some dispersion is present at lower fitted values (Figure S3.4a). The normal Q–Q plot indicates reasonable agreement with theoretical quantiles, with minor departures in the tails (Figure S3.4b). The histogram shows a slightly asymmetric residual distribution, which is acceptable given the Gamma error structure

(Figure S3.4c). The scale–location plot does not indicate strong heteroscedasticity, although residual spread is somewhat greater at low fitted values (Figure S3.4d).

To evaluate whether the fixed-effect relationships identified in the GLM framework remain consistent after accounting for month-to-month variability in cold-season hydrological conditions, models were refitted using a GLMM framework including a random intercept for month (Table S3.2). The inclusion of a random effect did not improve model performance, as reflected by higher AIC values compared to GLM counterparts. Although conditional R^2 values increased (e.g., 0.557 for A_1), this primarily reflects variance captured by temporal grouping rather than improved predictive skill. Frozen soil effects became less stable in the GLMM framework-for example, the interaction coefficient in A_3 decreased to 0.097 ± 0.335 ($p = 0.771$) compared with 0.363 ± 0.209 ($p = 0.089$) in the GLM-suggesting that the limited number of events and their uneven temporal distribution constrain reliable estimation of month-to-month variability. Several GLMM formulations also exhibited singular fits or convergence warnings, further indicating that the random month structure is not well supported at the available sample size.

3.4. Discussion

3.4.1. Hydrological Response Divergence Under FT Soil Conditions

The observed divergence between frozen and thawed runoff coefficients (Figure 3.2) emphasizes the role of soil FT state in controlling modulating water transmission within the Acadie agricultural catchment. During frozen conditions, reduced infiltration and permeability promote overland flow and accelerate the hydrological response, consistent with previous findings that frozen soil layers limit vertical infiltration, leading to higher runoff ratios in cold basins (Wu et al, 2025). The pronounced peak at a one--day lag across all seasons (Figure 3.3), with correlation coefficients reaching approximately $r \approx 0.64$ in winter and $r \approx 0.60–0.61$ in fall and spring, indicates that runoff response in the Acadie River catchment is not instantaneous but instead exhibits a short, systematic delay between liquid water input and streamflow. Numerical and process-based studies further show that FT history, snow insulation, and soil structure can shift the balance between

rapid surface runoff and delayed subsurface contributions, often with lags of weeks to months in discharge response (Gao et al, 2023; Zheng et al, 2018). In the Acadie catchment, these lags are likely amplified by agricultural drainage systems, which can rapidly transmit water to channels once connectivity is re-established during thaw periods.

The stronger one-day correlation observed during winter suggests a tighter coupling between liquid water inputs and discharge when soils are predominantly frozen. Under such conditions, ice formation in soil pores reduces hydraulic conductivity, limits vertical infiltration, and promotes lateral flow at or near the surface, enhancing the efficiency with which rainfall and snowmelt are converted to runoff, although this effect remains dependent on short time scales input magnitude and antecedent conditions (Jiang et al, 2024; Jiang et al, 2021). This behaviour is consistent with experimental and modeling studies showing that FT-induced reductions in infiltration and macropore blockage increase event-scale runoff production in frozen soils (Mohammed et al, 2021b).

In contrast, the lower peak correlations during fall and spring reflect more heterogeneous FT conditions, when partial thawing allows greater infiltration and transient storage within the soil profile. During these transitional periods, runoff generation involves a mixture of surface flow, shallow subsurface flow, and variable soil permeability, which weakens the short-term correspondence between input and discharge (Sanchez-Rodriguez et al, 2025; Zheng et al, 2018). Field and modeling studies in seasonally frozen catchments similarly report that patchy frost, evolving active-layer storage, and preferential flow can introduce short delays and reduce event-scale input–runoff coherence compared with fully frozen conditions (Ala-Aho et al, 2021). The rapid decay of correlations beyond lag 2 days across all seasons further indicates that the hydrological influence of individual rainfall or snowmelt events is short-lived in this small agricultural catchment, and that cold-season runoff response is governed primarily by short-term, FT-controlled processes rather than long antecedent memory (Rey et al, 2021; Tarasova et al, 2018).

The progressive increase in short-term streamflow response with rising I_{liq} (Figure 3.4) suggests a threshold-like behavior in runoff generation under seasonally frozen conditions, with a more pronounced increase in ΔQ beyond ~3 mm day^{-1}. Rather than exhibiting an abrupt hydrological threshold, the system transitions gradually as input magnitude increases, suggesting a progressive activation of runoff generation mechanisms. Inputs below approximately 3 mm day^{-1} are largely absorbed or temporarily stored within the snowpack, surface depressions, or partially thawed soil layers, whereas higher inputs increasingly exceed near-surface storage and infiltration capacity, promoting surface and near-surface lateral flow. The transition range identified between 3- and 4-mm day^{-1} corresponds to a regime in which runoff response becomes more efficient with increasing liquid water input, suggesting a shift in hydrological behavior without indicating a distinct threshold. Column experiments show that frozen soil below about −0.5 °C is practically impermeable, and that a temperature increase from −0.5 to −0.2 °C can increase hydraulic conductivity by more than four orders of magnitude, illustrating how thin frozen layers can sharply restrict vertical flux while deeper zones remain relatively conductive (Watanabe & Osada, 2017). This progressive activation of runoff generation with increasing input magnitude provides a physical basis for the modeling results (Table 3.2), where liquid water input emerges as the dominant control on event-scale runoff, while frozen soil modulates the runoff response under varying conditions.

The sensitivity analysis of the event definition threshold further supports the robustness of the modeling framework (Table 3.1). Across thresholds ranging from 2.0 to 5.0 mm day^{-1}, the best-supported formulations alternate between two conceptual representations of runoff generation. One formulation treats liquid water input as a baseline forcing and models how frozen soil conditions influence the efficiency with which this input is converted into runoff (e.g., B_2). The other formulation explicitly represents the modulation of runoff response by allowing the sensitivity of runoff to input to vary with frozen soil conditions (e.g., A_3). The small differences in AIC between competing formulations ($\Delta AIC < 2$) indicate that both representations provide comparable support across thresholds. This consistency suggests that runoff generation is primarily governed by input magnitude, while frozen soil conditions influence how this input is

translated into streamflow response. The consistent inclusion of frozen soil effects across top-ranked formulations indicates that their influence on runoff response is robust to the choice of event definition threshold.

The temporal organization of events revealed by the event-based analysis (Figure 3.5) highlights the importance of short-duration, high-intensity forcing in cold-season runoff generation. The prevalence of brief events, combined with the occurrence of larger inputs during transitional periods, suggests that runoff response is more sensitive to input intensity than to event duration. This interpretation is supported by the joint distribution of event duration and mean input intensity (Supplementary Figure S3.1), which shows that higher mean liquid water inputs are generally associated with shorter events (one to three days), whereas longer events tend to display lower average intensities. Such patterns are consistent with rainfall-on-snow events, mid-winter melt episodes, and early spring thaws, where rapid energy inputs or warm precipitation generate short-lived but strongly activating forcing for runoff (Tarasova et al, 2020; Tarasova et al, 2018). Longer-duration events, by contrast, likely reflect extended periods of moderate melt or intermittent precipitation, during which partial infiltration, refreezing, or redistribution processes dampen the immediate streamflow response (Mohammed et al, 2021a; Mohammed et al, 2019).

3.4.2. Frozen Soil Effects on Runoff Response in Event- and Daily-Scale Analyses

The weak and statistically non-significant linear relationships observed between frozen soil extent and runoff response indicate that frozen soil conditions alone do not exert a dominant, directly proportional control on runoff behavior, whether evaluated using the lag-1 daily RC or the event-averaged runoff coefficient. Although near-surface freezing imposes a physical constraint on infiltration, its influence on catchment-scale runoff generation does not translate into a simple linear increase in runoff response with increasing frozen extent at either temporal scale. Instead, the large dispersion in runoff response under similar frozen soil conditions suggests that freezing primarily acts as a modulating background state, whose hydrological impact depends on the concurrent magnitude of liquid water inputs and antecedent catchment wetness (Ala-Aho et al, 2021).

The weak relationships observed between frozen soil extent and runoff response are consistent across both daily lag-1 analyses (Figure 3.3) and event-based metrics (Figure 3.6). This indicates that the limited explanatory power of frozen soil is not related to the choice of temporal aggregation, but rather reflects the fact that runoff response is primarily controlled by liquid water input and varies with event conditions (Niu & Yang, 2006). Events occurring under comparable frozen conditions can therefore produce markedly different runoff responses depending on pre-event storage, rainfall or snowmelt intensity, and the degree of partial thaw development (Lin et al, 2022; Zheng et al, 2018). For example, previous studies have shown that runoff coefficients and stormflow often increase abruptly once a critical combination of soil freezing (or catchment wetness) and water input is exceeded, rather than responding proportionally to incremental changes in a single predictor, resulting in threshold-like or piecewise behavior between state and runoff response (Scaife et al, 2020; Stuurop et al, 2022). Consequently, these results underscore the limitations of linear soil-freezing metrics when considered independently of event-scale liquid water inputs and antecedent catchment conditions governing runoff response.

3.4.3. Runoff Event-Scale Runoff Response Under Frozen Soil Conditions

The event-scale analysis shows that runoff response in the Acadie catchment is primarily governed by the magnitude of liquid water input, with a consistent and strong scaling relationship observed across all model formulations (Table 3.2 and 3.3). This dominant role of input is further supported by the threshold analysis (Table 3.1), which demonstrates stable model selection across a wide range of event definitions (2.0–5.0 mm day^{-1}). The progressive increase in streamflow response with increasing input (Figure 3.4) indicates a gradual activation of runoff generation mechanisms rather than a sharp threshold behavior, reflecting the combined influence of storage filling and infiltration limitations under partially frozen conditions.

Frozen soil conditions influence how runoff response develops rather than acting as a standalone predictor of runoff magnitude. Across model formulations, the estimated frozen soil effects are consistently positive (e.g., 0.844 ± 0.529 in B3 and 0.363 ± 0.209

in A_3; Table 3.2), but not statistically significant, indicating that their contribution is present but uncertain. This behavior is clearly illustrated in Figure 3.7, where higher frozen soil conditions produce a steeper input-runoff relationship, suggesting reduced infiltration capacity and enhanced lateral flow under frozen conditions. However, the wide confidence intervals indicate that this effect varies substantially between events, reflecting the heterogeneity of soil freezing conditions and hydrological connectivity.

In contrast, antecedent wetness (API) shows minimal influence on runoff response across all models, with small and non-significant coefficients (Table 3.2 and 3.3). This suggests that, under the studied conditions, short-term hydrological response is more directly controlled by instantaneous water availability and near-surface soil conditions than by antecedent storage. Overall, the results indicate that runoff generation in this agricultural catchment emerges from the interaction between input magnitude and transient surface conditions, with frozen soil affecting how efficiently water is converted into runoff rather than determining runoff magnitude alone.

Although this research provides new insight into the role of near-surface soil FT states in cold-season runoff generation, several limitations should be acknowledged. Liquid water input was estimated as the sum of rainfall and modeled snowmelt from ERA5-Land, which captures the timing of surface water availability but does not explicitly represent internal snowpack processes such as refreezing, liquid water retention, or spatial heterogeneity in snowpack properties (Muñoz-Sabater et al, 2021). In addition, FT conditions were inferred from near-surface observations, without explicit representation of vertical freezing structure, which may influence infiltration capacity, groundwater–soil water exchanges, and subsurface connectivity (Sanchez-Rodriguez et al, 2025). Together, these limitations highlight the need for future studies integrating improved snowpack representation and subsurface FT characterization to better resolve how these factors interact with liquid water input in controlling runoff response.

Overall, the Acadie results indicate that, in humid, seasonally frozen agricultural catchments, frozen ground primarily influences how event water input is translated into

runoff response, rather than producing a simple monotonic relationship between frozen soil extent and runoff magnitude.

3.5. Conclusion

This study examined the role of near-surface soil freezing states in controlling event-scale runoff response in the Acadie agricultural catchment using satellite-derived indicators and statistical modeling. The results show that liquid water input is the dominant control on event-scale runoff, with a consistent and statistically significant relationship observed across all model formulations. Frozen soil conditions were consistently included in well-supported models and exhibited positive coefficients across all formulations, indicating a systematic influence on runoff response. However, these effects were not statistically significant and varied across model structures, suggesting that the magnitude of this influence remains uncertain. The effect of frozen soil is expressed through the modulation of runoff response, as illustrated by steeper input–runoff relationships under higher frozen conditions, which is consistent with reduced near-surface infiltration capacity.

3.6. Statements

Author Contributions: Conceptualization, C.K., A.R., S.T.; methodology, C.K., A.R., and S.T.; formal analysis, S.T., C.K., and A.R.; data curation, S.T.; writing-original draft preparation, S.T.; writing-review and editing, C.K. and A.R.; supervision, C.K. and A.R.; project administration, C.K. and A.R.; funding acquisition, C.K. and A.R. All authors have read and agreed to the published version of the manuscript.

Funding: This study was financially supported by Fonds de Recherche du Québec Nature et Technologies (FRQNT) under the Merit scholarship program for foreign students (PBEEE) program for doctoral research scholarships (File number: 275403; DOI: https://doi.org/10.69777/275403), Canadian Space Agency FAST (19FAQCTB19), and the FRQNT Team Research Project grant 2022-PR-299776 (C. Kinnard).

Data Availability Statement: The Python-based processing pipeline developed for the web-based FT detection tool is openly available on GitHub at https://github.com/Shahab-J/Freeze-Thaw-Detection, and the operational web interface can be accessed at https://freeze-thaw-detection-kmpqcuusaqtf5ypu5h3vyg.streamlit.app/. Additional event-based runoff and processed hydrological data used in this study are available from the corresponding author upon reasonable request.

Acknowledgments: We would like to express our sincere gratitude to the Centre d'expertise hydrique du Québec (CEHQ) for providing access to hydrometric data used in this study.

Generative AI Statement: The authors declare that generative artificial intelligence (OpenAI's GPT-4) was used to assist in the grammatical correction of text and in generating alternative phrasing for certain sentences within this manuscript.

Conflicts of Interest: The authors declare that the research was conducted in the absence of any commercial or financial relationships that could be construed as a potential conflict of interest.

3.7. References

Ala-Aho, P., Autio, A., Bhattacharjee, J., Isokangas, E., Kujala, K., Marttila, H., Menberu, M., Meriö, L., Postila, H. & Rauhala, A. (2021) What conditions favor the influence of seasonally frozen ground on hydrological partitioning? A systematic review. Environmental Research Letters, 16(4), 043008. doi:10.1088/1748-9326/abe82c

Ali, S., Ghosh, N. & Singh, R. (2010) Rainfall–runoff simulation using a normalized antecedent precipitation index. Hydrological Sciences Journal–Journal des Sciences Hydrologiques, 55(2), 266-274. doi:10.1080/02626660903546175

Appels, W. M., Bogaart, P. W. & van der Zee, S. E. (2016) Surface runoff in flat terrain: How field topography and runoff generating processes control hydrological connectivity. Journal of Hydrology, 534, 493-504. doi:10.1016/j.jhydrol.2016.01.021

Aygün, O., Kinnard, C., Campeau, S. & Krogh, S. A. (2020) Shifting hydrological processes in a Canadian agroforested catchment due to a warmer and wetter climate. Water, 12(3), 739. doi:doi.org/10.3390/w12030739

Baghdadi, N., Bazzi, H., El Hajj, M. & Zribi, M. (2018) Detection of frozen soil using Sentinel-1 SAR data. Remote Sens., 10(8), 1182. doi:10.3390/rs10081182

Baghdadi, N., Cresson, R., Hajj, M. E., Ludwig, R. & Jeunesse, I. L. (2012) Estimation of soil parameters over bare agriculture areas from C-band polarimetric SAR data using neural networks. Hydrology Earth System Sciences, 16(6), 1607-1621. doi:10.5194/hess-16-1607-2012

Baghdadi, N., King, C., Bourguignon, A. & Remond, A. (2002) Potential of ERS and Radarsat data for surface roughness monitoring over bare agricultural fields: application to catchments in Northern France. International journal of remote sensing

23(17), 3427-3442. doi:10.1080/01431160110110974

Beck, H. E., Zimmermann, N. E., McVicar, T. R., Vergopolan, N., Berg, A. & Wood, E. F. J. S. d. (2018) Present and future Köppen-Geiger climate classification maps at 1-km resolution, 5(1), 1-12. doi:10.1038/sdata.2018.214

Bronstert, A., Niehoff, D. & Schiffler, G. R. (2023) Modelling infiltration and infiltration excess: The importance of fast and local processes. Hydrological Processes, 37(4), e14875. doi:10.1002/hyp.14875

Burt, T. & Williams, P. J. J. E. S. P. (1976) Hydraulic conductivity in frozen soils, 1(4), 349-360. doi:10.1002/esp.3290010404

Cao, B., Gruber, S. & Zhang, T. J. G. M. D. (2017) REDCAPP (v1. 0): Parameterizing valley inversions in air temperature data downscaled from reanalyses, 10(8), 2905-2923. doi:10.5194/gmd-10-2905-2017

Chen, L., Chen, Z., Jia, G., Zhou, J., Zhao, J. & Zhang, Z. J. S. o. t. T. E. (2020) Influences of forest cover on soil freeze-thaw dynamics and greenhouse gas emissions through the regulation of snow regimes: A comparison study of the farmland and forest plantation, 726, 138403. doi:10.1016/j.scitotenv.2020.138403

Chen, Y., Li, S., Wang, L., Mittermeier, M., Bernier, M. & Ludwig, R. (2024) Retrieving freeze-thaw states using deep learning with remote sensing data in permafrost landscapes. Int. J. Appl. Earth Obs. Geoinf., 126, 103616. doi:10.1016/j.jag.2023.103616

Chow, V. (1971) Applied hydrologyMcGraw-hill.

Coles, A. & McDonnell, J. (2018) Fill and spill drives runoff connectivity over frozen ground. Journal of Hydrology, 558, 115-128. doi:10.1016/j.jhydrol.2018.01.016

Collins, M. J. J. H. P. (2019) River flood seasonality in the Northeast United States: Characterization and trends, 33(5), 687-698. doi:10.1002/hyp.13355

Commission for Environmental Cooperation (CEC) (2021) North American Land Cover, 2020 (Landsat, 30m), 2021. Available online: https://www.cec.org/north-american-environmental-atlas/land-cover-30m-2020/ [Accessed.

DeGuzman, K., Knappenberger, T., Brantley, E. & Olshansky, Y. J. H. P. (2023) Estimating runoff probability from precipitation data: A binomial regression analysis, 37(11), e15029. doi:10.1002/hyp.15029

Ding, B., Zhang, Y., Yu, X., Jia, G., Wang, Y., Zheng, P. & Li, Z. (2023) Comparative study of seasonal freeze–thaw on soil water transport in farmland and its shelterbelt. Catena, 225, 106982. doi:10.1016/j.catena.2023.106982

Fang, X. & Pomeroy, J. W. (2016) Impact of antecedent conditions on simulations of a flood in a mountain headwater basin. Hydrological Processes, 30(16), 2754-2772. doi:10.1002/hyp.10910

Favaro, E. A. & Lamoureux, S. F. J. G. A. S. A., Physical Geography (2014) Antecedent controls on rainfall runoff response and sediment transport in a High Arctic catchment, 96(4), 433-446. doi:10.1111/geoa.12063

Fayad, I., Baghdadi, N., Bazzi, H. & Zribi, M. (2020) Near real-time freeze detection over agricultural plots using Sentinel-1 data. Remote Sens., 12(12), 1976. doi:10.3390/rs12121976

Gao, H., Zhang, W. & Chen, H. (2018) An improved algorithm for discriminating soil freezing and thawing using AMSR-E and AMSR2 soil moisture products. Remote Sensing, 10(11), 1697. doi:10.3390/rs10111697

Gao, H., Zhang, Z., Chen, H., Zhang, W., Xu, C., Yi, Y., Liu, J. & Xiao, Z. (2023) Impacts of seasonally frozen soil hydrothermal dynamics on the watershed hydrological processes inferred from a spatially distributed numerical modelling approach. Journal of Hydrology, 624, 129947. doi:10.1016/j.jhydrol.2023.129947

Gao, H., Zhang, Z., Zhang, W., Chen, H. & Xi, M. (2021) Spatial Downscaling Based on Spectrum Analysis for Soil Freeze/Thaw Status Retrieved From Passive Microwave. IEEE Transactions on Geoscience Remote Sensing. doi:10.1109/TGRS.2021.3051683

Gray, D., Toth, B., Zhao, L., Pomeroy, J. & Granger, R. J. H. P. (2001) Estimating areal snowmelt infiltration into frozen soils, 15(16), 3095-3111. doi:10.1002/hyp.320

Guo, L.-m., Chang, J., Xu, H.-l. & Sun, W.-j. J. J. o. M. S. (2021) Modelling plant canopy effects on water-heat exchange in the freezing-thawing processes of active layer on the Qinghai-Tibet Plateau, 18(6), 1564-1579. doi:10.1007/s11629-020-6335-5

Hedges, L. V. & Olkin, I. (2014) Statistical methods for meta-analysisAcademic press.

Ireson, A., Van Der Kamp, G., Ferguson, G., Nachshon, U. & Wheater, H. J. H. J. (2013) Hydrogeological processes in seasonally frozen northern latitudes: understanding, gaps and challenges, 21(1), 53-66. doi:10.1007/s10040-012-0916-5

Jiang, H., Yi, Y., Yang, K., Zhao, L., Chen, D., Kimball, J. S. & Lu, F. (2024) Soil freeze/thaw dynamics strongly influences runoff regime in a Tibetan permafrost watershed: Insights from a process-based model. Catena, 243, 108182. doi:10.1016/j.catena.2024.108182

Jiang, R., Li, T., Liu, D., Fu, Q., Hou, R., Li, Q., Cui, S. & Li, M. (2021) Soil infiltration characteristics and pore distribution under freezing–thawing conditions. The Cryosphere, 15(4), 2133-2146. doi:10.1002/essoar.10504385.1

Katz, L., Lewis, G., Krogh, S., Drake, S., Hanan, E., Hatchett, B. & Harpold, A. (2023) Antecedent snowpack cold content alters the hydrologic response to extreme rain-on-snow events. Journal of Hydrometeorology, 24(10), 1825-1846. doi:10.1175/JHM-D-22-0090.1

Khaldoune, J., Van Bochove, E., Bernier, M. & Nolin, M. C. (2011) Mapping agricultural frozen soil on the watershed scale using remote sensing data. Applied Environmental Soil Science, 2011(1), 193237. doi:10.1155/2011/193237

Kim, Y., Kimball, J. S., Glassy, J. & Du, J. (2017) An extended global Earth system data record on daily landscape freeze–thaw status determined from satellite passive microwave remote sensing. Earth System Science Data, 9(1), 133-147. doi:10.5194/essd-9-133-2017

Kim, Y., Kimball, J. S., McDonald, K. C., Glassy, J. J. I. T. o. G. & Sensing, R. (2010) Developing a global data record of daily landscape freeze/thaw status using satellite passive microwave remote sensing, 49(3), 949-960. doi:10.1109/TGRS.2010.2070515

Kim, Y., Kimball, J. S., Xu, X., Dunbar, R. S., Colliander, A. & Derksen, C. (2019) Global assessment of the SMAP freeze/thaw data record and regional applications for detecting spring onset and frost events. Remote Sensing, 11(11), 1317. doi:10.3390/rs11111317

Kimball, J. S., McDonald, K. & Zhao, M. J. E. I. (2006) Spring thaw and its effect on terrestrial vegetation productivity in the western Arctic observed from satellite microwave and optical remote sensing, 10(21), 1-22. doi:10.1175/EI187.1

Kloffel, T., Larsbo, M., Jarvis, N. & Barron, J. (2024) Freeze-thaw effects on pore space and hydraulic properties of compacted soil and potential consequences with climate change. Soil Tillage Research, 239. doi:10.1016/j.still.2024.106041

Kompanizare, M., Costa, D., Macrae, M. L., Pomeroy, J. W. & Petrone, R. M. (2024) Developing a tile drainage module for the Cold Regions Hydrological Model: lessons from a farm in southern Ontario, Canada. Hydrology Earth System Sciences, 28(13), 2785-2807. doi:10.5194/hess-28-2785-2024

KOVAčIč, G. J. A. c. (2010) Hydrogeological study of the Malenščica karst spring (SW Slovenia) by means of a time series analysis, 39(2).

Lane, R. A., Bell, V. A., Chapman, R. M. & Kay, A. L. (2024) Evaluating soil moisture simulations from a national-scale gridded hydrological model over Great Britain. Journal of Hydrology: Regional Studies, 52, 101735. doi:10.1016/j.ejrh.2024.101735

Lazoglou, G., Economou, T., Anagnostopoulou, C., Zittis, G., Tzyrkalli, A., Georgiades, P. & Lelieveld, J. J. G. M. D. (2024) Multivariate adjustment of drizzle bias using machine learning in European climate projections, 17(11), 4689-4703. doi:10.5194/gmd-17-4689-2024

Leuther, F. & Schlüter, S. (2021) Impact of freeze–thaw cycles on soil structure and soil hydraulic properties. Soil, 7(1), 179-191. doi:10.5194/soil-7-179-2021

Lévesque, V. P., Boucher, É. & Proulx, G. (2019) Spatial distribution of ice jamming processes in the l'acadie river watershed, montérégie: a hydrogeomorphological approach. doi:10.7202/10.7202/1059878ar

Li, H., Li, X., Yang, D., Wang, J., Gao, B., Pan, X., Zhang, Y. & Hao, X. J. J. o. G. R. A. (2019) Tracing snowmelt paths in an integrated hydrological model for understanding seasonal snowmelt contribution at basin scale, 124(16), 8874-8895. doi:10.1029/2019JD030760

Li, T., Chen, Y.-Z., Han, L.-J., Cheng, L.-H., Lv, Y.-H., Fu, B.-J., Feng, X.-M. & Wu, X. (2021a) Shortened duration and reduced area of frozen soil in the Northern Hemisphere. The Innovation, 2(3). doi:10.1016/j.xinn.2021.100146

Li, X., Wei, Y. & Li, F. J. J. o. H. (2021b) Optimality of antecedent precipitation index and its application, 595, 126027. doi:10.1016/j.jhydrol.2021.126027

Liang, J., Hu, Z., Liu, S., Zhong, G., Zhen, Y., Makhinov, A. N. & Araruna, J. T. (2022a) Residual-oriented optimization of antecedent precipitation index and its impact on flood prediction uncertainty. Water, 14(20), 3222. doi:10.3390/w14203222

Liang, J., Hu, Z., Liu, S., Zhong, G., Zhen, Y., Makhinov, A. N. & Araruna, J. T. J. W. (2022b) Residual-Oriented Optimization of Antecedent Precipitation Index and Its Impact on Flood Prediction Uncertainty, 14(20), 3222. doi:10.3390/w14203222

Lin, P., He, Z., Du, J., Chen, L., Zhu, X. & Tian, Q. (2022) Understanding the hydrological regime based on the runoff events in a mountainous catchment with seasonally frozen soil in the Qinghai-Tibet plateau. Hydrological Processes, 36(10), e14716. doi:10.1002/hyp.14716

Lindström, G., Bishop, K. & Löfvenius, M. O. (2002) Soil frost and runoff at Svartberget, northern Sweden—measurements and model analysis. Hydrological processes, 16(17), 3379-3392. doi:10.1002/hyp.1106

Lundberg, A., Gustafsson, D., Stumpp, C., Kløve, B. & Feiccabrino, J. (2016a) Spatiotemporal variations in snow and soil frost—a review of measurement techniques. Hydrology Earth System Sciences, 3(3), 28. doi:10.3390/hydrology3030028

Lundberg, A., Gustafsson, D., Stumpp, C., Kløve, B. & Feiccabrino, J. J. H. (2016b) Spatiotemporal variations in snow and soil frost—A review of measurement techniques, 3(3), 28. doi:10.3390/hydrology3030028

Miller, S. D., Straka III, W., Mills, S. P., Elvidge, C. D., Lee, T. F., Solbrig, J., Walther, A., Heidinger, A. K. & Weiss, S. C. J. R. S. (2013) Illuminating the capabilities of the suomi national polar-orbiting partnership (NPP) visible infrared imaging radiometer suite (VIIRS) day/night band, 5(12), 6717-6766. doi:10.3390/rs5126717

Mohammed, A. A., Cey, E. E., Hayashi, M. & Callaghan, M. V. (2021a) Simulating preferential flow and snowmelt partitioning in seasonally frozen hillslopes. Hydrological Processes, 35(8), e14277. doi:10.1002/hyp.14277

Mohammed, A. A., Cey, E. E., Hayashi, M., Callaghan, M. V., Park, Y. J., Miller, K. L. & Frey, S. K. (2021b) Dual-permeability modeling of preferential flow and snowmelt partitioning in frozen soils. Vadose Zone Journal, 20(2), e20101. doi:10.1002/vzj2.20101

Mohammed, A. A., Kurylyk, B. L., Cey, E. E. & Hayashi, M. (2018) Snowmelt infiltration and macropore flow in frozen soils: Overview, knowledge gaps, and a conceptual framework. Vadose Zone Journal, 17(1), 1-15. doi:10.2136/vzj2018.04.0084

Mohammed, A. A., Pavlovskii, I., Cey, E. E. & Hayashi, M. (2019) Effects of preferential flow on snowmelt partitioning and groundwater recharge in frozen soils. Hydrology Earth System Sciences, 23(12), 5017-5031. doi:10.5194/hess-23-5017-2019

Molotch, N. P., Brooks, P. D., Burns, S. P., Litvak, M., Monson, R. K., McConnell, J. R., Musselman, K. J. E. E., Land & Water Process Interactions, E. (2009) Ecohydrological controls on snowmelt partitioning in mixed-conifer sub-alpine forests, 2(2), 129-142. doi:10.1002/eco.48

Muñoz-Sabater, J., Dutra, E., Agustí-Panareda, A., Albergel, C., Arduini, G., Balsamo, G., Boussetta, S., Choulga, M., Harrigan, S. & Hersbach, H. (2021) ERA5-Land: A state-of-the-art global reanalysis dataset for land applications. Earth Syst. Sci. Data, 13(9), 4349-4383. doi:10.5194/essd-13-4349-2021

Niu, G.-Y. & Yang, Z.-L. (2006) Effects of frozen soil on snowmelt runoff and soil water storage at a continental scale. J. Hydrometeorol., 7(5), 937-952. doi:10.1175/JHM538.1

Odey, G. & Cho, Y. (2025) Event-based vs. continuous hydrological modeling with HEC-HMS: A review of use cases, methodologies, and performance metrics. Hydrology 12 (2), 39.

Podest, E., McDonald, K. C. & Kimball, J. S. (2014) Multisensor microwave sensitivity to freeze/thaw dynamics across a complex boreal landscape. IEEE Transactions on Geoscience Remote Sensing, 52(11), 6818-6828. doi:10.1109/TGRS.2014.2303635

Pomeroy, J., Brown, T., Fang, X., Shook, K. R., Pradhananga, D., Armstrong, R., Harder, P., Marsh, C., Costa, D. & Krogh, S. A. (2022) The cold regions hydrological modelling platform for hydrological diagnosis and prediction based on process understanding. Journal of Hydrology, 615, 128711. doi:10.1016/j.jhydrol.2022.128711

Qin, Y., Bai, Y., Chen, G., Liang, Y., Li, X., Wen, B., Lu, X. & Li, X. (2021) The effects of soil freeze–thaw processes on water and salt migrations in the western Songnen Plain, China. Scientific Reports, 11(1), 3888. doi:10.1038/s41598-021-83294-x

Rey, D. M., Hinckley, E. L. S., Walvoord, M. A. & Singha, K. (2021) Integrating observations and models to determine the effect of seasonally frozen ground on hydrologic partitioning in alpine hillslopes in the Colorado Rocky Mountains, USA. Hydrological Processes, 35(10), e14374. doi:10.1002/hyp.14374

Ross, C. A., Ali, G. A., Spence, C. & Courchesne, F. J. W. R. R. (2021) Evaluating the ubiquity of thresholds in rainfall-runoff response across contrasting environments, 57(1), e2020WR027498. doi:10.1029/2020WR027498

Rowlandson, T. L., Berg, A. A., Roy, A., Kim, E., Lara, R. P., Powers, J., Lewis, K., Houser, P., McDonald, K. & Toose, P. (2018) Capturing agricultural soil freeze/thaw state through remote sensing and ground observations: A soil freeze/thaw validation campaign. Remote sensing of environment, 211, 59-70. doi:10.1016/j.rse.2018.04.003

Roy, A., Toose, P., Derksen, C., Rowlandson, T., Berg, A., Lemmetyinen, J., Royer, A., Tetlock, E., Helgason, W. & Sonnentag, O. (2017) Spatial variability of L-band brightness temperature during freeze/thaw events over a prairie environment. Remote Sensing, 9(9), 894. doi:10.3390/rs9090894

Sanchez-Rodriguez, I., Ireson, A., Brannen, R. & Brauner, H. (2025) Insights into freeze–thaw and infiltration in seasonally frozen soils from field observations. Vadose Zone Journal, 24(1), e20396. doi:10.1002/vzj2.20396

Scaife, C. I., Singh, N. K., Emanuel, R. E., Miniat, C. F. & Band, L. E. (2020) Non-linear quickflow response as indicators of runoff generation mechanisms. Hydrological Processes, 34(13), 2949-2964. doi:10.1002/hyp.13780

Schoener, G. & Stone, M. C. (2019) Impact of antecedent soil moisture on runoff from a semiarid catchment. Journal of Hydrology, 569, 627-636. doi:10.1016/j.jhydrol.2018.12.025

Shanley, J. B. & Chalmers, A. (1999) The effect of frozen soil on snowmelt runoff at Sleepers River, Vermont. Hydrological Processes, 13(12-13), 1843-1857. doi:10.1002/(SICI)1099-1085(199909)13:12/13<1843::AID-HYP879>3.0.CO;2-G

Shao, W. & Zhang, T. (2020) Assessment of Four Near-Surface Soil Freeze/Thaw Detection Algorithms Based on Calibrated Passive Microwave Remote Sensing Data Over China. Earth and Space Science, 7(7), e2019EA000807. doi:10.1029/2019EA000807

Shrestha, S., Zaramella, M., Callegari, M., Greifeneder, F. & Borga, M. J. C. (2023) Scale dependence of errors in snow water equivalent simulations using ERA5 reanalysis over alpine basins, 11(7), 154. doi:10.3390/cli11070154

Song, S. & Wang, W. (2019) Impacts of antecedent soil moisture on the rainfall-runoff transformation process based on high-resolution observations in soil tank experiments. Water, 11(2), 296. doi:10.3390/w11020296

Stähli, M. (2017) Hydrological significance of soil frost for pre-alpine areas. Journal of Hydrology, 546, 90-102. doi:10.1016/j.jhydrol.2016.12.032

Starkloff, T., Stolte, J., Hessel, R., Ritsema, C. & Jetten, V. J. C. (2018) Integrated, spatial distributed modelling of surface runoff and soil erosion during winter and spring, 166, 147-157. doi:10.1016/j.catena.2018.04.001

Stuurop, J. C., van der Zee, S. E. & French, H. K. (2022) The influence of soil texture and environmental conditions on frozen soil infiltration: A numerical investigation. Cold regions science technolog, 194, 103456. doi:10.1016/j.coldregions.2021.103456

Taghipourjavi, S., Kinnard, C. & Roy, A. (2024) Sentinel-1-Based Soil Freeze–Thaw Detection in Agro-Forested Areas: A Case Study in Southern Québec, Canada. Remote Sens., 16(7), 1294. doi:10.3390/rs16071294

Taghipourjavi, S., Kinnard, C. & Roy, A. (2026a) On Demand Machine Learning-Driven Surface Freeze-Thaw Retrieval Across Canadian Agricultural Regions Using Sentinel-1 SAR Data. Frontiers in Remote Sensing. doi:10.3389/frsen.2025.1728399

Taghipourjavi, S., Kinnard, C. & Roy, A. (2026b) On demand machine learning-driven surface freeze-thaw retrieval across Canadian agricultural regions using Sentinel-1 SAR data. Frontiers in Remote Sensing, 6, 1728399. doi:10.3389/frsen.2025.1728399

Tarasova, L., Basso, S., Wendi, D., Viglione, A., Kumar, R. & Merz, R. (2020) A process-based framework to characterize and classify runoff events: The event typology of Germany. Water Resources Research, 56(5), e2019WR026951. doi:10.1029/2019WR026951

Tarasova, L., Basso, S., Zink, M. & Merz, R. (2018) Exploring controls on rainfall-runoff events: 1. Time series-based event separation and temporal dynamics of event runoff response in Germany. Water Resources Research, 54(10), 7711-7732. doi:10.1029/2018WR022587

Tramblay, Y., Bouvier, C., Martin, C., Didon-Lescot, J.-F., Todorovik, D. & Domergue, J.-M. J. J. o. H. (2010) Assessment of initial soil moisture conditions for event-based rainfall–runoff modelling, 387(3-4), 176-187. doi:10.1016/j.jhydrol.2010.04.006

Tsai, Y.-L. S., Dietz, A., Oppelt, N. & Kuenzer, C. (2019) Remote sensing of snow cover using spaceborne SAR: A review. Remote Sensing, 11(12), 1456. doi:10.3390/rs11121456

Walker, V. A., Colliander, A. & Kimball, J. S. (2022) Satellite retrievals of probabilistic freeze-thaw conditions from SMAP and AMSR brightness temperatures. IEEE Transactions on Geoscience Remote Sensing, 60, 1-11. doi:10.1109/TGRS.2022.3174807

Wang, G., Hu, H. & Li, T. J. J. o. H. (2009) The influence of freeze–thaw cycles of active soil layer on surface runoff in a permafrost watershed, 375(3-4), 438-449. doi:10.1016/j.jhydrol.2009.06.046

Wang, J., Jiang, L., Rautiainen, K., Zhang, C., Xiao, Z., Li, H., Yang, J. & Cui, H. (2022) Daily High-Resolution Land Surface Freeze/Thaw Detection Using Sentinel-1 and AMSR2 Data. Remote Sensing, 14(12), 2854. doi:10.3390/rs14122854

Watanabe, K. & Osada, Y. (2017) Simultaneous measurement of unfrozen water content and hydraulic conductivity of partially frozen soil near 0 C. Cold Regions Science Technology, 142, 79-84. doi:10.1016/j.coldregions.2017.08.002

Wu, N., Zhang, K., Naghibi, A., Hashemi, H., Ning, Z., Zhang, Q., Yi, X., Wang, H., Liu, W. & Gao, W. (2025) Predicting snow cover and frozen ground impacts on large basin runoff: developing appropriate model complexity. Hydrology Earth System Sciences, 29(15), 3703-3725. doi:10.5194/hess-29-3703-2025

Xu, Y., Yang, H., Yue, J., Wei, H., Che, R., Duan, Q., Zhou, S. & Sun, M. J. A. S. (2025) Freezing Behavior of Clayey Sand and Spatiotemporal Evolution of Seasonally Frozen Soil Distribution in the Qinghai–Tibet Plateau, 15(13), 7498. doi:10.3390/app15137498

Yang, K., Wang, C. J. A. & Meteorology, F. (2019) Water storage effect of soil freeze-thaw process and its impacts on soil hydro-thermal regime variations, 265, 280-294. doi:10.1016/j.agrformet.2018.11.011

Yi, J., Zhao, Y., Shao, M. a., Zhang, J., Cui, L. & Si, B. (2014) Soil freezing and thawing processes affected by the different landscapes in the middle reaches of Heihe River Basin, Gansu, China. Journal of Hydrology, 519, 1328-1338. doi:10.1016/j.jhydrol.2014.08.042

Zheng, D., van der Velde, R., Su, Z., Wen, J., Wang, X. & Yang, K. (2018) Impact of soil freeze-thaw mechanism on the runoff dynamics of two Tibetan rivers. Journal of Hydrology, 563, 382-394. doi:10.1016/j.jhydrol.2018.06.024

Chapter III Supplementary Information

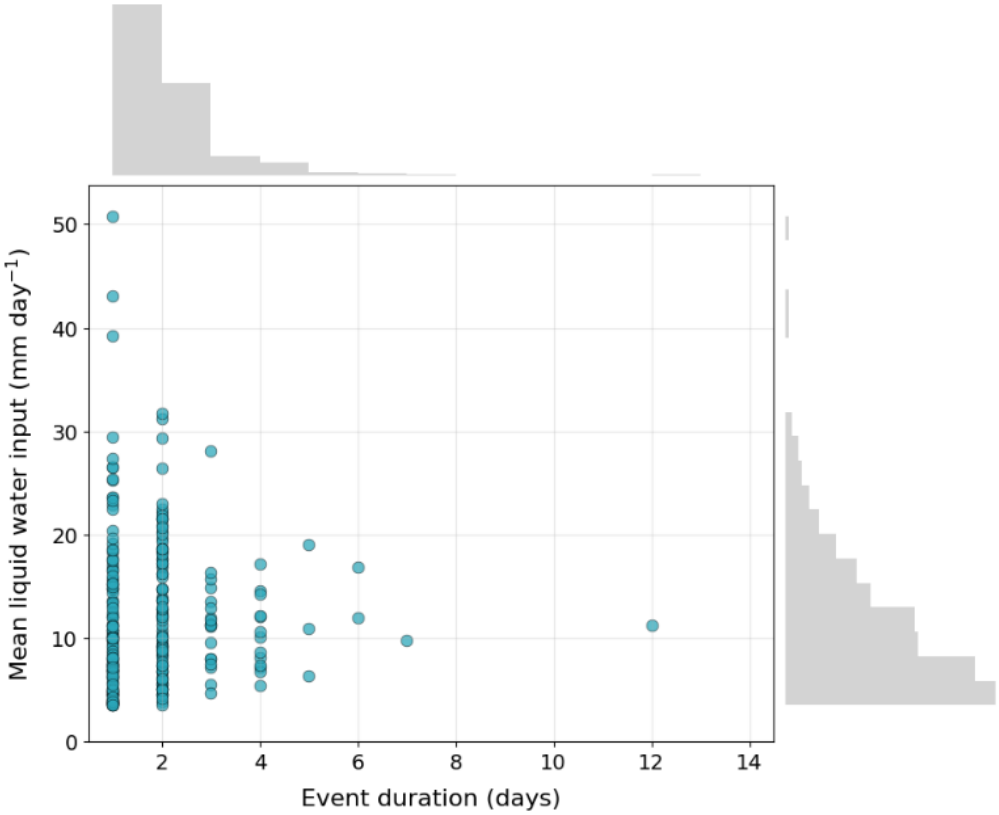

Figure S3.1. Joint distribution of hydrological event duration and mean liquid water input for cold-season events (October-April 2015–2025) identified using the 3.5 mm day^{-1} liquid water input threshold. Points represent individual hydrological events, with event duration expressed in days and mean liquid water input calculated over each event. Marginal histograms illustrate the distributions of event duration (top) and mean liquid water input (right).

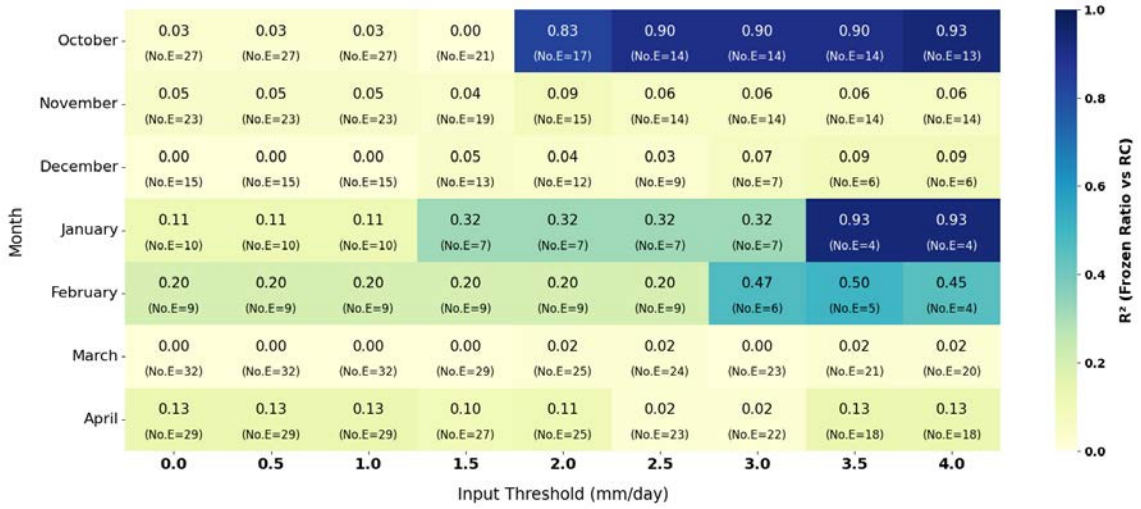

Figure S3.2. Diagnostic analysis of the relationship between frozen soil conditions and the daily runoff coefficient across a range of *Iliq* thresholds (0–4 mm day^{-1}). The heatmap shows the R^2 from linear regressions between the mean frozen soil ratio and the RC_{daily} (without lag) stratified by month and input threshold. Here, RC is computed at the daily scale using daily specific discharge (Q) and daily total liquid water input (rainfall + snowmelt). Numbers within each cell indicate the R^2 value, while values in parentheses denote the number of daily observations included. This analysis is intended as a diagnostic sensitivity assessment illustrating how the strength of daily-scale frozen soil–runoff relationships vary with input magnitude and season. It was not used to select or optimize the event-onset threshold adopted in the event-based analysis.

Table S3.1. AIC values for all candidate Gamma GLM formulations across liquid water input (I_{liq}) thresholds used for event definition. A-type models treat liquid water input as an explicit predictor, whereas B-type models include log-transformed liquid water input as an offset term to model runoff efficiency. Lower AIC values indicate better relative model support.

Threshold (mm day^{-1})	**Events with FT**	**Final model events**	**A1**	**A2**	**A3**	**A4**	**A5**	**B1**	**B2**	**B3**	**B4**	**B5**
2.0	119	77	202.82	203.65	197.78	199.75	201.68	205.08	206.94	201.88	202.81	204.81
2.5	110	75	195.99	197.13	191.36	193.41	195.48	195.52	197.41	192.2	193.67	195.73
3.0	104	73	189.57	191.38	184.46	185.88	187.38	188.73	190.37	184.3	184.81	186.43
3.5	94	69	181.35	183.19	178.13	179.88	181.82	180.34	182.19	177.37	178.54	180.49
4.0	91	67	187.03	188.32	185.8	187.95	190.14	185.82	187.66	184.15	186.23	188.37
4.5	87	64	186.73	187.94	185.58	187.68	189.86	185.16	186.87	183.5	185.6	187.75
5.0	80	61	177.91	179.35	174.48	176.55	178.22	177.63	179.51	175.1	176.06	177.55

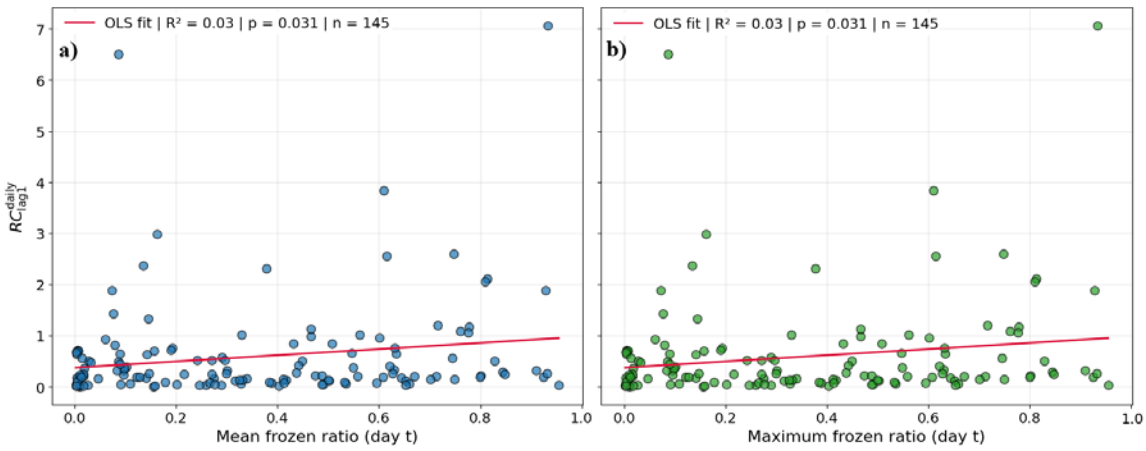

Figure S3.3. Daily-scale relationship between frozen soil extent and daily lagged runoff coefficient (RC_{lag1}^{daily}) in the Acadie River catchment during the cold season. (**a**) RC_{lag1}^{daily} as a function of the mean frozen soil ratio on day *t*. (**b**) RC_{lag1}^{daily} as a function of the maximum frozen soil ratio on day *t*. Each point represents one cold-season day with liquid water input ≥ 1.0 mm day^{-1} (n = 145). Solid red lines show OLS regression fits, with corresponding R^2 and p-values reported in each panel.

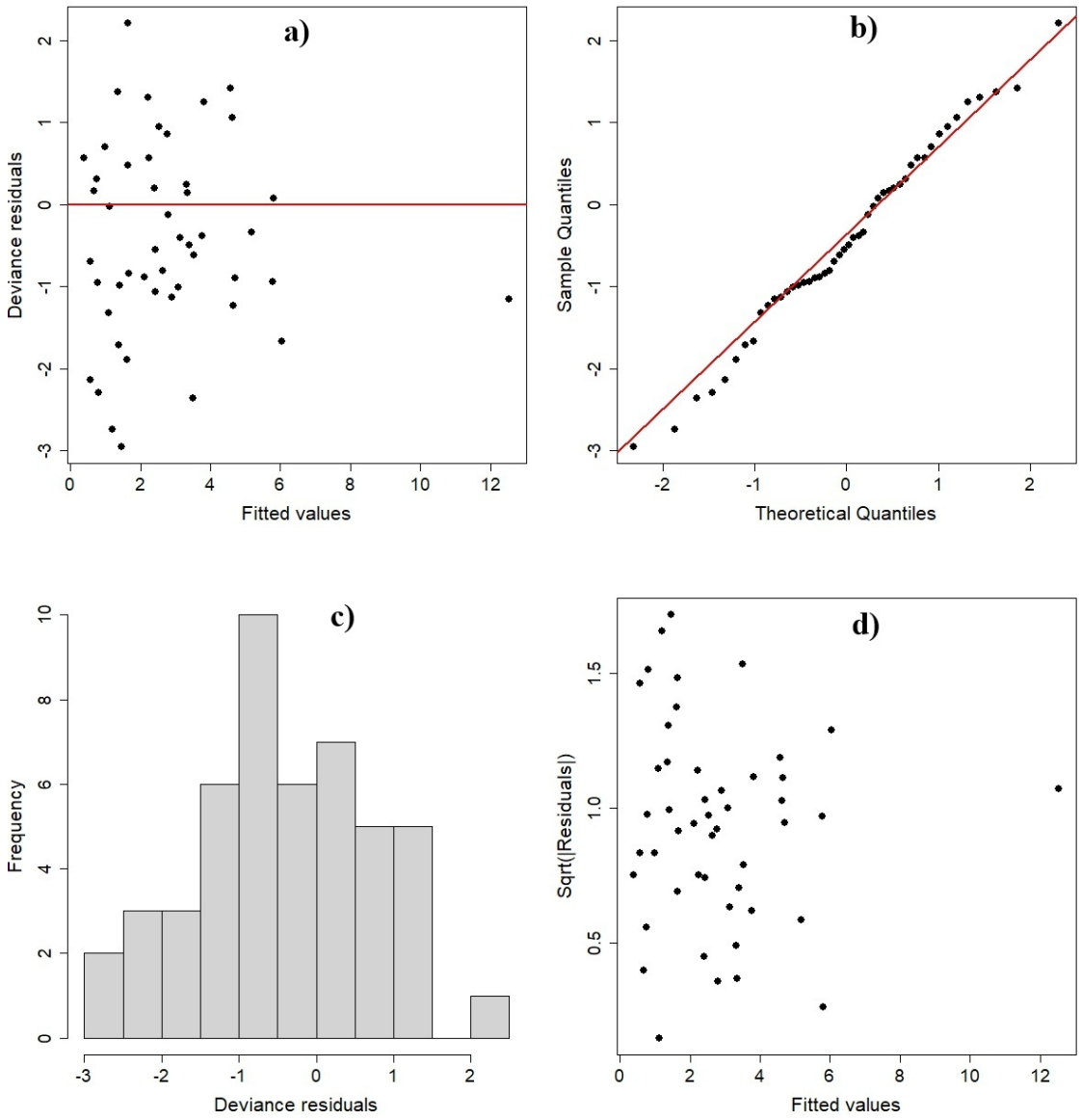

Figure S3.4. Residual diagnostics for the A_3 Gamma generalized linear model, including (**a**) residuals versus fitted values, (**b**) normal Q–Q plot, (**c**) histogram of deviance residuals, and (**d**) scale-location plot. The diagnostics indicate no major violations of model assumptions and support the adequacy of the model fit.

Table S3.2. Comparison of Gamma generalized linear mixed models (GLMMs) including a random intercept for month. Models are ranked by Akaike Information Criterion (AIC). Marginal R^2 ($MarR^2$) indicates the variance explained by fixed effects only, while Conditional R^2 ($ConR^2$) represents the variance explained by both fixed and random effects. F denotes the frozen soil ratio. Coefficients (coef) are reported as estimates ± standard errors (SE).

Model	AIC	Pse-R^2	$MarR^2$	$ConR^2$	Input effect	F effect (coef ± SE)	p(F)	API effect	p(API)
A1	179.16	0.247	0.385	0.557	1.581 ± 0.359 ($p < 0.001$)	—	—	—	—
B1	179.57	0.208	0.000	0.193	fixed	—	—	—	—
B3	180.81	0.221	0.079	—	fixed	0.844 ± 0.518	0.103	—	—
B2	180.88	0.219	0.021	0.244	fixed	—	—	0.012 ± 0.012	0.340
A3	181.08	0.248	0.393	0.537	1.548 ± 0.380 ($p < 0.001$)	0.097 ± 0.335	0.771	—	—
A2	181.09	0.248	0.382	0.555	1.537 ± 0.063 ($p < 0.001$)	—	—	0.001 ± 0.005	0.762
B4	181.67	0.239	0.123	—	fixed	1.131 ± 0.561	0.044	0.017 ± 0.014	0.241
A4	182.90	0.251	0.394	0.521	1.459 ± 0.018 ($p < 0.001$)	0.150 ± 0.018	<0.001	0.002 ± 0.004	0.586
B5	183.55	0.241	0.124	—	fixed	1.113 ± 0.557	0.046	0.012 ± 0.018	0.484
A5	184.62	0.255	0.404	0.522	1.495 ± 0.020 ($p < 0.001$)	0.160 ± 0.020	<0.001	0.000 ± 0.005	0.921

GENERAL DISCUSSION AND CONCLUSIONS

Considering the results presented across the three preceding chapters, this final section provides an integrated synthesis of the contributions of this thesis to the understanding of near-surface soil freeze-thaw (FT) dynamics and their hydrological relevance in agricultural and agro-forested environments. By combining high-resolution Sentinel-1 C-band SAR observations with probabilistic, machine-learning, and hydrological modeling frameworks, this thesis demonstrates how soil FT processes can be robustly detected, characterized, and interpreted across multiple spatial and temporal scales. Collectively, the three chapters show that soil freezing is best represented as a continuous, context-dependent state rather than a rigid binary condition, and that near-surface FT acts primarily as a modulating background constraint that conditions hydrological response rather than directly controlling runoff magnitude.

The first chapter establishes a physically informed and probabilistic framework for detecting near-surface soil FT conditions at the plot scale, emphasizing the importance of accounting for spatial heterogeneity and transitional thermal states. The second chapter extends this framework to the national scale, demonstrating its robustness, scalability, and operational potential across diverse Canadian agricultural landscapes. The third chapter integrates satellite-derived FT information with hydrometeorological forcing and event-based statistical modeling to examine how frozen soil conditions influence runoff timing, efficiency, and variability at the catchment scale. Together, these chapters provide a coherent progression from process-level FT detection to large-scale monitoring, and finally to hydrological interpretation.

The overarching objective of this thesis was to evaluate the capability of Sentinel-1 SAR observations to retrieve near-surface soil FT states using advanced statistical frameworks and to assess the hydrological relevance of these states in seasonally frozen agricultural systems. Rather than focusing solely on FT classification accuracy, this work sought to understand how radar-derived FT information behaves across space and time, how uncertainty arises during transitional periods, and how FT conditions interact with hydrometeorological drivers to shape runoff response. The discussion that follows revisits

each chapter through this lens, emphasizing detection capability, robustness, interpretability, and process relevance.

Observation and Detection of Near-Surface Soil FT States

A primary contribution of this thesis lies in the development and evaluation of a robust framework for observing near-surface soil FT dynamics using Sentinel-1 SAR data. Central to this framework is the Exponential Freeze-Thaw Algorithm (EFTA), which was designed to address key limitations of traditional change-detection approaches. Conventional methods based on fixed thresholds or simple backscatter differences were shown to be vulnerable to misclassification during fall and spring transition periods, when backscatter variations are often driven by surface drying, roughness changes, or vegetation effects rather than phase changes in soil water. By explicitly damping transient backscatter fluctuations during expected thaw periods while preserving sensitivity during frozen conditions, the EFTA improves the temporal consistency of FT detection.

The probabilistic formulation adopted in the first chapter further advances FT detection by explicitly accounting for uncertainty in both observations and surface conditions. Rather than forcing soil states into discrete frozen or thawed classes, the freezing probability framework captures intermediate conditions that are common in agricultural soils subject to partial freezing, snow insulation, and heterogeneous moisture distribution. This approach proved particularly valuable in grassland and forested plots, where frequent FT transitions and insulating effects produce complex thermal regimes that are poorly represented by binary classifications. The results demonstrate that near-surface (2–5 cm) soil freezing can be reliably detected using Sentinel-1 SAR, whereas deeper freezing exhibits reduced detectability due to the limited penetration depth of C-band radar signals.

Across both plot-scale and national-scale analyses, VH polarization consistently emerged as the most informative radar configuration. The strong performance of VH-based indicators reflects their sensitivity to surface roughness, vegetation residues, and moisture-related effects that accompany freezing processes in agricultural landscapes.

These findings confirm that radar sensitivity to FT is not governed solely by dielectric contrasts but is strongly modulated by surface structure and land management practices. Mixed-effects modeling further revealed that interactions between radar-derived indicators and crop types explain a substantial portion of spatial variability in FT detection, highlighting the importance of incorporating land-use information when interpreting radar signals over agricultural regions.

Model validation results across multiple spatial and temporal cross-validation strategies demonstrate that the proposed detection framework captures fundamental relationships between radar backscatter and soil freezing processes rather than site-specific artifacts. Strong performance under leave-one-plot-out, leave-one-station-out, and leave-one-year-out validation confirms the transferability of the approach across heterogeneous environments. At the same time, reduced performance in environments experiencing limited freezing underscores the importance of balanced training data and cautions against over-interpreting FT predictions in regions dominated by a single thermal state.

Methodological and Modeling Advances in FT Representation

Beyond FT detection itself, this thesis provides important methodological insights into how FT states should be represented and modeled. The systematic comparison between binary classification and probability-based regression approaches clarifies the strengths and limitations of each framework. Binary models were shown to be more robust under stable frozen or thawed conditions, exhibiting lower error rates outside the critical transition zone near 0 °C. In contrast, probability-based models offer a more nuanced representation of partial freezing but exhibit increased uncertainty during transitional periods, where rapid changes in soil moisture, surface roughness, and snowmelt conditions produce complex radar responses.

At the national scale, diagnostic analyses confirmed that variability in the VH-based EFTA is overwhelmingly controlled by near-surface soil freezing conditions, accounting for more than 90% of total model importance. Snow-related variables contributed only

marginally, reflecting both the predominance of dry to moderately shallow snowpacks across Canadian agricultural regions and the capacity of the EFTA formulation to suppress transient signal perturbations during non-frozen periods. The use of a local thawed reference backscatter effectively normalizes site-specific variability, enabling strong generalization across diverse soil types, crop classes, and climatic zones without site-specific recalibration.

Uncertainty analyses consistently showed that FT detection errors are concentrated during fall freeze-up and spring thaw, when mixed-phase soil conditions dominate radar backscatter variability. These findings highlight inherent physical limitations of C-band SAR for resolving partial freezing and rapid wetting events using radar data alone. While the EFTA substantially improves FT discrimination relative to raw backscatter, accurately resolving transitional FT states remains challenging without complementary information on soil moisture or surface energy balance. Importantly, these limitations are explicitly characterized within the proposed framework, providing a clear basis for interpreting FT products in applied contexts.

Hydrological Interpretation of Seasonal Soil Freezing

The third chapter extends the FT detection framework into a hydrological context, examining how near-surface FT states influence cold-season runoff generation in an intensively agricultural catchment. Daily-scale analyses revealed a consistent divergence in runoff behavior under frozen versus thawed soil conditions, with runoff coefficients systematically higher when a large fraction of the catchment surface was frozen. Elevated runoff efficiency at short temporal windows, combined with a rapid decline toward stable values at longer windows, indicates that soil freezing primarily affects short-term infiltration capacity and lateral flow pathways rather than producing sustained discharge increases.

Cross-correlation analyses further demonstrated a dominant one-day response lag between liquid water input and river discharge across all cold-season periods, with the strongest coupling occurring during winter when soils are predominantly frozen. These

results suggest that frozen conditions are associated with stronger short-term runoff response, but the event-scale analyses show that frozen soil extent alone does not explain runoff magnitude. Event-based analyses confirmed substantial variability in runoff response under similar frozen soil conditions, with weak and statistically non-significant linear relationships between frozen soil extent and event-averaged runoff coefficients. This behavior indicates that frozen soil extent alone explains only a limited fraction of event-scale runoff variability, and that runoff response is mainly shaped by liquid water input and event-specific conditions.

Gamma generalized linear models provided a quantitative synthesis of these interactions, showing that event-scale runoff generation was primarily governed by liquid water input. Models including frozen soil effects showed positive coefficients and comparable support, but these effects did not reach conventional levels of statistical significance. In contrast, antecedent wetness showed weak and non-significant influence. These results indicate that frozen soil conditions may contribute to runoff efficiency, but they do not exert an independent or statistically dominant control on runoff magnitude. Instead, spatially distributed FT information is best interpreted as a contextual variable that helps describe the environmental conditions under which liquid water input is converted into runoff.

Limits, Generalization, and Research Outlook

While the objectives of this thesis are met, several limitations must be acknowledged. From a methodological perspective, the limited penetration depth of C-band SAR restricts FT detection primarily to near-surface soil layers, and uncertainty remains highest during transitional periods characterized by partial freezing and rapid wetting. The reliance on balanced freezing conditions for model calibration also limits performance in environments dominated by persistent thaw or limited freezing. From a process perspective, vertical freezing structure, snow–soil energy exchanges, and subsurface flow pathways are not explicitly represented within the current framework.

Despite these limitations, the strong spatial and temporal transferability demonstrated across plot, regional, and national scales indicates that the proposed framework is well suited for large-scale agricultural FT monitoring. The integration of optimized FT detection models into a web-based, cloud-enabled mapping tool further illustrates the operational potential of this work. At the catchment scale, the results highlight that satellite-derived FT information enhances hydrological process understanding when interpreted in conjunction with hydrometeorological forcing and antecedent conditions but should not be used in isolation for runoff prediction.

Overall, this thesis demonstrates the capability to retrieve near-surface soil freeze–thaw states from Sentinel-1 C-band SAR backscatter by explicitly accounting for seasonal signal evolution, surface heterogeneity, and transitional conditions through a probabilistic framework. By showing that radar-derived indicators, particularly VH-based EFTA, reliably capture near-surface soil freezing across plot, regional, and catchment scales, this work establishes a transferable methodological framework for using SAR backscatter to infer near-surface soil thermal state in cold region agricultural areas.

Building on this capability, this thesis supports an emerging conceptual view in which near-surface soil FT states act as a modulating background condition rather than a dominant standalone driver of hydrological response in humid, seasonally frozen agricultural catchments. Accurate representation of cold-season runoff processes therefore requires consideration of soil FT conditions together with liquid water input and seasonal hydrometeorological conditions, while recognizing that liquid water input remains the primary control on event-scale runoff generation. By integrating satellite-based FT observations with probabilistic modeling and event-scale hydrological analysis, this work contributes a robust and scalable framework for improving the representation of FT processes in agricultural hydrology and provides a foundation for future advances in cold-season environmental monitoring.

References

Ala-Aho, P., Autio, A., Bhattacharjee, J., Isokangas, E., Kujala, K., Marttila, H., Menberu, M., Meriö, L., Postila, H. & Rauhala, A. (2021) What conditions favor the influence of seasonally frozen ground on hydrological partitioning? A systematic review. *Environmental Research Letters*, 16(4), 043008. doi:10.1088/1748-9326/abe82c

Aldrich, C. (2020) Process variable importance analysis by use of random forests in a shapley regression framework. *Minerals*, 10(5), 420. doi:10.3390/min10050420

Ali, S., Ghosh, N. & Singh, R. (2010) Rainfall–runoff simulation using a normalized antecedent precipitation index. *Hydrological Sciences Journal–Journal des Sciences Hydrologiques*, 55(2), 266-274. doi:10.1080/02626660903546175

Alpar, S., Berger, J., Rysbaiuly, B. & Belarbi, R. (2024) Estimation of soils thermophysical characteristics in a nonlinear inverse heat transfer problem. *International Journal of Heat Mass Transfer*, 218, 124727. doi:10.1016/j.ijheatmasstransfer.2023.124727

Amani, M., Brisco, B., Afshar, M., Mirmazloumi, S. M., Mahdavi, S., Mirzadeh, S. M. J., Huang, W. & Granger, J. (2019) A generalized supervised classification scheme to produce provincial wetland inventory maps: An application of Google Earth Engine for big geo data processing. *Big Earth Data*, 3(4), 378-394. doi:10.1080/20964471.2019.1690404

An, R., Gao, H., Chen, C. & Zhang, X. (2024) Quantification and division of unfrozen water content of frozen soils during freezing and the influence of freeze-thaw cycles. *Bulletin of Engineering Geology the Environment*, 83(11), 440. doi:10.1007/s10064-024-03954-w

Appels, W. M., Bogaart, P. W. & van der Zee, S. E. (2016) Surface runoff in flat terrain: How field topography and runoff generating processes control hydrological connectivity. *Journal of Hydrology*, 534, 493-504. doi:10.1016/j.jhydrol.2016.01.021

Appels, W. M., Coles, A. E. & McDonnell, J. J. (2018) Infiltration into frozen soil: From core-scale dynamics to hillslope-scale connectivity. *Hydrological Processes*, 32(1), 66-79. doi:10.1002/hyp.11399

Asmuß, T., Bechtold, M. & Tiemeyer, B. (2019) On the potential of Sentinel-1 for high resolution monitoring of water table dynamics in grasslands on organic soils. *Remote Sensing*, 11(14), 1659. doi:10.3390/rs11141659

Aygün, O., Kinnard, C. & Campeau, S. (2020a) Impacts of climate change on the hydrology of northern midlatitude cold regions. *Progress in Physical Geography: Earth Environment*, 44(3), 338-375. doi:10.1177/0309133319878123

Aygün, O., Kinnard, C., Campeau, S. & Krogh, S. A. (2020b) Shifting hydrological processes in a Canadian agroforested catchment due to a warmer and wetter climate. *Water*, 12(3), 739. doi:doi.org/10.3390/w12030739

Baghdadi, N., Bazzi, H., El Hajj, M. & Zribi, M. (2018) Detection of frozen soil using Sentinel-1 SAR data. *Remote Sens.*, 10(8), 1182. doi:10.3390/rs10081182

Baghdadi, N., Cresson, R., Hajj, M. E., Ludwig, R. & Jeunesse, I. L. (2012) Estimation of soil parameters over bare agriculture areas from C-band polarimetric SAR data using neural networks. *Hydrology Earth System Sciences*, 16(6), 1607-1621. doi:10.5194/hess-16-1607-2012

Baghdadi, N., El Hajj, M., Zribi, M. & Bousbih, S. (2017) Calibration of the water cloud model at C-band for winter crop fields and grasslands. *Remote Sensing*, 9(9), 969. doi:10.3390/rs9090969

Baghdadi, N., King, C., Bourguignon, A. & Remond, A. (2002a) Potential of ERS and RADARSAT data for surface roughness monitoring over bare agricultural fields: application to catchments in Northern France. *Int. J. Remote Sens.*, 23(17), 3427-3442. doi:10.1080/01431160110110974

Baghdadi, N., King, C., Bourguignon, A. & Remond, A. (2002b) Potential of ERS and Radarsat data for surface roughness monitoring over bare agricultural fields: application to catchments in Northern France. *International journal of remote sensing*

23(17), 3427-3442. doi:10.1080/01431160110110974

Bartsch, A., Muri, X., Hetzenecker, M., Rautiainen, K., Bergstedt, H., Wuite, J., Nagler, T. & Nicolsky, D. (2025) Benchmarking passive-microwave-satellite-derived freeze–thaw datasets. *The Cryosphere*, 19(1), 459-483. doi:10.5194/tc-19-459-2025

Bauer-Marschallinger, B., Cao, S., Navacchi, C., Freeman, V., Reuß, F., Geudtner, D., Rommen, B., Vega, F. C., Snoeij, P. & Attema, E. (2021) The normalised Sentinel-1 Global Backscatter Model, mapping Earth's land surface with C-band microwaves. *Scientific Data*, 8(1), 277. doi:10.1038/s41597-021-01059-7

Beck, H. E., Zimmermann, N. E., McVicar, T. R., Vergopolan, N., Berg, A. & Wood, E. F. J. S. d. (2018) Present and future Köppen-Geiger climate classification maps at 1-km resolution, 5(1), 1-12. doi:10.1038/sdata.2018.214

Beer, C., Lucht, W., Gerten, D., Thonicke, K. & Schmullius, C. (2007) Effects of soil freezing and thawing on vegetation carbon density in Siberia: A modeling analysis with the Lund-Potsdam-Jena Dynamic Global Vegetation Model (LPJ-DGVM). *Global Biogeochem. Cycles*, 21(1). doi:10.1029/2006GB002760

Benninga, H.-J. F., van der Velde, R. & Su, Z. (2019) Impacts of radiometric uncertainty and weather-related surface conditions on soil moisture retrievals with Sentinel-1. *Remote Sens.*, 11(17), 2025. doi:10.3390/rs11172025

Bergstedt, H. & Bartsch, A. (2017) Surface state across scales; temporal and spatial patterns in land surface freeze/thaw dynamics. *Geosci.*, 7(3), 65. doi:10.3390/geosciences7030065

Bergstedt, H., Bartsch, A., Neureiter, A., Höfler, A., Widhalm, B., Pepin, N. & Hjort, J. (2020) Deriving a frozen area fraction from metop ASCAT backscatter based on Sentinel-1. *IEEE Transactions on Geoscience Remote Sensing*, 58(9), 6008-6019. doi:10.1109/TGRS.2020.2967364

Bernier, M. & Fortin, J.-P. (1998) The potential of times series of C-band SAR data to monitor dry and shallow snow cover. *IEEE Trans. Geosci. Remote Sens.*, 36(1), 226-243. doi:10.1109/36.655332

Bi, J., Wang, G., Wu, Z., Wen, H., Zhang, Y., Lin, G. & Sun, T. (2023) Investigation on unfrozen water content models of freezing soils. *Frontiers in Earth Science*, 10, 1039330. doi:10.3389/feart.2022.1039330

Black, T., Chen, W., Barr, A., Arain, M., Chen, Z., Nesic, Z., Hogg, E., Neumann, H. & Yang, P. (2000) Increased carbon sequestration by a boreal deciduous forest in years with a warm spring. *Geophys. Res. Lett.*, 27(9), 1271-1274. doi:10.1029/1999GL011234

Bo, L., Li, Z., Li, P., Xu, G., Xiao, L. & Ma, B. (2021) Soil freeze-thaw and water transport characteristics under different vegetation types in seasonal freeze-thaw areas of the loess plateau. *Frontiers in Earth Science*, 9, 704901. doi:10.3389/feart.2021.704901

Brangers, I., Marshall, H.-P., De Lannoy, G., Dunmire, D., Mätzler, C. & Lievens, H. (2024) Tower-based C-band radar measurements of an alpine snowpack. *TC*, 18(7), 3177-3193. doi:10.5194/tc-18-3177-2024

Breiman, L. (2001) Random forests. *Mach. Learn.*, 45, 5-32. doi:10.1023/A:1010933404324

Bronstert, A., Niehoff, D. & Schiffler, G. R. (2023) Modelling infiltration and infiltration excess: The importance of fast and local processes. *Hydrological Processes*, 37(4), e14875. doi:10.1002/hyp.14875

Burt, T. & Williams, P. J. J. E. S. P. (1976) Hydraulic conductivity in frozen soils, 1(4), 349-360. doi:10.1002/esp.3290010404

Cade-Menun, B. J., Bell, G., Baker-Ismail, S., Fouli, Y., Hodder, K., McMartin, D. W., Perez-Valdivia, C. & Wu, K. (2013) Nutrient loss from Saskatchewan cropland and pasture in spring snowmelt runoff. *Can. J. Soil Sci.*, 93(4), 445-458. doi:10.4141/cjss2012-042

Cao, B., Gruber, S. & Zhang, T. J. G. M. D. (2017) REDCAPP (v1. 0): Parameterizing valley inversions in air temperature data downscaled from reanalyses, 10(8), 2905-2923. doi:10.5194/gmd-10-2905-2017

Chang, A. & Cao, M. (1996) Monitoring soil condition in the northern Tibetan Plateau using SSM/I data. *Hydrology Research*, 27(3), 175-184. doi:10.2166/nh.1996.0003

Chang, Z., Qi, P., Zhang, G., Sun, Y., Tang, X., Jiang, M., Sun, J. & Li, Z. (2022) Latitudinal characteristics of frozen soil degradation and their response to climate change in a high-latitude water tower. *Catena*, 214, 106272. doi:10.1016/j.catena.2022.106272

Chen, C., Peng, X., Frauenfeld, O. W., Zhao, Y., Yang, G., Tian, W., Li, X., Du, R. & Li, X. (2022) Comprehensive assessment of seasonally frozen ground changes in the Northern Hemisphere based on observations. *Journal of Geophysical Research: Atmospheres*, 127(20), e2022JD037306. doi:10.1029/2022JD037306

Chen, L., Chen, Z., Jia, G., Zhou, J., Zhao, J. & Zhang, Z. J. S. o. t. T. E. (2020) Influences of forest cover on soil freeze-thaw dynamics and greenhouse gas emissions through the regulation of snow regimes: A comparison study of the farmland and forest plantation, 726, 138403. doi:10.1016/j.scitotenv.2020.138403

Chen, L., Voss, C. I., Fortier, D. & McKenzie, J. M. (2021) Surface energy balance of sub-Arctic roads with varying snow regimes and properties in permafrost regions. *Permafrost Periglacial Processes*, 32(4), 681-701. doi:10.1002/ppp.2129

Chen, Y., Li, S., Wang, L., Mittermeier, M., Bernier, M. & Ludwig, R. (2024) Retrieving freeze-thaw states using deep learning with remote sensing data in permafrost landscapes. *Int. J. Appl. Earth Obs. Geoinf.*, 126, 103616. doi:10.1016/j.jag.2023.103616

Cheng, Y., Li, P., Xu, G., Li, Z., Wang, T., Cheng, S., Zhang, H. & Ma, T. (2018) The effect of soil water content and erodibility on losses of available nitrogen and phosphorus in simulated freeze-thaw conditions. *Catena*, 166, 21-33. doi:10.1016/j.catena.2018.03.015

Chou, Y.-l. & Wang, L.-j. (2021) Seasonal freezing-thawing process and hydrothermal characteristics of soil on the Loess Plateau, China. *Journal of Mountain Science*, 18(11), 3082-3098. doi:10.1007/s11629-020-6599-9

Chow, V. (1971) *Applied hydrology*McGraw-hill.

Cober, J. R., Macrae, M. L. & Van Eerd, L. L. (2018) Nutrient release from living and terminated cover crops under variable freeze–thaw cycles. *Agronomy Journal*, 110(3), 1036-1045. doi:10.2134/agronj2017.08.0449

Cohen, J., Lemmetyinen, J., Ruiz, J. J., Rautiainen, K., Ikonen, J., Kontu, A. & Pulliainen, J. (2024a) Detection of soil and canopy freeze/thaw state in the boreal region with L and C Band Synthetic Aperture Radar. *Remote Sens. Environ.*, 305, 114102. doi:10.1016/j.rse.2024.114102

Cohen, J., Lemmetyinen, J., Ruiz, J. J., Rautiainen, K., Ikonen, J., Kontu, A. & Pulliainen, J. J. R. S. o. E. (2024b) Detection of soil and canopy freeze/thaw state in the boreal region with L and C Band Synthetic Aperture Radar, 305, 114102. doi:10.1016/j.rse.2024.114102

Coles, A. & McDonnell, J. (2018) Fill and spill drives runoff connectivity over frozen ground. *Journal of Hydrology*, 558, 115-128. doi:10.1016/j.jhydrol.2018.01.016

Coles, A. E., Appels, W. M., McConkey, B. G. & McDonnell, J. (2016) The hierarchy of controls on snowmelt-runoff generation over seasonally-frozen hillslopes. *Hydrology Earth System Sciences Discussions*, 2016, 1-27. doi:10.5194/hess-2016-564

Collins, M. J. J. H. P. (2019) River flood seasonality in the Northeast United States: Characterization and trends, 33(5), 687-698. doi:10.1002/hyp.13355

Comite, D., Cenci, L., Colliander, A. & Pierdicca, N. (2020) Monitoring freeze-thaw state by means of GNSS reflectometry: An analysis of TechDemoSat-1 data. *IEEE Journal of Selected Topics in Applied Earth Observations Remote Sensing*, 13, 2996-3005. doi:10.1109/JSTARS.2020.2986859

Commission for Environmental Cooperation (CEC) (2021) *North American Land Cover, 2020 (Landsat, 30m)*, 2021. Available online: https://www.cec.org/north-american-environmental-atlas/land-cover-30m-2020/ [Accessed.

Decker, K., Wang, D., Waite, C. & Scherbatskoy, T. (2003) Snow removal and ambient air temperature effects on forest soil temperatures in northern Vermont. *Soil Science Society of America Journal*, 67(4), 1234-1242. doi:10.2136/sssaj2003.1234

DeGuzman, K., Knappenberger, T., Brantley, E. & Olshansky, Y. J. H. P. (2023) Estimating runoff probability from precipitation data: A binomial regression analysis, 37(11), e15029. doi:10.1002/hyp.15029

Deng, Y., Li, X., Wang, Z., Shi, F., Zhao, S. & Hu, G. (2025) Natural seasonal freeze-thaw processes influenced soil quality in alpine grasslands: Insights from soil functions. *Soil Biology Biochemistry*, 200, 109642. doi:10.1016/j.soilbio.2024.109642

Derksen, C., Xu, X., Dunbar, R. S., Colliander, A., Kim, Y., Kimball, J. S., Black, T. A., Euskirchen, E., Langlois, A. & Loranty, M. M. (2017a) Retrieving landscape freeze/thaw state from Soil Moisture Active Passive (SMAP) radar and radiometer measurements. *Remote Sens. Environ.*, 194, 48-62. doi:10.1016/j.rse.2017.03.007

Derksen, C., Xu, X., Dunbar, R. S., Colliander, A., Kim, Y., Kimball, J. S., Black, T. A., Euskirchen, E., Langlois, A. & Loranty, M. M. (2017b) Retrieving landscape freeze/thaw state from Soil Moisture Active Passive (SMAP) radar and radiometer measurements. *Remote Sensing of Environment*, 194, 48-62. doi:10.1016/j.rse.2017.03.007

Derksen, C., Xu, X., Dunbar, R. S., Colliander, A., Kim, Y., Kimball, J. S., Black, T. A., Euskirchen, E., Langlois, A. & Loranty, M. M. J. R. S. o. E. (2017c) Retrieving landscape freeze/thaw state from Soil Moisture Active Passive (SMAP) radar and radiometer measurements. *Remote Sensing of Environment*, 194, 48-62. doi:10.1016/j.rse.2017.03.007

Dharmadasa, V., Kinnard, C. & Baraër, M. (2023) Topographic and vegetation controls of the spatial distribution of snow depth in agro-forested environments by UAV lidar. *The Cryosphere*, 17(3), 1225-1246. doi:10.5194/tc-17-1225-2023

Dharmadasa, V., Kinnard, C. & Baraër, M. J. R. S. (2022) An accuracy assessment of snow depth measurements in agro-forested environments by UAV lidar. *Remote Sensing*, 14(7), 1649. doi:10.3390/rs14071649

Ding, B., Zhang, Y., Yu, X., Jia, G., Wang, Y., Zheng, P. & Li, Z. (2023) Comparative study of seasonal freeze–thaw on soil water transport in farmland and its shelterbelt. *Catena*, 225, 106982. doi:10.1016/j.catena.2023.106982

Domg, Y. & Milne, A. K. (2001) Toward edge sharpening: a SAR speckle filtering algorithm. *IEEE Transactions on Geoscience Remote Sensing*, 39(4), 851-863. doi:10.1109/36.917910

Donahue, K., Kimball, J. S., Du, J., Bunt, F., Colliander, A., Moghaddam, M., Johnson, J., Kim, Y. & Rawlins, M. A. (2023a) Deep learning estimation of northern hemisphere soil freeze-thaw dynamics using satellite multi-frequency microwave brightness temperature observations. *Frontiers in big Data*, 6, 1243559. doi:10.3389/fdata.2023.1243559

Donahue, K., Kimball, J. S., Du, J., Bunt, F., Colliander, A., Moghaddam, M., Johnson, J., Kim, Y. & Rawlins, M. A. (2023b) Deep learning estimation of northern hemisphere soil freeze-thaw dynamics using satellite multi-frequency microwave brightness temperature observations. *Front. Big Data*, 6, 1243559. doi:10.3389/fdata.2023.1243559

Du, J., Kimball, J. S., Azarderakhsh, M., Dunbar, R. S., Moghaddam, M. & McDonald, K. C. (2014) Classification of Alaska spring thaw characteristics using satellite L-band radar remote sensing. *IEEE Transactions on Geoscience Remote Sensing*, 53(1), 542-556. doi:10.1109/TGRS.2014.2325409

Du, J., Kimball, J. S., Jones, L. A., Kim, Y., Glassy, J. & Watts, J. D. (2017) A global satellite environmental data record derived from AMSR-E and AMSR2 microwave Earth observations. *Earth System Science Data*, 9(2), 791-808. doi:10.5194/essd-9-791-2017

Edwards, L. M. (2013) The effects of soil freeze–thaw on soil aggregate breakdown and concomitant sediment flow in Prince Edward Island: A review. *Can. J. Soil Sci.*, 93(4), 459-472. doi:10.4141/cjss2012-059

Ekici, A., Chadburn, S., Chaudhary, N., Hajdu, L., Marmy, A., Peng, S., Boike, J., Burke, E., Friend, A. & Hauck, C. (2015) Site-level model intercomparison of high latitude and high altitude soil thermal dynamics in tundra and barren landscapes. *TC*, 9(4), 1343-1361. doi:10.5194/tc-9-1343-2015

Escobar, A. M. d. A. (2017) *Analysis of Surface Roughness in Agricultural Soils Using In-Situ Measurements and Remote Sensing Techniques*. Ph.D. Thesis PhD. Public University of Navarre.

Fang, X. & Pomeroy, J. W. (2016) Impact of antecedent conditions on simulations of a flood in a mountain headwater basin. *Hydrological Processes*, 30(16), 2754-2772. doi:10.1002/hyp.10910

Favaro, E. A. & Lamoureux, S. F. J. G. A. S. A., Physical Geography (2014) Antecedent controls on rainfall runoff response and sediment transport in a High Arctic catchment, 96(4), 433-446. doi:10.1111/geoa.12063

Fayad, I., Baghdadi, N., Bazzi, H. & Zribi, M. (2020) Near real-time freeze detection over agricultural plots using Sentinel-1 data. *Remote Sens.*, 12(12), 1976. doi:10.3390/rs12121976

Filipponi, F. (2019) Sentinel-1 GRD preprocessing workflow, *International Electronic Conference on Remote Sensing*. MDPI.

Fitzhugh, R. D., Driscoll, C. T., Groffman, P. M., Tierney, G. L., Fahey, T. J. & Hardy, J. P. (2001) Effects of soil freezing disturbance on soil solution nitrogen, phosphorus, and carbon chemistry in a northern hardwood ecosystem. *Biogeochemistry*, 56(2), 215-238. doi:10.1023/A:1013076609950

Fox, E. W., Hill, R. A., Leibowitz, S. G., Olsen, A. R., Thornbrugh, D. J. & Weber, M. H. (2017) Assessing the accuracy and stability of variable selection methods for random forest modeling in ecology. *Environ. Monit. Assess.*, 189(7), 316. doi:10.1007/s10661-017-6025-0

Frauenfeld, O. W. & Zhang, T. (2011) An observational 71-year history of seasonally frozen ground changes in the Eurasian high latitudes. *Environmental Research Letters*, 6(4), 044024. doi:10.1088/1748-9326/6/4/044024

Fu, Q., Hou, R., Li, T., Wang, M. & Yan, J. (2018) The functions of soil water and heat transfer to the environment and associated response mechanisms under different snow cover conditions. *Geoderma*, 325, 9-17. doi:10.1016/j.geoderma.2018.03.022

Fu, Q., Hou, R., Li, T., Yan, P. & Ma, Z. (2017) The critical depth of freeze-thaw soil under different types of snow cover. *Water*, 9(6), 370. doi:10.3390/w9060370

Fuhrmann, T. & Garthwaite, M. C. (2019) Resolving three-dimensional surface motion with InSAR: Constraints from multi-geometry data fusion. *Remote Sensing*, 11(3), 241. doi:10.3390/rs11030241

Gao, C., Bai, W., Wang, Z., Wu, X., Liu, L., Deng, N. & Xia, J. (2021a) Simulations and Analysis of GNSS Multipath Observables for Frozen and Thawed Soil under Complex Surface Conditions. *Water*, 13(14), 1986. doi:10.3390/w13141986

Gao, D., Zhang, L., Liu, J., Peng, B., Fan, Z., Dai, W., Jiang, P. & Bai, E. (2018a) Responses of terrestrial nitrogen pools and dynamics to different patterns of freeze-thaw cycle: A meta-analysis. *Global Change Biology*, 24(6), 2377-2389. doi:10.1111/gcb.14010

Gao, H., Zhang, W. & Chen, H. (2018b) An improved algorithm for discriminating soil freezing and thawing using AMSR-E and AMSR2 soil moisture products. *Remote Sensing*, 10(11), 1697. doi:10.3390/rs10111697

Gao, H., Zhang, Z., Chen, H., Zhang, W., Xu, C., Yi, Y., Liu, J. & Xiao, Z. (2023) Impacts of seasonally frozen soil hydrothermal dynamics on the watershed hydrological processes inferred from a spatially distributed numerical modelling approach. *Journal of Hydrology*, 624, 129947. doi:10.1016/j.jhydrol.2023.129947

Gao, H., Zhang, Z., Zhang, W., Chen, H. & Xi, M. (2021b) Spatial Downscaling Based on Spectrum Analysis for Soil Freeze/Thaw Status Retrieved From Passive Microwave. *IEEE Transactions on Geoscience Remote Sensing*. doi:10.1109/TGRS.2021.3051683

Gill, J. P., Yackel, J. J., Geldsetzer, T. & Fuller, M. C. (2015) Sensitivity of C-band synthetic aperture radar polarimetric parameters to snow thickness over landfast smooth first-year sea ice. *Remote Sens. Environ.*, 166, 34-49. doi:10.1016/j.rse.2015.06.005

Goldstein, A., Kapelner, A., Bleich, J. & Pitkin, E. (2015) Peeking inside the black box: Visualizing statistical learning with plots of individual conditional expectation. *J. Comput. Graphical Stat.*, 24(1), 44-65. doi:10.1080/10618600.2014.907095

Gorelick, N., Hancher, M., Dixon, M., Ilyushchenko, S., Thau, D. & Moore, R. (2017) Google Earth Engine: Planetary-scale geospatial analysis for everyone. *Remote Sens. Environ.*, 202, 18-27. doi:10.1016/j.rse.2017.06.031

Gorjizade, A. & Shahbazi, A. J. E. S. I. (2025) Analysis of spatial distribution of precipitation using hydrological modeling of watersheds (Case Study: Dez Dam Watershed), 18(1), 154. doi:10.1007/s12145-024-01612-z

Gray, D., Landine, P. & Granger, R. (1985) Simulating infiltration into frozen prairie soils in streamflow models. *Can. J. Earth Sci.*, 22(3), 464-472. doi:10.1139/e85-045

Gray, D., Toth, B., Zhao, L., Pomeroy, J. & Granger, R. J. H. P. (2001) Estimating areal snowmelt infiltration into frozen soils, 15(16), 3095-3111. doi:10.1002/hyp.320

Guo, D. & Wang, H. (2014) Simulated change in the near-surface soil freeze/thaw cycle on the Tibetan Plateau from 1981 to 2010. *Chinese Science Bulletin*, 59(20), 2439-2448. doi:10.1007/s11434-014-0347-x

Guo, D., Yang, M. & Wang, H. (2011) Sensible and latent heat flux response to diurnal variation in soil surface temperature and moisture under different freeze/thaw soil conditions in the seasonal frozen soil region of the central Tibetan Plateau. *Environmental Earth Sciences*, 63(1), 97-107. doi:10.1007/s12665-010-0672-6

Guo, L.-m., Chang, J., Xu, H.-l. & Sun, W.-j. J. J. o. M. S. (2021) Modelling plant canopy effects on water-heat exchange in the freezing-thawing processes of active layer on the Qinghai-Tibet Plateau, 18(6), 1564-1579. doi:10.1007/s11629-020-6335-5

Hagos, S. M., Leung, L. R., Garuba, O. A., Demott, C., Harrop, B., Lu, J. & Ahn, M.-S. J. J. o. C. (2021) The relationship between precipitation and precipitable water in CMIP6 simulations and implications for tropical climatology and change, 34(5), 1587-1600. doi:10.1175/JCLI-D-20-0211.1

Hallikainen, M. T., Ulaby, F. T., Dobson, M. C., El-Rayes, M. A. & Wu, L.-K. (1985) Microwave dielectric behavior of wet soil-part 1: Empirical models and experimental observations. *IEEE Transactions on geoscience remote sensing*(1), 25-34. doi:10.1109/TGRS.1985.289497

Hedges, L. V. & Olkin, I. (2014) *Statistical methods for meta-analysis*Academic press.

Henry, H. A. (2007) Soil freeze–thaw cycle experiments: trends, methodological weaknesses and suggested improvements. *Soil Biology Biochemistry*, 39(5), 977-986. doi:10.1016/j.soilbio.2006.11.017

Holah, N., Baghdadi, N., Zribi, M., Bruand, A. & King, C. (2005) Potential of ASAR/ENVISAT for the characterization of soil surface parameters over bare agricultural fields. *Remote sensing of environment*, 96(1), 78-86. doi:10.1016/j.rse.2005.01.008

Hou, R., Wang, L., O'Connor, D., Tsang, D. C., Rinklebe, J. & Hou, D. (2020) Effect of immobilizing reagents on soil Cd and Pb lability under freeze-thaw cycles: Implications for sustainable agricultural management in seasonally frozen land. *Environ. Int.*, 144, 106040. doi:10.1016/j.envint.2020.106040

Huang, S., Ding, J., Zou, J., Liu, B., Zhang, J. & Chen, W. (2019) Soil moisture retrival based on sentinel-1 imagery under sparse vegetation coverage. *Sensors*, 19(3), 589. doi:10.3390/s19030589

Hudier, E. & Gosselin, J.-S. (2010) Impact of daily melt and freeze patterns on sea ice large scale roughness features extraction, *Geoscience and Remote Sensing New Achievements*IntechOpen.

IPCC (2019) *Special report on the ocean and cryosphere in a changing climate*.

Ireson, A., Van Der Kamp, G., Ferguson, G., Nachshon, U. & Wheater, H. (2013a) Hydrogeological processes in seasonally frozen northern latitudes: understanding, gaps and challenges. *Hydrogeol. J.*, 21(1), 53. doi:10.1007/s10040-012-0916-5

Ireson, A., Van Der Kamp, G., Ferguson, G., Nachshon, U. & Wheater, H. J. H. J. (2013b) Hydrogeological processes in seasonally frozen northern latitudes: understanding, gaps and challenges, 21(1), 53-66. doi:10.1007/s10040-012-0916-5

Jagdhuber, T., Stockamp, J., Hajnsek, I. & Ludwig, R. (2014) Identification of soil freezing and thawing states using SAR polarimetry at C-band. *Remote Sens.*, 6(3), 2008-2023. doi:10.3390/rs6032008

Jagtar Bhatti, V. B., Mark Castonguay, R. E. & Arp, P. A. (2006) Modeling snowpack and soil temperature and moisture conditions in a jack pine, black spruce and aspen forest stand in central Saskatchewan (BOREAS SSA). *Canadian Journal of Soil Science*, 86(Special Issue), 203-217. doi:10.4141/S05-088

Jansson, J. K. & Hofmockel, K. S. (2020) Soil microbiomes and climate change. *Nature Reviews Microbiology*, 18(1), 35-46. doi:10.1038/s41579-019-0265-7

Ji, X., Liu, M., Yang, J. & Feng, F. (2022) Meta-analysis of the impact of freeze–thaw cycles on soil microbial diversity and C and N dynamics. *Soil Biology Biochemistry*, 168, 108608. doi:10.1016/j.soilbio.2022.108608

Jiang, H., Yi, Y., Yang, K., Zhao, L., Chen, D., Kimball, J. S. & Lu, F. (2024) Soil freeze/thaw dynamics strongly influences runoff regime in a Tibetan permafrost

watershed: Insights from a process-based model. *Catena*, 243, 108182. doi:10.1016/j.catena.2024.108182

Jiang, R., Li, T., Liu, D., Fu, Q., Hou, R., Li, Q., Cui, S. & Li, M. (2021) Soil infiltration characteristics and pore distribution under freezing–thawing conditions. *The Cryosphere*, 15(4), 2133-2146. doi:10.1002/essoar.10504385.1

Jin, R., Zhang, T., Li, X., Yang, X. & Ran, Y. (2015) Mapping surface soil freeze-thaw cycles in China based on SMMR and SSM/I brightness temperatures from 1978 to 2008. *Arctic, Antarctic, Alpine Research*, 47(2), 213-229. doi:10.1657/AAAR00C-13-304

Johnston, J. M., Houser, P. R., Maggioni, V., Kim, R. S. & Vuyovich, C. (2021) Informing improvements in freeze/thaw state classification using subpixel temperature. *IEEE Trans. Geosci. Remote Sens.*, 60, 1-19. doi:10.1109/TGRS.2021.3099292

Joseph, G. & Henry, H. A. (2008) Soil nitrogen leaching losses in response to freeze–thaw cycles and pulsed warming in a temperate old field. *Soil Biology Biochemistry*, 40(7), 1947-1953. doi:10.1016/j.soilbio.2008.04.007

Karthikeyan, L., Pan, M., Wanders, N., Kumar, D. N. & Wood, E. F. (2017) Four decades of microwave satellite soil moisture observations: Part 1. A review of retrieval algorithms. *Adv. Water Resour.*, 109, 106-120. doi:10.1016/j.advwatres.2017.09.006

Katz, L., Lewis, G., Krogh, S., Drake, S., Hanan, E., Hatchett, B. & Harpold, A. (2023) Antecedent snowpack cold content alters the hydrologic response to extreme rain-on-snow events. *Journal of Hydrometeorology*, 24(10), 1825-1846. doi:10.1175/JHM-D-22-0090.1

Khaldoune, J., Van Bochove, E., Bernier, M. & Nolin, M. C. (2011) Mapping agricultural frozen soil on the watershed scale using remote sensing data. *Applied Environmental Soil Science*, 2011(1), 193237. doi:10.1155/2011/193237

Kim, Y., Kimball, J. S., Glassy, J. & Du, J. (2017) An extended global Earth system data record on daily landscape freeze–thaw status determined from satellite passive microwave remote sensing. *Earth System Science Data*, 9(1), 133-147. doi:10.5194/essd-9-133-2017

Kim, Y., Kimball, J. S., McDonald, K. C. & Glassy, J. (2010a) Developing a global data record of daily landscape freeze/thaw status using satellite passive microwave remote sensing. *IEEE Trans. Geosci. Remote Sens.*, 49(3), 949-960. doi:10.1109/TGRS.2010.2070515

Kim, Y., Kimball, J. S., McDonald, K. C. & Glassy, J. (2010b) Developing a global data record of daily landscape freeze/thaw status using satellite passive microwave remote sensing. *IEEE Transactions on Geoscience Remote Sensing*, 49(3), 949-960. doi:10.1109/TGRS.2010.2070515

Kim, Y., Kimball, J. S., McDonald, K. C., Glassy, J. J. I. T. o. G. & Sensing, R. (2010c) Developing a global data record of daily landscape freeze/thaw status using satellite passive microwave remote sensing, 49(3), 949-960. doi:10.1109/TGRS.2010.2070515

Kim, Y., Kimball, J. S., Xu, X., Dunbar, R. S., Colliander, A. & Derksen, C. (2019) Global assessment of the SMAP freeze/thaw data record and regional applications for detecting spring onset and frost events. *Remote Sensing*, 11(11), 1317. doi:10.3390/rs11111317

Kimball, J. S., McDonald, K., Frolking, S. & Running, S. W. (2004) Radar remote sensing of the spring thaw transition across a boreal landscape. *Remote Sensing of Environment*, 89(2), 163-175. doi:10.1016/j.rse.2002.06.004

Kimball, J. S., McDonald, K., Keyser, A. R., Frolking, S. & Running, S. W. (2001) Application of the NASA scatterometer (NSCAT) for determining the daily frozen and nonfrozen landscape of Alaska. *Remote Sensing of Environment*, 75(1), 113-126. doi:10.1016/S0034-4257(00)00160-7

Kimball, J. S., McDonald, K. & Zhao, M. J. E. I. (2006) Spring thaw and its effect on terrestrial vegetation productivity in the western Arctic observed from satellite microwave and optical remote sensing, 10(21), 1-22. doi:10.1175/EI187.1

Kinnard, C., Nemri, S. & Assani, A. (2024) Mechanisms of spring freshet generation in southern Quebec, Canada. *Canadian Water Resources Journal/Revue canadienne des ressources hydriques*, 49(4), 421-440. doi:10.1080/07011784.2024.2375346

Kirchner, J. W. J. H. & Sciences, E. S. (2019) Quantifying new water fractions and transit time distributions using ensemble hydrograph separation: theory and benchmark tests, 23(1), 303-349.

Kloffel, T., Larsbo, M., Jarvis, N. & Barron, J. (2024) Freeze-thaw effects on pore space and hydraulic properties of compacted soil and potential consequences with climate change. *Soil Tillage Research*, 239. doi:10.1016/j.still.2024.106041

Kompanizare, M., Costa, D., Macrae, M. L., Pomeroy, J. W. & Petrone, R. M. (2024) Developing a tile drainage module for the Cold Regions Hydrological Model: lessons from a farm in southern Ontario, Canada. *Hydrology Earth System Sciences*, 28(13), 2785-2807. doi:10.5194/hess-28-2785-2024

Kondo, J. & Yamazaki, T. (1990) A prediction model for snowmelt, snow surface temperature and freezing depth using a heat balance method. *Journal of Applied Meteorology*, 375-384. doi:http://www.jstor.org/stable/26184709

Kreyling, J., Schumann, R. & Weigel, R. (2020) Soils from cold and snowy temperate deciduous forests release more nitrogen and phosphorus after soil freeze–thaw cycles than soils from warmer, snow-poor conditions. *Biogeosciences*, 17(15), 4103-4117. doi:10.5194/bg-17-4103-2020

Krogstad, K. (2021) *Impact of Winter Soil Processes on Nutrient Leaching in Cold Region Agroecosystems*. Master of Science Master of Science in Earth Sciences (Water). University of Waterloo, 2021.

Lafrenière, M. J., Laurin, E. & Lamoureux, S. F. (2013) The impact of snow accumulation on the active layer thermal regime in high Arctic soils. *Vadose Zone Journal*, 12(1), vzj2012. 0058. doi:10.2136/vzj2012.0058

Lai, Y., Pei, W., Zhang, M. & Zhou, J. (2014) Study on theory model of hydro-thermal–mechanical interaction process in saturated freezing silty soil. *International Journal of Heat Mass Transfer*, 78, 805-819. doi:10.1016/j.ijheatmasstransfer.2014.07.035

Lane, R. A., Bell, V. A., Chapman, R. M. & Kay, A. L. (2024) Evaluating soil moisture simulations from a national-scale gridded hydrological model over Great Britain. *Journal of Hydrology: Regional Studies*, 52, 101735. doi:10.1016/j.ejrh.2024.101735

Lazoglou, G., Economou, T., Anagnostopoulou, C., Zittis, G., Tzyrkalli, A., Georgiades, P. & Lelieveld, J. J. G. M. D. (2024) Multivariate adjustment of drizzle bias using machine learning in European climate projections, 17(11), 4689-4703. doi:10.5194/gmd-17-4689-2024

Lee, J.-S., Wen, J.-H., Ainsworth, T. L., Chen, K.-S. & Chen, A. (2008) Improved sigma filter for speckle filtering of SAR imagery. *IEEE Transactions on Geoscience and Remote Sensing*, 47(1), 202-213. doi:10.1109/TGRS.2008.2002881

Leonardini, G., Anctil, F., Abrahamowicz, M., Gaborit, É., Vionnet, V., Nadeau, D. F. & Fortin, V. (2020) Evaluation of the Soil, Vegetation, and Snow (SVS) land surface model for the simulation of surface energy fluxes and soil moisture under snow-free conditions. *Atmosphere*, 11(3), 278. doi:10.3390/atmos11030278

Leuther, F. & Schlüter, S. (2021) Impact of freeze–thaw cycles on soil structure and soil hydraulic properties. *Soil*, 7(1), 179-191. doi:10.5194/soil-7-179-2021

Lévesque, V. P., Boucher, É. & Proulx, G. (2019) Spatial distribution of ice jamming processes in the l'acadie river watershed, montérégie: a hydrogeomorphological approach. doi:10.7202/10.7202/1059878ar

Li, H., Li, X., Yang, D., Wang, J., Gao, B., Pan, X., Zhang, Y. & Hao, X. J. J. o. G. R. A. (2019) Tracing snowmelt paths in an integrated hydrological model for understanding seasonal snowmelt contribution at basin scale, 124(16), 8874-8895. doi:10.1029/2019JD030760

Li, N., Cuo, L. & Zhang, Y. (2021a) On the freeze–thaw cycles of shallow soil and connections with environmental factors over the Tibetan Plateau. *Climate Dynamics*, 57(11), 3183-3206. doi:10.1007/s00382-021-05860-3

Li, N., Cuo, L., Zhang, Y. & Flerchinger, G. N. (2024) Diurnal soil freeze-thaw cycles and the factors determining their changes in warming climate in the upper Brahmaputra basin of the Tibetan Plateau. *Journal of Geophysical Research: Atmospheres*, 129(20), e2023JD040369. doi:10.1029/2023JD040369

Li, T., Chen, Y.-Z., Han, L.-J., Cheng, L.-H., Lv, Y.-H., Fu, B.-J., Feng, X.-M. & Wu, X. (2021b) Shortened duration and reduced area of frozen soil in the Northern Hemisphere. *The Innovation*, 2(3). doi:10.1016/j.xinn.2021.100146

Li, T., Chen, Y.-Z., Han, L.-J., Cheng, L.-H., Lv, Y.-H., Fu, B.-J., Feng, X.-M. & Wu, X. J. T. I. (2021c) Shortened duration and reduced area of frozen soil in the Northern Hemisphere. *The Innovation*, 2(3). doi:10.1016/j.xinn.2021.100146

Li, X., Wei, Y. & Li, F. J. J. o. H. (2021d) Optimality of antecedent precipitation index and its application, 595, 126027. doi:10.1016/j.jhydrol.2021.126027

Li, Y., Fu, Q., Li, T., Liu, D., Hou, R., Li, Q., Yi, J., Li, M. & Meng, F. (2021e) Snow melting water infiltration mechanism of farmland freezing-thawing soil and determination of meltwater infiltration parameter in seasonal frozen soil areas. *Agricultural Water Management*, 258, 107165. doi:10.1016/j.agwat.2021.107165

Liang, J., Hu, Z., Liu, S., Zhong, G., Zhen, Y., Makhinov, A. N. & Araruna, J. T. (2022a) Residual-oriented optimization of antecedent precipitation index and its impact on flood prediction uncertainty. *Water*, 14(20), 3222. doi:10.3390/w14203222

Liang, J., Hu, Z., Liu, S., Zhong, G., Zhen, Y., Makhinov, A. N. & Araruna, J. T. J. W. (2022b) Residual-Oriented Optimization of Antecedent Precipitation Index and Its Impact on Flood Prediction Uncertainty, 14(20), 3222. doi:10.3390/w14203222

Light, C. X., Arbic, B. K., Martin, P. E., Brodeau, L., Farrar, J. T., Griffies, S. M., Kirtman, B. P., Laurindo, L. C., Menemenlis, D. & Molod, A. J. C. d. (2022) Effects of grid spacing on high-frequency precipitation variance in coupled high-resolution global ocean–atmosphere models, 59(9), 2887-2913. doi:10.1007/s00382-022-06257-6

Lin, P., He, Z., Du, J., Chen, L., Zhu, X. & Tian, Q. (2022) Understanding the hydrological regime based on the runoff events in a mountainous catchment with seasonally frozen soil in the Qinghai-Tibet plateau. *Hydrological Processes*, 36(10), e14716. doi:10.1002/hyp.14716

Lindström, G., Bishop, K. & Löfvenius, M. O. (2002) Soil frost and runoff at Svartberget, northern Sweden—measurements and model analysis. *Hydrological processes*, 16(17), 3379-3392. doi:10.1002/hyp.1106

Liu, J. & Lobb, D. A. (2021) An overview of crop and crop residue management impacts on crop water use and runoff in the Canadian prairies. *Water*, 13(20), 2929. doi:10.3390/w13202929

Lund, J., Forster, R. R., Deeb, E. J., Liston, G. E., Skiles, S. M. & Marshall, H.-P. (2022) Interpreting Sentinel-1 SAR backscatter signals of snowpack surface melt/freeze, warming, and ripening, through field measurements and physically-based SnowModel. *Remote Sens.*, 14(16), 4002. doi:10.3390/rs14164002

Lundberg, A., Gustafsson, D., Stumpp, C., Kløve, B. & Feiccabrino, J. (2016a) Spatiotemporal variations in snow and soil frost—a review of measurement techniques. *Hydrology Earth System Sciences*, 3(3), 28. doi:10.3390/hydrology3030028

Lundberg, A., Gustafsson, D., Stumpp, C., Kløve, B. & Feiccabrino, J. J. H. (2016b) Spatiotemporal variations in snow and soil frost—A review of measurement techniques, 3(3), 28. doi:10.3390/hydrology3030028

Luo, S., Wang, J., Pomeroy, J. W. & Lyu, S. (2020a) Freeze–thaw changes of seasonally frozen ground on the Tibetan Plateau from 1960 to 2014. *Journal of Climate*, 33(21), 9427-9446. doi:10.1175/JCLI-D-19-0923.1

Luo, X., Fan, X., Ji, X. & Li, Y. (2020b) Hydrological impacts of interannual variations in surface soil freezing processes in the upper Nu–Salween River basin. *Arctic, Antarctic, Alpine Research*, 52(1), 1-12. doi:10.1080/15230430.2019.1698893

Manickam, S. & Barros, A. (2020) Parsing synthetic aperture radar measurements of snow in complex terrain: Scaling behaviour and sensitivity to snow wetness and landcover. *Remote Sens.*, 12(3), 483. doi:10.3390/rs12030483

Matzler, C. & Wegmuller, U. (1987) Dielectric properties of freshwater ice at microwave frequencies. *J. Phys. D: Appl. Phys.*, 20(12), 1623. doi:10.1088/0022-3727/20/12/013

Matzner, E. & Borken, W. (2008) Do freeze-thaw events enhance C and N losses from soils of different ecosystems? A review. *European Journal of Soil Science*, 59(2), 274-284. doi:10.1111/j.1365-2389.2007.00992.x

Mavrovic, A., Pardo Lara, R., Berg, A., Demontoux, F., Royer, A. & Roy, A. (2021) Soil dielectric characterization during freeze–thaw transitions using L-band coaxial and soil moisture probes. *Hydrol. Earth Syst. Sci.*, 25(3), 1117-1131. doi:10.5194/hess-25-1117-2021

McColl, K. A., Roy, A., Derksen, C., Konings, A. G., Alemohammed, S. H. & Entekhabi, D. (2016) Triple collocation for binary and categorical variables: Application to validating landscape freeze/thaw retrievals. *Remote Sens. Environ.*, 176, 31-42. doi:10.1016/j.rse.2016.01.010

McDonald, K., Podest, E., Dunbar, S., Njoku, E. & Kimball, J. (2012) *Algorithm Theoretical Basis Document (ATBD) SMAP Level 3 Radar Freeze/Thaw Data Product (L3_FT_A)* California (USA): Technology, J. P. L. C. I. o.

McDonald, K. C., Kimball, J. S., Zhao, M., Njoku, E., Zimmermann, R. & Running, S. W. (2004) Spaceborne microwave remote sensing of seasonal freeze-thaw processes in the terrestrial high latitudes: Relationships with land-atmosphere CO2 exchange, *Microwave Remote Sensing of the Atmosphere and Environment IV*. International Society for Optics and Photonics.

McNairn, H. & Brisco, B. (2004) The application of C-band polarimetric SAR for agriculture: A review. *Can. J. Remote Sens.*, 30(3), 525-542. doi:10.5589/m03-069

Miller, S. D., Straka III, W., Mills, S. P., Elvidge, C. D., Lee, T. F., Solbrig, J., Walther, A., Heidinger, A. K. & Weiss, S. C. J. R. S. (2013) Illuminating the capabilities of the suomi national polar-orbiting partnership (NPP) visible infrared imaging radiometer suite (VIIRS) day/night band, 5(12), 6717-6766. doi:10.3390/rs5126717

Mohammed, A. A., Cey, E. E., Hayashi, M. & Callaghan, M. V. (2021a) Simulating preferential flow and snowmelt partitioning in seasonally frozen hillslopes. *Hydrological Processes*, 35(8), e14277. doi:10.1002/hyp.14277

Mohammed, A. A., Cey, E. E., Hayashi, M., Callaghan, M. V., Park, Y. J., Miller, K. L. & Frey, S. K. (2021b) Dual-permeability modeling of preferential flow and snowmelt partitioning in frozen soils. *Vadose Zone Journal*, 20(2), e20101. doi:10.1002/vzj2.20101

Mohammed, A. A., Kurylyk, B. L., Cey, E. E. & Hayashi, M. (2018) Snowmelt infiltration and macropore flow in frozen soils: Overview, knowledge gaps, and a conceptual framework. *Vadose Zone Journal*, 17(1), 1-15. doi:10.2136/vzj2018.04.0084

Mohammed, A. A., Pavlovskii, I., Cey, E. E. & Hayashi, M. (2019) Effects of preferential flow on snowmelt partitioning and groundwater recharge in frozen soils. *Hydrology Earth System Sciences*, 23(12), 5017-5031. doi:10.5194/hess-23-5017-2019

Molotch, N. P., Brooks, P. D., Burns, S. P., Litvak, M., Monson, R. K., McConnell, J. R., Musselman, K. J. E. E., Land & Water Process Interactions, E. (2009) Ecohydrological controls on snowmelt partitioning in mixed-conifer sub-alpine forests, 2(2), 129-142. doi:10.1002/eco.48

Moradi, M., Cho, E., Jacobs, J. M. & Vuyovich, C. M. (2023a) Seasonal soil freeze/thaw variability across North America via ensemble land surface modeling. *Cold Regions Science Technology*, 209, 103806. doi:10.1016/j.coldregions.2023.103806

Moradi, M., Cho, E., Jacobs, J. M. & Vuyovich, C. M. (2023b) Seasonal soil freeze/thaw variability across North America via ensemble land surface modeling. *Cold Reg. Sci. Technol.*, 209, 103806. doi:10.1016/j.coldregions.2023.103806

Moradi, M., Kraatz, S., Johnston, J. & Jacobs, J. M. J. R. S. (2024) Comparing Three Freeze-Thaw Schemes Using C-Band Radar Data in Southeastern New Hampshire, USA, 16(15), 2784. doi:10.3390/rs16152784

Mugunthan, J. S., Duguay, C. R. & Zakharova, E. (2023) Machine learning based classification of lake ice and open water from Sentinel-3 SAR altimetry waveforms. *Remote Sens. Environ.*, 299, 113891. doi:10.1016/j.rse.2023.113891

Muñoz-Sabater, J., Dutra, E., Agustí-Panareda, A., Albergel, C., Arduini, G., Balsamo, G., Boussetta, S., Choulga, M., Harrigan, S. & Hersbach, H. (2021) ERA5-Land: A state-of-the-art global reanalysis dataset for land applications. *Earth Syst. Sci. Data*, 13(9), 4349-4383. doi:10.5194/essd-13-4349-2021

Niu, G.-Y. & Yang, Z.-L. (2006) Effects of frozen soil on snowmelt runoff and soil water storage at a continental scale. *J. Hydrometeorol.*, 7(5), 937-952. doi:10.1175/JHM538.1

Norouzi, E., Li, B. J. I. J. f. N. & Geomechanics, A. M. i. (2024) Finite element modeling of thermal-hydro-mechanical coupled processes in unsaturated freezing soils considering air-water capillary pressure and cryosuction, 48(11), 2944-2970. doi:10.1002/nag.3761

Odey, G. & Cho, Y. (2025) Event-based vs. continuous hydrological modeling with HEC-HMS: A review of use cases, methodologies, and performance metrics. Hydrology 12 (2), 39.

Osei, A. K., Rezanezhad, F. & Oelbermann, M. (2024) Impact of freeze-thaw cycles on greenhouse gas emissions in marginally productive agricultural land under different perennial bioenergy crops. *J. Environ. Manage.*, 357, 120739. doi:10.1016/j.jenvman.2024.120739

Outcalt, S. I., Nelson, F. E. & Hinkel, K. M. (1990) The zero-curtain effect: Heat and mass transfer across an isothermal region in freezing soil. *Water Resour. Res.*, 26(7), 1509-1516. doi:10.1029/WR026i007p01509

Pardo Lara, R., Berg, A., Warland, J. & Tetlock, E. (2020) In situ estimates of freezing/melting point depression in agricultural soils using permittivity and temperature measurements. *Water Resources Research*, 56(5), e2019WR026020. doi:10.1029/2019WR026020

Park, S.-E. (2015) Variations of microwave scattering properties by seasonal freeze/thaw transition in the permafrost active layer observed by ALOS PALSAR polarimetric data. *Remote Sensing*, 7(12), 17135-17148. doi:10.3390/rs71215874

Park, S.-E., Bartsch, A., Sabel, D., Wagner, W., Naeimi, V. & Yamaguchi, Y. (2011) Monitoring freeze/thaw cycles using ENVISAT ASAR Global Mode. *Remote Sensing of Environment*, 115(12), 3457-3467. doi:10.1016/j.rse.2011.08.009

Peng, X., Frauenfeld, O. W., Cao, B., Wang, K., Wang, H., Su, H., Huang, Z., Yue, D. & Zhang, T. (2016a) Response of changes in seasonal soil freeze/thaw state to climate change from 1950 to 2010 across china. *Journal of Geophysical Research: Earth Surface*, 121(11), 1984-2000. doi:10.1002/2016JF003876

Peng, X., Frauenfeld, O. W., Huang, Y., Chen, G., Wei, G., Li, X., Tian, W., Yang, G., Zhao, Y. & Mu, C. (2024) The thermal effect of snow cover on ground surface temperature in the Northern Hemisphere. *Environmental Research Letters*, 19(4), 044015. doi:10.1088/1748-9326/ad30a5

Peng, X., Zhang, T., Cao, B., Wang, Q., Wang, K., Shao, W. & Guo, H. (2016b) Changes in freezing-thawing index and soil freeze depth over the Heihe River Basin, western China. *AAAR*, 48(1), 161-176. doi:10.1657/AAAR00C-13-127

Pivot, F. C. (2012) C-band SAR imagery for snow-cover monitoring at Treeline, Churchill, Manitoba, Canada. *Remote Sens.*, 4(7), 2133-2155. doi:10.3390/rs4072133

Podest, E., McDonald, K. C. & Kimball, J. S. (2014) Multisensor microwave sensitivity to freeze/thaw dynamics across a complex boreal landscape. *IEEE Transactions on Geoscience Remote Sensing*, 52(11), 6818-6828. doi:10.1109/TGRS.2014.2303635

Pomeroy, J., Brown, T., Fang, X., Shook, K. R., Pradhananga, D., Armstrong, R., Harder, P., Marsh, C., Costa, D. & Krogh, S. A. (2022) The cold regions hydrological modelling platform for hydrological diagnosis and prediction based on process understanding. *Journal of Hydrology*, 615, 128711. doi:10.1016/j.jhydrol.2022.128711

Pomeroy, J. & Brun, E. (2001) Physical properties of snow, *Snow ecology: An interdisciplinary examination of snow-covered ecosystems*, 118.

Pomeroy, J. W., Marks, D., Link, T., Ellis, C., Hardy, J., Rowlands, A. & Granger, R. (2009) The impact of coniferous forest temperature on incoming longwave radiation to melting snow. *Hydrological Processes: An International Journal*, 23(17), 2513-2525. doi:10.1002/hyp.7325

Pozníková, G., Fischer, M., van Kesteren, B., Orság, M., Hlavinka, P., Žalud, Z. & Trnka, M. (2018) Quantifying turbulent energy fluxes and evapotranspiration in agricultural field conditions: A comparison of micrometeorological methods. *Agricultural water management*, 209, 249-263. doi:10.1016/j.agwat.2018.07.041

Putkonen, J. & Roe, G. (2003) Rain-on-snow events impact soil temperatures and affect ungulate survival. *Geophysical research letters*, 30(4). doi:10.1029/2002GL016326

Qin, Y., Bai, Y., Chen, G., Liang, Y., Li, X., Wen, B., Lu, X. & Li, X. (2021a) The effects of soil freeze–thaw processes on water and salt migrations in the western Songnen Plain, China. *Scientific Reports*, 11(1), 1-12. doi:10.1038/s41598-021-83294-x

Qin, Y., Bai, Y., Chen, G., Liang, Y., Li, X., Wen, B., Lu, X. & Li, X. (2021b) The effects of soil freeze–thaw processes on water and salt migrations in the western Songnen Plain, China. *Scientific Reports*, 11(1), 3888. doi:10.1038/s41598-021-83294-x

Rautiainen, K., Lemmetyinen, J., Pulliainen, J., Vehvilainen, J., Drusch, M., Kontu, A., Kainulainen, J., Seppanen, J. J. I. T. o. G. & Sensing, R. (2011) L-band radiometer observations of soil processes in boreal and subarctic environments, 50(5), 1483-1497.

Rautiainen, K., Lemmetyinen, J., Schwank, M., Kontu, A., Ménard, C. B., Mätzler, C., Drusch, M., Wiesmann, A., Ikonen, J. & Pulliainen, J. (2014) Detection of soil freezing from L-band passive microwave observations. *Remote Sensing of Environment*, 147, 206-218. doi:10.1016/j.rse.2014.03.007

Rautiainen, K., Parkkinen, T., Lemmetyinen, J., Schwank, M., Wiesmann, A., Ikonen, J., Derksen, C., Davydov, S., Davydova, A. & Boike, J. (2016) SMOS prototype algorithm for detecting autumn soil freezing. *Remote Sensing of Environment*, 180, 346-360. doi:10.1016/j.rse.2016.01.012

Ren, J. & Vanapalli, S. K. (2020) Effect of freeze–thaw cycling on the soil-freezing characteristic curve of five Canadian soils. *Vadose Zone Journal*, 19(1), e20039. doi:10.1002/vzj2.20039

Rey, D. M., Hinckley, E. L. S., Walvoord, M. A. & Singha, K. (2021) Integrating observations and models to determine the effect of seasonally frozen ground on hydrologic partitioning in alpine hillslopes in the Colorado Rocky Mountains, USA. *Hydrological Processes*, 35(10), e14374. doi:10.1002/hyp.14374

Richardson, E., Trevizani, R., Greenbaum, J. A., Carter, H., Nielsen, M. & Peters, B. (2024) The receiver operating characteristic curve accurately assesses imbalanced datasets. *Patterns*, 5(6). doi:10.1016/j.patter.2024.100994

Rignot, E. & Way, J. B. (1994) Monitoring freeze—thaw cycles along North—South Alaskan transects using ERS-1 SAR. *Remote Sensing of Environment*, 49(2), 131-137. doi:10.1016/0034-4257(94)90049-3

Rodionova, N. (2019a) Identification of Frozen/Thawed Soils in the Areas of Anadyr (Chukotka) and Belaya Gora (Sakha) from the Sentinel 1 Radar Data. *Atmospheric and Oceanic Physics*, 55(9), 1314-1321. doi:10.1134/S0001433819090433

Rodionova, N. V. (2019b) Correlation of the Sentinel 1 Radar Data with Ground-Based Measurements of the Soil Temperature and Moisture. *Izvestiya, Atmospheric and Oceanic Physics*, 55, 939-948. doi:10.1134/S0001433819090421

Rodriguez-Alvarez, N., Munoz-Martin, J. F., Bosch-Lluis, X. & Oudrhiri, K. (2024) Full polarimetric GNSS-R assessment of the freeze and thaw states of the terrestrial cryosphere. *IEEE Transactions on Geoscience Remote Sensing*, 62, 1-11. doi:10.1109/TGRS.2024.3408054

Ross, C. A., Ali, G. A., Spence, C. & Courchesne, F. J. W. R. R. (2021) Evaluating the ubiquity of thresholds in rainfall-runoff response across contrasting environments, 57(1), e2020WR027498. doi:10.1029/2020WR027498

Rowlandson, T. L., Berg, A. A., Roy, A., Kim, E., Lara, R. P., Powers, J., Lewis, K., Houser, P., McDonald, K. & Toose, P. (2018) Capturing agricultural soil freeze/thaw state through remote sensing and ground observations: A soil freeze/thaw validation campaign. *Remote sensing of environment*, 211, 59-70. doi:10.1016/j.rse.2018.04.003

Roy, A., Toose, P., Derksen, C., Rowlandson, T., Berg, A., Lemmetyinen, J., Royer, A., Tetlock, E., Helgason, W. & Sonnentag, O. (2017a) Spatial variability of L-band brightness temperature during freeze/thaw events over a prairie environment. *Remote Sensing*, 9(9), 894. doi:10.3390/rs9090894

Roy, A., Toose, P., Williamson, M., Rowlandson, T., Derksen, C., Royer, A., Berg, A. A., Lemmetyinen, J. & Arnold, L. (2017b) Response of L-Band brightness temperatures to freeze/thaw and snow dynamics in a prairie environment from ground-based radiometer measurements. *Remote Sensing of Environment*, 191, 67-80. doi:10.1016/j.rse.2017.01.017

Royer, A., Picard, G., Vargel, C., Langlois, A., Gouttevin, I. & Dumont, M. (2021) Improved simulation of arctic circumpolar land area snow properties and soil temperatures. *Frontiers in Earth Science*, 9, 685140. doi:10.3389/feart.2021.685140

Ruan, L. & Robertson, G. P. (2017) Reduced snow cover increases wintertime nitrous oxide (N2O) emissions from an agricultural soil in the upper US Midwest. *Ecosystems*, 20(5), 917-927. doi:10.1007/s10021-016-0077-9

Saarela, M. & Jauhiainen, S. (2021) Comparison of feature importance measures as explanations for classification models. *SN Appl. Sci.*, 3(2), 272. doi:10.1007/s42452-021-04148-9

Sakai, A. & Larcher, W. (2012) *Frost survival of plants: responses and adaptation to freezing stress*, *62*Springer Science & Business Media.

Sanchez-Rodriguez, I., Ireson, A., Brannen, R. & Brauner, H. (2025) Insights into freeze–thaw and infiltration in seasonally frozen soils from field observations. *Vadose Zone Journal*, 24(1), e20396. doi:10.1002/vzj2.20396

Sarady, M. & Sahlin, E. A. (2016) The influence of snow cover on ground freeze-thaw frequency, intensity, and duration: An experimental study conducted in coastal northern Sweden. *Norsk Geografisk Tidsskrift-Norwegian Journal of Geography*, 70(2), 82-94. doi:10.1080/00291951.2016.1154102

Scaife, C. I., Singh, N. K., Emanuel, R. E., Miniat, C. F. & Band, L. E. (2020) Non-linear quickflow response as indicators of runoff generation mechanisms. *Hydrological Processes*, 34(13), 2949-2964. doi:10.1002/hyp.13780

Schaufler, S., Bauer-Marschallinger, B., Hochstöger, S. & Wagner, W. (2018) Modelling and correcting azimuthal anisotropy in Sentinel-1 backscatter data. *Remote Sens. Lett.*, 9(8), 799-808. doi:10.1080/2150704X.2018.1480071

Schoener, G. & Stone, M. C. (2019) Impact of antecedent soil moisture on runoff from a semiarid catchment. *Journal of Hydrology*, 569, 627-636. doi:10.1016/j.jhydrol.2018.12.025

Schuur, E. A., Abbott, B. W., Commane, R., Ernakovich, J., Euskirchen, E., Hugelius, G., Grosse, G., Jones, M., Koven, C. & Leshyk, V. (2022) Permafrost and climate change: carbon cycle feedbacks from the warming Arctic. *Annu. Rev. Environ. Resour.*, 47, 343-371. doi:10.1146/annurev-environ-012220-011847

Schuur, E. A., McGuire, A. D., Schädel, C., Grosse, G., Harden, J. W., Hayes, D. J., Hugelius, G., Koven, C. D., Kuhry, P. & Lawrence, D. M. (2015) Climate change and the permafrost carbon feedback. *Nat.*, 520(7546), 171-179. doi:10.1038/nature14338

Sedlar, J., Tjernström, M., Mauritsen, T., Shupe, M. D., Brooks, I. M., Persson, P. O. G., Birch, C. E., Leck, C., Sirevaag, A. & Nicolaus, M. (2011) A transitioning Arctic surface energy budget: the impacts of solar zenith angle, surface albedo and cloud radiative forcing. *Climate dynamics*, 37(7), 1643-1660. doi:10.1007/s00382-010-0937-5

Shan, W., Wu, J. & Guo, Y. (2025) Establishment and Experimental Validation of a Temperature–Unfrozen Water Content Model for Frozen Soil. *Water*, 17(6), 846. doi:10.3390/w17060846

Shanley, J. B. & Chalmers, A. (1999) The effect of frozen soil on snowmelt runoff at Sleepers River, Vermont. *Hydrological Processes*, 13(12-13), 1843-1857. doi:10.1002/(SICI)1099-1085(199909)13:12/13<1843::AID-HYP879>3.0.CO;2-G

Shao, W. & Zhang, T. (2020a) Assessment of Four Near-Surface Soil Freeze/Thaw Detection Algorithms Based on Calibrated Passive Microwave Remote Sensing Data Over China. *Earth and Space Science*, 7(7), e2019EA000807. doi:10.1029/2019EA000807

Shao, W. & Zhang, T. (2020b) Assessment of Four Near-Surface Soil Freeze/Thaw Detection Algorithms Based on Calibrated Passive Microwave Remote Sensing Data Over China. *ESS*, 7(7), e2019EA000807. doi:10.1029/2019EA000807

Sharratt, B. (2002) Corn stubble height and residue placement in the northern US Corn Belt: Part I. Soil physical environment during winter. *Soil Tillage Research*, 64(3-4), 243-252. doi:10.1016/S0167-1987(01)00260-4

Shi, H., Huang, H., Chang, J., Yuan, C. & Fan, H. (2025) The spatial and temporal distribution of freeze–thaw characteristics of near-surface soil in the Northeast of China and its influencing factors. *Catena*, 249, 108644. doi:10.1016/j.catena.2024.108644

Shrestha, S., Zaramella, M., Callegari, M., Greifeneder, F. & Borga, M. J. C. (2023) Scale dependence of errors in snow water equivalent simulations using ERA5 reanalysis over alpine basins, 11(7), 154. doi:10.3390/cli11070154

Singh, S. K., Prasad, R., Srivastava, P. K., Yadav, S. A., Yadav, V. P. & Sharma, J. (2023) Incorporation of first-order backscattered power in Water Cloud Model for improving the Leaf Area Index and Soil Moisture retrieval using dual-polarized Sentinel-1 SAR data. *Remote Sensing of Environment*, 296, 113756. doi:10.1016/j.rse.2023.113756

Skolunov, A. (1997) Frequency-temperature curve of the complex dielectric constant and refractive index of water. *Fibre Chem.*, 29(6), 367-373. doi:10.1007/BF02418871

Smith, M. W. J. C. J. o. E. S. (1975) Microclimatic influences on ground temperatures and permafrost distribution, Mackenzie Delta, Northwest Territories. *Canadian Journal of Earth Sciences*, 12(8), 1421-1438. doi:10.1139/e75-129

Soltanpour, S. & Foriero, A. (2025) Numerical Modelling of Coupled Thermal–Hydraulic–Mechanical Processes in Unsaturated Soils During Freezing and Thawing. *Water*, 17(5), 677. doi:10.3390/w17050677

Song, S. & Wang, W. (2019) Impacts of antecedent soil moisture on the rainfall-runoff transformation process based on high-resolution observations in soil tank experiments. *Water*, 11(2), 296. doi:10.3390/w11020296

Song, Y., Zou, Y., Wang, G. & Yu, X. (2017) Altered soil carbon and nitrogen cycles due to the freeze-thaw effect: A meta-analysis. *Soil Biology and Biochemistry* 109, 35-49. doi:10.1016/j.soilbio.2017.01.020

Soudani, K., Delpierre, N., Berveiller, D., Hmimina, G., Vincent, G., Morfin, A. & Dufrêne, É. (2021) Potential of Synthetic Aperture Radar Sentinel-1 time series for the monitoring of phenological cycles in a deciduous forest. *bioRxiv*, 2021.02. 04.429811. doi:10.1016/j.jag.2021.102505

Stähli, M. (2017) Hydrological significance of soil frost for pre-alpine areas. *Journal of Hydrology*, 546, 90-102. doi:10.1016/j.jhydrol.2016.12.032

Starkloff, T., Stolte, J., Hessel, R., Ritsema, C. & Jetten, V. J. C. (2018) Integrated, spatial distributed modelling of surface runoff and soil erosion during winter and spring, 166, 147-157. doi:10.1016/j.catena.2018.04.001

Steyerberg, E. W., Vickers, A. J., Cook, N. R., Gerds, T., Gonen, M., Obuchowski, N., Pencina, M. J. & Kattan, M. W. (2010) Assessing the performance of prediction models: a framework for traditional and novel measures. *Epidemiology*, 21(1), 128-138. doi:10.1097/EDE.0b013e3181c30fb2

Stuurop, J. C., van der Zee, S. E. & French, H. K. (2022) The influence of soil texture and environmental conditions on frozen soil infiltration: A numerical investigation. *Cold regions science technolog*, 194, 103456. doi:10.1016/j.coldregions.2021.103456

Sun, L., Chang, X., Yu, X., Jia, G., Chen, L., Wang, Y. & Liu, Z. (2021) Effect of freeze-thaw processes on soil water transport of farmland in a semi-arid area. *Agric. Water Manag.*, 252, 106876. doi:10.1016/j.agwat.2021.106876

Sweidan, A., Niggemann, K., Heider, Y., Ziegler, M. & Markert, B. (2022) Experimental study and numerical modeling of the thermo-hydro-mechanical processes in soil freezing with different frost penetration directions. *Acta Geotechnica*, 17(1), 231-255. doi:10.1007/s11440-021-01191-z

Taghavi-Bayat, A., Ullmann, T., Riedel, B. & Gerke, M. (2024) Detecting soil freeze-thaw dynamics with C-band SAR over permafrost in Northern Sweden and seasonally frozen grounds in the Tibetan Plateau, China. *International Journal of Remote Sensing*, 45(16), 5317-5358. doi:10.1080/01431161.2024.2372079

Taghipourjavi, S., Kinnard, C. & Roy, A. (2024a) *In-situ Soil Temperature Data (2 and 10 cm) in Agro-forested Areas of St-Marthe and St-Maurice for 2020-21 and 2021-22*. (2024, Borealis. Available online: https://doi.org/10.5683/SP3/LGLCKW.

Taghipourjavi, S., Kinnard, C. & Roy, A. (2024b) Sentinel-1-Based Soil Freeze–Thaw Detection in Agro-Forested Areas: A Case Study in Southern Québec, Canada. *Remote Sens.*, 16(7), 1294. doi:10.3390/rs16071294

Taghipourjavi, S., Kinnard, C. & Roy, A. (2026a) On demand machine learning-driven surface freeze-thaw retrieval across Canadian agricultural regions using Sentinel-1 SAR data. *Frontiers in Remote Sensing*, 6, 1728399. doi:10.3389/frsen.2025.1728399

Taghipourjavi, S., Kinnard, C. & Roy, A. (2026b) On Demand Machine Learning-Driven Surface Freeze-Thaw Retrieval Across Canadian Agricultural Regions Using Sentinel-1 SAR Data. *Frontiers in Remote Sensing*. doi:10.3389/frsen.2025.1728399

Tarasova, L., Basso, S., Wendi, D., Viglione, A., Kumar, R. & Merz, R. (2020) A process-based framework to characterize and classify runoff events: The event typology of Germany. *Water Resources Research*, 56(5), e2019WR026951. doi:10.1029/2019WR026951

Tarasova, L., Basso, S., Zink, M. & Merz, R. (2018) Exploring controls on rainfall-runoff events: 1. Time series-based event separation and temporal dynamics of event runoff

response in Germany. *Water Resources Research*, 54(10), 7711-7732. doi:10.1029/2018WR022587

Tetlock, E., Toth, B., Berg, A., Rowlandson, T. & Ambadan, J. T. (2019) An 11-year (2007–2017) soil moisture and precipitation dataset from the Kenaston Network in the Brightwater Creek basin, Saskatchewan, Canada. *Earth Syst. Sci. Data*, 11(2), 787-796. doi:10.5194/essd-11-787-2019

Torres, R., Snoeij, P., Geudtner, D., Bibby, D., Davidson, M., Attema, E., Potin, P., Rommen, B., Floury, N. & Brown, M. (2012) GMES Sentinel-1 mission. *Remote sensing of environment*, 120, 9-24. doi:10.1016/j.rse.2011.05.028

Touati, C., Ratsimbazafy, T., Poulin, J., Bernier, M., Homayouni, S. & Ludwig, R. (2021) Landscape freeze/thaw mapping from active and passive microwave Earth observations over the Tursujuq National Park, Quebec, Canada. *Écoscience*, 28(3-4), 421-433. doi:10.1080/11956860.2021.1969790

Tramblay, Y., Bouvier, C., Martin, C., Didon-Lescot, J.-F., Todorovik, D. & Domergue, J.-M. J. J. o. H. (2010) Assessment of initial soil moisture conditions for event-based rainfall–runoff modelling, 387(3-4), 176-187. doi:10.1016/j.jhydrol.2010.04.006

Tsai, Y.-L. S., Dietz, A., Oppelt, N. & Kuenzer, C. (2019) Remote sensing of snow cover using spaceborne SAR: A review. *Remote Sensing*, 11(12), 1456. doi:10.3390/rs11121456

Vreugdenhil, M., Navacchi, C., Bauer-Marschallinger, B., Hahn, S., Steele-Dunne, S., Pfeil, I., Dorigo, W. & Wagner, W. J. R. S. (2020) Sentinel-1 cross ratio and vegetation optical depth: A comparison over Europe, 12(20), 3404.

Vreugdenhil, M., Wagner, W., Bauer-Marschallinger, B., Pfeil, I., Teubner, I., Rüdiger, C. & Strauss, P. (2018) Sensitivity of Sentinel-1 backscatter to vegetation dynamics: An Austrian case study. *Remote Sens.*, 10(9), 1396. doi:10.3390/rs10091396

Wackerly, D. D. (2008) Mathematical Statistics with Applications. 7th Edition ed. USA: Thomson Learning, Inc.

Walker, V. A., Colliander, A. & Kimball, J. S. (2022) Satellite retrievals of probabilistic freeze-thaw conditions from SMAP and AMSR brightness temperatures. *IEEE Transactions on Geoscience Remote Sensing*, 60, 1-11. doi:10.1109/TGRS.2022.3174807

Walvoord, M. A. & Kurylyk, B. L. (2016) Hydrologic impacts of thawing permafrost—A review. *Vadose Zone Journal* 15(6), vzj2016. 01.0010. doi:10.2136/vzj2016.01.0010

Wan, X., Pei, W., Lu, J., Zhang, X., Yan, Z. & Pirhadi, N. (2022) Prediction of the unfrozen water content in soils based on premelting theory. *Journal of Hydrology*, 608, 127505. doi:10.1016/j.jhydrol.2022.127505

Wang, C., Li, K., Lin, Z., Yang, Z., Cai, H., Lai, Y. & Li, S. (2023) Study on the supercooling characteristics of freezing soil based on nucleation theory. *Water Resources Research*, 59(9), e2023WR034800. doi:10.1029/2023WR034800

Wang, G., Hu, H. & Li, T. J. J. o. H. (2009) The influence of freeze–thaw cycles of active soil layer on surface runoff in a permafrost watershed, 375(3-4), 438-449. doi:10.1016/j.jhydrol.2009.06.046

Wang, J., Jiang, L., Rautiainen, K., Zhang, C., Xiao, Z., Li, H., Yang, J. & Cui, H. (2022) Daily High-Resolution Land Surface Freeze/Thaw Detection Using Sentinel-1 and AMSR2 Data. *Remote Sensing*, 14(12), 2854. doi:10.3390/rs14122854

Wang, K., Zhang, T. & Zhong, X. (2015) Changes in the timing and duration of the near-surface soil freeze/thaw status from 1956 to 2006 across China. *The Cryosphere*, 9(3), 1321-1331. doi:10.5194/tc-9-1321-2015

Wang, R., Zhu, Q., Ma, H. & Ai, N. (2017) Spatial-temporal variations in near-surface soil freeze-thaw cycles in the source region of the Yellow River during the period 2002–2011 based on the Advanced Microwave Scanning Radiometer for the Earth Observing System (AMSR-E) data. *Journal of Arid Land*, 9(6), 850-864. doi:10.1007/s40333-017-0032-4

Wang, T., Li, P., Li, Z., Hou, J., Xiao, L., Ren, Z., Xu, G., Yu, K. & Su, Y. (2019) The effects of freeze–thaw process on soil water migration in dam and slope farmland on the Loess Plateau, China. *Science of The Total Environment* 666, 721-730. doi:10.1016/j.scitotenv.2019.02.284

Watanabe, K. & Osada, Y. (2017a) Simultaneous measurement of unfrozen water content and hydraulic conductivity of partially frozen soil near 0 C. *Cold Regions Science Technology*, 142, 79-84. doi:10.1016/j.coldregions.2017.08.002

Watanabe, K. & Osada, Y. (2017b) Simultaneous measurement of unfrozen water content and hydraulic conductivity of partially frozen soil near 0 C. *Cold Regions Science*

Technology, 142, 79-84. doi:10.1016/j.coldregions.2017.08.002

Watanabe, T., Tateno, R., Imada, S., Fukuzawa, K., Isobe, K., Urakawa, R., Oda, T., Hosokawa, N., Sasai, T. & Inagaki, Y. (2019) The effect of a freeze–thaw cycle on dissolved nitrogen dynamics and its relation to dissolved organic matter and soil microbial biomass in the soil of a northern hardwood forest. *Biogeochemistry*, 142(3), 319-338. doi:10.1007/s10533-019-00537-w

Wei, X., Huang, C., Wei, N., Zhao, H., He, Y. & Wu, X. (2019) The impact of freeze–thaw cycles and soil moisture content at freezing on runoff and soil loss. *LDD*, 30(5), 515-523. doi:10.1002/ldr.3243

Westerberg, I., McMillan, H. K. J. H. & Sciences, E. S. (2015) Uncertainty in hydrological signatures, 19(9), 3951-3968. doi:10.5194/hess-19-3951-2015

Williams, C. M., Henry, H. A. & Sinclair, B. J. (2015) Cold truths: how winter drives responses of terrestrial organisms to climate change. *Biological Reviews*, 90(1), 214-235. doi:10.1111/brv.12105

Wu, N., Zhang, K., Naghibi, A., Hashemi, H., Ning, Z., Zhang, Q., Yi, X., Wang, H., Liu, W. & Gao, W. (2025) Predicting snow cover and frozen ground impacts on large basin

runoff: developing appropriate model complexity. *Hydrology Earth System Sciences*, 29(15), 3703-3725. doi:10.5194/hess-29-3703-2025

Wu, S., Zhao, T., Pan, J., Xue, H., Zhao, L. & Shi, J. (2022) Improvement in modeling soil dielectric properties during freeze-thaw transitions. *IEEE Geoscience Remote Sensing Letters*, 19, 1-5. doi:10.1109/LGRS.2022.3154291

Wu, X., Dong, Z., Jin, S., He, Y., Song, Y., Ma, W. & Yang, L. (2020) First measurement of soil freeze/thaw cycles in the Tibetan Plateau using CYGNSS GNSS-R data. *Remote Sens.*, 12(15), 2361. doi:10.3390/rs12152361

Wu, X., Jin, S. & Chang, L. (2017) Monitoring bare soil freeze–thaw process using GPS-interferometric reflectometry: Simulation and validation. *Remote Sensing*, 10(1), 14. doi:10.3390/rs10010014

Xu, G., Huang, M., Li, P., Li, Z. & Wang, Y. (2021) Effects of land use on spatial and temporal distribution of soil moisture within profiles. *Environmental Earth Sciences*, 80(4), 1-12. doi:10.1007/s12665-021-09464-2

Xu, S., Fu, Q., Li, T., Meng, F., Liu, D., Hou, R., Li, M. & Li, Q. (2022) Spatiotemporal characteristics of the soil freeze-thaw state and its variation under different land use types-A case study in Northeast China. *Agricultural Forest Meteorology*, 312, 108737. doi:10.1016/j.agrformet.2021.108737

Xu, Y., Yang, H., Yue, J., Wei, H., Che, R., Duan, Q., Zhou, S. & Sun, M. J. A. S. (2025) Freezing Behavior of Clayey Sand and Spatiotemporal Evolution of Seasonally Frozen Soil Distribution in the Qinghai–Tibet Plateau, 15(13), 7498. doi:10.3390/app15137498

Xusheng, W., Jishuai, Z., Wansheng, P., Fengxi, Z., Jianguo, L., Zhongrui, Y. & Da, W. (2023) A theoretical model on unfrozen water content in soils and verification. *Journal of Hydrology*, 622, 129675. doi:10.1016/j.jhydrol.2023.129675

Yang, K., Wang, C. J. A. & Meteorology, F. (2019) Water storage effect of soil freeze-thaw process and its impacts on soil hydro-thermal regime variations, 265, 280-294. doi:10.1016/j.agrformet.2018.11.011

Yang, Y., Chen, R.-S., Ding, Y.-J., Li, H.-Y. & Liu, Z.-W. (2024) Changes in global land surface frozen ground and freeze–thaw processes during 1950–2020 based on ERA5-Land data. *Advances in Climate Change Research*, 15(2), 265-274. doi:10.1016/j.accre.2024.03.007

Yi, J., Zhao, Y., Shao, M. a., Zhang, J., Cui, L. & Si, B. (2014) Soil freezing and thawing processes affected by the different landscapes in the middle reaches of Heihe River Basin, Gansu, China. *Journal of Hydrology*, 519, 1328-1338. doi:10.1016/j.jhydrol.2014.08.042

Yu, Z., Wang, W., Li, C., Liu, W. & Yang, J. (2018) Speckle noise suppression in SAR images using a three-step algorithm. *Sens.*, 18(11), 3643. doi:10.3390/s18113643

Zhang, L., Ren, F., Li, H., Cheng, D. & Sun, B. (2021) The influence mechanism of freeze-thaw on soil erosion: a review. *Water*, 13(8), 1010. doi:10.3390/w13081010

Zhang, L., Zhao, T., Jiang, L. & Zhao, S. (2010) Estimate of phase transition water content in freeze–thaw process using microwave radiometer. *IEEE transactions on geoscience remote sensing*, 48(12), 4248-4255. doi:10.1109/TGRS.2010.2051158

Zhang, T. (2005) Influence of the seasonal snow cover on the ground thermal regime: An overview. *Reviews of Geophysics*, 43(4). doi:10.1029/2004RG000157

Zhang, T. & Armstrong, R. (2001) Soil freeze/thaw cycles over snow-free land detected by passive microwave remote sensing. *Geophysical Research Letters*, 28(5), 763-766. doi:10.1029/2000GL011952

Zhang, T., Armstrong, R. & Smith, J. (2003) Investigation of the near-surface soil freeze-thaw cycle in the contiguous United States: Algorithm development and validation. *Journal of Geophysical Research: Atmospheres*, 108(D22). doi:10.1029/2003JD003530

Zhao, Q., Tan, X., Zeng, Q., Zhao, H., Wu, J.-w. & Huang, J.-s. (2021) Combined effects of temperature and precipitation on the spring runoff generation process in a seasonal freezing agricultural watershed. *Environmental Earth Sciences*, 80(15), 490. doi:10.1007/s12665-021-09777-2

Zhao, T., Zhang, L., Jiang, L., Zhao, S., Chai, L. & Jin, R. (2011) A new soil freeze/thaw discriminant algorithm using AMSR-E passive microwave imagery. *Hydrological Processes*, 25(11), 1704-1716. doi:10.1002/hyp.7930

Zhao, Y., Li, Y. & Yang, F. (2020) Critical review on soil phosphorus migration and transformation under freezing-thawing cycles and typical regulatory measurements. *Science of the Total Environment*, 141614. doi:10.1016/j.scitotenv.2020.141614

Zheng, D., van der Velde, R., Su, Z., Wen, J., Wang, X. & Yang, K. (2018) Impact of soil freeze-thaw mechanism on the runoff dynamics of two Tibetan rivers. *Journal of Hydrology*, 563, 382-394. doi:10.1016/j.jhydrol.2018.06.024

Zheng, D., Wang, X., van der Velde, R., Zeng, Y., Wen, J., Wang, Z., Schwank, M., Ferrazzoli, P. & Su, Z. (2017) L-band microwave emission of soil freeze–thaw process in the third pole environment. *IEEE Transactions on Geoscience Remote Sensing*, 55(9), 5324-5338. doi:10.1109/TGRS.2017.2705248

Zheng, G., Yang, Y., Yang, D., Dafflon, B., Yi, Y., Zhang, S., Chen, D., Gao, B., Wang, T. & Shi, R. (2020) Remote sensing spatiotemporal patterns of frozen soil and the environmental controls over the Tibetan Plateau during 2002–2016. *Remote Sensing of Environment*, 247, 111927. doi:10.1016/j.rse.2020.111927

Zhong, W., Yuan, Q., Liu, T. & Yue, L. (2022) Freeze/thaw onset detection combining SMAP and ASCAT data over Alaska: A machine learning approach. *J. Hydrol.*, 605, 127354. doi:10.1016/j.jhydrol.2021.127354

Zhou, X., Zhang, Z., Shen, Q., Chen, Q. & Liu, X. (2021) Identifying soil freeze/thaw states using scattering and coherence time series of high-resolution C-band synthetic aperture radar in the Qinghai-Tibet Plateau. *Journal of Selected Topics in Applied Earth Observations Remote Sensing*, 15, 519-532. doi:10.1109/JSTARS.2021.3137187

Zou, Y., Jiang, H., Wang, E., Liu, X. & Du, S. (2023) Variation and prediction of unfrozen water content in different soils at extremely low temperature conditions. *Journal of Hydrology*, 624, 129900. doi:10.1016/j.jhydrol.2023.129900

Zribi, M., Sahnoun, M., Baghdadi, N., Le Toan, T. & Hamida, A. B. (2016) Analysis of the relationship between backscattered P-band radar signals and soil roughness. *Remote Sensing of Environment* 186, 13-21. doi:10.1016/j.rse.2016.08.006

Zuerndorfer, B. W., England, A. W., Dobson, M. C. & Ulaby, F. T. (1990) Mapping freeze/thaw boundaries with SMMR data. *Agricultural Forest Meteorology*, 52(1-2), 199-225. doi:10.1016/0168-1923(90)90106-G